COMPUTER-AIDED MOLECULAR DESIGN OF DIARYLPYRIMIDINE DERIVATIVES AS HIV-1 NNRTIS: MOLECULAR DOCKING CALCULATIONS AND QSAR STUDIES

Kodchakon Kun-asa[1], Pharit Kamsri[1], Apinya Srisupan[1], Namfon Koohatammakun[1], Auradee Punkvang[2], Patchareenart Saparpakorn[3], Supa Hannongbua[3], Peter Wolschann[4,5], Supakit Prueksaaroon[6] and Pornpan Pungpo[1,*]

[1]*Department of Chemistry, Faculty of Science, Ubon Ratchathani University, 85 Sthollmark Rd., Warinchamrap, Ubonratchathani 34190, Thailand*
[2]*Faculty of Liberal Arts and Sciences, Division of Science, Nakhon Phanom University, Nakhon Phanom, 48000, Thailand*
[3]*Department of Chemistry, Kasetsart University, Chatuchak, Bangkok 10900, Thailand*
[4]*Department of Pharmaceutical Technology and Biopharmaceutics, Faculty of Life Sciences, University of Vienna, Althanstrasse 14, A-1090 Vienna, Austria*
[5]*Department of Drug and Natural Product Synthesis, University of Vienna, Althanstrasse 14, 1090 Vienna, Austria*
[6]*Large-Scale Simulation Research Laboratory, National Electronic and Computer Technology Center (NECTEC), Phatumtani 12120, Thailand*
[*] Author for correspondence; E-Mail: pornpan_ubu@yahoo.com, Tel. +66 45353400 4124, Fax. +66 45288379

Abstract: Diarylpyrimidines (DAPYs) are one of the most commonly compounds for anti- HIV-1 RT as non-nucleoside reverse transcriptase inhibitors. Moreover, the DAPYs derivatives show potential activity in wild type and mutant types. To evaluate the binding interactions of the DAPYs to the HIV-1 RT and the key structural features relating to activities of DAPYs, molecular docking calculations and QSAR approaches based on 2D and 3D-QSAR using HQSAR, CoMFA and CoMSIA, are convenient tools to establish correlations between activities and various molecular properties. Our results indicate that hydrogen bond, interaction and hydrophobic interaction play a key role in the binding and probably also in its biological activity. Moreover, QSAR models using the data sets of wild type HIV-1RT are satisfying based on statistical parameters and predictive ability. Graphical contour interpretations in CoMFA and CoMSIA models indicate the structure requirement to improve the activities of the DAPYs derivatives. The contribution maps obtained from HQSAR model were used to explain the individual atomic contributions to the overall activity. Consequently, the obtained results suggest a structural guideline more efficiently in the rational design of novel compounds which will display a better potency against wild type HIV-1 RT.

1. Introduction

Multi-drug therapy against the human immune-deficiency virus (HIV), known as highly active anti-retroviral therapy (HAART) [1], has drastically reduced the morbidity and mortality of HIV-infected patients during the last decade and slowed down the progression of acquired immunodeficiency syndrome (AIDS). Diarylpyrimidine (DAPY) analogues represent a class of highly potent non-nucleoside reverse transcriptase inhibitors (NNRTIs), endowed with micromolar to nanomolar activity against wild-type (WT) human immunodeficiency virus type 1 (HIV-1) and clinically relevant mutant HIV-1 strains [2]. Highly effective drug against wild-type and drug-resistance of HIV-1 remains essential are required.

Diarylpyrimidine derivatives (DAPY) have been proven to be a next generation of NNRTIs that are extremely potent against both wild-type (WT) and mutant type HIV-1 RT. Naphthyl diarylpyrimidine derivatives are the novel class of DAPY inhibitors. The antiviral and cytotoxicity evaluation indicated that these compounds displayed strong activity against wild-type HIV-1 at nanomolar concentrations. Furthermore, inhibitors exhibited activity against the double mutant (K103N+Y181C) strains [3-5].

To understand the molecular requirement of a novel class of DAPY derivatives, the computer aided molecular design approaches based on molecular docking calculations, and the quantitative structure activity relationship based on 3D-QSAR (Comparative Molecular Field Analysis, CoMFA and Comparative Molecular Similarity Indices Analysis, CoMSIA), and the 2D-QSAR (using Hologram Quantitative Structure Activity Relationship, HQSAR) were performed on a series of DAPY derivatives to achieve the insight into the inhibitor-enzyme interactions and structure activity relationship of DAPY in wild-type.

2. Materials and Methods

2.1 Structures and biological activity of DAPY derivatives

The structures and biological activity of DAPY derivatives were taken from literatures [6-8] as shown in Table 1. Figure 1 shows the general structure of DAPY derivatives in this study. The biological activity was expressed as $\log(1/EC_{50})$, where EC_{50} is the effective concentration of a compound required to achieve 50% protection of MT-4 cell infected with the HIV-1 wild-type virus.

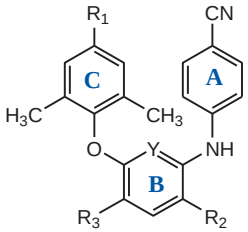

Figure 1 General structure of DAPY derivatives

Table1. Structure and biological activity of DAPY derivatives

2.2 Computational details

No	R_1	R_2	R_3	Y	Log ($1/EC_{50}$)
1	H	NO_2	H	N	6.63
2	CH_3	NO_2	H	N	7.64
3*	CH_2OH	NO_2	H	N	6.32
4	I	NO_2	H	N	7.21
5*	CN	NO_2	H	N	7.66
6	$C\equiv CC(OH)(CH_3)_2$	NO_2	H	N	4.38
7	$C \equiv CH$	NO_2	H	N	6.95
8*	H	NH_2	H	N	8.40
9	CH_3	NH_2	H	N	8.78
10*	CH_2OH	NH_2	H	N	7.96
11*	I	NH_2	H	N	8.12
12	CN	NH_2	H	N	9.17
13	$C\equiv CC(OH)(CH_3)_2$	NH_2	H	N	6.62
14*	$C\equiv CH$	NH_2	H	N	8.17
15	$CH=CHCOCH_3$	NH_2	CF_3	CH	5.07
16	$CH_2CH_2COCH_3$	NH_2	CF_3	CH	4.95
17	CN	NH_2	CF_3	CH	4.88
18*	NH_2	NH_2	CF_3	CH	4.80
19*	CH=CHCN	NH_2	CF_3	CH	4.82
20*	CH_2CH_2CN	NH_2	CF_3	CH	5.15
21	CH=CHCN	NH_2	SO_2NH_2	CH	4.03
22	CH_2CH_2CN	NH_2	SO_2NH_2	CH	3.42
23	CH=CHCN	NH_2	$COOCH_3$	CH	5.56
24*	CH_2CH_2CN	NH_2	$COOCH_3$	CH	5.36
25*	CH=CHCN	NH_2	COOH	CH	3.64
26	CH_2 CH_2CN	NH_2	COOH	CH	4.02
27	CH=CHCN	NH_2	$CONH_2$	CH	6.06
28*	CH_2 CH_2CN	NH_2	$CONH_2$	CH	5.86
29*	CH=CHCN	NH_2	$CONHCH_3$	CH	5.24
30	CH_2 CH_2CN	NH_2	$CONHCH_3$	CH	5.56
31	CH_2 CH_2CN	NH_2	$CONHNH_2$	CH	4.72
32*	CH=CHCN	NH_2	CH_2OH	CH	6.28
33*	CH_2CH_2CN	NH_2	CH_2OH	CH	6.41
34	CH_2CH_2CN	NH_2	NH_2	CH	5.14
35	CH_2OH	NH_2	CH_2OH	CH	5.00
36	Br	NO_2	H	N	7.30
37	Br	NH_2	H	N	8.14
38	$CH_2CH=CH_2$	NH_2	H	N	8.16
39	$C\equiv CC(OH)(CH_2)_2$	NO_2	H	N	4.38
40	$C\equiv CC(OH)(CH_2)_2$	NH_2	H	N	6.62
41	$C\equiv CCH$ $(CH_2)_2$	NO_2	H	N	4.32
42	$C\equiv CCH$ $(CH_2)_2$	NH_2	H	N	7.04
43	$CH(OH)CH_2OH$	NO_2	H	N	6.51
44	$CH(OH)CH_2OH$	NH_2	H	N	8.00
45	CH=CHCOOH	NO_2	H	N	4.83
46*	CH=CHCOOH	NH_2	H	N	6.22
47	$CH=CHCOCH_3$	NO_2	H	N	7.61
48	$CH_2CH_2COCH_3$	NH_2	H	N	8.71
49	CH=CHCN	NO_2	H	N	8.10
50*	CH=CHCN	NH_2	H	N	9.15
51	CH=CHCN	NO_2	H	CH	7.98
52	CH=CHCN	NH_2	H	CH	9.26
53	$CH=CHCOCH_3$	NO_2	NO_2	CH	6.84
54	$CH=CHCOCH_3$	NH_2	NO_2	CH	8.20
55	CH=CHCN	NO_2	NO_2	CH	7.01
56	CH=CHCN	NH_2	NO_2	CH	9.42
57	CH=CHCN	NO_2	NH_2	CH	8.37

*Test set

2.2.1 Molecular docking calculations

All DAPY derivatives were constructed by standard tools in Gaussview 3.07 program and then fully optimized by HF/3-21G method using Gaussian 03 program. Molecular docking calculations were applied to study the binding interactions and molecular alignment for 3D-QSAR studies using Autodock 3.05 program. All DAPY compounds were docked into the wild-type of HIV-1 RT binding pockets which obtained structure of WT HIV-1 RT from X-ray crystallographic data (PDB code: 2ZD1).

2.2.2 QSAR Studies

The binding modes of DAPY in the WT HIV-1 RT binding pocket obtained from molecular docking calculations were used for molecular alignment in CoMFA and CoMSIA studies. SYBYL 8.0 software was used to build the CoMFA, CoMSIA and HQSAR models. To study the relationship between molecular descriptors and activities, the partial least square (PLS) method was employed. To evaluate the predictive ability of the CoMFA, CoMSIA and HQSAR models, the cross-validated correlation coefficient (q^2) and non-cross-validated correlation coefficient (r^2) values were considered. The HQSAR module based on PLS method was used to establish a correlation of the molecular hologram descriptors with the biological data of DAPY inhibitors.

3. Results and Discussion

3.1 The binding interactions of DAPY derivative in WT HIV-1 RT binding pocket

To assess the reliability of the binding modes obtained from molecular docking calculations, compound in the InhA X-ray crystal structure was extracted and docked back into the binding pocket. The root mean-square deviation (rmsd) between the docked and crystallographic conformation of DAPY compound is less than 1 Å, indicating that the molecular docking calculations performed enable highly reliable reproduction of the binding mode of DAPY in the HIV-1 RT binding pocket. Therefore, the molecular docking calculation parameters were applied to all DAPY derivatives in the data set. The binding mode of the highest active compound, compound 56, in the WT HIV-1 RT binding pocket derived by docking calculation is shown in Figure 2. The crucial interactions of the highest active compound can be summarized as following; at phenyl A ring, two hydrogen bond interactions between H atom and OH group of Tyr318, and between N atom and NH backbone of His235 were formed with the distance of 1.81 Å and 3.43 Å, respectively. The NH_2 group attached to the phenyl B ring possibly formed the hydrogen bond linker with NH backbone of Lys101 and NH_3 group of Lys103. Moreover, NH between phenyl A and B rings formed hydrogen bond with O carbonyl group of Lys101 with 2.23 Å. At the R_3 subsitituent, the nitro group possibly formed hydrogen bond interaction with NH backbone of Ile180. The phenyl C ring could form pi-pi interaction

with Tyr181, Phe227 and hydrogen pi interaction with Tye188 and Trp229, respectively. In addition, hydrophobic and van der Waal's interactions between the DAPY scaffold and amino acid residuals surrounding the binding pocket were found, effecting to improve the binding affinities of DAPY derivatives.

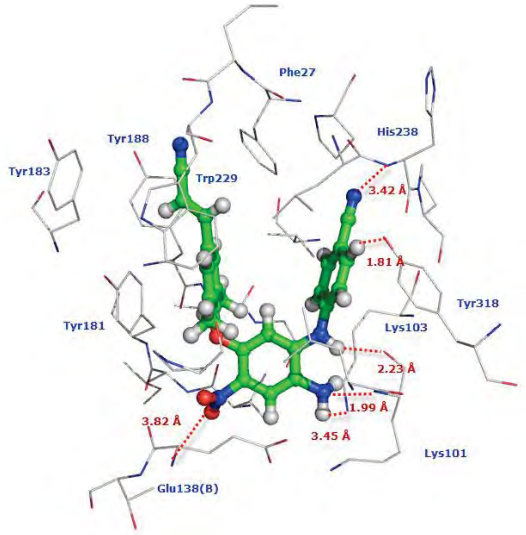

Figure 2 The binding interactions of compound 56, the highest active DAPY compound in HIV-1 RT binding pocket.

3.2 QSAR models

The statistic results of the best CoMFA, CoMSIA and HQSAR models are satisfied based on the predictive ability and statistical significance as shown in Table 2. The CoMFA model composing the steric and electrostatic fields gives cross-validated correlation coefficient (q^2) of 0.61 and non- cross-validated correlation coefficient (r^2) of 0.97. The best CoMSIA model including hydrophobic and hydrogen acceptor fields and hydrogen donor fields give q^2 value of 0.61 and r^2 value of 0.92. The best HQSAR model with satisfied predictive ability value, (q^2 = 0.60) was generated based on the combination of the different fragment types, atom (A), bond (B), connection (C), Hydrogen atom (H) and donor and acceptor (DA).

Table 2 Summary of statistical results of CoMFA, CoMSIA and HQSAR models

Models	Statistical parameters						
	q^2	r^2	N	s	SEE	F	Fraction
CoMFA							
S/E	0.61	0.97	6	1.13	0.32	153	0.51/0.48
CoMSIA							0.07/0.37/
S/E/H/A	0.61	0.92	5	1.13	0.50	81	0.15/0.40
HQSAR							
A/C/B/D/A	0.60	0.91	6	1.17	0.55	-	-

q^2, leave-one-out (LOO) cross-validated correlation coefficient; r^2, non-cross-validated correlation coefficient; N, optimum number of components; s, standard error of prediction; SEE, standard error of estimate; F, F-test value; S, steric field; E, electrostatic field; H, hydrophobic field; A, atom; B, bond; C, connection

3.3 Validation of QSAR models

High correlations between experimental and predicted biological activities of DAPY training set obtained from the best models of CoMFA, CoMSIA and HQSAR, are depicted in Figure 3. These results indicate that QSAR models show high predictive ability for the training set, whereas the predicted biological activities of the compounds in the test set compounds are rather poor with r^2 value of 0.001, 0.001 and 0.7 for CoMFA, CoMSIA and HQSAR models, respectively.

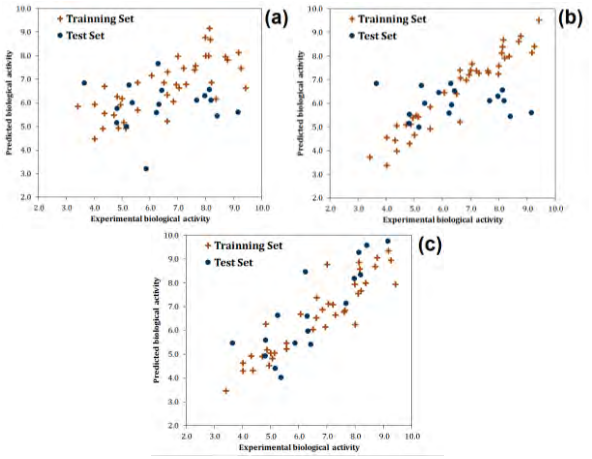

Figure 3 Plots between the experimental biological and predicted biological activities from the best CoMFA (a), CoMSIA (b) and HQSAR (c) models, respectively.

3.4 Graphical interpretation of CoMFA and CoMSIA contour maps of the derivatives

To gain insight into the relationship of structural properties and biological activities of DAPY derivatives, steric, electrostatic, hydrophobic and H-acceptor contour maps for the best CoMFA and CoMSIA models are presented in Figure 4. The interpretation of the contour maps are following; the green, red, magenta and orange contours located at the R_1 substituent attached to the phenyl C ring indicate that the bulky substituents with electron withdrawing would be preferable. Moreover, hydrophobic and hydrogen bond acceptor properties are favorable to improve the biological of DAPY derivatives. This trend is observed by DAPY derivatives, compounds 48-57, substituted at the R_1 positions with bulky, electron withdrawing, hydrophobic and hydrogen bond acceptor groups possessing promising biological activities. These suggestions agree well to the experimental data that highly active compounds possessing log ($1/EC_{50}$) value > 9 have CH=CHCN group attached at the R_1 position. This evidence indicates that the R_1 substituent plays an important role for enhancing the binding activities. The hydrophobic interactions, pi-pi interactions, hydrogen-pi interactions between amino acid residues surrounding the phenyl ring C, namely, Tyr181, Tyr183, Tyr188, Leu228 and Trp229, and the substituent at R_1 position are required to improve the binding affinity and the biological activity. The structural requirement for the R_2 substituent was explained by cyan contour indicating that substituent with hydrogen bond donor property is favorable to enhance the activity of DAPY derivatives. This suggestion is in agreement to the

experimental data showing that for all of DAPY derivatives, there are only two groups, namely NO_2 and NH_2, as the R_2 substituent. The hydrogen bond donor group such as amino group is required for interacting with Lys101 in the HIV-1 RT binding pocket. Gray and orange contours located close to the R_3 substituent indicate that the hydrophilic and hydrogen bond acceptor properties are favorable to increase the anti-HIV-1 RT activity. It can be clearly seen that compounds **53** to **57** possessing the hydrogen bond acceptor and hydrophilic group show high biological activities. These importance of the contour maps at the R_3 position can be described by the hydrogen bond interaction with Val179 and Ile180 backbone of chain A of the R_3 substituent. Moreover, the van der Wall's interaction and electrostatic interaction can be firmed in the HIV-1 RT binding pocket.

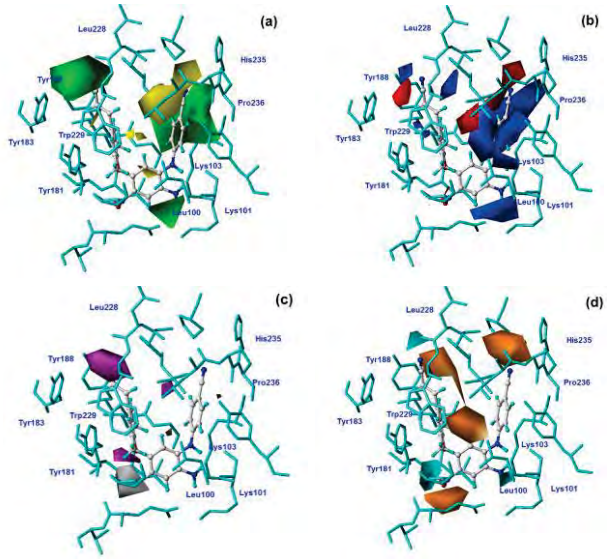

Figure 4 steric (a), electrostatic (b), hydrophobic (c), and H-acceptor (d) contour maps.

3.5 HQSAR contributions

To investigate the individual atomic contributions to the biological activities of DAPY derivatives, HQSAR models were analyzed, as depicted in Figure 5. The atomic contributions corresponding to medium active compounds, as exemplified by compound **42** and the highest active compound, compound **56**, show that NH linker between phenyl A ring and B ring of compound **42** and **56** are in white and green color code, respectively. These contributions indicated that the NH linker is crucial rule for the biological activity. Moreover, phenyl A ring of compound **42** and **56** shows different contributions which can be described by the effect of substituent on the DAPY derivatives. The yellow contribution at the R_1 substituent of compound 24 indicated that C≡CCH $(CH_2)_2$ group is unfavorable substituent for compound **56**. The HQSAR results are highly consistent to the obtained molecular docking and 3D QSAR results.

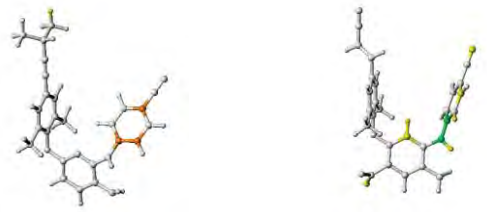

(a) **(b)**

Figure 5 Individual atomic contribution for the activity of (a) medium active compound **42** and (b) highest active compound **56**

4. Conclusions

Molecular docking calculations and QSAR studies were successfully applied to investigate the crucial interaction and structural requirements of DAPY derivatives. Based on structural requirement guideline derived by our CoMFA, CoMSIA and HQSAR studies, novel DAPY derivatives with the suitable combination of substituents should display the better profile against HIV-1 RT. Accordingly, the results obtained from molecular docking and QSAR approaches aid to rational design for new and more NNRTIs inhibitors that might be next generation of anti-HIV-1 RT.

Acknowledgements

The financial support from Science Achievement Scholarship of Thailand (SAST) to K. Kun-asa is gratefully acknowledged. This work was supported by Thailand Research Fund (DBG5380006 and RTA5380010), Royal Golden Jubilee Ph.D. program (PHD/004/2554) and National Research Council of Thailand. Faculty of Science, Ubon Ratchathani University, University of Vienna, ASEA-Uninet, NECTEC are gratefully acknowledged for supporting research.

References

[1] D.G. Prajapati, R. Ramajayam, M.R. Yadav and R.Giridhar, Bioorg. *Med. Chem*. **17** (2009), 5744–5762

[2] M.-P. de Béthune, *Antiviral Res*. **85** (2010), 75–90.

[3] X.-Q. Feng, Y.-H. Liang, Z.-S. Zeng, F.-E. Chen, J. Balzarini, C. Pannecouque and E.D. Clercq, *ChemMedChem*. **4** (2009), 219 – 224.

[4] S.-X. Gu, X.-D. Ma, F.-E. Chen, E.-D Clercq, J. Balzarini and C. Pannecouque, *Bioorg. Med. Chem.* **19** (2011), 5117-5124.

[5] C. Mordant, B. Schmitt, E. Pasquier, C. Demestre, L. Queguiner, C. Masungi, A. Peeters, L. Smeulders, E. Bettens, K. Hertogs, J. Heeres, P. Lewi and J. Guillemont, *Eur. J. Med. Chem.* **42** (2007), 567-579.

[6] X. Tian, B. Qin, H. Lu, W. Lai, S. Jiang, K.-H. Lee,. C.H. Chen and L. Xie, *Bioorg. Med. Chem. Lett*. **19** (2009) 5482–5485.

[7] X. Tian, B. Qin, Z. Wu, X. Wang, H. Lu, S.L. Morris-Natschke, C.H. Chen, S. Jiang, K.-H. Lee, and L. Xie, *J. Med. Chem*. **53** (2010) 8287–8297.

[8] L.-Qi Sun, L. Zhu, K. Qian, B. Qin, L. Huang, C.H. Chen, K.-H. Lee,and L. Xie, *J. Med. Chem*. **55** (2012) 7219−7229.

A STUDY OF INTERACTION ENERGY ON WILD TYPE AND K103N HIV-1 RT COMPLEXED WITH TMC278, BASED ON QUANTUM MECHANICAL METHOD

Syahrie Anggara[1*], P. Penprapai[2]

[1] *Faculty of Science and Technology, Rajamanggala University of Technology Srivijaya, Nakhon si Thammarat, Thailand.*
[2] *Faculty of Science and Technology, Rajamanggala University of Technology Srivijaya, Nakhon si Thammarat, Thailand.*

[*]Author for correspondence; E-Mail*: Anch.anggara@gmail.com*

Abstract: The interaction energies between TMC278 and allosteric binding site of HIV-1 reverse transcriptase (RT) of single mutant K103N, and wild-type were calculated at the MP2/6-31g(d,p) level. Leading to the specific interactions between TMC278 and key residues in the two complex structures, it was found that the attractive interactions between TMC278 and residue positions 101 and 103 of single mutant K103N were slighly reduced by -1.93 kcal/mol and -1.92 kcal/mol compared to wild-type RT. Moreover the results show that all of 21 residues from single mutant K103N and wild-type create attractive interactions with the inhibitor, and confirmed that TMC278 shows higher inhibitory affinities against wild-type and single mutant K103N, which exhibits no significant difference between the interactions energy from both enzymes when its compared. Understanding the interaction energy of these structural interactions can be useful for the design of new inhibitors to HIV-1 RT.

1. Introduction

HIV-1 RT (reverse transcriptase) is a multifunctional heterodimeric enzyme with RNA- and DNA-dependent DNA polymerase and RNase H activities, and is responsible for the conversion of the viral genomic RNA into double-stranded pre-integrative DNA [1]. The asymmetric heterodimers consisting of a p66 subunit and p51 subunit. The two subunits, p66 and p51, consisting of 560 and 440 residues, respectively [2].

HIV-1 reverse transcriptase (RT) is a major target for the treatment of acquired immunodeficiency syndrome (AIDS). Acquired Immunodeficiency Syndrome (AIDS) occurs when infection with the Human Immunodeficiency Virus (HIV) destroys the body's natural protection from illness. In the world, more than 33 million people are currently infected with HIV, which is retrovirus [3].

Nucleoside inhibitors (NRTIs) and non-nucleoside inhibitors (NNRTIs) are two types of RT inhibitors, and they are among the drugs most widely used for the treatment of AIDS [4, 5, 6]. Non-nucleoside reverse transcriptase inhibitors (NNRTIs) have proven efficacy against human immunodeficiency virus type 1 (HIV-1). Evafirenz (EFV) and nevirapine (NVP) are called the first generation of NNRTIs is highly active antiretroviral therapy for patients infected with HIV-1 RT [7]. TMC278 (rilpivirine) is second NNRTI of diarylpyrimidine (DAPY), the first one is etravirine (ETR) that show activity against wild-type enzyme. TMC278 interacts directly with hydrophobic allosteric binding site at the HIV-1 RT and highly active against wild-type and various single and double mutant strains of HIV-1 RT conferring high resistence to NNRTIs than efavirenz (EFV), nevirapine (NVP), and etravirine (ETR) [8, 9, 10].

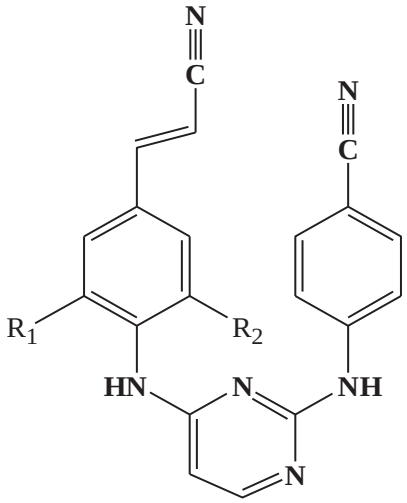

Figure 1. Structural formula of TMC278

Recently, the quantum mechanical method such as second-order Møller–Plesset perturbation theory (MP2) method with the 6-31G(d,p) basis set was successfully used to calculate the interactions energies of TMC278 to wild-type and double mutant L100I/K103N. The result showed that the mutations in the L100I/K103N enzyme leads to a reduction in the stabilization energy of the complex and induces destabilization in the cavity by reducing contact between K101 and TMC278. TMC278 also shows higher inhibitory affinities with the wild-type [11]. Another method such as ONIOM3(MP2/6-31G(d):HF/3-21G:PM3) level has been successfully reported [12] in the optimization of nevirapine and TYR181 geometry in the pocket of 16 amino acid residues at theoretical investigation of nevirapine and HIV-1 RT binding site interaction.

The quantum mechanical method, second-order Møller–Plesset perturbation theory (MP2) with 6-31g(d,p) basis set is applied on this study to calculate the interaction energies of TMC278 with single mutant K103N and wild-type of HIV-1 RT. Understanding of these particular structural interactions can be useful for

the design of new inhibitors to HIV-1 RT, especially on the single mutant.

2. Computational Methods

2.1 System Studied

The basic models for interaction energy calculations were obtained from the X-ray structures of TMC278 bound to HIV-1 RT for the wild-type and single mutant K103N enzymes, listed in the Protein Data Bank with PDB entry codes 2ZDI and 3MEG respectively [13].The studied binding pocket included residues surrounding the non-nucleoside inhibitor binding pocket (NNIBP) with at least one atom interacting with any of the atoms of the TMC278 inhibitor within the interatomic distance of 7.0 Å. These residues of the studied system are PRO95, GLY99, LEU100, LYS101, LYS102, LYS/ASN103, VAL106, VAL179, ILE180, TYR181, TYR188, VAL189, GLY190, PRO225, PHE227, TRP229, LEU234, HIS235, PRO236, TYR318 from the p66 domain of reverse transcriptase and GLU138 from the p51 domain of reverse transcriptase (Figure 2). These residues were added proton by GAUSSIAN 03 program. All of residues were assumed to be in their neutral form. The N- and C- terminal ends of cut residues were capped with hydrogen atoms [CH-{NH_2-CH(-R)-CH=O}]. All of 21 complete structures and their positions were optimized by semi-empirical PM3 method as available in the GAUSSIAN 03 program running in linux on a Pentium IV 3.2 GHz PC. The optimization was carried out taking into account the approximation of the heavy atom fixed. This structure was used as the starting geometry for interaction energy calculations.

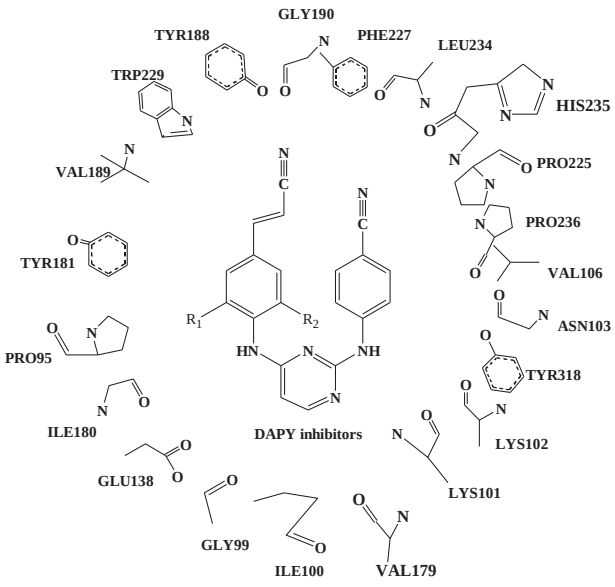

Figure 2. Model system used for TMC278 bound to allosteric site of HIV-1 RT consisting of 21 residues wild-type and single mutant K103N HIV-1 RT NNRTIs.

2.2 Interaction Energy Calculation

The interaction energies, $E_{(TMC278+Xi)}$, between TMC278 and individual residues, Xi, were calculated at the MP2/6-31g(d,p) level. The total interaction energy, INT, can be expressed as: [14]

$$INT_{(TMC278+Xi)}=E_{(TMC278+Xi)}-E_{(TMC278)}-E_{(Xi),}$$

where $E_{(TMC278)}$ and $E_{(Xi)}$ are electronic energies of TMC278 and each individual residue, respectively.

3. Results and Discussion

Interaction energy of TMC278 with individual residues of HIV-1 RT binding pocket

The interaction energies between TMC278 and the individual residues (Xi) of HIV-1 RT binding pocket for single mutant K103N, and wild-type enzymes were calculated at MP2/6-31G(d,p) levels, and the result are shown in Table 1. In the single mutant K103N and wild-type, the main contributions to the interactions with TMC278 come from LEU100, LYS101, LYS103, TYR181, TYR188, PHE227, TRP229, and HIS235 which produce attractive interactions greater than 3kcal/mol. Strongest interaction, such as in LYS101 is caused by hydrogen bond between a linker nitrogen atom of TMC278 and the main chain carbonyl oxygen of LYS101. All of 21 residues on both of enzymes are produced with an attractive interactions to TMC278. For the specific attractive interactions between TMC278 and key residues in the two complexs structure, LYS101 which has higher interaction energy value with 13.21 kcal/mol than others 20 residue and LYS103/ASN that is mutated residue, of the binding pocket of single mutant K103N , the ΔEa is slighly different with -1.93 and -1.92 kcal/mol, respectively (Table 1). The total interaction energy from the single mutant K103N is also close to the wild-type enzyme with total -86.06, and -76.3 kcal/mol, respectively.

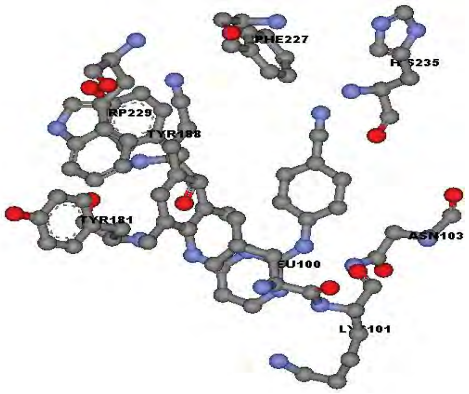

Figure 2. Orientation of TMC278 and residues with largest interactions in the binding pocket of K103N RT.

From the Table 1, we can see that the interaction energies between TMC278 and each residue of both the single mutant K103N RT and wild-type RT are

similar. Comparing the single mutant K103N RT and wild-type RT at the MP2/6-31g(d,p) level, no significant difference was observed between the interactions is shown.

Table 1. The interactions energy of TMC278 with 21 residues of K103N and wild-type at MP2/6-31g(d,p) level.

Residue (Xi)	Interaction Energy (kcal/mol)		
	K103N	Wild-type	ΔEa
PRO95	-0.71	-0.44	-0.27
GLY99	-0.11	-0.15	0.04
LEU100	**-7.54**	**-8.32**	0.79
LYS101	**-13.21**	**-11.3**	-1.93
LYS102	-0.51	-0.41	-0.11
LYS103(ASN)	**-5.12**	**-3.20**	-1.92
VAL106	-2.28	-2.50	0.21
VAL179	-2.92	-1.12	-1.80
ILE180	-1.12	-2.35	1.24
TYR181	**-7.10**	**-6.43**	-0.67
TYR188	**-8.24**	**-9.07**	0.83
VAL189	-0.27	-0.76	0.50
GLY190	-0.84	-1.15	0.31
PRO225	-2.52	-1.23	-1.30
PHE227	**-6.07**	**-3.14**	-2.94
TRP229	**-7.33**	**-8.35**	1.02
LEU234	-2.80	-1.45	-1.35
HIS235	**-5.82**	**-5.99**	0.18
PRO236	-4.18	-2.99	-1.19
TYR318	-2.77	-3.36	0.59
GLU138	-4.59	-2.57	-2.03
Total Energy	**-86.06**	**-76.3**	**-9.80**

$\Delta Ea = E_{K103N\ mutant} - E_{wild\text{-}type}$

K103N is one of drug-resistant mutations most frequently observed in patients treated with NNRTIs, and viruses carrying these mutations show high levels of resistence to existing NNRTIs. On wild-type RT/TMC278 structure, K103 is located on the other side of the pyrimidine ring of TMC278 [11]. Because of the position of cyanovinyl group which fits to the hydrophobic tunnel formed by the side chains of amino acid residues PHE227 and TRP229, it may cause that TMC 278 is most potent from others NNRTIs such as nevirapine (NVP), efavirenz (EFV), and also others DAPPY compound. TMC278 can more flexible to bind to HIV-1 RT and interacts with aromatic side chains of TYR181, TYR188, PHE227, TRP229, and also HIS235 via CH-π interactions as shown in figure 2. The total interaction energy from both studied enzymes, which shown that TMC278/K103N HIV-1 RT complex (-86.06 kcal/mol) is slighly differencce with wild-type RT (-76.3 kcal/mol). From these results, we can see that there is no significantly difference about the interaction energy between TMC278 to single mutant K103N and wild-type. TMC278 shows a little higher attractive interaction to K103N mutant RT than wild-type RT, that means TMC278 gave a little bit higher inhibitory affinity to K103N mutant RT than wild-type RT. These results are consistent with experiments that TMC278 shows high inhibitory affinities against for both K103N and wild-type enzymes, and also good agreement with the experimentally observed EC_{50} for 0.0003 μM K103N mutant RT and EC_{50}= 0.0004 μM for wild-type RT [13].

4. Conclusions

The quantum mechanical method, Møller–Plesset perturbation theory (MP2) with 6-31g(d,p) basis set level has been applied on this study to calculate the interaction energy between TMC278 to single mutant K103N and wild-type. In the K103N RT, two specific interactions, residue LYS101 and LYS/ASN103 was slightly reduced by -1.93 and -1.92 kcal/mol compared to wild-type RT. There is no residues that shows repulsive interaction from both of studied enzymes. The total calculated interactions for single mutant K103RT (-86.06 kcal/mol) is close to the wild-type RT (-76.3 kcal/mol). This is consistent to the experiment that TMC278 is show high inhibitory affinities to K103N mutant RT and also to the wild-type RT. Which is TMC278 is shows a little bit higher inhibitory affinities to the single mutan K103N enzyme than wild-type enzyme. Understanding this particular interactions, with theoretical investigation may useful for the design of higher potency inhibitors specific to the single mutant of HIV-1.

Acknowledgements

This work was supported by Faculty of Science and Technology, Rajamanggala University of Technology Srivijaya is acknowledging for partial financial support. Also, partial supporting by National Nanotechnology Center (NANOTEC) through its program Center of Excellent Kasetsart University, Ministry of Science and Technology, Thailand.

References

[1]. A. Telesnitsky, and S. P. Goff (1997) Reverse transcriptase and the generation of retroviral DNA. *In Retroviruses* (Coffin, J. W., Hughes, S. H. and Varmus, H. E., eds.), pp. 121–160.

[2]. P. L. Boyer, S. G. Sarafianos, E. Arnold , and S.H. Hughes (2002) The M184V mutation reduces the selective excision of zidovudine 5′-monophosphate (AZTMP) by the reverse transcriptase of human immunodeficiency virus type 1. *J. Virol* 76:3248–3256.

[3]. J. Balzarini, H. Pelemans, G. Riess, M. Roesner, I. Winkler, De Clercq, J.P Kleim (1998) Retention of

marked sensitivity to (S)-4-isopropoxycarbonyl-6-methoxy-3-(methylthiomethyl)-3,4-dihy-droquinoxaline-2-(1H)-thione (HBY 097) by an azidothymidine (AZT)-resistant human immunodeficiency virus type 1 (HIV-1) strain subcultured in the combined presence of quinoxaline HBY 097 and 2′,3′-dideoxy-3′-thiacytine (lamivudine). *Biochem Pharmacol*. 55, pp. 617–621.

[4]. E. De Clercq (1994) HIV resistance to reverse transcriptase inhibitors. *Biochem Pharmacol*. 47, pp. 155–169.

[5]. E. De Clercq (1995) Toward improved anti-HIV chemotherapy therapeutic strategies for intervention with HIV infections. *J. Med. Chem* 38, pp. 2491–2517.

[6]. C. Tantillo, J. Ding, A. Jacobo-Molina, R.G. Nanni, P.L. Boyer, S.H. Hughes, R. Pauwels, K. Andries, P.A.J. Janssen, E. Arnold (1994) Locations of anti-AIDS drug binding sites and resistance mutations in the three-dimensional structure of HIV-1 reverse transcriptase implications for mechanisms of drug inhibition and resistance. *J. Mol. Biol*., 243, pp. 369–387.

[7]. B. Gazzard, E. J. Bernard, M. Boffito, D. Churchill, S. Edwards, N. Fisher, A. M. Geretti, M. Johnson, C. Leen, B. Peters, A. Pozniak, J. Ross, J. Walsh, E. Wilkins, and M. Youle (2006) British HIV Association (BHIVA) guidelines for the treatment of HIV-infected adults with antiretroviral therapy. *HIV Med*. 7**:**487-503.

[8]. Y. Van Herrewege, J. Michiels, A. Waeytens, G. De Boeck, E. Salden, L. Heyndrickx, G. Van den Mooter, M.-P. De Béthune, K. Andries, P. Lewi, M. Praet, G. Vanham (2007) A dual chamber model of female cervical mucosa for the study of HIV transmission and for the evaluation of candidate HIV microbiocides. *Antiviral Res*. pp. 111–124.

[9]. Y. Van Herrewege, G. Vanham, J. Michiels, K. Fransen, L. Kestens, K. Andries, P. Janssen, P. Lewi (2004) A series of diaryltriazines and diarylpyrimidines are highly potent non-nucleoside reverse transcriptase inhibitors with possible applications as microbiocides Antimicrob. *Agents Chemother*. 48, pp. 3684–3689.

[10]. P. A. Janssen, P.J. Lewi, E. Arnold, F. Daeyaert, M. de Jonge, J. Heeres, L. Koymans, M. Vinkers, J. Guillemont, E.Pasquier, M. Kukla, D. Ludovici, K. Andries, M.-P. de Béthune, R. Pauwels, K. Das, A.D. Clark Jr., Y.V. Frenkel, S.H. Hughes, B. Medaer, F. De Knaep, H. Bohets, F. De Clerck, A. Lampo, P. Williams, P. Stoffels (2005) In search of a novel anti-HIV drug: multidisciplinary coordination in the discovery of 4-[[4-[[-[(1E)-2-cyanoethenil]-2,6 dimethylphenyl]-amino]-2-pyrimidinyl]-amino]-benzonitrile (R278272: rilpivirine). *J. Med, Chem*., 48, pp.1901-1909

[11]. P. Srivub, P. Nokkaew and S. Hannongbua. (2011) Theoretical Investigation on Wild-type and L100I/K103N HIV-1 RT complexed with TMC278, based on Quantum Mechanical Methods, pp. 986-990.

[12]. Mayuso Kuno, Supa Hannongbua, and Keiji Morokuma (2003) Theoretical investigation on nevirapine and HIV-1 reverse transcriptase binding site interaction, based on ONIOM methods, science direct, *Chemical Physics Letters*, 380, pp. 455-463.

[13]. K.Das, J.D. Bauman, A.D. Clark, Y.V. Frenkel, P.J. Lewi, A.J. Shatkin. S. H. Hughes, and E. Arnold (2008) High-resolution structures of HIV-1 reverse transcriptase/TMC278 complexes: Strategic flexibility explains potency against resistance mutations. *PNAS.* 105(5), pp. 1466-1471.

[14]. S. Saen-oon, M. Kuno, S. Hannongbua (2005) Binding energy analysis for wild-type and Y181C mutant HIV-1 RT/8-Cl *TIBO* complex structures: Quantum chemical calculations based on the ONIOM method. *Proteins Struct. Funt. Genet*. 61, pp.198-202.

AMMONIA NITROGEN ADSORPTION FROM LATEX WASTEWATER BY ADSORBENT PREPARED FROM BETEL NUT PEEL

Panita Kongsune[1]*, Lakana Chotitham[1], Yatima Lengjae[1]

[1] Department of Chemistry, Faculty of Science, Thaksin University, Phathalung, Thailand

* Author for correspondence; E-Mail: panita487@hotmail.com, Tel. +66 74609600 ext 2362

Abstract: Excess ammonia nitrogen may lead to the eutrophication of river, resulting in increase dissolved oxygen depletion and fish toxicity. To remove ammonia nitrogen from wastewater, the adsorption method using low-cost adsorbents prepared from biomass is more economically feasible and environmentally friendly. In this work, we attempt to study the ammonia nitrogen adsorption from latex waste water using the Betel nut peel which was the general agricultural wastes. The Betel nut peels were washed with water and were dried 24 h at room temperature. The sample was then dried at 105 °C for 24 h in air oven. The sample was ground to pass 50 mesh sieve for use as adsorbent. The adsorption experiments were performed according to the batch method. The concentration of ammonia in each material was analyzed using the titrimetric method. The maximum ammonia nitrogen removal was obtained with following conditions: a system pH of 7, a contact time of 60 min, a particle size of ~50 mesh sieve and initial nitrogen ammonia 100 ppm. The maximum adsorption capacity of ammonia nitrogen from latex wastewater was 50%. The equilibrium data were found to fit well to both the Langmuir model and Freundlich model. Therefore, it can be conclude that it is possible to prepare the absorbent from Betel nut peel..

1. Introduction

Ammonia is a widely used refrigerant in industrial refrigeration systems found in the food, beverage, petro-chemical and cold storage industries. It is also used in the rubber industry for the stabilization of natural and synthetic latex to prevent premature coagulation. Excess ammonia nitrogen may lead to the eutrophication of river, resulting in increasing dissolved oxygen depletion and fish toxicity [1]. Therefore, it is important to find ways to efficiently control the removal of ammonia from wastewater. To remove ammonia nitrogen from wastewater, the adsorption method using low-cost adsorbents prepared from biomass is more economically feasible and environmentally friendly when compared with biological nitrification-denitrification method [2]. Most studies on ammonium adsorption from aqueous solution have been focused on mineral materials as adsorbents, such as zeolites [3-4]. However, a little information is available on the removal of ammonia nitrogen by adsorbents prepared from biomass [1] from aqueous solution. The present work attempted to study the ammonia nitrogen adsorption from latex waste water using the Betel nut peel which was the general agricultural wastes.

2. Materials and Methods

2.1. Preparation of the adsorbent and adsorbate

The Betel nut peels were washed repeatedly with water to remove dust and soluble impurities on the surface and were dried 24 h at room temperature. The sample was then dried at 105 °C for 24 h in air oven. Then the sample was ground to pass a 50 mesh sieve (Fig. 1). The fine Betel nut peel powder was preserved in plastic bags for use as adsorbent.

Fig. 1 The adsorbent prepared from Betel nut peel.

The 1000 mg/L stock solution of ammonia nitrogen was prepared by dissolving 3.819 g ammonium chloride (NH_4Cl) in deionized water. The experimental solutions were prepared by diluting the stock solution with deionized water when necessary.

2.2 Experimental methods

The adsorption experiments were performed according to the batch method. In this method, 1 g 2.5 g and 5 g of adsorbent were mixed with 100 mL ammonia solution of certain concentration. The mixtures were sealed and shaken at 250 rpm for 24 h to reach equilibrium. The concentration of ammonia in each material was analyzed using the titrimetric method. Experiments were performed in triplicate and the results were averaged. Controls were obtained by mixing distilled water with each sample. The effect of initial pH on ammonium adsorption was investigated with pH range of 2-12, and the initial ammonia concentration was 25, 50 100, 150, 200, 250 and 300 mg/L. The latex wastewater was pretreated before investigate the adsorption capacity.

The removal efficiency (%) of ammonia by Betel nut peel powder was calculated using the following equations:

$$\text{Removal efficiency (\%)} = = \left(\frac{C_0 - C_e}{C_0} \right) \times 100$$

The ammonia nitrogen adsorption capacity (q, mg/g) were calculated by:

$$q = \left(\frac{C_0 - C_e}{M} \right) V$$

where C_0 (mg/L) and C_e (mg/L) is the initial and equilibrium ammonia nitrogen concentrations in the solution respectively, V (L) is the solution volume, and M (g) is the mass of adsorbent.

3. Results and Discussion

3.1 Iodine Number

Iodine number is the most fundamental parameter used to characterize adsorbent performance. It is a measure of activity level, often reported in mg g^{-1}. It is a measure of the micropore content of the adsorbent by adsorption of iodine from solution. The Iodine number of the absorbent prepared from the Betel nut peel was 191 mg g^{-1}.

3.2 Moisture content

This is the amount of water on the Betel nut peel under normal condition. High moisture content indicates poor quality and the moisture content of the absorbent prepared from the Betel nut peel was 60.07%.

3.3 Calibration curve of ammonia nitrogen adsorption by adsorbent prepared from Betel nut peel

From the calibration curve (Fig.2), it was found that the concentration of ammonia in Latex wastewater was 114 mg L^{-1}.

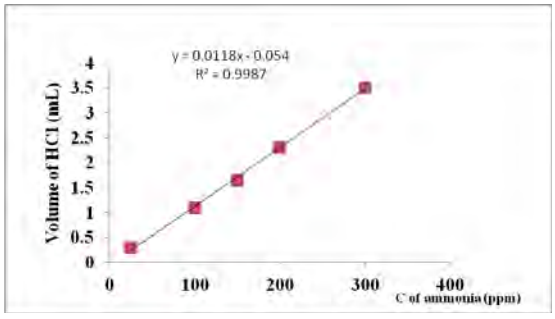

Fig.2 Calibration curve of ammonia nitrogen adsorption by absorbent prepared from Betel nut peel.

3.4 The effects of adsorbent dosage and contact time

The results of experiments to determine the effects of adsorbent dosage on ammonia removal are shown in Fig. 3. The removal efficiency of ammonia nitrogen at 2.5 g of adsorbent dosage was much higher than 1 g. Thus, 1 g of adsorbent dosage was selected as the optimum dosage for adsorption of ammonia nitrogen. All active sites on the adsorbent surface are then occupied and increase in adsorbent dosage do not provide higher uptake of ammonia nitrogen.

The adsorption capacity of ammonia nitrogen removed by Betel nut peel powder versus contact time is also displayed in Fig. 3. It can be seen that the removal efficiencies were initially a fast process of the removal being achieved within the first 60 min. Thereafter, with increase of contact time the rate of removal slowed down considerably and after passage of 90 min was almost negligible. Therefore, 60 min was selected as optimum contact time for all further experiments.

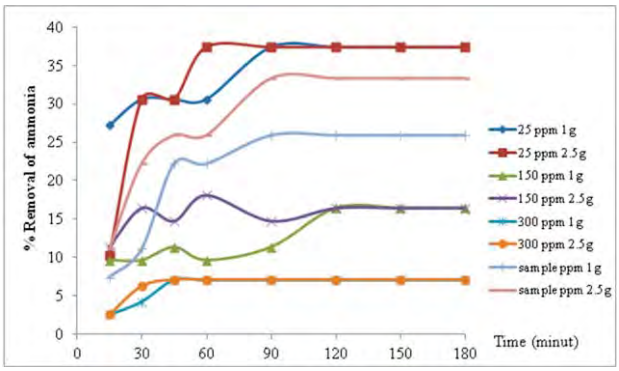

Fig. 3 Effect of adsorbent dosage on the removal of ammonia.

3.5 The effect of pH

Ammonia nitrogen removal by adsorbent prepared from Betel nut peel was observed at pH values ranging between 5 and 9. The results are shown in Fig. 4. The figure shows that as solution pH increases in the range of 5-7, the removal efficiency of ammonia nitrogen increases gradually and reaches a maximum value (68%) when the pH value is 7. When the pH increases to 8, the removal efficiency drops dramatically (64%). This finding agrees with the observations reported by H. Huang et al [2].

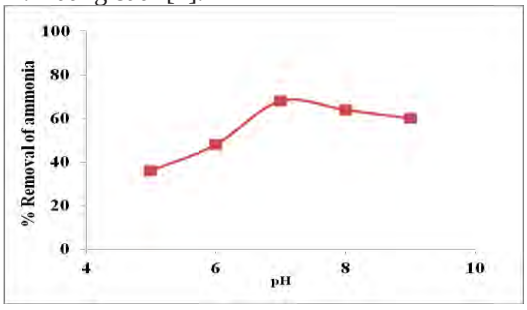

Fig. 4 Effect of pH on the removal of ammonia (adsorbent dosage: 1 g/L; contact time: 60 min; initial ammonium concentration: 100 mg/L).

3.6 Adsorption isotherms

The adsorption isotherms reveal the specific relation between adsorption capacity and concentration of the remaining adsorbate at constant temperature. Freundlich and Langmuir models are the two most frequent used models. In this work both models were used to quantify the adsorption capacity of adsorbent prepared from the Betel nut peel for the removal of ammonia nitrogen from synthetic wastewater.

Freundlich isotherm describes the heterogeneous surface energies by multilayer adsorption and is expressed by the following equation:

$$\log q_e = \frac{1}{n}\log C_e + \log K_F$$

where K_F and n are constants of Freundlich isotherm incorporating adsorption capacity (mg g^{-1}) and intensity. The isotherm data fitted the Freundlich model relatively with an R^2 of 0.9712. One of the Freundlich constants K_F indicates the adsorption capacity of the adsorbent and the values of K_F at equilibrium of 0.1 mg g^{-1}. The other Freundlich constant n is a measure of the deviation from linearity of the adsorption and the numerical value of n = 0.64.

Langmuir isotherm is based on the monolayer sorption and is represented by the following equation:

$$\frac{1}{q_e} = \frac{1}{K_L q_m}\frac{1}{C_e} + \frac{1}{q_m}$$

where q_m indicates the maximum monolayer adsorption capacity (mg g^{-1}) and K_L indicates Langmuir constant or capacity factor. The plot of isotherm shows that a straight line could be well observed between $1/q_m$ and $1/C_e$. This implies that the isotherm data fitted the Langmuir equation quite well (R_2 = 0.9813). The values of q_m and K_L determined from the Langmuir plot were 9.44 and 2.05 mg/g, respectively.

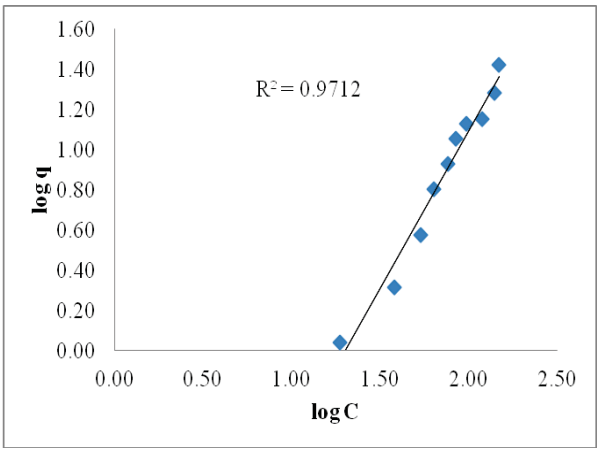

Fig. 5. Linear plot of Freundlich isotherm of ammonia adsorption on Betel nut peel.

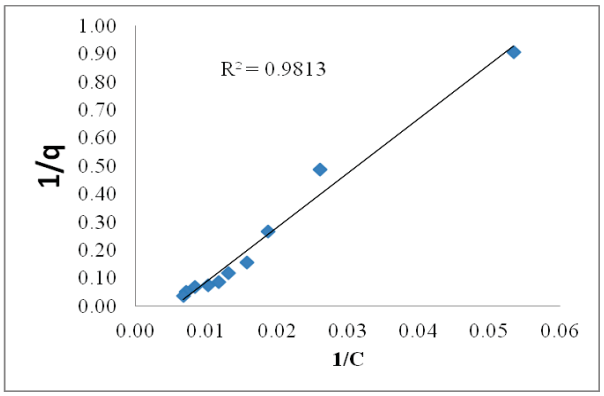

Fig. 6 Linear plot of Langmuir isotherm of ammonia adsorption on Betel nut peel.

4. Conclusions

The findings of this work indicated that basic conditions such as solution pH, contact time, and adsorbent dosage influence the removal of ammonia from aqueous solutions and Latex wastewater by adsorbent prepared from Betel nut peel.

The maximum ammonia nitrogen removal was obtained with following conditions: a system pH of 7, a contact time of 60 min, a particle size of < 50 mesh sieve and initial nitrogen ammonia 100 ppm. The maximum adsorption capacity of ammonia nitrogen from latex wastewater was ~50%. The equilibrium data were found to fit well to the Langmuir model and quit well to the Freundlich model. Therefore, it can be conclude that it is possible to prepare the adsorbent from Betel nut peel.

Acknowledgements

This work was financially supported by the fund of Thaksin University.

References

[1] H. Liu, Y. Dong, H. Wanga, Y. Liu, *Desalination*. **263** (2010) 70-75.
[2] H. Huang, X. Xiao, B. Yan, L. Yang, *J. Hazard. Mater*. **175** (2010) 247-252.
[3] L. Lei, X. Li, X. Zhang, *Sep. Purif. Technol.*, **58** (2008) 359-366.
[4] E. Ivanova, M. Karsheva, B. Koumanova, *J Univer. Chem. Tech. and Metall.* **45** (2010) 295-302.

SUBSTITUENT EFFECT ON THE DONOR IN ORGANIC DYES FOR DYE-SENSITIZED SOLAR CELLS: A DFT / TDDFT STUDY

Yaowarat Surakhot[1], Kajornsak Ketdon[1], Palita Kochpradist[1], Taweesak Sudyoadsuk[1], Tinnagon Keawin[1], Sayant Saengsuwan[1], Vinich Promarak[2] and Siriporn Jungsuttiwong[1*]

[1]Center for Organic Electronic and Alternative Energy, Department of Chemistry and Center of Excellence for Innovation in Chemistry, Faculty of Science, Ubon Ratchathani University, Ubon Ratchathani, 34190 Thailand
[2]School of chemistry insitute of science, Suranaree University of Technology
111 University Avenue, Nakhon Ratchasima 30000, Thailand

[*] Author for correspondence; jsiriporn_2000@yahoo.com, Tel. +66 16922125

Abstract: The structural and energetic properties of organic dye forming D-π-A system as photosensitizes in dye-sensitized solar cells (DSCs) were investigated. The ground-state structures of all molecules were fully optimized using density functional theory (DFT) at B3LYP/6-31G(d,p) level. The energy gap (E_g) and the electronic absorption (λ_{abs}) of dye molecules were computed using time-dependent density functional theory (TDDFT) at CAM-B3LYP/6-31G(d,p) level. The effect of different donor groups with shared linker and anchoring groups was studied. The phenyl and thiophene were acting as π-conjugated linker, the cyanoacrylic acid was acting as anchoring groups. It was found that the effect of different donor groups affected to the HOMO and LUMO energy levels resulting in variable E_g values. The frontier molecular orbital results indicated that the intramolecular charge transfer (ICT) was occurred. These results can provide useful information for improving an efficiency of new organic dyes for DSCs applications.

1. Introduction

Dye-sensitized solar cells (DSCs) are one of the most promising alternatives to compete with the traditional silicon solar cell because organic dye molecules in DSCs show distinguished advantages such as their high optical absorption extinction coefficient, adjustable spectral wavelength response, low cost materials, and their environmental friendly [1-3]. In general the molecular structure of an organic dye for DSCs has been designed and synthesized based on following properties: (i) matching of oxidation potentials of the ground and exited states for a dye, which are usually replaced by the highest occupied molecular orbital (HOMO) and the lowest unoccupied molecular orbital (LUMO), with the energy levels of I^-/I_3^- redox potential and E_{CB} of the TiO_2 electrode, respectively; (ii) a donor-linkage-acceptor (D-π-A) system required for a wide range absorption extending to the near-infrared [2]. Because the electron donor part in organic dye plays a crucial role in determining the overall conversion efficiency, a series of organic sensitizers containing identical linkers (phenyl-thiophene) and electron acceptor (cyanoacrylic acid) but different electron donor [4]. A general TDDFT procedure has been set up that accurately evaluates the UV/vis absorption spectra of organic dyes [5-7]. The long-range-corrected CAM-B3LYP function, which has been widely used to explain the intramolecular charge transfer (ICT) transition of organic dye [8]. In order to disclose the relationship among the performances, the structures and the properties, the theoretical investigations of the physical properties of organic dyes are indispensable. The calculated results are also helpful to design and synthesis of novel dye sensitizers with higher performance. In this work, we interested in the effect of electron donating capability of dye molecules as shown in Figure 1, to improve the structural and optical properties of these dyes for using in highly efficient DSCs.

2. Computational details

The ground-state structures were fully optimized using DFT by means of the B3LYP functional [the Becke3 (exchange) and the Lee-Yang-Parr (correlation) hybrid functional] with 6-31G (d,p) basis set. The electronic absorption wavelengths were investigated using TDDFT at CAM-B3LYP/6-31G(d,p). The optical spectral were plotted using the Swizard program. All calculations were performed using Gaussian 09 program package [9]. The contribution of molecular orbitals in the electronic transitions was calculated using the Gaussum program version 2.2.1.

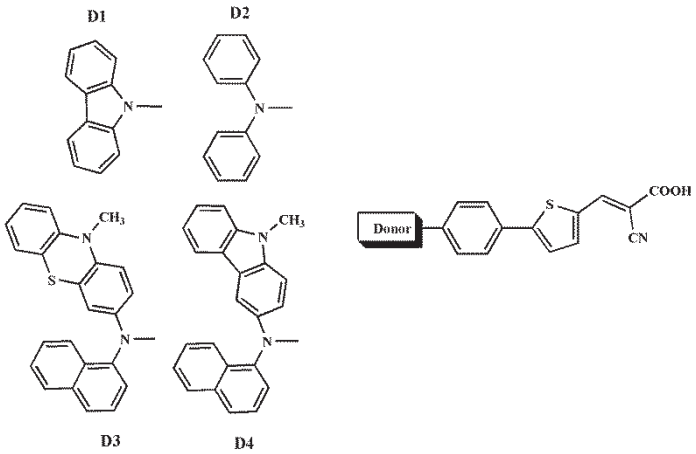

Figure 1. Molecular structure of target molecules

3. Results and discussion

3.1 Ground-state geometries

The optimized geometries obtained by density functional theory (DFT) B3LYP/6-31G(d,p) level of **D1**, **D2**, **D3**, and **D4** are shown in Figure 2, and the important inter-ring distance and dihedral angle parameters are shown in Table 1 . It was found that dihedral angles between donor group and linker group (D-L) can be computed to be -51.55°, -29.89°, -24.47°, and -21.01° respectively, dihedral angles between linker group and linker group (L-L) can be computed to be in rang 16.75°-22.47°, dihedral angles between linker group and acceptor group (L-A) can be computed to be in rang 0.73°-1.37°. The dihedral angles of L-L and L-A are slightly different, the effect of different donor groups affect co-planarity molecule between donor group and linker group. However the electron can be delocalized from donor to linker by lone pair of nitrogen atom.

Table 1 Selected important inter-ring distances (Å) and dihedral angles (°) calculated by B3LYP/6-31G(d,p) calculations

	Inter-ring distances in angstrom (Dihedral angles in degree)		
	D-L	**L-L**	**L-A**
D1	1.41 (-51.55)	1.46 (22.47)	1.42 (-0.80)
D2	1.40 (-29.89)	1.45 (16.75)	1.41 (-1.37)
D3	1.40 (-24.47)	1.45 (20.56)	1.42 (0.42)
D4	1.40 (-21.01)	1.45 (-17.38)	1.42 (-0.73)

Note: **D** = donor, **L** = linker, **A** = acceptor

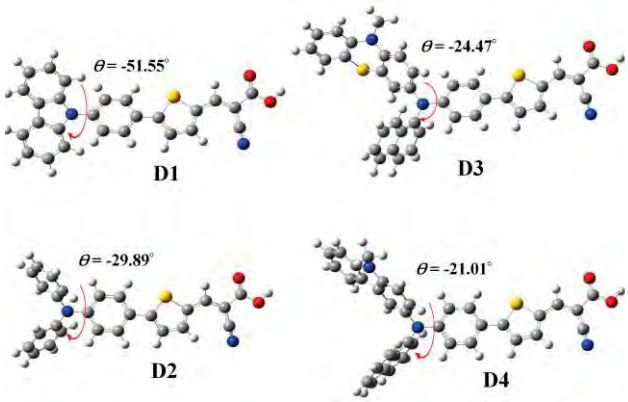

Figure 2. Optimized structure of target molecules by DFT/B3LYP/6-31G(d,p)

3.2 Electronic structure

To gain insight into the electronic structures, frontier molecular orbital were obtained to examine the highest occupied molecular orbital (HOMO) and the lowest unoccupied molecular orbital (LUMO) due to the relative ordering of the HOMO and LUMO providing a reasonable qualitative indication of the excitation properties. The molecular orbital surfaces of **D1**, **D2**, **D3**, and **D4** are shown in Figure 3 and the density of state (DOS) are presented in Table 2. In all molecules, the electron density on HOMO is delocalized on donor group and the electron density on LUMO is delocalized on acceptor group, the HOMO to LUMO transition that corresponding mixed transition between intramolecular charge transfer (ICT) from donor group to acceptor group and $\pi \rightarrow \pi^*$ of linker group. Moreover, suitable energy level and location of HOMO and LUMO orbitals of the dye are required to match the I^-/I_3^- redox potential and conduction band level of the TiO_2 semiconductor. The calculated molecular orbital energies of **D1**, **D2**, **D3**, and **D4** were computed by using B3LYP/6-31G(d,p) the conduction band (CB) of TiO_2 as shown in Figure 3. The results were found that the HOMO energy levels of **D1**, **D2**, **D3**, and **D4** are -5.52, -5.17, -5.03, and -5.01 eV respectively, the LUMO energy levels are -2.80, -2.69, -2.72, and -2.64 eV, respectively. We found that, for **D4** the HOMO energy is lying above the redox couple of the electrolyte which is the most suitable for donation of electrons from the I^-/I_3^- redox couple in the electrolyte solution. Whereas the LUMO is lying closer to the conduction band of TiO_2 compared to that of others leading to the excited electrons are then efficiently injected into semiconductor electrode.

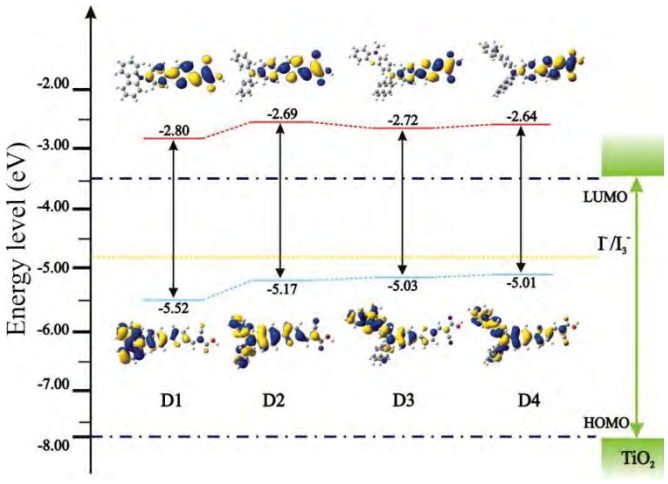

Figure 3. Energy diagram calculated by DFT/B3LYP/6-31G(d,p) level using C-PCM in dichloromethane

Table 2. Energies and percentage composition of several frontier molecular orbital

	Molecular orbitals	Percentage composition		
		Donor	Linker	Acceptor
D1	LUMO	1	50	49
	HOMO	78	19	3
D2	LUMO	15	38	48
	HOMO	77	14	8
D3	LUMO	1	50	49
	HOMO	61	36	3
D4	LUMO	3	48	49
	HOMO	63	32	5

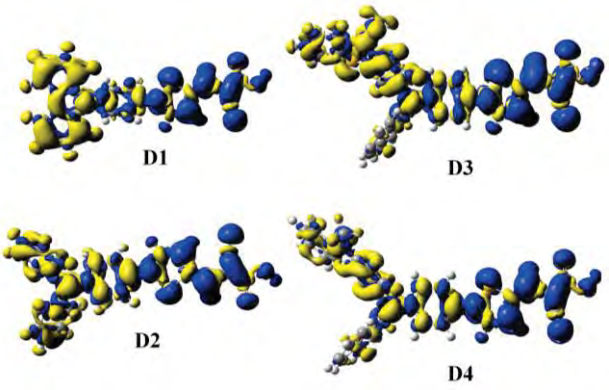

Figure 4. The electronic density differences maps between the group state and the excited state (yellow color indicate a decrease and blue color indicate increase of charge density)

The electronic density differences between the ground state and first excited state (shown in Figure 4) were clearly assigned to the character of excited state unambiguously. Obviously, the decreasing electron density mainly localize on the electronic donor and linker group, whereas the increasing electron density mainly localizes on the linker and acceptor group, which is indicative of an intramolecular charge transfer when transition occurs, agreeing well with electronic structure analysis discussed above

3.3 UV/Vis absorption spectra

The UV/Vis absorption spectra of these molecules were studied by TD-DFT//CAM-B3LYP/6-31G(d,p) level. The transition energies of electronic spectra, oscillator strength, configurations of the orbital, and the calculated values of the absorption wavelength in the gas phase of **D1**, **D2**, **D3**, and **D4** are listed in table 3. The UV/vis absorption spectra of **D1**, **D2**, **D3**, and **D4** are shown in Figure 5. It was found that, the λ_{max} of **D1**, **D2**, **D3**, and **D4** are 393, 440, 350, and 443 nm, respectively. These results indicate that **D4** dye exhibits red-shifted compared to that of organic dyes.

Table 3. Electronic transition, absorption wavelength and oscillator strength (f) obtained by TD-DFT at the CAM-B3LYP/6-31G(d,p)

	Electronic Transitions	Wavelength (nm)	f	Main contribution	Character
D1	$S_0 \rightarrow S_1$	393	1.3938	H → L (56%) H-2 → L (39%)	ICT, π-π^*
D2	$S_0 \rightarrow S_1$	440	1.4631	H → L (82%) H-1→ L (13%)	ICT, π-π^*
D3	$S_0 \rightarrow S_1$	350	0.9847	H-3 → L (31%) H → L (23%) H-1 → L (20%)	ICT, π-π^*
D4	$S_0 \rightarrow S_1$	443	1.5225	H → L (72%) H-1 → L (11%)	ICT, π-π^*

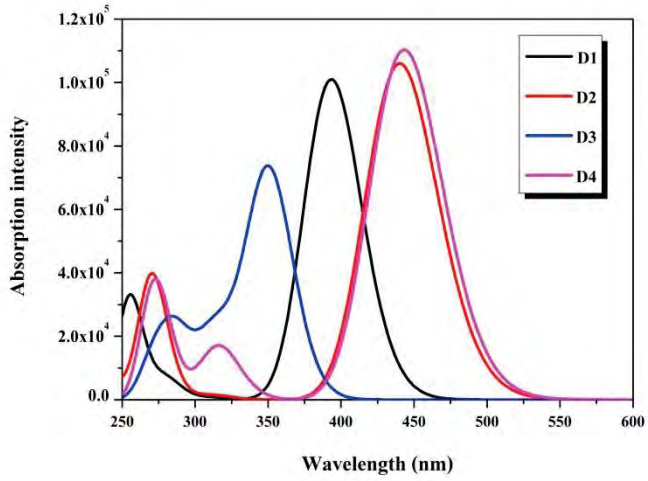

Figure 5. Calculated absorption spectra of **D1**, **D2**, **D3**, and **D4** by TD-CAM/B3LYP/6-31G(d,p)

4. Conclusions

In this paper, we have successfully designed four metal-free organic dyes that contain donors with carbazole, TPA, diarylamine-phenotiazine and diarylamine-carbazole for D1, D2, D3 and D4, respectively and cyanoacrylic acid acceptors bridged by thiophene fragment. The results based on computation show that extending the π-system of donor part appropriately can systematically control the spectral response of the dyes and further improve the energy conversion efficiency of DSCs. We also found

that, optimized structure in the effects of different electron donating groups does affect coplanarity of linker to acceptor part of dye molecules and the frontier molecular orbital and DOS results reveal that our design D4 dyes are promising in the development of DSCs.

Acknowledgements

This work was fully supported by Center of Excellence for Innovation in Chemistry (PERCH-CIC), Commission of Higher Education, Ministry of Education and Ubon Ratchathani University are also acknowledged for some partial supports.

References

[1] Z. S. Wang, N. Komura, Y. Cui, M. Takahashi, H. Sekiguchi, A. Mori, H. Kubo, A. Furube, and K. Hara, *Chem. Mater.* **20** (2008) 3993-4003.
[2] X. Zhang, J. J. Zhang, and Y. Y. Xia, *J. Photochem. Photobiol. A: Chemistry*. **194** (2008) 167-172.
[3] C. S. Chou, Y. J. Lin, R. Y. Yang and K. H. Liu, *Adv. Powder Technolo.* **22** (2011) 31-42.
[4] Z. Wan, C. Jia, L. Zhou, W. Huo, X. Yao and Y. Shi, *Dyes. Pigm.* **95** (2012) 41-46.
[5] J. Preat C. Michaux, D. Jacquemin and E. A. Perpète, *J. Phys. Chem. C.* **113** (2009) 16821-16833.
[6] T. Yakhanthip, S. Jungsuttiwong, S. Namuangruk, N. Kungwan, V. Promarak, T. Sudyoadsuk, and P. Kochpradist, *J. Comput. Chem.* **32** (2011) 1568-1576.
[7] S. Jungsuttiwong, T. Yakhanthip, Y. Surakhot, J. Khunchalee, T. Sudyoadsuk, V. Promarak, N. Kungwan and S. Namuangruk, *J. Comput. Chem.* **33** (2012) 1517-1523.
[8] J. Zhang, Y. H. Kan, H. B. Li, Y. Geng, Y. Wu and Z. M. Su, *Dyes. Pigm.* **95** (2012) 313-321.
[9] M.J. Frisch, G.W. Trucks, H.B. Schlegel, G.E. Scuseria, M.A. Robb, J.R. Cheeseman, G. Scalmani, V. Barone, B. Mennucci, G.A. Petersson, H. Nakatsuji, M. Caricato, X. Li, H.P. Hratchian, A.F. Izmaylov, J. Bloino, G. Zheng, J.L. Sonnenberg, M. Hada, M. Ehara, K. Toyota, R. Fukuda, J. Hasegawa, M. Ishida, T. Nakajima, Y. Honda, O. Kitao, H. Nakai, T. Vreven, J.A. Montgomery, Jr., J.E. Peralta, F. Ogliaro, M. Bearpark, J.J. Heyd, E. Brothers, K.N. Kudin, V.N. Staroverov, R. Kobayashi, J. Normand, K. Raghavachari, A. Rendell, J.C. Burant, S.S. Iyengar, J. Tomasi, M. Cossi, N. Rega, J.M. Millam, M. Klene, J.E. Knox, J.B. Cross, V. Bakken, C. Adamo, J. Jaramillo, R. Gomperts, R.E. Stratmann, O. Yazyev, A.J. Austin, R. Cammi, C. Pomelli, J.W. Ochterski, R.L. Martin, K. Morokuma, V.G. Zakrzewski, G.A. Voth, P. Salvador, J.J. Dannenberg, S. Dapprich, A.D. Daniels, O. Farkas, J.B. Foresman, J.V. Ortiz, J. Cioslowski, D.J. Fox, Gaussian 09, Revision A.02, Gaussian, Inc., Wallingford CT, 2009.

COMPUTATIONAL INVESTIGATION OF THE INFLUENCE OF DIFFERENT ACCEPTORS ON ORGANIC CHROMOPHORES FOR DYE-SENSITIZED SOLAR CELLS

Rattanawalee Rattanawan[1], Tanika Khanasa[1], Taweesak Sudyoadsuk[1], Tinagon Keawin[1], Sayant saengsuwan[1], Vinich Promarak[2] ,Supawadee Namuangruk [3] Siriporn Jungsuttiwong *[1]

[1] Center for Organic Electronic and Alternative Energy, Department of Chemistry and Center of Excellence for Innovation in Chemistryy, Faculty of Science, Ubon Ratchathani University, Ubon Ratchathani, 34190 Thailand
[2] The school of chemistry insitute of science at Suranaree University of Technology 111 University Avenue, Muang district, Nakhon Ratchasima 30000, Thailand
[3] National Sceince and Technology Development Agency, 111 Phahon Yothin Rd, Klong Luang, Pathumthani ,Thailand 12120
E-mail: jsiriporn_2000@yahoo.com

Abstract: The conformations and energies of two organic chromophores have been investigated by means of quantum mechanical calculations. Their structural backbones consist of carbazole-fluorene as an electron donor and pyran-4H-ylidenemalononitrile-thiophene as a π-conjugation linker. Two different anchoring groups, acrylic acid and cyanoacrylic acid, acting as an electron acceptor were introduced to structural backbones forming the TK1 and TK2 analogues, respectively. The structural, electronic and optical properties of TK1 and TK2 dyes were calculated by DFT/TDDFT method. The ground state structures were optimized at the B3LYP/ 6-31G(d,p) level of theory implemented in Gaussian 09 program. The excitation energies were evaluated by single point energy calculation using time-dependent density functional theory with the B3LYP method. Our results show that organic sensitizer with cyanoacrylic acid as the anchoring group induces red-shifted spectrum. Furthermore, the calculation results show that TK2 dye with strong electronic-withdrawing CN group performed better in intramolecular charge transfer (ICT) than TK1 dye without CN. These investigation suggests that the structural and optical properties can be gradually tuned, rendering possible the identification of dyes with desirable, electronic and optical properties.

1. Introduction

Dye-sensitized solar cell has been investigated as an alternative to the conventional solar cell because of it high photoelectric conversion efficiency, simple assemble technology and potential low cost [1]. The ruthenium complexed photosensitizers such as the N3 and N719 compounds show a solar energy to electricity conversion efficiency of 10% on average. However, ruthenium is a rare and expensive metal, which limits the potentially wide application of these complexes. Due to this, metal free sensitizers are being investigated as alternative sensitizers for DSCs applications [2]. Because of the strong emission and absorption properties, carbazole and their derivatives have been exploited as electroluminescent, non-linear optical (NLO) and photorefractive materials. The hole-transporting capability has been explored in OLEDs and, moreover, the wide band gap of carbazole has been utilized in constructing photovoltaic devices. Nagatoshi Koumura and co-workers designed and sensitized organic sensitizer based-on carbazole, MK1, MK2 and MK3, for application in dye-sensitized solar cells. It was found that the maximum value of 7.7% was obtained with the DSCs based-on MK-2 sensitizer [3]. Moreover, Samuel G. Awuah and coworkers report the synthesis, photophysical, electrochemical and theoretical properties of novel pyran-based organic dyes (D1, D2, and D3) as well as their applications in DSCs for the first time. The designed dyes possess a cyanoacrylic acid group as an acceptor and arylamine group as a donor group in a D-π-A configuration. The introduction of varying donor groups resulted in correspondingly different photophysical and electrochemical properties. The DSCs fabricated using dye D1 shown the highest photovoltaic performance with the overall conversion efficiency is 2.17%. The synthesized dyes with a pyran chromophore and arylamine donor groups showed potentials for applications in DSCs [4].

In this study, theoretical calculations were performed to study the ground-state structures and optical properties of carbazole-fluorene derivatives. The series of metal-free organic dyes containing carbazole act as electron donor, fluorene, phenyl and pyran act as linker. The influence of different acceptor, acrylic acid and cyanoacrylic acid were investigated.

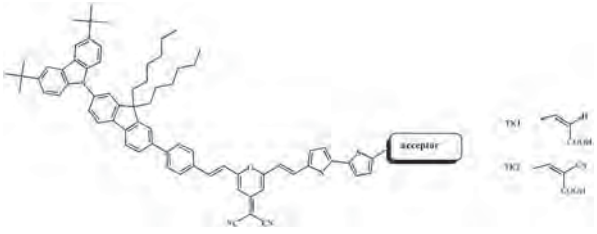

Figure 1. Molecular structure of target molecule

2. Materials and Methods

To gain insight into the factor responsible for the absorption spectral, we perform DFT and TDDFT calculations on the ground state of organic dyes [5]. The ground state structure of TK1 and TK2 were optimized by the DFT method using the B3LYP exchange–correlation function with 6-31G(d,p) basis set. Electronic population of the HOMO and LUMO were calculated to show the position of localization of

electron populations along with the calculated molecular orbital energy diagram. The electronic absorption spectra require calculations of the allowed excitation and oscillator strengths, these calculations were carried out using TDDFT with the same basis set and exchange–correlation functional. The absorption spectra of all organic dyes were calculated using the Swizard program and the results were compared with the experimental data. Effect of solvent polarity for dichloromethane was included by means of the conductor–like polarizable continuum model (C-PCM). This computational approach allows us to provide a detailed assignment of the excited state involved in the absorption process. All calculations were carried out using the Gaussian 09 program package [6].

3. Results and Discussion

In the investigation of D-π-A systems, the molecular structure of the ICT states is an important point of discussion. Herein, theoretical calculations were performed to study the ground-state structures of carbazole-fluorene dye.

3.1 Optimized structure

We optimized the geometries of TK1 and TK2 in the gas phase obtaining the geometries shown in Figure 2 and the selected bond distances and dihedral angles are listed in Table 1.

Table 1 The selected bond distances and dihedral angles of TK1 and TK2 by B3LYP/6-31G(d,p)

Dyes		**C-F**	**F-P**	**P-E**	**E-Py**
TK1	Dihedral (*Φ*)	-54.03	34.67	-0.62	2.93
	Distance (*r*)	1.42	1.48	1.46	1.44
TK2	Dihedral (*Φ*)	-54.72	34.90	-1.46	-2.50
	Distance (*r*)	1.42	1.48	1.46	1.44
Dye		**Py-E**	**E-T**	**T-T**	**T-A**
TK1	Dihedral (*Φ*)	-2.79	-0.79	1.90	-0.18
	Distance(*r*)	1.45	1.43	1.43	1.44
TK2	Dihedral (*Φ*)	2.14	0.32	0.72	-0.01
	Distance(*r*)	1.45	1.44	1.43	1.43

Note: C is Carbazole, F is Fluorene, P is phenyl, E is ethene, Py is pyran, T is thiophene, A is accepter

Figure 2. The optimize structure of TK1 and TK2 calculated by B3LYP/6-31G (d,p) level

The dihedral angle of TK1 and TK2 dyes was determined C-F dihedral angle were calculated to be -54.03 degree and -54.72 degree, respectively. The T-A dihedral angle are calculated to be -0.18 degree and -0.01 degree. We found that the cyanoacrylic acid group was located to be coplanar with the thiophene. From the calculated results indicate that the linker and acceptor moieties are fully conjugated as demonstrated by the co-planarity of the linker and acceptor groups.

3.2 Electronic structure

To gain insight into the geometrical electronic structures of the dyes, molecular orbital and density of state were performed by using B3LYP/6-31G(d,p) level of theory. The frontier molecular orbitals of the TK1 and TK2 dyes are shown in Figure 3

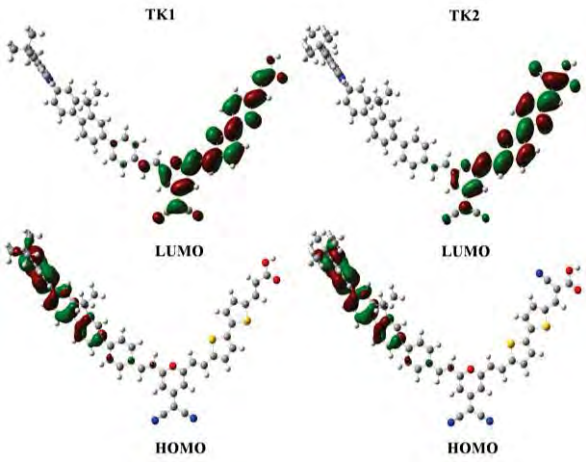

Figure 3. (a) Frontier molecular orbital of TK1 and frontier molecular orbital of TK2 calculated by B3LYP/6-31G (d,p) level of theory

For the TK1, the HOMO is a delocalized π orbital over the carbazole and fluorene unit while the LUMO is π* orbital that localized in pyran unit, thiophene unit and cyanoacylic unit. The electron density distribution of HOMO state for TK1, electron density of carbazole and fluorene are calculated to be 80% and 19%. While at the LUMO level, the electron density of pyran and thiophene in TK1 are calculated to be 44% and 43%, respectively. The percentage contributions of cyanoacrylic acid are calculated to be 12%.

For the TK2, at HOMO level is a delocalized π orbital over the donor and π-spacer, while the LUMO level is π* orbital that localized in π - spacer and acceptor unit. The percentage contributions of electron density of carbazole and fluorene are calculated to be 80% and 19%. While at the LUMO level the electron density of pyran and thiophene in TK1 are calculated to be 28% and 47%, respectively. The percentage contributions of cyanoacrylic acid are calculated to be 25%. These results indicate that electron density on cyanoacrylic acid unit of TK2 dye more than electron density on acrylic acid of TK1 dye. From the calculation results suggesting that TK2 dye might be easier injecting electron from acceptor to the conduction band of TiO_2 providing higher efficient electron injection.

Table 2 Summarizes the Energies and Character of Forntier Orbitals of TK1 and TK2 Calculated by B3LYP/6-31G(d, p)

Dyes	Molecular orbital	percentage composition				
		C	F-P	Py	T	A
TK1	L+1	0	24	60	10	6
	LUMO	0	2	44	43	12
	HOMO	80	19	1	0	0
	H-1	1	3	63	28	5
TK2	L+1	0	15	59	13	13
	LUMO	0	0	28	47	25
	HOMO	80	19	1	0	0
	H-1	100	0	0	0	0

Note: C is Carbazole, F is Fluorene, P is phenyl, Py is pyran, T is thiophene, A is accepter

The energy gap of TK1 without CN was calculated to be 2.10 eV. While the energy gap of TK2 with CN was calculated to be 1.77 eV. The HOMO-LUMO gap of TK2 is smaller than those of TK1 indicated that difference of acceptors affect to the HOMO-LUMO gap. The calculation results indicate that the energy gabs of dye is decreased when CN was introduced in to dye molecule. The one property which indicates a good dye-sensitizer is that the LUMO of dye should be located above and closed to the conduction band of TiO_2.

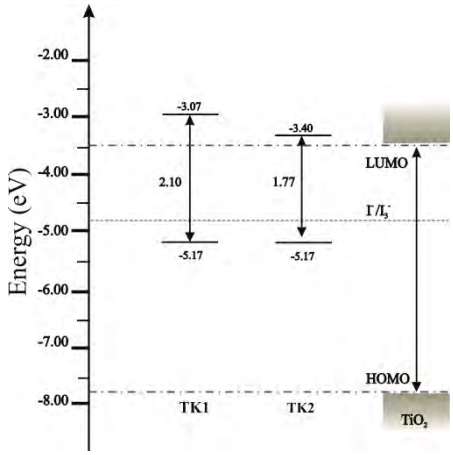

Figure 4. Molecular orbital energy diagram of TK1 and TK2

The energy level diagram of TK1 and TK2 are shown in Figure 4 The LUMO level of TK2 with cyanoacrylic acid as anchoring group are closer to the conduction band of TiO_2 than TK1 which have acrylic acid as anchoring group. These can be explained that the strong withdrawing CN group has ability in lowering LUMO level [7]. The results also imply that TK2 would have suitable property for injection of electron from excited dye to conduction band of semiconductor TiO_2.

3.3 Absorption spectra

TDDFT calculations on a B3LYP/6-31G(d,p) level of theory show transitions with large oscillator strengths consistent with the absorption spectrum. The UV-vis absorption spectra of all compounds are shown in Figure 5 Their optical characteristics are listed in Table 3.

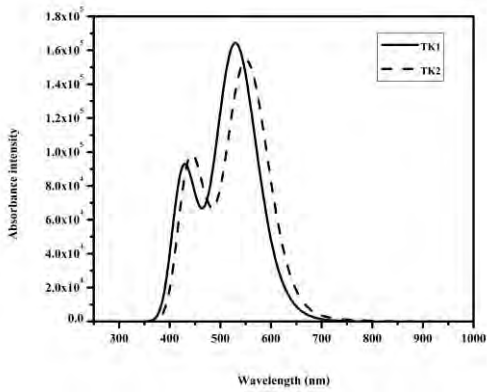

Figure 5. Calculated absorption spectra of TK1 and TK2 by TD-B3LYP/6-31G (d,p)

The main absorption peak of TK1 and TK2 is 463.0nm and 478.7 nm, respectively. The absorption band could be attributed to the π–π* transition of linker and acceptor and intramolecular charge transfer (ICT) between the donor and the acceptor.

The absorption spectra show that the calculated absorption spectra of TK2 with cyanoacrylic acid are red-shifted with respect to absorption spectra of TK1 with acrylic acid. These results suggest that the dyes containing cyanoacrylic acid group as acceptor promise a better property since it is beneficial for absorbing the longer-wavelength light than TK1 [8].

Table 3 The excitation energies, oscillator strengths and molecular compositions for the lowest states by the TD-B3LYP/6-31G (d,p) level

Dye	State	Excitation energy (eV, nm)	*f*	Assignment	Character
TK1	$S_0 \rightarrow S_2$	2.29 (542.5)	1.6468	H-1 → L (73%), H → L+1(7%)	π-π*
	$S_0 \rightarrow S_3$	2.48 (500.3)	0.6230	H → L+1 (87%) H-1 → L (6%)	π-π*
TK2	$S_0 \rightarrow S_2$	2.21 (560.6)	1.5163	H-3 → L (76%), H-2→L (37%), H → L+1 (6%)	CT, π-π*
	$S_0 \rightarrow S_3$	2.25 (551.2)	0.2780	H-2 → L (84%), H-1 → L (9%)	CT, π-π*

4. Conclusions

For carbazole-fluorene derivatives, the influence of different acceptor, acrylic acid and cyanoacrylic acid were investigated. From the calculation results, we found that the acrylic and cyanoacrylic acid group was located to be coplanar with the linker. It is indicating that the linker and acceptor moieties are fully conjugated as demonstrated by the co-planarity of the linker and acceptor. The absorption spectra of the dye

with difference acceptor show that the calculated absorption spectra of TK2 with cyanoacrylic acid are red-shifted with respect to absorption spectra of TK1 with acrylic acid. These results suggest that the dyes containing cyanoacrylic acid group as acceptor promise a better property since it is beneficial for absorbing the longer-wavelength light than the dyes containing cyanoacrylic acid group.

Acknowledgements

The authors would like to express grateful acknowledgments to Department of Chemistry, Faculty of Science, Ubon Ratchathani University and Thailand Graduate Institute of Science and Technology (TGIST).

References

[1] B. Oregan and M. Grätzel, *Nature*. **353** (1991) 737-740.
[2] M. Grätzel, *J. Photochem. Photobiol. C.* **4** (2003) 145–153.
[3] N. Koumura, Z.S. Wang, S. Mori, M. Miyashita, E. Suzuki, and K. Hara, *J. Am. Chem. Soc.* **128** (2006) 14256-14257.
[4] S. G. Awuah, J. Polreis, J. Prakash, Q. Qiao and Y. You, *J. Photochem. Photobiol A.* **224** (2011) 116-122.
[5] Z. Cai-Rong, L. Zi-Jiang, C. Yu-Hong, C. Hong-Shan, W. You-Zhi and Y. Li-Hua, *Comp. Theor. Chem* **899**(2009) 86-93.
[6] M.J. Frisch, G.W. Trucks, H.B. Schlegel, G.E. Scuseria, M.A. Robb, J.R. Cheeseman, G. Scalmani, V. Barone, B. Mennucci, G.A. Petersson, H. Nakatsuji, M. Caricato, X. Li, H.P. Hratchian, A.F. Izmaylov, J. Bloino, G. Zheng, J.L. Sonnenberg, M. Hada, M. Ehara, K. Toyota, R. Fukuda, J. Hasegawa, M. Ishida, T. Nakajima, Y. Honda, O. Kitao, H. Nakai, T. Vreven, J.A. Montgomery, Jr., J.E. Peralta, F. Ogliaro, M. Bearpark, J.J. Heyd, E. Brothers, K.N. Kudin, V.N. Staroverov, R. Kobayashi, J. Normand, K. Raghavachari, A. Rendell, J.C. Burant, S.S. Iyengar, J. Tomasi, M. Cossi, N. Rega, J.M. Millam, M. Klene, J.E. Knox, J.B. Cross, V. Bakken, C. Adamo, J. Jaramillo, R. Gomperts, R.E. Stratmann, O. Yazyev, A.J. Austin, R. Cammi, C. Pomelli, J.W. Ochterski, R.L. Martin, K. Morokuma, V.G. Zakrzewski, G.A. Voth, P. Salvador, J.J. Dannenberg, S. Dapprich, A.D. Daniels, O. Farkas, J.B. Foresman, J.V. Ortiz, J. Cioslowski, D.J. Fox, Gaussian 09, Revision A.02, Gaussian, Inc., Wallingford CT, 2009
[7] T. Yahhanthip, S. Jungsuttiwong, V. Promarak, S. Namuangruk, T. Sudyodsuk,P. Kochapradist and N. Kungwan, *J. Comp. Chem.* **32** (2011): 1568–1576.
[8] S. Meng, E. Kaxiras, M. K. Nazeeruddin and M. Gratzel, *J. Phy. Chem C.* **115**(2011):9276-82

SCREENING FOR ANTI-TUBERCULOSIS AGENTS USING COMPUTATIONAL TOOL

Auradee Punkvang[1*], Pharit Khamsri[2], Patchreenart Saparpakorn[3], Supa Hannongbua[3], Peter Wolschann[4] and Pornpan Pungpo[2]

[1]Faculty of Liberal Arts and Sciences, Nakhon Phanom University, Nakhon Phanom, Thailand
[2]Department of Chemistry, Faculty of Science, Ubon Ratchathani University, Ubon Ratchathani, Thailand
[3]Department of Chemistry, Faculty of Science, Kasetsart University, Bangkok, Thailand
[4]Institute for Theoretical Chemistry, University of Vienna, Vienna, Austria

[*] E-mail: auradee_pk@hotmail.com, Tel. 0906158793, Fax. +66 42587306

Abstract: To combat the drug-resistance of isoniazid (INH), the main drug for tuberculosis treatment, many series of direct InhA inhibitors have been developed such as arylamide, pyrrolidine carboxamide, diphenyl ether and triclosan derivatives. However, these direct InhA inhibitors have poor activities against whole cells of *M. tuberculosis*, the causative agent of tuberculosis (TB). Therefore, here we report the discovery of more potent direct InhA inhibitors as anti-tuberculosis agents through virtual screening approach. Initially, compounds with the structure similar to the reference compound were collected from ZINC database containing over 21 million purchasable compounds. Then, compounds which did not follow the Lipiniski's rule were removed. Further, the validated HQSAR model was used to select the compounds on the basis of the better predicted activity against whole cells of *M. tuberculosis*. Finally, 54 compounds possessing the better predicted activity against *M. tuberculosis* were yielded in this work. Therefore, these yielded compounds might be the good starting point to develop novel direct InhA inhibitors as anti-tuberculosis agents.

1. Introduction

Tuberculosis (TB) caused by *Mycobacterium tuberculosis* (*M. tuberculosis*) remains as a major world health problem, particularly in South-East Asia region [1]. In particular, the standard regimens using the existing drug to treat tuberculosis completely failed due to drug resistance of *M. tuberculosis* [2]. Isoniazid (INH) targeting at the enoyl-acyl ACP reductase (InhA) of *M. tuberculosis* is one of the most effective first-line anti-TB drugs [3]. However, the efficiency of this drug is diminished by the drug resistance of *M. tuberculosis*. To overcome the drug-resistance of isoniazid (INH), many series of direct InhA inhibitors have been developed such as arylamide, pyrrolidine carboxamide, diphenyl ether and triclosan derivatives [4-10]. A large number of these inhibitors have impressive activity against the purified target enzyme in vitro. However, they lack the activity against whole cells of *M. tuberculosis* due to the nature of the *M. tuberculosis* cell wall. Accordingly, the finding of new drugs to treat TB is an urgent priority. Therefore, the virtual screening approach was employed in this work to identify direct InhA inhibitors with the better activity against *M. tuberculosis*. These screened compounds might be the good starting template to develop novel direct InhA inhibitors as anti-tuberculosis agents.

2. Materials and Methods

2.1 Virtual screening of the more potent direct InhA inhibitors

Compound **VH07** (Figure 1) , one of direct InhA inhibitors containing the minimal inhibitory concentration (MIC) of 5.7 μM against *M. tuberculosis* [11], was selected as the reference structure to identify the potent anti-TB agents from the ZINC database consisting over 21 million purchasable compounds [12]. Initially, compounds with the identity greater than 70% to the reference structure were collected from ZINC database. Then, compounds which did not follow the criteria of the Lipiniski's rule (not more than 5 hydrogen bond donors, not more than 10 hydrogen bond acceptors, a molecular mass less than 500 daltons and an octanol-water partition coefficient log P not greater than 5) were removed. Finally, the validated Hologram Quantitative Structure Activity Relationship model (HQSAR model) [13] constructed from the experimental MIC values of direct InhA inhibitors was used as the filter to collect compounds containing the better predicted MIC values. The q^2 and r^2 of this HQSAR model are 0.6 and 0.97, respectively. Therefore, this model is reliable to predict the MIC values of screened compounds.

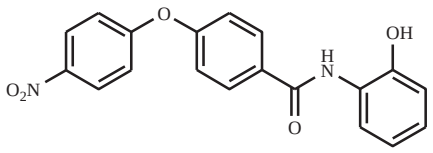

Figure 1. The chemical structure of compound **VH07**

3. Results and Discussion

In this work, the similarity search of an inhibitor has been used in combination with HQSAR approach for the virtual screening of direct InhA inhibitors as anti-tuberculosis agents. Figure 2 shows the virtual screening workflow used in this study.

In the first step, 4,274 compounds with the identity greater than 70% to the reference compounds were

collected from the ZINC database. Then, 3,461 compounds were yielded after the removal of compounds which did not follow the Lipiniski's rule. The selected compounds from this filter were subjected to the HQSAR to select compounds containing the predicted MIC values better than that of compound **VH07**. Finally, 54 hit compounds were obtained as listed in Table 1. Among of these compounds, compound 7 with ZINC ID of ZINC33751550 (Figure 3) shows the best activity against *M. tuberculosis* with the predicted MIC of 0.7 μM.

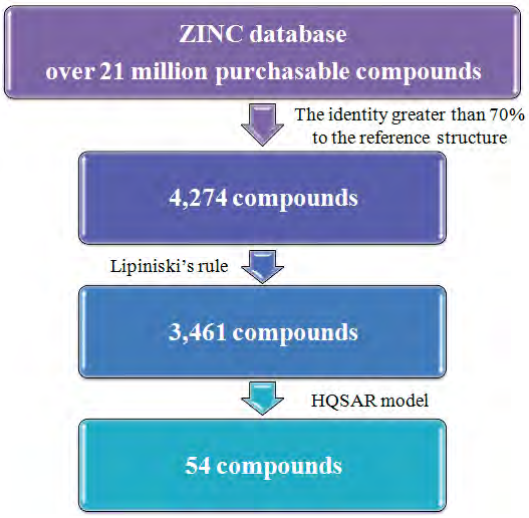

Figure 2. The virtual screening workflow

Table 1: The predicted activities of 54 hit compounds

No.	ZINC ID	Predicted MIC (μM)
Compound **VH07**		5.7[a]
1	ZINC01010611	1.4
2	ZINC01225242	1.4
3	ZINC02929282	2.1
4	ZINC03144051	2.0
5	ZINC03144062	4.2
6	ZINC20258831	1.1
7	**ZINC33751550**	**0.7**
8	ZINC36703911	3.5
9	ZINC00827834	2.1
10	ZINC01161025	2.0
11	ZINC03196894	1.2
12	ZINC07763927	4.9
13	ZINC14793456	4.0
14	ZINC25579729	5.2
15	ZINC00692454	2.1
16	ZINC00754579	3.6
17	ZINC00929332	5.0
18	ZINC01193051	3.0
19	ZINC07758362	4.0
20	ZINC14794216	5.5
21	ZINC20835853	5.5
22	ZINC01136839	2.1
23	ZINC01138251	5.4
24	ZINC03143990	2.1
25	ZINC04722006	2.4
26	ZINC08907795	3.1
27	ZINC12782480	2.7
28	ZINC64315742	5.1
29	ZINC01097315	1.8
30	ZINC03426341	2.6
31	ZINC22990368	4.2
32	ZINC32855789	5.0
33	ZINC00850636	3.3
34	ZINC00968753	1.1
35	ZINC06538978	4.8
36	ZINC09544678	4.7
37	ZINC11651793	5.3
38	ZINC14794237	5.1
39	ZINC20969157	4.4
40	ZINC00028991	1.8
41	ZINC01097335	1.4
42	ZINC04084227	1.2
43	ZINC04743913	2.4
44	ZINC07758331	5.4
45	ZINC09134896	3.7
46	ZINC10461671	2.0
47	ZINC11651462	3.8
48	ZINC19358091	5.6
49	ZINC25679958	5.6
50	ZINC00969354	1.4
51	ZINC01071839	1.7
52	ZINC15654171	3.6
53	ZINC19358253	4.6
54	ZINC16320121	2.6

[a]The actual value

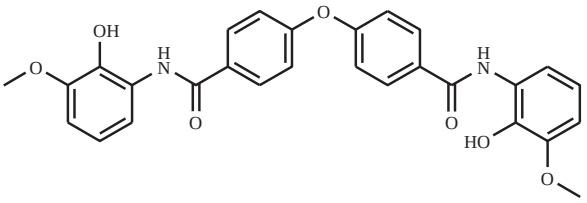

Figure 3. The chemical structure of compound 7

4. Conclusions

Virtual screening approach using the combination of the similarity search of an inhibitor and HQSAR methods is successfully to identify the direct InhA inhibitors as anti-tuberculosis agents. The predicted MIC values of most of the final hit compounds show significantly better than that of the reference compound. Therefore, the yielded compounds might be the good starting template to develop novel direct InhA inhibitors as anti-tuberculosis agents.

Acknowledgements

This study was partially supported by Faculty of Liberal Arts and Sciences, Nakhon Phanom University. Ubon Ratchathani University and University of Vienna are gratefully acknowledged for computing facilities.

References

[1] WHO report 2011, Global Tuberculosis Control, World Health Organization.

[2] World Health Organization. Multidrug and extensively drug-resistant TB (M/XDR-TB): 2010 global report on surveillance and response.

[3] K. Johnsson, D.S. King, P.G. Schultz, *J. Am. Chem. Soc.* **117** (1995) 5009–5010.

[4] J.S. Freundlich, F. Wang, C. Vilcheze, G. Gulten, R. Langley, G.A. Schiehser, D.P. Jacobus, W.R. Jacobs Jr., J.C. Sacchettini, *Chem. Med. Chem.* **4** (2009) 241-248.

[5] C.W. am Ende, S.E. Knudson, N. Liu, J. Childs, T.J. Sullivan, M. Boyne, H. Xu, Y. Gegina, D.L. Knudson, F. Johnson, C.A. Peloquin, R.A. Slayden, P.J. Tonge, *Bioorg. Med. Chem. Lett.* **18** (2008) 3029-3033.

[6] M.E. Boyne, T.J. Sullivan, C.W. am Ende, H. Lu, V. Gruppo, D. Heaslip, A.G. Amin, D. Chatterjee, A. Lenaerts, P.J. Tonge, R.A. Slayden, *Antimicrob. Agents Chemother.* **51** (2007) 3562-3567.

[7] T.J. Sullivan, J.J. Truglio, M.E. Boyne, P. Novichenok, X. Zhang, C.F. Stratton, H.J. Li, T. Kaur, A. Amin, F. Johnson, R.A. Slayden, C. Kisker, P.J. Tonge, *ACS Chem Biol.* **17** (2006) 43-53.

[8] X. He, A. Alian, R. Stroud, P.R. Ortiz de Montellano, *J. Med. Chem.* **49** (2006) 6308-6323.

[9] X. He, A. Alian, P.R. Ortiz de Montellano, *Bioorg. Med. Chem.* **15** (2007) 6649–6658.

[10] M.R. Kuo, H.R. Morbidoni, D. Alland, S.F. Sneddon, B.B. Gourlie, M.M. Staveski, M. Leonard, J.S. Gregory, A.D. Janjigian, C. Yee, J.M. Musser, B. Kreiswirth, H. Iwamoto, R. Perozzo, W.R. Jacobs Jr, J.C. Sacchettini, D.A. Fidock, *J. Biol. Chem.* **278** (2003) 20851-20859.

[11] M. Muddassar, J.W. Jang, S.K. Hong, Y.S. Cho, E.E. Kim, K.C. Keum, T. Oh, S.N. Cho, A.N. Pae, *Bioorg. Med. Chem.* **15** (2010) 6914-21.

[12] J.J. Irwin, T. Sterling, M.M. Mysinger, E.S. Bolstad, R.G. Coleman, *J. Chem. Inf. Model.* **52** (2012) 1757–1768.

[13] A. Punkvang, P. Kamsri, K. Kunasa, P. Saparpakorn, S. Hannongbua, P.Wolschann, P. Pungpo, *Science against Microbial Pathogens: Communicating Current Research and Technological Advances* Vol. 1, FORMATEX (2011), pp. 160-168.

ELUCIDATING THE STRUCTURAL CHARACTERISTICS OF 1,4-POLYISOPRENE BASED ON QUANTUM CHEMICAL CALCULATIONS

Pornpan Pungpo[1,*], Saisamorn Lumlong[1], Peter Wolschann[2], Alfred Karpfen[3] and Dieter Baurecht[4]

[1] Department of Chemistry, Faculty of Science, Ubon Ratchathani University, 85 Sthollmark Rd., Warinchamrap, Ubonratchathani 34190, Thailand
[2]Department of Pharmaceutical Technology and Biopharmaceutics, Faculty of Life Sciences, University of Vienna, Althanstrasse 14, A-1090 Vienna, Austria
[3] Institute for Theoretical Chemistry, University of Vienna, Währinger Straße 17, A-1090 Vienna, Austria
[4] Institute of Physical Chemistry, University of Vienna, Althanstrasse 14, Vienna A-1090, Austria

[*] Author for correspondence; E-Mail: pornpan_ubu@yahoo.com, Tel. +66 45 353400 ext 4124, Fax. +66 45 288379

Abstract: Natural rubber has been used extensively in many applications and products. Polyisoprene, mostly *cis*-1,4-polyisoprene, is the main component in natural rubber latex. Although the crystal structures of natural rubber were previously studied, but no acceptable crystal structure has been reported. Therefore, quantum chemical calculations were performed on five systems of monomer, dimer, trimer, tetramer and pentamer of 1,4-isoprene as the representative of *cis*-1,4-polyisoprene with the aim to elucidate the structural behaviours and conformation analysis of *cis*-1,4-polyisoprene. The optimized geometries of five molecular targets were carried out using high level of M062X calculations with 6-31G(d) and cc-pVDZ basis sets. The vibrational frequencies of the optimized structures were then calculated. The trend of calculated spectroscopic properties agrees well with the experimentally vibrational frequency spectra derived from the experimental ATR-IR. The results obtained from the present study are fruitful for better understanding of the structural and vibrational spectra of *cis*-1,4-polyisoprene within molecular level.

1. Introduction

Natural rubber from the tropical tree *Hevea brasiliensis*, has been used to provide about one-quarter of rubber based products trading worldwide [1-2]. Natural rubber is a mixture of polyisoprene and small amounts of other organic compounds as well as proteins, fatty acids, resins and inorganic materials (salts). Natural polymer of *cis*-1,4-polyisoprene is a major component in natural rubber [3-4]. The crystal structure of natural rubber has been studied by many researchers [5-7]. However, no acceptable crystal structure has been reported.

To predict the structural and vibrational modes of 1,4-polyisoprene, the quantum chemical calculations based on the density functional theory (DFT) had been performed. Five models based on number of 1,4-polyisoprene monomers were used in this study. The obtained results aid to fruitful the information data of 1,4-polyisoprene structures and vibrational frequencies for spectroscopic characteristics of natural rubber.

2. Materials and Methods

2.1 Structures of 1,4-polyisoprene and quantum chemical calculations

The structural models of 1,4-polyisoprene (n =1-5) were constructed using the standard tool in Guassview3.07 program as shown in Figure 1.

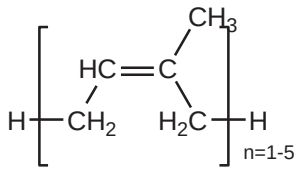

Figure 1 General structure of 1,4-polyisoprene

Five models of 1,4-polyisoprene (n =1-5) were calculated using Gaussian09 program. Fully geometry optimizations and the related vibrational frequency spectra calculations were performed using high level density functional theory of the highly parametrized, empirical exchange correlation functionals M062X calculations with 6-31G(d) and cc-pVDZ basis sets.

3. Results and Discussion

3.1 The geometry optimizations of 1,4-polyisoprene

Five systems of the molecular structures of 1,4-polyisoprene in the ground state (in vacuo) were optimized using M062X calculations with 6-31G(d) basis set. To validate the systems used in this study, the distance from the backbone carbon to carbon atom and the angles of 1,4-polyisoprene results obtained from the calculations were compared with the experimental data [5], as listed in Table 1. The results show that two systems of 1,4-polyisoprene, trimer and tetramer systems, are high correspondence to the experimental data.

Table 1. The structural information of the optimized structures of 1,4-polyisoprene obtained from M062X/6-31G (d) method

	Expt. [a]	Calculated models				
		Mono	Di	Tri	Tetra	Penta
Bond length (Angstrom)						
C1-C2	1.53	1.501	1.501	1.501	1.501	1.501
C2=C3	1.34	1.337	1.337	1.337	1.337	1.336
C3-C4	1.53	1.506	1.512	1.512	1.512	1.512
C4-C1'	1.54		1.543	1.543	1.543	1.542
Bond angle (degree)						
C1-C2=C3	121.2	128.2	126.8	126.9	126.8	126.8
C2=C3-C4	129.0	125.0	123.3	123.4	123.3	123.3
C3-C4-C1'	108.6	-	111.7	111.8	111.7	111.9
C4-C1'-C2'	111.4	-	112.1	112.2	112.3	112.0

[a] the experimental data obtained from reference [5]

Table 2. The structural information of the optimized structures of the 1,4-polyisoprene tetramer derived from different basis sets of calculations

	Expt. [a]	M062X	
		6-31G(d)	cc-pVDZ
Bond (Å)			
C1-C2	1.53	1.501	1.500
C2=C3	1.34	1.337	1.340
C3-C4	1.53	1.512	1.512
C4-C1'	1.54	1.543	1.541
Angle (degree)			
C1-C2=C3	121.2	125.7	126.7
C2=C3-C4	129.0	123.0	123.0
C3-C4-C1'	108.6	112.1	111.9
C4-C1'-C2'	111.4	122.1	111.9

[a] the experimental data obtained from reference [5]

Therefore, trimer and tetramer of 1,4-polyisoprene systems can be accurately used as the representative model of 1,4-polyisoprene for further study. To validate the methods of calculations, the geometry optimization using M062X with 6-31G (d) and cc-pVDZ basis sets were performed. The bond lengths and bond angles of 1,4-polyisoprene tetramer derived from the calculations and experimental data were compared as reported in Table 2. The results show that the structural information derived from cc-pVDZ basis set is high correspondence to the experimental data compared to those of the calculated results obtained from the 6-31G(d) basis set. Therefore, M062X calculations with cc-pVDZ basis set are chosen for further study. The optimized structures of 1,4-polyisoprene trimer and tetramer calculated using M062X/cc-pVDZ are illustrated in Figure 2.

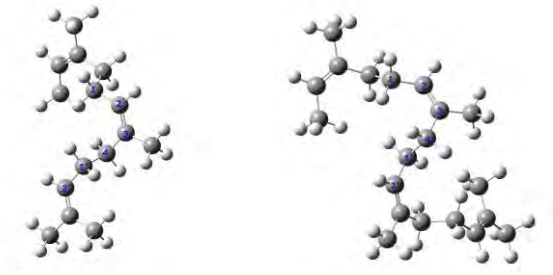

(a) **(b)**

Figure 2 The optimized structures of 1,4-polyisoprene trimer (a) and tetramer (b) calculated using M062X/ cc-pVDZ method

3.2 IR spectra and vibrational frequency results

The IR spectra of 1,4-polyisoprene trimer, tetramer, and pentamer models were calculated using M062X calculations with cc-pVDZ basis set as shown in Figure 3. The calculated vibrational spectra show similar within the range of 350-4000 cm^{-1}. Mainly, IR spectra were found in three regions. First two regions

in range of 3000-3250 cm^{-1} and 1600-1800 cm^{-1}, are the functional group regions. The third region, in the range of 350-1500 cm^{-1}, is the fingerprint region.

The analysis of vibrational frequencies and intensities of 1,4-polyisoprene are summarized in Table 3. As the experimental vibrational frequencies obtained from the ATR spectroscopy are available [8], the calculated vibrational frequencies were compared. The vibrational frequencies obtained from M062X/ cc-pVDZ calculations can be analyzed as follows; Increasing unit numbers of 1,4-polyisoperne from n = 3 to n = 5 result in broader peaks of vibrational spectra providing more details of vibrational modes. The calculated spectra obtained show high correspondence to the experimental data [8]. These results may be explained by the occurred hydrophobic interaction occurred between methyl group and isoprene backbone of the larger models of 1,4-polyisoperne. The vibrational frequency and intensity analysis of the 1,4-polyisoprene tetramer show the highest correspondence to the experimental data [8]. Therefore, the results derived from the 1,4-polyisoperne tetramer were selected for further analysis regarding mode of vibration.

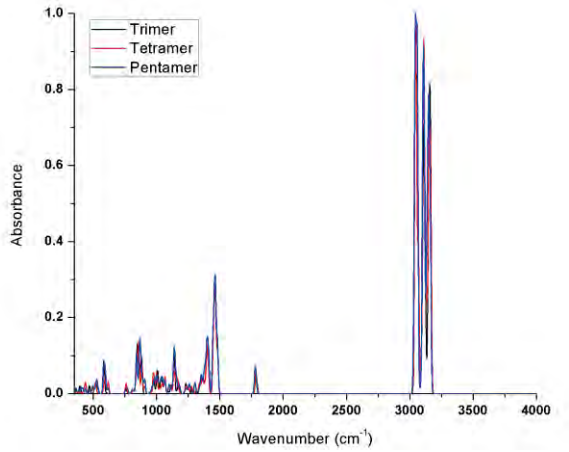

Figure 3 IR spectrum of 1,4-polyisoprene obtained from M062X/cc-pVDZ

The modes of vibration information of 1,4-polyisoprene can be predicted as following details; i) The peak at 3,152.50 cm^{-1} is dominated by linkage asymmetric C-H stretch vibrations of methyl group of 1,4-polyisoprene; ii) the peak at 3,069.60 cm^{-1} is dominated by linkage asymmetric C-H stretch in -CH_2-; iii) the peak at 3,042.60 cm^{-1} belongs to the mode of symmetric C-H stretch in -CH_3 and -CH_2-; iv) the peak at 1,735 cm^{-1} belongs to the mode of C=C stretch vibration; v) -CH_2- deformation displays in a range of 1,460-1,480 cm^{-1}; and vi) the peak at 884.00 cm^{-1} is dominated by linkage =CH out of plane bending. The important modes of vibration results obtained from M062X/cc-pVDZ calculations show good agreement with the experimental ATR vibrational frequency [6].

Table 3. The vibrational frequencies and intensities of 1,4-polyisoprene

Tri		Tetra		Penta	
cm^{-1}	Int.	cm^{-1}	Int.	cm^{-1}	Int.
849.90	17.60	842.00	12.05	864.30	16.28
881.10	12.84	884.00	12.90	872.90	18.01
1,138.00	13.99	1,401.60	10.58	1139.10	21.83
1,410.90	13.05			1411.40	13.01
1,454.30	13.37			1445.70	10.16
1,460.40	19.75	1,462.80	14.05	1460.30	19.52
		1,463.40	10.91	1464.70	13.40
		1,480.70	12.93	1482.40	10.26
		3,038.20	26.69	3034.60	24.05
				3036.20	15.61
				3036.80	30.80
3,040.20	26.70	3,042.60	39.73	3042.90	16.16
3,043.30	32.11	3,045.00	41.93	3043.60	34.01
3,045.20	35.80	3,045.50	17.10	3045.30	34.17
3,047.90	22.89	3,048.70	31.02	3046.10	34.30
3,048.60	20.99			3047.20	22.99
3,053.70	31.21	3,051.90	34.75	3057.20	77.19
		3,054.20	20.83	3059.90	41.90
3,064.40	33.03	3,066.30	25.75	3061.40	11.74
3,068.80	22.30	3,069.60	39.42	3062.20	29.09
3,104.80	17.41	3,102.60	18.25	3101.10	18.44
3,106.10	32.44	3,104.60	15.12	3103.00	12.25
		3,107.40	22.02	3104.10	32.00
		3,109.40	60.10	3104.50	25.89
				3108.00	29.32
3,111.90	20.86	3,111.20	17.37	3110.10	19.23
3,116.20	12.50	3,114.50	13.77	3110.70	13.44
3,116.50	34.76	3,115.50	24.08	3111.70	18.85
		3,118.10	25.60	3112.90	16.04
				3116.80	29.15
				3117.90	10.76
3,121.60	25.08	3,130.80	35.31	3134.80	53.63
3,144.30	10.16	3,141.40	11.17	3143.60	14.72
		3,146.30	17.73	3144.90	16.36
				3148.60	26.87
				3149.60	30.78
3,150.20	14.17	3,150.50	13.10	3151.70	28.32
3,151.90	26.50	3,151.50	10.63	3155.60	36.24
3,155.60	25.85	3,152.50	36.43		
		3,154.20	26.15		

4. Conclusions

The structural and vibrational spectra of 1,4-polyisoprene were successfully predicted using the M062X calculations with cc-pVDZ basis set. The 1,4-polyisoperne tetramer have been chosen as a suitable model providing the accurate results, regarding to the structural and vibrational information. The calculated structural and vibrational properties agree well with the experimental data. In the present study, the results provide better insight of the structural and normal mode of vibration of 1,4-polyisprene at molecular level.

Acknowledgements

ASEA-Uninet, OeAD-scholarship, University of Vienna, Faculty of Science, Ubon Ratchathani University are gratefully acknowledged for financial supports.

References

[1] http://www.nmce.com/files/study/rubber.pdf (Retrieved February 27, 2013).
[2] http://www.imf.org/external/pubs/ft/weo/2012/02/pdf/text.pdf (Retrieved February 27, 2013).
[3] A. R. Arnold and P. Evans, *J. Natl. Rubb. Res.* **6** (1991) 75–86.
[4] R.C. Crafts, J.E. Davey, G.P. McSweeney, I.S. Stephens, *J. Natl. Rubb. Res.* **5** (1990) 275–285.
[5] Y. Takahashi and T. Kumano, *Macromolecules* **37** (2004) 4860-4864.
[6] G. Rajkumar, J.M. Squire, and S. Arnott, *Macromolecules* **39** (2006) 7004-7014.
[7] M. Hernández, M.A. López-Manchado, A. Sanz, A. Nogales, and T.A. Ezquerra, *Macromolecules* **44** (2011) 6574-6580.
[8] P. Thawan, N. Srichak and S. Lumlong, *Senior project report for the science and rubber technology program,* Faculty of Science, Ubonratchathani University, Thailand, 2011.

Polymer Chemistry

PLASMA SURFACE MODIFICATION OF CELLULOSE MEMBRANE FROM WATER HYACINTH FOR IMPROVEMENT OF HYDROPHOBIC PROPERTY

Yannawit Chanpirom[1,*], Boonchoat Paosawatyanyong[2,3], Worawan Bhanthumnavin[4]

[1]*Program of Petrochemistry and Polymer Science, Faculty of Science, Chulalongkorn University, Bangkok 10330, Thailand.*
[2]*Department of Physics, Faculty of Science, Chulalongkorn University, Bangkok 10330, Thailand.*
[3]*ThEP Center, Commission on Higher Education, Bangkok 10400, Thailand.*
[4]*Department of Chemistry, Faculty of Science, Chulalongkorn University, Bangkok 10330, Thailand.*

[*] Author for correspondence; E-Mail: Yannawit.Ch@Student.chula.ac.th, Tel. +66 867154642

Abstract: The aim of this study is to modify surface hydrophobicity of regenerated cellulose fibers prepared from water hyacinth, a common weed found in canals. The obtained cellulose was subjected to regenerate procedure with sodium hydroxide and thiourea followed by treatment with ammonium sulfate. Membrane surface was then modified with sulfur hexafluoride (SF_6) plasma for improvement of hydrophobic property. The conditions used were power of 20 to 70 watts, 0.05 to 0.5 torr of pressure, and the treatment time is 1 to 20 minutes. Membrane surface was analyzed by Scanning Electron Microscopic technique. It was found that the cellulose membranes possess higher porosity than that of the cellulose sheet, a normal sheet of paper made by automatic sheet former. Moreover, higher roughness was observed in the case of membranes modified with SF_6 plasma than that of the non-modified counterpart. The functional groups were investigated by Attenuated Total Reflectance-Fourier Transform Infrared spectroscopy to show most characteristics of cellulose. However, absorbing frequencies corresponding to an incorporation of fluorine was difficult to observe since characteristic absorption bands of cellulose in the 1000-1400 cm^{-1} are overwhelming. Alternatively, an Electron Probe Microanalysis technique was employed to monitor the incorporation of fluorine. It was found that surface modification with SF_6 plasma resulted in attachment of fluorine content. Contact angle measurement has also been used to detect the wettability of the surface. Wettability cannot be measured on unmodified RCM since water was absorbed instantly which reflects a superhydrophilicity of the membrane while a contact angle of the RCM modified with SF_6 plasma higher than 90 degrees.

1. Introduction

The most important skeletal component in plants and the most abundant renewable material in nature are cellulose[1, 2]. The cellulose structures are highly crystalline because they have strongly inter-molecular and intra-molecular hydrogen-bonded structure[2, 3].

Regenerated cellulose membranes (RCM) have been actively studied over the last decade because of wide range of application of RCM in the field of membrane separation technologies such as haemodialysis, ultrafiltration and particle removal from solvents[4-6]. RCM prepared from cupric oxide process usually comes high toxicity and high cost[7]. In this work, we used same regenerated process from previous reseach groups, the cellulose obtained was subjected to regenerating procedure with sodium hydroxide and thiourea followed by treatment with ammonium sulfate[4, 5, 8].

Cellulose fibers were prepared form water hyacinth, a common weed found in canals[9]. It can quickly grow to very high densities; thereby completely clogging water bodies, which in turn may have negative effects on the environment and economic development[10]. Due to various socio-economic problems that it causes, several attempts have been made to seek for solutions to turn this waste material into useful products[11].

Low temperature plasma processing have been extensively used in research to improve the surface properties of polymer materials and membranes by various gasses[12, 13]. In this work, sulfur hexafluoride (SF_6) plasma was used as the fluorine source to improve the hydrophobic property[12].

The purpose of this research was to design a multifunctional cellulose membrane, which possesses hydrophobic, antibacterial and cytotoxic property[14]. To achieve a multifunctional property, the cellulose membrane surface was modified by SF_6 plasma treatment.

2. Materials and Methods

2.1 Materials

The dry water hyacinth was supplied by the Department of Botany, Faculty of Science, Chulalongkorn university. All of the chemical reagents used in this research were of analytical grade, and were purchased from Loba Chemie (Bangkok, Thailand) and Merck (Bangkok, Thailand).

2.2 Membrane preparation

Cellulose solutions in NaOH/thiourea solutions were prepared according to previous reports[4, 5, 8]. Cellulose fibers were dispersed in a 1.5M NaOH/0.65M thiourea aqueous solution and then stirred for 18 hours to obtain a slurry. The cellulose slurry was freezed at −6 °C for about 18 h and then thawed with vigorously stirring at room temperature. The slurry was centrifuged at 4900 rpm for 15 min to obtain a transparent solution containing 1.8wt.% cellulose.

Aqueous $(NH_4)_2SO_4$ solutions with 5wt.% concentration (*c*NHSO) was chosen as coagulants, and the coagulation bath was kept at room temperature. The cellulose solution was spread over a glass plate to give a gel sheet with a thickness of 0.10 mm, and then immediately immersed in coagulant for 5 minutes. The resulting fresh membranes were washed with running water about 20 min and then deionized water, finally air-dried at ambient temperature.

2.3 Plasma treatment

Regenerated cellulose membrane made from cellulose fibers, 1 cm x 5 cm in size was modified with radio frequency (RF) SF_6 plasma[12]. RF magnetron sputtering unit was used to produce SF_6 plasma. The chamber and the electrodes were made of stainless steel. The sample was placed on the lower electrode which was grounded. The frequency of the RF system was 13.56 MHz. The process parameters that were varied during the plasma treatment were treatment time, RF power, and SF_6 pressure[12, 15].

2.4 Properties characterization

The functional groups of unmodified RCM and RCM modified with SF_6 plasma were investigated by Attenuated Total Reflectance-Fourier Transform Infrared spectroscopy to show most characteristics of cellulose.

Membrane surface was analyzed by Scanning Electron Microscopic technique. It was shown that the cellulose membranes and the cellulose sheet porosities. The cellulose sheet is a normal sheet of paper made by automatic sheet former (hot pressing).

An Electron Probe Microanalysis technique was employed to monitor the incorporation of fluorine. It was shown that fluorine content on the membrane surfaces.

Contact angle measurement has also been used to detect the wettability of the surface. To minimize experimental errors, all the contact angle data were an average of three measurements at different locations of cellulose membrane surface. A hydrophicility, hydrophobicity, absorption time and aging time were measured by contact angle technique.

3. Results and Discussion

3.1 Structure of membranes

The IR spectroscopic analysis of unmodified RCM and RCM modified with SF_6 was analyzed. It is known that a C–F bond should show a characteristic peak between 1100 to 1360 cm^{-1} due to the −C–F bond stretching. However, absorbing frequencies corresponding to an incorporation of fluorine was difficult to observe since characteristic absorption bands of cellulose in the 1000-1400 cm^{-1} are overwhelming.

3.2 Pore size and surface roughness by SEM

The porosity and pore sizes have been used to classified between cellulose membrane and cellulose sheet. Cellulose membrane must have porosity and pore size over than cellulose sheet. Fig. 1. shows the membrane surface of cellulose sheet, a normal sheet of paper made by automatic sheet former (hot pressing) and RCM. It was found that the cellulose membranes (b) possess higher porosity than that of the cellulose sheet (a) because cellulose fibers on cellulose sheet were melted by the hot pressing. Then, cellulose sheet must possess lower porosity than regenerated cellulose membrane. RCM pore sized (c) were observed by SEM micrographs. The pore sizes of RCM (c) have less than 5 micrometer. But, SEM photograph could not observed the cellulose sheet's porosity.

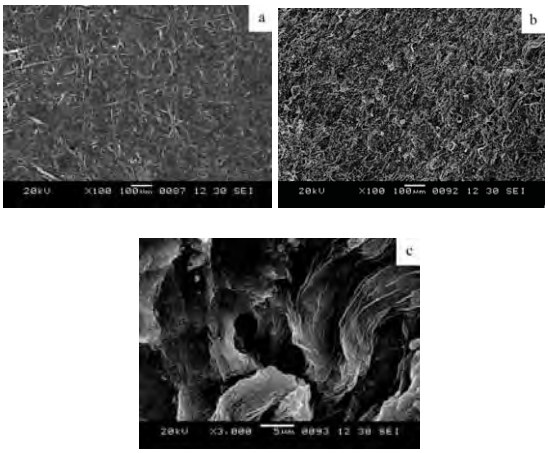

Fig. 1. SEM micrographs of the top views (a) cellulose sheet, (b) regenerated cellulose membrane and (c) pore sizes of RCM.

Moreover, Fig. 2. shows that higher roughness was observed in the case of membranes modified with SF_6 plasma than that of the non-modified counterpart. Smooth surface was shown in unmodified RCM (0m) micrograph. However, RCM modified with SF_6 plasma 20 minutes (20m) had higher roughness than RCM modified with SF_6 plasma 3 minutes (3m) and 10 minutes (10m). The key factor, treatment time, was used to control the surface roughness of membranes. The result of fluorine contents when increasing treatment time have been explained by EPMA mapping technique.

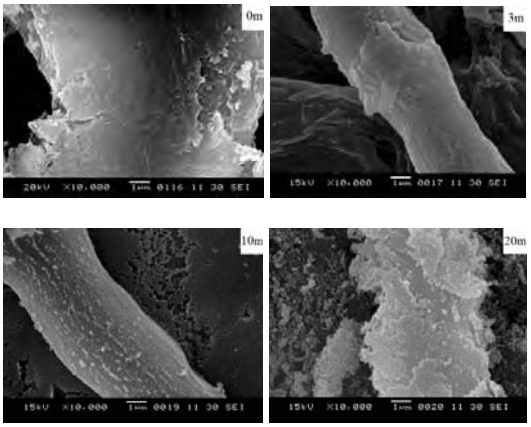

Fig. 2. SEM micrographs of surface roughness of the unmodified RCM (0m), RCM modified with SF_6 plasma 3 minutes (3m), 10 minutes (10m) and 20 minutes (20m).

3.3 Fluorine atoms and elemental contents

Fig. 3. shows the elemental analysis results by EPMA technique. It was found that surface modification with SF_6 plasma resulted in attachment of fluorine content. Table 1. shows the EPMA cannot detected fluorine atoms on (a) unmodified RCM surface but (b) RCM modified with SF_6 plasma 35 watts ,0.5 torr and treatment time 5 min (35W5) had 1.027%F by atom value. Fluorine contents were explained how RCM modified with SF_6 plasma surface had higher roughness than unmodified RCM. Fig. 2. when increasing treatment time, fluorine contents must be higher than low treatment time. Then, surface roughness of RCM modified with SF_6 plasma 20 minutes (20m) must higher than RCM modified with SF_6 plasma 3 minutes (3m).

Sulfur atoms were not detected on both surfaces and oxygen atoms value had not changed significantly.

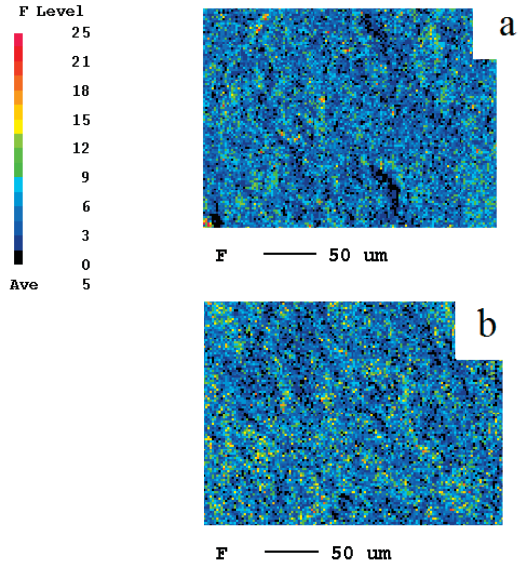

Fig. 3. fluorine contents on (a) unmodified RCM and (b) RCM modified with SF_6 plasma by EPMA mapping.

Table 1. Elemental contents (% atom on surface) of RCM (a) and (b) surface by EPMA mapping.

% Atoms / Samples	F	O	S
unmodified RCM	0	0.292	0
RCM modified with SF_6 35W5	1.027	0.299	0

3.4 Contact angle, absorption times and aging times

Contact angle measurement has also been used to detect the wettability of the surface. Fig. 4. shows the wettability cannot be measured on SF_6-modified RCM since water was absorbed instantly which reflects a superhydrophilicity of the membrane while a contact angle of the RCM modified with SF_6 plasma was higher than 90°. Table 2. shows the contact angle of RCM modified with SF_6 plasma. SF_6 plasma treatment would decreased a surface energy of membrane. 35W1 (35 watts, 0.5 torr and 1 min) shows high contact angle about 115° and 35W3 (35 watts, 0.5 torr and 3 min) shows the highest contact angle of all. But, 35W5-35W20 (35 watts, 0.5 torr and 5 to 20 min) show lower contact angle than 35W1-35W3. Roughness has been assumed in this study. High treatment time can increased higher roughness. Then, the contact angle must lower than low treatment time.

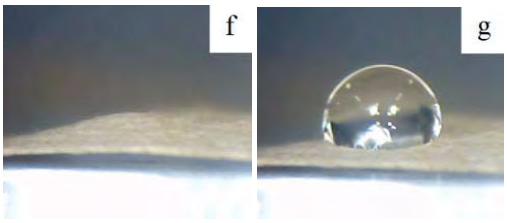

Fig. 4. Contact angle of unmodified RCM and RCM modified with SF_6 plasma.

Table 2. Contact angle of RCMs were showed on table.

Samples	Conditions	Power (watts)	Pressure (torr)	Time (min)	Contact angle(°)
1	unmodified	-	-	-	a
2	35W1	35	0.5	1	115
3	35W3	35	0.5	3	120
4	35W5	35	0.5	5	100
5	35W10	35	0.5	10	100
6	35W20	35	0.5	20	100

[a] Fabric too hydrophilic, it absorbs drop in less than 300 ms, not allowing contact angle measurement.

It is known that plasma treatment tend to undergo an aging process. Therefore, the hydrophobic property of RCM modified with SF_6 plasma and stored for 20 weeks tested, displaying a few lower hydrophobic property as fresh samples, so it can be concluded that the functional groups created on the surface of cellulose membrane with this treatment do not undergo fast ageing.

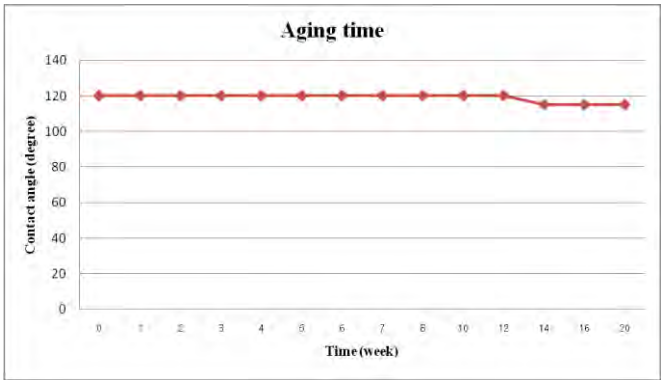

Fig. 5. Aging times of RCM modified with SF_6 plasma (35W3).

4. Conclusions

Regenerated cellulose membranes from water hyacinth can be prepared from treatment of sodium hydroxide/thiourea solutions with ammonium sulfate as coagulant. A surface treatment technique to chemically modified regenerated cellulose membranes was used to create a highly hydrophobic surface through an increase in surface roughness and incorporation of fluorine atoms. Regenerated cellulose membranes were modified with SF_6 plasma showed the highest hydrophobicity of 120°.

Acknowledgements

This work was supported by ThEP Center, Commission on Higher Education, Thailand and Assist. Prof. Sehanart Prasongsuk, Botany Laboratory and Photographic Science and Printing technology Laboratory and Petrochemistry and Polymer Science program Chulalongkorn university of Thailand.

References

[1] D. Johansson, *carbohydrate degradation and dissolution during Kraft cooking - Modelling of kinetic results*, Master's Thesis. Karlstad University, (2008).
[2] G. Odian, Editor, Principle of Polymerization, Vol.4,Wiley & Sons, New Jersy (2004), pp. 745-748.
[3] D. Klemm, B. Heublein, H.P. Fink and A. Bohn, *Angewandte Chemie International Edition*. **44 (**2005) 3358-3393.
[4] J. Zhou, L. Zhang, J. Cai, H. Shu, *J. Mem Sci.* **210** (2002) 77-90.
[5] Y. Mao, J. Zhou, J. Cai and L. Zhang, *J. Mem Sci.* **279** (2006) 246-255.
[6] N. Singh, Z. Chen, N. Tomer, S.R. Wickramasinghe, N. Soice and S.M. Husson, *J. Mem Sci.* **311** (2008) 225-234.
[7] N. A. Hoenich, C. Woffindin, J. N. S. Mathews, J. Vienken, *Bio.* **16** (1995) 587-592.
[8] D. Ruan, *J. Mem Sci.* **241** (2004) 265-274.
[9] W. J. Nolan, D. W. KIRMSE, *Hyacinth Control Journal* **12** (1974) 90-97.
[10] A. Malik, *Environ Int.* **33** (2007) 122-138.
[11] B.K. Barai, R.S. Singhal and P.R. Kulkarni, *Carb. Pol*. **32** (1997) 229-231.
[12] K. Kamlangkla, B. Paosawatyanyong, V. Pavarajarn, J. H. Hodak and S. K. Hodak, *Appl. Surf. Sci.* **256** (2010) 5888-5897.
[13] R.A. N. Pertile, F. K. Andrade, C. Alves, M. Gama, *Carb. Pol.* **82** (2010) 692-698.
[14] K. Tan, S. K. Obendorf, *J. Mem. Sci.* **289** (2007) 199-209.
[15] D. Boonyawan, S. Sarapirom, S. Tunma, C. Chaiwong, P. Rachtanapun, R. Auras, *Surf. Coat. Technol.* **205** (2011) S552-S557.

THE EFFECTS OF BUTYLCHLORIDE PRECURSOR ON ETHYLENE POLYMERIZATION ACTIVITY

Goond Hongmanee[1*], Saovalak Sripothongnak[2], Bunjerd Jongsomjit[1], Piyasan Praserttham[1]

[1] Department of Chemical Engineering, Faculty of Engineering, Chulalongkorn University, Thailand.
[2] Catalyst Research, Thai Polyethylene Co.,Ltd, Thailand.

[*] E-Mail: h.goond@gmail.com, Tel. +66 22186869, Fax. +66 2218 6766

Abstract: In the present study, roles of butylchloride (BuCl) in the Ziegler-Natta catalyst synthesis were investigated. BuCl was found to have two main functions; (i) formation of magnesium chloride support, and (ii) chlorinating agent. The main reaction for description of the support followed the Grignard reaction. The particle size of catalysts, which measured by SEM, showed fine particles when the amount of BuCl was increased. Moreover, it was found that the catalytic activity linearly increased with BuCl content. This phenomenon was hypothesized that chloride eliminated an inactive group which contained in catalyst such as an alkoxide group. The decrease of alkoxide group was proven by FT-IR technique. The peak at 1070 cm^{-1} of FT-IR patterns, which implies to an alkoxide group, decreased consequently as the amount of BuCl was increased. In addition, the titanium residue contained in polymer measured by XRF also supported the activity and FT-IR results. It decreased consequently as the content of BuCl was increased.

1. Introduction

In present, Ziegler-Natta catalyst (ZN) has been considered as the main catalyst for general polyethylene and polypropylene production[1] because of low production cost and high productivity. However, there are many works that are still developing the catalyst to achieve higher activity.

There are many factors affecting on the catalytic activity such as, temperature, Al/Ti ratio[2], cocatalyst type[3], and precursor. Alkyl chloride (RCl), such as butylchloride (BuCl), is one of the precursors for ZN synthesis. It was found that RCl can act as chlorinating agent[4] and relate with the magnesium chloride supported formation via the Grignard reaction route. Thus, the addition of BuCl also directly affects on catalytic activity.

Although the catalytic activity can improve by adjusting the amount of BuCl, the polymer properties such as particle size, molecular weight and crystallinity must be also considered. For example, it was found that fine particle of polymer is the cause of fouling in production process.

In this work, the effect of BuCl as precursor of ZN synthesis was investigated to achieve the requirement of catalyst and polymer properties.

2. Materials and Methods

2.1 Materials

All reactions were performed under purified argon atmospheres using a standard glove box and Schlenk techniques. Polymerization grade ethylene and argon were purchased from Linde Co., Ltd. Butylchloride (BuCl), titanium(IV)chloride, titaniumisopropoxide ($Ti(OPr)_4$), and hexane were purchased from Sigma-Aldrich Co. Ltd. Tri-n-octylaluminum (TnOA) was donated by Thai Polyethylene Co.,Ltd.

2.2 Catalyst preparation

The catalyst was synthesized according to the company's procedure.

2.2 Polymerization

The ethylene polymerization was carried out with 2l autoclave reactor connected with the lines available for argon, hydrogen and ethylene gases and also the hexane feed line. The reactor and all connected feed lines were free from humidity and oxygen by evacuation, and then followed by purging with the argon many times. First, 1l of hexane was filled and heated to 80 ^{0}C. The desired amount of TnOA was injected into the reactor subsequence by the injection of desired amount of titanium. In the condition with the presence of hydrogen, the reactor was pressurized with 1 bar of argon followed by pressurizing with hydrogen and finally pressurizing with ethylene gas.

3. Results and Discussion

3.1 Catalyst characterization

As seen in Figure 1, the XRD patterns of catalyst were noticeably changed. The peaks at 2θ≈32, 34, 36, 48, 58, 63, 68 and 70 assigned to magnesium carbonate[5], were decreased with increasing of BuCl:Mg ratios. Inversely, the peak at 2θ≈51 referred to δ-$MgCl_2$ was more obvious. These indicated that an insufficient amount of BuCl affected on a formation of δ-$MgCl_2$ and crystallinity of $MgCl_2$ supported. Moreover, BuCl also affected on $MgCl_2$-supported via Equation 1. The effect of BuCl could be seen in the size of catalyst which decreased with an increasing of BuCl. The size of catalyst can be seen in Table 1.

$$RMgX + BuCl \longrightarrow MgClX + R\text{-}Bu \qquad \text{Equation 1}$$

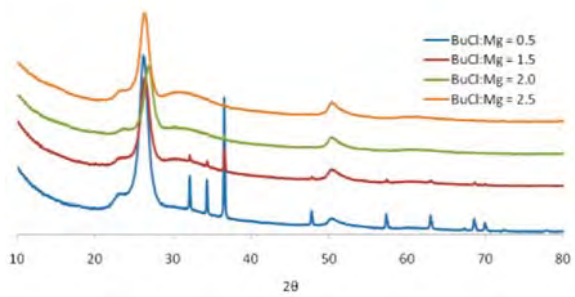

Figure 1. XRD patterns of catalyst with various BuCl:Mg ratios

Table 1: Average size of catalyst

BuCl:Mg	Particle size (μm)
0.5	59.52
1.5	52.14
2.0	29.86
2.5	< 20

3.2 Catalytic activity

As seen in Table 2 and Figure 2, the activities of 2 units had the same trends. This is suggested that the amount of BuCl did not affect on a quality of titanium active species. The increasing of BuCl amount affected on a formation of $MgCl_2$ support because BuCl played a key role as a chlorinating agent for Grignard reaction pathway, as seen in Equation 1.

Table 2: Amounts of titanium and magnesium in catalysts and catalytic activity

BuCl:Mg	Activity (kPE/molTi.h)
0.5	1,713
1.5	2,546
2.0	3,103
2.5	3,792

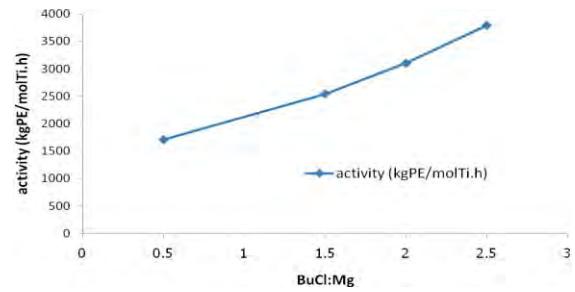

Figure 2. Catalytic activity, kPE/molTi.h.

Which R and X referred to electron withdrawing group and halogen atom, respectively. The FT-IR patterns as seen in Figure 3, also informed another role of BuCl, which is the elimination of alkoxide group. This can be

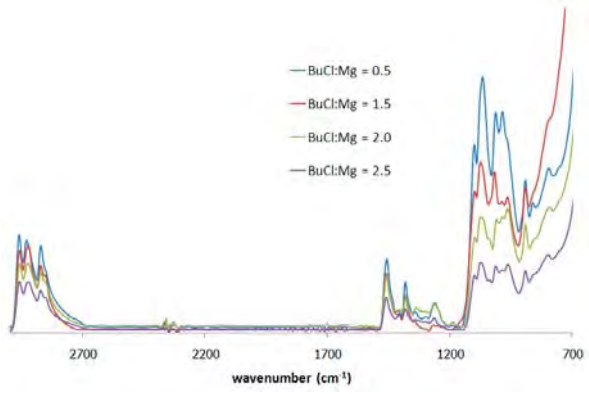

Figure 3 FT-IR spectra of catalyst with various BuCl:Mg ratios

seen in Figure 3. The decrease of height of the peak at 1070 cm^{-1} implies an existence of alkoxide group. The increased amount of BuCl decreased the crystallinity of $MgCl_2$ support, or increased the disorder of $MgCl_2$ support, resulting in more smooth of the XRD patterns, as seen in Figure 1. However, the disorder of $MgCl_2$ affected on the catalytic activity. Although the titanium content was decreased with increasing of BuCl, the catalytic activity was increased.

3.3 Polymer properties

Table 3: Polymer properties

BuCl:Mg	Ti residue (ppm)	Particle size (μm)
0.5	63	295
1.5	48	260
2.0	37	226
2.5	31	151

As seen in Equation 1, BuCl directly affects on support formation. It was found that more amount higher content of BuCl can generate more support and resulting in finer catalyst particles. This can be described by 2 possible ways. First, the decrease of polymer particle size is the result of replication phenomena, which occurs during the polymerization reaction. Moreover, BuCl as a chlorinating agent probably eliminates alkoxide group, which makes catalyst more active. The highly active catalyst is the cause of more fragmentation. Ti residue also supports this description. It was decreaseed because the catalyst contained less alkoxide species, which is an inactive species for ethylene polymerization. Thus, the more content of polymer can result in less Ti residue contained in polymer.

4. Conclusions

Butylchloride (BuCl) has an effect on both of catalyst properties and polymer properties. The increase of BuCl results in more active of catalyst and finer particles of catalyst. For polymer properties,

titanium residue and polymer particle size decrease with an increase of BuCl. However, the optimum amount of BuCl cannot be summarized yet because there are many others factor to be also considered such as molecular weight of polymer.

Acknowledgements

Thank you for financial support from Thai Polyethylene Co.,Ltd, Thailand.

References

[1] D. B. Malpass, *Introduction to Industrial Polyethylene*, Scrivener, Massachusetts, **2010**, p. 136.
[2] M. M. M. G. H. Zohuri, R. Jamjah, S. Ahmadjo, *Journal of Applied Polymer Science* **2004**, *93*, 2597-2605.
[3] G. A. H. NOOIJEN, *European Polymer Journal* **1994**, *30*, 11-15.
[4] C. W. K. Van C. Vives, Roger F. Kleinschmidt in *USE OF tert-BUTYL CHLORIDE AS A CHLORINATION AGENT IN THE PRODUCTION OF TERTIARY MONOOLEFINS*, *Vol.* Miami, **1969**.
[5] S. S. Pathak, M. D. Blanton, S. K. Mendon and J. W. Rawlins, *Corrosion Science* **2010**, *52*, 3782-3792.

PREPARATION AND CHARACTERIZATION OF TERMURIC EXTRACT-COCONUT OIL NANOPARTICLES WITH MODIFIED CARBOXYLMETHYL CELLULOSE AND SODIUM ALGINATE

Sa-Ad Riyajan* and Janthanipa Nuim,

Department of Materials Science and Technology Faculty of Science Prince of Songkla University Songkhla 90112, Thailand

* Author for correspondence; E-Mail: saadriyajan@hotmail.com, Tel. +66 74288398, Fax. +66 74 3446925

Abstract: The coconut oil (c-oil) can be used to treat the cancer since it contains lauric acid, capric acid and mystistic acid. In addition, turmeric extract has attracted the attention of researchers in the fields of cancer. But their drawback is poor water solubility. Therefore, the aim of this work was to prepare the turmeric extract/ c-oil nanoparticle from modified carboxylmethyl cellulose (MCMC) and sodium alginate (MNaAlg). The c-oil nanoparticles were obtained from Tween 80 and Pluronic F127 as a non-ionic surfactant by using high pressure homogenizer and coated with MCMC and MNaAlg. First, the CMC and NaAlg were modified by microwave to reduce the molecular weight and to obtain MCMC and MNaAlg. The c-oil was added in distilled water in presence of Tween 80 or pluronic F127 by high-shear homogenization and sonication at room temperature. In addition, the nanoemulsion was coated with MCMC and MNaAlg. The viscosity of MCMC and MNaAlg decreased as a function of H_2O_2 observing from MCMC and MNaAlg weight. All formulations of prepared nanoparticle were found to have good particle size stability. The particle size of the turmeric extract/c-oil nanoemulsion decreased as a function of Tween 80 and Pluronic F127 concentrations as well as the pressure used in homogenizer. But the particle size of the nanoemulsion increased with increasing c-oil content. In addition, the influence of modified MNaAlg and MCMC concentrations on the particle size of the c-oil nanoemulsion was discussed. The particles of coated turmeric extract/c-oil nanoemulsion with MNaAlg and MCMC were about 300-500 nm.

1. Introduction

Coconut palm is a plant which is cultivated in most tropical countries. A coconut fruit consists of 38.5% shell, 51.7% kernel and 8.9% water [1]. The coconut oil (c-oil) is widely used in milk and cream products. In the case of turmeric (Curcuma longa), it is a plant which is cultivated in most tropical countries. Turmeric extract has attracted the attention of researchers in the fields of Alzheimer's disease and breast cancer. However, the widespread clinical application of these efficient agents in cancer and other applications have been limited by their poor aqueous solubility and bioavailability [2-4]. Consequently, they have low efficiency to inhibit the cancer. Therefore, the emulsion technique has been used to solve this problem [5-6]. In recent years, nanotechnology has been explored due to its potential to revolutionize the medical field [7-9]. Nanoemulsion system could be another alternative for effective delivery of medical actives [8]. Nanoemulsion is a non-equilibrium colloidal system comprising of oil(s)/surfactant(s)/ water with particle size of diameter typically in the region of 20–200 nm. It is optically translucent/ transparent and kinetically stable and the process of formation is non-spontaneous [10]. The uses of nano-emulsions were reported in pharmaceutical drugs for topical transport of hydrophilic compounds, cosmetic formulations for a vehicle for skincare products, polymerization industry for polymer nanospheres [9] and food-related areas for food [11] as well as engineering processing [6]. Moreover, nanocapsules have great potential as a nanoreservoir system. With nanoemulsions, they share a liquid core within which a high loading capacity can be achieved. They also have a rigid capsule shell which can be made from biocompatible polymer. However, there is very limited information on the development of nanoemulsion system for c-oil and turmeric extract. In this work, the development of nanoemulsions system for turmeric extract/c-oil formulations was done. The objective of this work was to prepare the turmeric extract/ c-oil nanoparticle from modified carboxylmethyl cellulose (MCMC) and sodium alginate (MNaAlg). The c-oil nanoparticles were obtained by using Tween 80 and Pluronic F127 as non-ionic surfactants and a high pressure homogenizer followed by coating with MCMC and MNaAlg. The effect of modified MNaAlg and MCMC concentrations on the particle size of the c-oil nanoemulsion was discussed.

2. Materials and Methods

2.1 Materials

NaAlg and CMC were provided from Fluka company. C-oil and turmeric extract were supplied by Crop Protection (Thailand) and Osot company (Thailand), respectively. White hydrogen peroxide was purchased from Ajax Finechem Pty Ltd (Australia).

Non-ionic surfactant, Tween 80 was purchased from Sigma company. Pluronic F 272 was provided by Dow Corning (Singapore). Deionized water was prepared using Milli-Q water system (Milipore, USA).

2.2 Preparation of the MNaAlg and MCMC

NaAlg was dissolved in distilled water to get the NaAlg solution at 2%(w/w). The chemical modification was performed at room temperature. Initially, the effect of H_2O_2 on the reduction of viscosity was studied. The chemical modification of NaAgl/MCMC was carried out by microwave method for 1 min [12]. The NaAlg solution at different concentrations (10.0 ml) was immediately transferred into the tube of 20 ml plastic syringe. The record of the viscometer output parameters was started 1 min after the onset of experiment. The mass of unmodified and modified NaAlg/ MCMC was recorded, in grams, flowing in 2 min through a capillary of syringe with a specific diameter and length by a pressure applied *via* prescribed alternative gravimetric weights **[14]**. The method is adaptation from melt flow index in the similar standards ASTM D1238. The degree of reduction in viscosity was estimated by equation 1.

Degree of reduction in viscosity = W_{mo}/ W_{um}....(1)

Where W_{un} is mass of unmodified NaAlg or CMC, in grams, flowing in 2 minutes through a capillary of syringe and W_{mo} is mass of modified NaAlg or CMC, in grams, flowing in 2 minutes through a capillary of syringe.

2.3 Preparation and characterization of turmeric extract/c-oil nanoemulsion

The 2.5 g of c-oil was added in 50 g of distilled water in presence of Tween 80 or Pluronic F127 under stirring by magnetic stirrer. The c-oil liquid formed was blended with 5 g turmeric extract under stirring by high-shear homogenization (Pro Scientific Pro250, Monroe, CT, USA) for 2 min and intensity sonicated by a probe-type sonicator at a 35 W for 5 min at room temperature. The effects of pressure, 5%w/w of Tween 80 and 5%w/w of Pluronic F127 with different contents at 0.25, 0.50, 0.75 and 1.00 g, and c-oil concentration on the particle size of nanoemulsion were investigated. In addition, the nanoemulsion was coated with MNaAgl/MCMC solution.
The particle sizes of nanoemulsion were measured by using Zeta seizer (Malvern, United Kingdom). The resulting nanoemulsion samples were loaded into 1 cm^3 cuvettes and then put into a thermostated chamber. Dynamic light scattering was monitored at a 90^o angle.

3. Results and Discussion

The objective of NaAlg/CMC viscosity reduction by H_2O_2 was to prepare the smallest particle size of turmeric extract/c-oil nanoemulsion particle. Control of particle size is important with regard to the particular application of the resulting nanoemulsion. It was found that the particle size decreased rapidly with decreasing viscosity of NaAlg/CMC.

Effect of H_2O_2 on viscosity of NaAlg /MCMC

Figure 1 shows the changes of viscosity observing from W_{mo}/W_{un}. Then, the degradation of NaAlg molecules was activated by using H_2O_2 under microwave. The formed hydroxyl radical and hydrogen atoms are able to abstract hydrogen atoms from the polymer under microwave [12]. Thus, macroradicals are formed. Subsequent, lowering of NaAlg molecular weight was achieved observing from the reaction of viscosity. Degradation rate of NaAlg increased with increasing of the H_2O_2 concentration. This was due to more population of OH free radical formation leading to reduced viscosity (or increasing W_{mo}/W_{um}). The hydrogen peroxide was decomposed into H_2O and $0.5O_2$ under microwave [12].

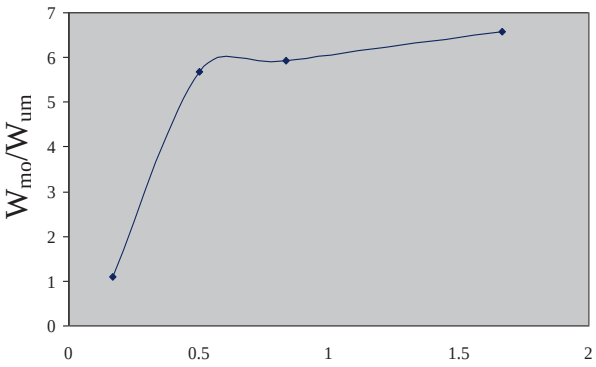

Figure 1 Influence of H_2O_2 on W_{mo}/W_{un} of NaAlg solution

The effect of hydrogen peroxide on W_{mo}/W_{un} value of CMC for 1 min of microwave time is presented in Figure 2. It was clear that the W_{mo}/W_{un} of sample modified with H_2O_2 was dramatically increased. This indicated that the chain scission of CMC was achieved by using H_2O_2 as a catalyst. Since W_{mo}/W_{un} value is inversely with viscosity. The formed hydroxyl radical and hydrogen atoms were able to abstract hydrogen atoms from the polymer.

Preparation of turmuric/c-oil nanoemulsion

Effect of pressure

Figure 3 shows the influence of the pressure and types of surfactant on the particle size of turmeric extract/c-oil nanoemulsion.

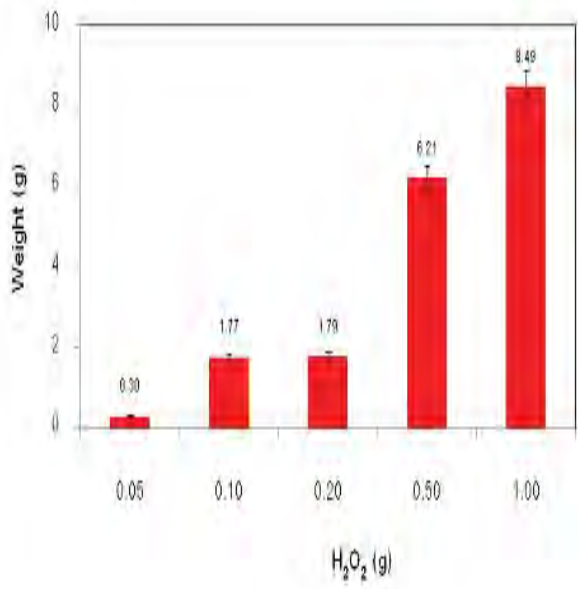

Figure 2 Effect of H_2O_2 on W_{mo}/W_{un} of CMC

It is clear that the particle size decreased with increasing pressure. In order to create a c-oil in water emulsion (one that remains stable for a long enough time), work must be done to overcome the interfacial tension between c-oil and water phases in presence of non-ionic surfactant. This can be achieved by high pressure homogenizer.

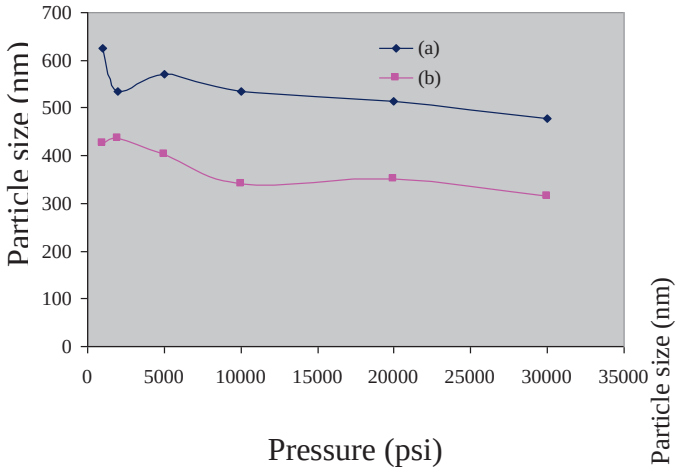

Figure 3 Effect of pressure on particle size of turmeric/c-oil nanoemulsion in the presence of (a) Pluronic F127 and (b) Tween 80 observing Zeta sizer

The optimal pressure for preparing turmeric extract/c-oil nanoemulsion was 30,000 psi. In addition, the particle size obtained from Tween 80 was smaller than that of the latex obtained from Pluronic F 127 as shown in Figure 3. This result is due to difference in hydrophilic-lipophilic blance (HLB) of two surfactants. The HLB of Tween 80 and Pluronic F 127 was 15 and 22, respectively [13]. In addition, the HLB value of Tween 80 was close to that required of the oil phase. Thus, the smaller in nanoemulsion was well achieved by using Tween 80 as a non-ionic surfactant. The effect of Tween 80/Pluronic F127 concentration on the particle size of turmeric extract/ c-oil nanoemulsion observing by Zeta sizer is presented in Figure 4. Results show that the particle size of the turmeric extract/c-oil nanoemulsion stabilized with Pluronic F 127 dramatically decreased after addition of 0.5% w/w Pluronic F127 concentration. The particle size of nanoemulsion decreased when the amount of surfactant increased thereby leading to critically stabilized turmeric extract/c-oil nanoemulsion particles. In case of Tween 80, this result was similar with Pluronic F 127. But the particle size of the turmeric extract/c-oil nanoemulsion obtained from Tween 80 was lower than that of Pluronic F127 due to its HLB value, as above mentioned. The optimal surfactant concentrations for preparing turmeric extract/c-oil nanoemulsion were 0.75 and 1 g for Pluronic F127 and Tween 80, respectively.

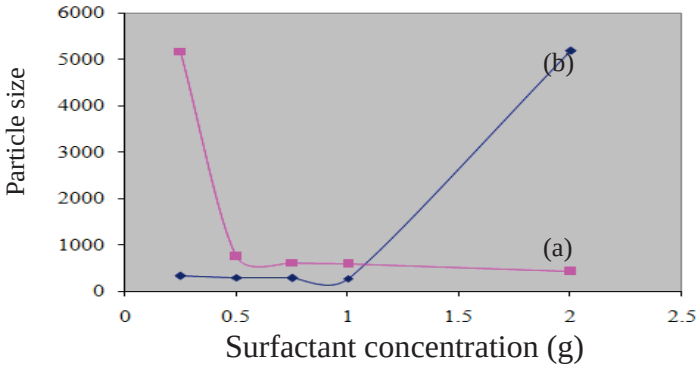

Figure 4 Effect of (a) Pluronic F127 and (b)Tween 80 concentration on particle size of turmeric extract/c-oil nanoemulsion observing Zeta sizer

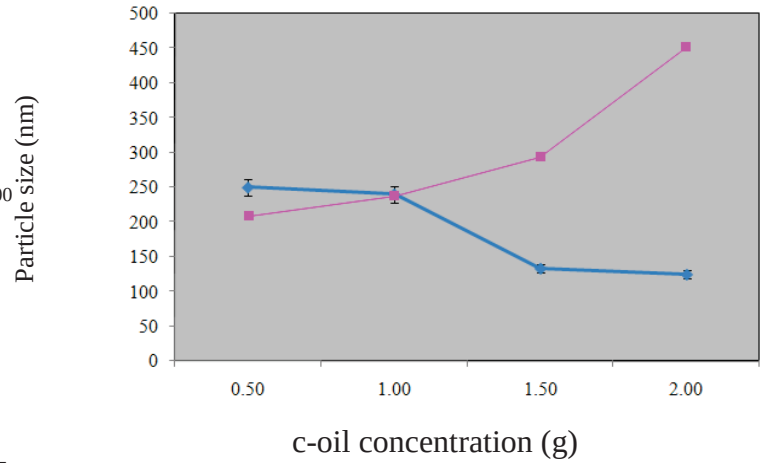

Figure 5 Effect of oil concentration on particle size of turmeric extract/c-oil nanoemulsion observing Zeta sizer

Figure 5 displays the influence of c-oil concentration on the particle size of turmeric extract/c-oil nanoemulsion. The particle size of nanoemulsion stabilized prepared with Tween 80 decreased as a function of c-oil concentration. This was due to the stabilization of c-oil with Tween 80. The optimal

concentration of c-oil for this purpose was 1.5 g. In the case of Pluronic F127, the particle size of turmeric extract/c-oil nanoemulsion increased with increasing c-oil concentration. Since the HLB of Pluronic F127 was higher that of c-oil, thus adding more amount of c-oil, the particle size increased. The effect of H_2O_2 concentration on the particle size of turmeric extract/c-oil nanoemulsion coated with CMC (called "capsule") observing from Zeta sizer was presented in Figure 6. Results show that the particle size of the capsule dramatically decreased with increasing with H_2O_2. The lowest particle size of nanoemulsion was found at 1 g of H_2O_2 due to the reduction of viscosity of CMC as above mentioned.

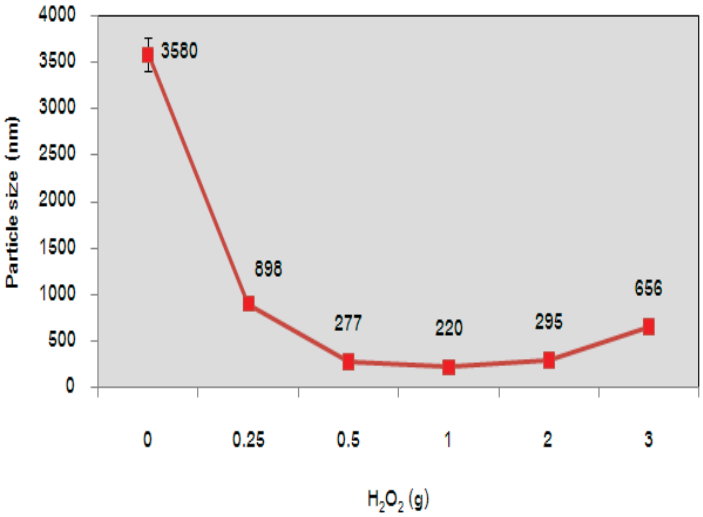

Figure 6 Effect of H_2O_2 on particle size of coated turmeric extract/c-oil nanoemulsion with MCMC observing Zeta sizer

The effect of H_2O_2 on particle size of turmeric extract/c-oil nanoemulsion was coated with NaAlg observing Zeta sizer is given in Figure 7.

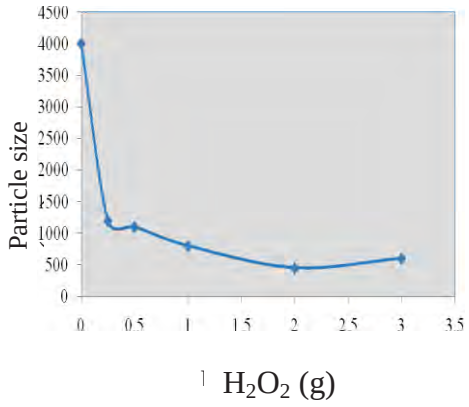

Figure 7 influence of H_2O_2 on particle size of coated turmeric extract/c-oil nanoemulsion with MNaAlg observing Zeta sizer

These results show the same trend as reported with MCMC. The particle size of capsule decreased as a function of H_2O_2 due to its low viscosity.

4. Conclusions

The successfully modified NaAlg and CMC with H_2O_2 under microwave method was achieved. Interestingly, the turmeric extract/c-oil nanoemulsion formulations were obtained with small particle sizes (<500 nm). All formulations were found to have good particle size stability. The particle size of the turmeric extract/c-oil nanoemulsion decreased as a function of Tween 80 and Pluronic F127 concentrationa and high pressure homogenizer. Tween 80 was a good surfactant for preparing turmeric extract/c-oil nanoemulsion. The particle of coated turmeric extract/c-oil nanoemulsion with MCMC/MNaAlg was about 300-500 nm.

Acknowledgements

The authors would like to acknowledge the financial support from the Research, Development and Engineering (RD&E) fund through The National Nanotechnology Center (NANOTEC), The National Science and Technology Development Agency (NSTDA), Thailand (P-11-00981) to Prince of Songkla.

References

[1] M. Thierry, M. Cedric, V. B. Laurent, Inform. *Process. Lett.* 106 (2008) 120-126**.**

[2] M.D. Mandal, S. Mandal, *Trop. Med*. 4 (2011) 241-247

[3] C.V. Floruta, *Wocn*, 28 (2001) 28-31**.**

[4] S. Rodrigues, G.A.S. Pinto, *Food Eng.* 80, 3, 869-872 (2007).

[5] C.C. Loi, H.C. Boo, A.S. Mohammed, A.A. Ariffin, Food Chem. 128, 1, 223-226 **(2011)**.

[6] Z. Fu, M. Liu, J. Xu, Q. Wang, Z. Fan, *Fuel*. 89, 2838-2843 **(2010)**.

[7] G. Calderó, M.J. García-Celma, C. Solans. *Colloid Inter. Sci*. 353, 406-411 **(2011).**

[8] J. Zhou, Q. Chang, Y. Wang, J. Wang, G.. Meng, *Sep Pur Technol*. **75** (2010) 243-248**.**

[9] A. Serrano-Medina, J.M. Cornejo-Bravo, A. Licea-Claveríe. *Colloid Inter Sci*. **369** (2012) 82-90**.**

[10] S.P. Gumfekar, K.J. Kunte, L. Ramjee, K.H. Kate, S.H. Sonawane, *Prog Org. Coat*. **72**, 632-637**.**

[11] L.C. Jiang, M. Basri, D. Omar, M.B. Abdul Rahman, A. B. Salleh, R.N. Zalih, R.A. Rahman, Molecular Liquid. **158** (2011) 175-181 **.**

[12] H. Shahriari, M. Warith, M. Hamoda, *Waste Manage*.**32**(2012) 41-52**.**

[13] A.S. Prakash, *J. Excipients and Food Chem.* **1**, (2010) 51-59 **.**

[14] ASTM D1238 **:** Standard Test Method for Melt Flow Rates of Thermoplastics by Extrusion Plastometer

ANTISTATIC PERFORMANCE OF POLY(VINYL ALCOHOL) - FERROFLUID COMPOSITES FOR USE AS ELECTROSTATIC DISSIPATIVE COATING

Winatthakan Phuchaduek[1], Supranee Kaewpirom[1*]

[1] Department of Chemistry and Center of Excellence for Innovation in Chemistry, Faculty of Science, Burapha University, Bangsaen, Chonburi 20131, Thailand

[*] Author for correspondence; E-Mail: kaewpiro@buu.ac.th, Tel: +66-38-103-066

Abstract: The main purpose of this study was to prepare polymer composites for use as electrostatic dissipative (ESD) coatings. Polyvinyl alcohol, PVA, was used as a matrix and ferrofluid was used as a conductive filler. Ferrofluid was prepared by co-precipitation method between iron (III) chloride hexahydrate and iron (II) chloride tetrahydrate, using tetramethyl ammonium hydroxide as a surfactant. The obtained magnetic particles (Fe_3O_4) were characterized by FT-IR. The effect of ferrofluid content on the electrical and mechanical properties of the composites was investigated. The distribution of the conductive filler and the morphology of the composites were also examined by SEM. The experimental results provided useful information for understanding the behaviour of electrical conductivity and mechanical properties of the proposed ESD coating. In addition, the adhesion strength and wettability of the coatings on a glass substrate were analyzed by cross-cut adhesion test and water contact angle measurement, respectively.

1. Introduction

The estimated annual losses in products containing sensitive electronics due to electrostatic discharge (ESD) during manufacturing, assembling, storage and shipping are in billions of dollars [1]. The occurrence of these electrostatic charges is related to the surface resistance of materials. One way to solved such electrostatic problems is by using conductive polymer composites (CPCs) as packaging or coating for such sensitive products.

CPCs are important in technological applications and constitute an ongoing topic of tremendous commercial interest [2]. CPCs based on insulating polymer matrices and formulated using electrically conductive fillers. Conductive fillers may be particulate or fibrous such as carbon black, graphite, metal powder, aluminium flakes or conductive polymers [3, 4]. These multifunctional materials are routinely employed in various commercial applications due to their good electrical conductivity, corrosion resistance, light weight, enhanced mechanical properties, and the ability to be readily adapted to the needs of a specific application. Examples of applications that use CPCs include electronics, automotive and aerospace manufacture, antistatic packaging and coatings [2, 5], as well as antistatic and ESD materials. Whatever be the application used, one main parameter determining CPCs properties is the conductive pathways structure, depending on many parameters such as filler content, filler dispersion, filler distribution, filler conductivity, surface free energy of the filler and the matrix, polymer matrix crystallinity, reticulation and exclusion volume. Polymer composites used for the ESD applications, the optimum surface resistivity is in the range 10^6 – 10^9 Ω/sq [1, 4].

Polyvinyl alcohol (PVA) is one of the promising representatives of polymeric materials and there are numerous proposals for its application in electronics, as well as packaging, textile and food products. This is due to its easy preparation, high clarity, high gloss, excellent durability, chemical resistance, physical properties, lowest permittivity coefficient and completely biodegradable [3]. Addition of conductive fillers converts the non-conductive PVA for formulation into an electrically conductive system.

Ferrofluid (FF) was colloidal dispersions of small single-domain magnetic particles suspended in a carrier fluid. Recently, FF has been the subject of much interest because of their unusual optical, electronic, and magnetic properties, which can be changed by applying an external magnetic field. FF-composite materials have potential for the EMI shielding and ESD, due to the magnetic particles have formed like a hillock and tending to form elongated in the direction of the applied magnetic field in polymer composites [6, 7].

In this study, CPC composites from PVA and FF were prepared, using glutaraldehyde as a crosslinker. The effect of FF content on the electrical conductivity of the composites was investigated. The changes of the effective parameters including FF distribution and the composite morphology were also studied as well as the adhesion strength, wettability, thermal and mechanical properties of the composite films.

2. Materials and Methods

2.1 Materials

Polyvinyl alcohol (PVA, Mw 85,000-124,000 g/mol) was purchased from Sigma-Aldrich Company, Germany. Iron (II) chloride tetrahydrate ($FeCl_2 \cdot 4H_2O$) and Iron (III) chloride hexahydrate ($FeCl_3 \cdot 6H_2O$) were from QRëc Company, New Zealand. Ammonium hydroxide solution (25% NH_4OH) was from Loba chemie private limited Company, India. Tetramethyl

ammonium hydroxide (TMAOH, 10% in water), the surfactant, was from J.T.Baker Company, Germany and glutaraldehyde (GA, 1.2%, w/v), the crosslinking agent, was from Fluka Company, Switzerland. The other chemical reagents used (hydrochloric acid, sulphuric acid, acetic acid and methanol) were from QRëc Company, New Zealand.

2.2 Synthesis of magnetite particles

To synthesize Fe_3O_4 particles, 2 g (1.0 M) of $FeCl_2{\cdot}4H_2O$ was dissolved in 5 mL 2.0M HCl solution and 3.2 g (2.0 M) of $FeCl_3{\cdot}6H_2O$ in 20 mL 2.0M HCl solution. $FeCl_2{\cdot}4H_2O$ and $FeCl_3{\cdot}6H_2O$ solution were combined in a flask and stirred vigorously. In the mean time, 50 mL of 1.0M NH_4OH was added slowly over a period of 5 minutes into the flask by a dropper. Just after mixing the solutions, the color of the solution changed from light brown to black, indicating the forming of Fe_3O_4 particles and stirring was continued for 15 min. Stirring was then stopped and a strong magnet was used to settle the black precipitate (5-10 min). Most of the liquid was then decanted and disposed of. The products (Fe_3O_4 particles) were also washed and re-dispersion three times with de-ionized water. Then, the final products were dried in a vacuum oven at room temperature for 24 h, and the Fe_3O_4 particles were finally obtained.

2.3 Preparation of ferrofluid (FF)

12.5 mL of 10 % TMAOH, Fe_3O_4 particles obtained from magnetic separation and de-ionized water were mixed together. The mixture was gently stirred with a glass rod for at least a minute to suspend the solid in the liquid and pour into a plastic glass. A strong magnet was used to attract the FF to the bottom of the plastic glass, while the dark liquid was pour off and discarded. Finally, FF was obtained.

2.4 Preparation of composites

A PVA solution with a concentration of 10 % (w/v) was prepared by dissolving PVA powder in deionized water at 90 ºC under stirring for 2 h. To prepare the composites, 10 mL of PVA solution was mixed with FF (20, 30, 40, 50 and 60 wt%). Then 2.8 mL of crosslink solution (50% w/v methanol (the quencher), 10% w/v acetic acid (the pH controller) 1.20% (w/v) of glutaraldehyde and 10% (w/v) sulfuric acid (the catalyst), make up a 3:2:1:1 weight ratio solution) was added into the mixture under constant stirring for 15 min, in order to obtain uniform distribution of filler. The mixtures were poured into a Petri disk or coated, using a bar-coater, on glass substrate and cured for 12 h at 50 °C in hot air oven and for 24 h at 40 °C in vacuum oven. The thickness of the dry film were 0.10 and 0.05 mm, respectively.

2.5 Characterization

The functional groups of the Fe_3O_4 particles were analyzed by FT-IR spectrometer (model system 2000 FT-IR, Perkin Elmer) at wavenumbers 400 to 4000 cm^{-1}. The water contact angle (WCA) was measured after a drop of DI water was set on the composite films and the side view pictures of the droplet were taken. The averaged WCA value was obtained by measuring five randomly selected droplets. The tensile stress-strain test of the composite films was achieved using a tension mode of Testometric (Micro 350) at room temperature. The size of the cured film was 5 cm × 0.5 cm and thickness was about 100 µm (sample number, n = 10). The gauge length was 3 cm and the cross-head speed was 6 mm/min. Cross-cut adhesion of the composite films was carried out according to ASTM D3359-97. Square boxes of 1 mm^2 were made on a 1 cm × 1 cm square of the test specimen. The boxes were covered by adhesion tape. The adhesion tape was then peeled off and the number of boxes removed from the glass surface was counted to check the adhesion of the films. Surface morphology and the conductive fillers distribution in the composite films were carried out using scanning electron microscope (model LEO-1450 VP) at 10 kV accelerating voltage. Surface resistivity was measured according to ASTM D257-90.

3. Results and Discussion

3.1 Structure analysis of ferrofluid (FF)

The co-precipitation method was used to synthesize FF. The synthesis was based on reacting iron(II) and iron(III) ions in an aqueous ammonia solution to form magnetite, Fe_3O_4, as shown in eq 1.

$$2FeCl_3+FeCl_2+8NH_3+4H_2O \rightarrow Fe_3O_4+8NH_4Cl \quad (1)$$

FF was colloidal suspensions of Fe_3O_4 particles, with the viscosity of 11.2±0.1 cP. Due to the Fe_3O_4 particles exhibited superparamagnetic behavior, Fe_3O_4 particles were prone to aggregate. TMAOH, therefore, was adding as a surfactant to the aqueous medium in order to produce an electrostatic repulsion in an aqueous medium [8].

Fig. 1 shows the FT-IR spectrum of Fe_3O_4. In this spectrum, the peak at 3437 cm^{-1} is attributed to the stretching vibrations of the –OH, which is assigned to OH^- absorbed by Fe_3O_4 particles. The peak at 598 cm^{-1} is attributed to the Fe-O bond vibration of Fe_3O_4 [9]. Other peaks at 1590-1650 cm^{-1} and 1351 cm^{-1} are assumed as the conjugated of COO–Fe and the C–O stretching vibration, respectively, which are the result of the reaction between remaining Fe^{3+}/Fe^{2+} and CO_2 in air [10].

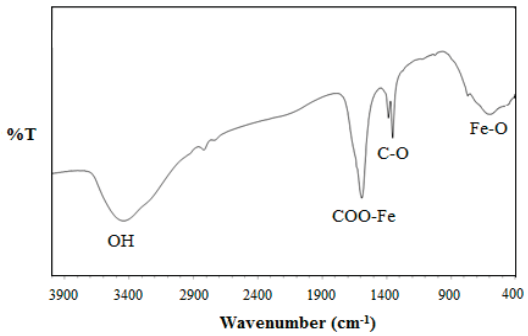

Figure 1. FT-IR spectrum of Fe_3O_4 particles.

3.2 Electrical conductivity

The electrical conductivity of the composites generally depends on the concentration of the FF. The effect of FF content on the surface resistivity of FF filled PVA composites are presented in Fig. 2. It can be seen that the resistivity of the composites can be reduced by addition of FF filler. With 20 wt% FF, when a conductive Fe_3O_4 particles network was not formed in the PVA matrix, the resistivity of the composites was slightly different from the PVA. The electrical percolation threshold of the PVA-FF composites was between 20 and 30 wt%, the resistivity showed a sudden drop and reached 1.83 ($\times 10^7$) ohm per square at 30 wt%. The sudden drop of resistivity in the composites was ascribed to the enhanced dispersion of FF in PVA as the Van der Waals force of attraction among the particles decreases in presence of PVA. Beyond a critical filler loading, a significant increase in the conductivity of the composites indicates the formation of filler networks above the percolation threshold [11]. Above 30wt%, the resitivity decreased slowly with the increase of FF content, and reached 4.39 ($\times 10^6$) ohm per square at 60wt%. Hence, within 20-60 wt% concentration of FF the composites behaved like semiconducting materials suitable for ESD applications.

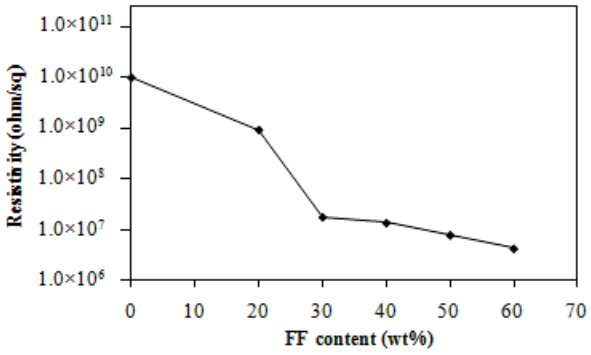

Figure 2. Electrical resistivity of PVA composites as a function of FF content.

3.3 Water contact angle (WCA)

In our experiments, it was proved that the neat PVA and crosslinked PVA films coated on the glass substrate is hydrophilic, with the WCA of 53º and 58º, respectively.

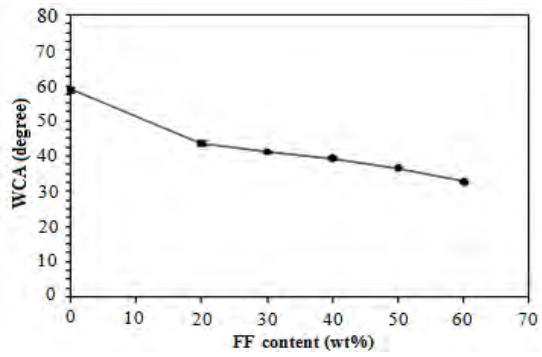

Figure 3. WCA on the glass substrates coated with PVA composites filled FF.

WCA on the glass substrate coated with PVA-FF composite films were also measured and the data are shown in Fig. 3. Each value represents an average of 5 measurements with the standard deviation less than 1º. As seen in the figure, the PVA-FF composite films showed lower values of WCA when compared with that of crosslinked PVA films. The values of WCA for the obtained PVA-FF composites were in the range 33-44º. The presence of Fe_3O_4 particles in PVA matrix, therefore, leads to the decrease of the WCA of composites in the whole concentration range studied.

3.4 The morphology studies

SEM Microscopy studies were performed for the PVA-FF composites. Fig. 4a displayed micrograph for crosslinked film PVA, showing smooth and relatively homogeneous appearance. Figure. 4b-2f displayed the SEM micrographs for the PVA-FF composites. It can be observed that at the lower filler concentration (Figure. 4b), Fe_3O_4 particles discretely distributed, with relatively large inter-particle distances. At the higher FF-filler concentrations (Figure 4c, d, e and f), the SEM micrographs revealed large Fe_3O_4 agglomerates dispersed within the PVA matrix, yielding a conductive composite. In both cases, the Fe_3O_4 particles displayed clear phase boundaries within continuous PVA matrix.

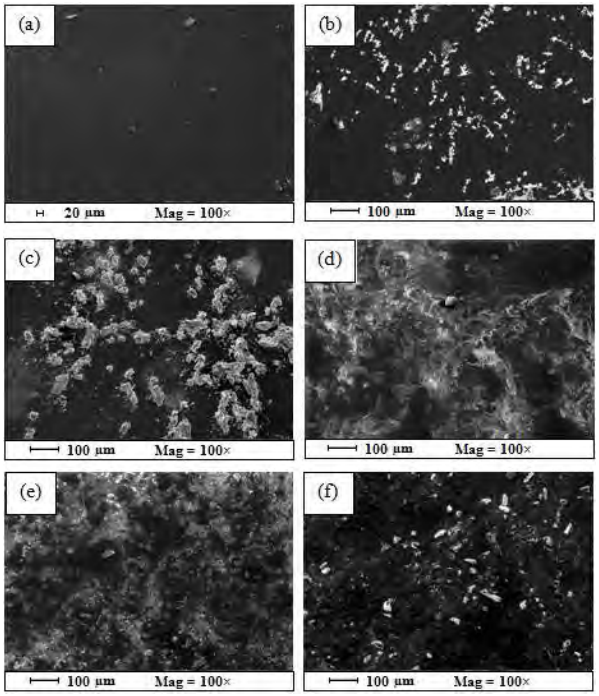

Figure 4. SEM micrographs of PVA-FF composites filled with (a) 0 wt% FF; (b) 20 wt% FF; (c) 30 wt% FF; (d) 40 wt% FF; (e) 50 wt% FF ; (f) 60 wt% FF.

3.5 Mechanical properties

In order to investigate the effects of FF content, the mechanical properties of the PVA-FF composites films were measured and compared with the crosslinked PVA film.

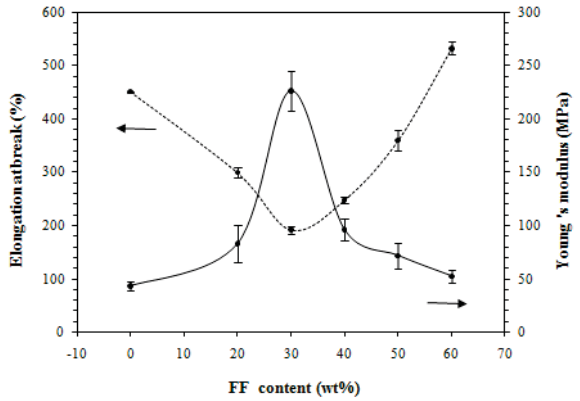

Figure 5. Effect of FF content on Young's modulus and elongation at break of the PVA-FF composite films.

The Young's modulus and elongation at break of the PVA-FF composites films are shown in Fig. 5. Compared with the crosslinked PVA film, the elongation at break decreased with increasing the FF content from 20-30 wt%, whereas the Young's modulus of the PVA-FF composite films increased. It is well established that the presence of the fillers had reduced the ductility of the composite films and increased their stiffness. This is true for Fe_3O_4 particles in which reinforcing fillers added to a polymer restrains the movement of its chains, thereby increasing its Young's modulus. However, after 30 wt% of the FF filler, the elongation at break of the composite films increased and the Young's modulus of the PVA-FF composite films decreased. There is a noticeable decrease in Young's modulus due to the surfactant acted as a plasticizer. Such plasticizer diluted polymer matrix and weaken interaction between polymer chains, so the Young's modulus of polymer matrix was decreased. Therefore, a suitable concentration of surfactants is an important factor to improve the overall mechanical properties of PVA-FF composites [12].

3.7. Cross-cut adhesion

The surface adhesion of the prepared composites, on glass surface was investigated by cross-cut technique. The adhesion performances for the prepared PVA-FF composite films are shown in Table 1. As seen in the table, the adhesion strength of the composite films on glass surface decreases with increasing of FF content. This was due to either the decrease of adhesion strength between Fe_3O_4 particles or the increase of brittleness of the coating as the PVA content decreased [13].

Table 1 Cross-cut adhesion performance of the PVA-FF composite films

Specimens	FF0	FF20	FF30	FF40	FF50	FF60
FF (wt%)	0	20	30	40	50	60
Adhesion	5B	0B	0B	0B	1B	1B

4. Conclusions

FF was synthesized successfully by a co-precipitation method between $FeCl_3 \cdot 6H_2O$ and $FeCl_2 \cdot 4H_2O$ in NH_4OH solution, using TMAOH as a surfactant. The synthesized FF exhibited the viscosity of 11.2 cP. The synthesized FF was later used as conductive filler in the preparation of PVA/FF composites to evaluate the potential for use as ESD coating. The hydrophilic nature of the composites increased with the addition of FF due to presence of Fe_3O_4 particles on the surface. The mechanical properties such as Young's modulus and elongation at break, can be affected by variation in FF content. The coating film has poor adhesion on the glass substrate. The microstructure showed that Fe_3O_4 was well dispersed in PVA matrix, but discontinuity of conductive phase still existed in some segments of composites.

The electrical conductivity of composite coatings on glass substrate was improved by addition of FF. Within the concentration range of FF used in this study, the composites behaved like semiconducting materials suitable for ESD applications and 30 wt% FF was the suitable amount for preparing the composite for use as ESD coating.

Acknowledgements

Financial support from the Center of Excellence for Innovation in Chemistry (PERCH-CIC), office of the Higher Education Commission, Ministry of Education is gratefully acknowledged.

References

[1] M. Al-Saleh, and U. Sundararaj, *Compos. A* **39** (2008) 284-293.
[2] S. Naficy, and H. Garmabi, *Compos. Sci. Technol.* **67** (2007) 3233–3241.
[3] J. Jin, S. Leesirisan, and M. Song, *Compos. Sci. Technol.* **70** (2010) 1544.
[4] J.F. Feller, D. Langevin, and S. Marais, *Syn. Mets* **144** (2004) 81-88.
[5] K. Strzelec, and P. Pospiech, *Prog. Org. Coat.* **63** (2008) 133-138.
[6] P. Businova, J. Chomoucka, J. Prasek, R. Hrdy, J. Drbohlavova, P. Sedlacek, and J. Hubalek, *Nanocon*. **9** (2011) 21-23.
[7] R.P. Pant, S.K. Dhawan, N.D. Kataria, and D.K. Suri, *J. Magnetism and Magnetic Mat*s **252** (2002) 16-19.
[8] P. Berger, N.B. Adelman, K.J. Beckman, D.J. Campbell, A.B. Ellis, and G.C. Lisensky, *Chem. Edu.* **76** (1999) 943-948.
[9] J-M Zhang, S-R Zhai, B. Zhai, Q-D An, and G. Tian, *J. Sol-Gel Sci. Technol.*, 2012.
[10] P. Jareonthanawong, A. Sedthisakko, R. Yodsawat, and S. Kaewpirom, *J. Indus. Tech*. **9** (2012).
[11] K. Subramaniam, A. Das, and G. Heinrich, *Elastomer and Plastics* **7-8** (2012) 44-46.
[12] Z. Ying, J-H. Du, S. Bai, F. Li, C. Liu, and H-M. Cheng, *Int. J. Nanosci*. **1** (2002) 1-6.
[13] G. Pan, Q. Guo, J. Ding, W. Zhang, and X. Wang, *Tribology international* **43** (2010) 1318-1325.

SYNTHESIS AND CHARACTERIZATION OF ASYMMETRIC DIAMINE FOR TRANSPARENT POLYIMIDE FILM

Napasin Thevase[1], Supakanok Thongyai[2], Piyasan Praserthdam[3] ,

Center of Excellence on Catalysis and Catalytic Reaction Engineering
Department of Chemical Engineering, Faculty of Engineering
Chulalongkorn University, Bangkok, Thailand 10330

*E-mail: tsupakan@chula.ac.th , Tel: +66-2-218-6860

Abstract: Polyimides are widely used in microelectronic applications because they have good mechanical, electrical and thermal properties. However, most polyimides colour are yellow-orange that limit the usage in optical application. The colour in polyimide occurs from electron charge transfer between amine groups and benzene ring. To reduce it, the asymmetric diamine was introduced to polymer backbone. The sample from conversion of 2,2 Dinitrobiphenyl to 2,2' Diaminobiphenyl was successfully prepared by hydrogenation reaction in hydrogen atmosphere. It was then examined by Nuclear Magnetic Resonance (NMR) and Fourier Transform Infrared (FTIR) spectroscopy to confirm the structure. The transparent free-standing film, made by thermal imidization, will be further characterized by Thermogravimetric analysis (TGA), Ultraviolet-Visible spectrophotometer (UV-vis) and Universal Testing Machine (UTM) in the near future. The target of cut off wavelength below 350 nm will be tested and verified by changing the combination of the dianhydride comonomer of polyimide.

1. Introduction

Polyimide is a high performance polymer that has various applications in electronics industry for application as substrate, cover-layer, dielectric barrier etc. However, the simple polyimide such as Kapton possessed a colour of yellow to orange that limits its usage in the optical application such as transparent circuit, cover layer of LED and LCD display and substitution of glass cover layer in solar cell.

Recently, many methodologies to prepare the transparent polyimide have been investigated and developed. In 2010, Du Pont launched a new product of transparent colorless Kapton that utilized the asymmetric dianhydride and fluorinated diamine for colorless application.[1] The transparent or color property are obviously depends on Intermolecular interactions such as charge-transfer complex, electronic interaction, and intermolecular cohesive[2].

This work studied the reduction of Intermolecular interactions by putting the unsymmetrical or twisty units into the polymer backbone. Synthesize of diamine monomer by using Hydrogenation on Pd/C have been applied to converse 2,2 Dinitrobiphenyl to 2,2'-Diaminobiphenyl.

2. Materials and Methods

2.1 Materials

2,2 Dinitrobiphenyl, 5% Pd/C, Hydrazine monohydrate and 4,4'-(Hexafluoroisopropylidene) dianiline (6F-Diamine) were purchased from the Tokyo Chemical Industry Co., Ltd (TCI). 4,4'-(Hexafluoroiso-propylidene) bis(phthalic anhydride) (6FDA) was purchased from the Sigma, Aldrich & Supelco. S.M. Chemical Supplies Co.,Ltd. the solvent, N-Methyl-2-pyrrolidone (NMP) was purchased from Fisher Scientific Co. Leics, UK

2.2 Measurements

The structures of 2,2' Diaminobiphenyl have been investigated using nuclear magnetic resonance (NMR) (Bruker 400 UltraShield) at 300 MHz for 1H and 13C using $CDCL_3$ as solvent. Then, Polyimide films have been investigated using Fourier-transform infrared-spectroscopy (FT-IR) (Nicolet 6700).

2.3 Synthesis of the monomer

2,2' Diaminobiphenyl **(1)**

2,2-Dinitrobiphenyl 2 g (0.0083 mole) was dissolved in 10 ml of ethanol in Parr Bomb reactor then 0.05 g of 5% Pd/C and 0.5 ml of $NH_2NH_2.H_2O$ were added. The mixture was stirred at 60 ^oC in 4 bar H_2 atmosphere for 4 h as can be shown in Scheme 1, and then filtered. The filtrate was poured in to 100 ml water, the small yellow-white crystalline was precipitated out, which was collected and purified by recrystallized in water/hexane. The structure of **(1)** was characterized by ^1H-NMR with $CDCL_3$ solvent.

2.4 Polyimide synthesis and film preparation

The dried diamine monomer **(1)** was collaborated with 6F-Diamine to reacted with commercially available aromatic dianhydrides, 6FDA to give the polyimides as shown in Scheme 2. The mole ratio and solid content of **(1)**:6F-Diamine:6FDA is 1:1:2 and 18 wt% respectively. 6F-Diamine and **(1)** was dissolved in NMP and then 6FDA was added. The solution was stirred at room temperature for 1 hour to forming the poly(amic acid)(PAA) in NMP as a viscous solution Then it was poured into 10 x 20 cm glass plate which

the solvent was removed partly in Vacuum Oven at 90 ^{o}C for 2 hours. Then, the haft-dried PAA was continued to cure at 250 ^{o}C in Oven for 3 hour forming polyimide film.

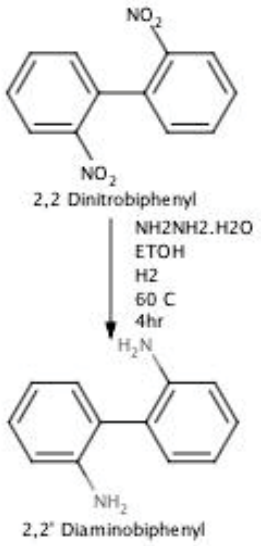

Scheme 1. Synthesis of diamine monomer **(1)**

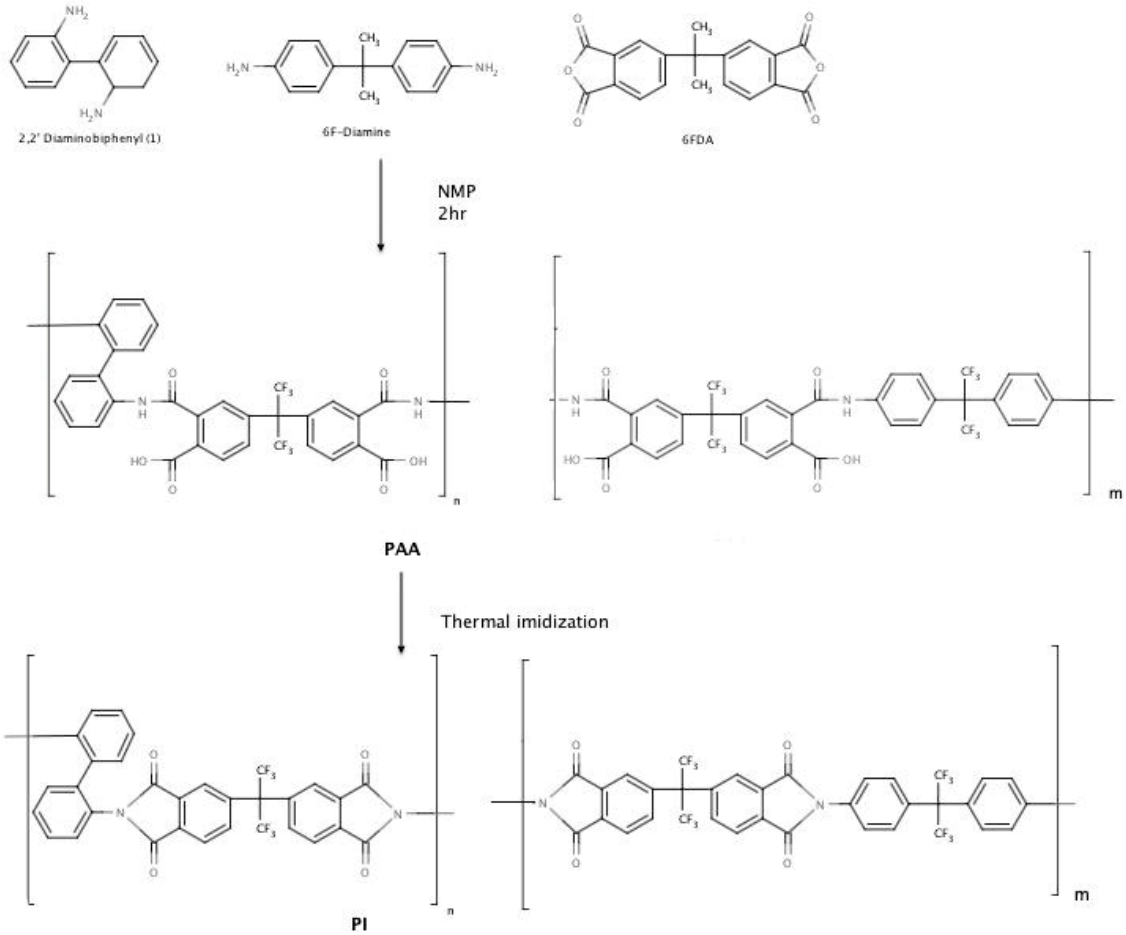

Scheme 2. Synthesis of polyimides

3. Results and Discussion

3.1 Monomer synthesis

In this study, 2,2'Diaminobiphenyl **(1)** can be obtained from 2,2 Dinitrobiphenyl by Hydrogenation reaction under heat and high pressure of H_2 as shown in **Scheme 1**. The white-yellow crystal of diamines was stable in atmosphere at room temperature. The structure of **(1)** was characterized by 1H and 13C NMR compared with the reference papers [3,4]. The results of NMR spectra are shown in Figure 1 and 2. For 1H NMR spectra, signal in the range of 6.80-7.25 ppm were ascribed to the protons of the aromatic ring. The signal of protons from amine groups was appeared at 3.664 ppm. The peak intergrade ratio was matched with a structure. In the 13C NMR spectra, the signal of carbon which it contained the amine group was occurred at 144 ppm.

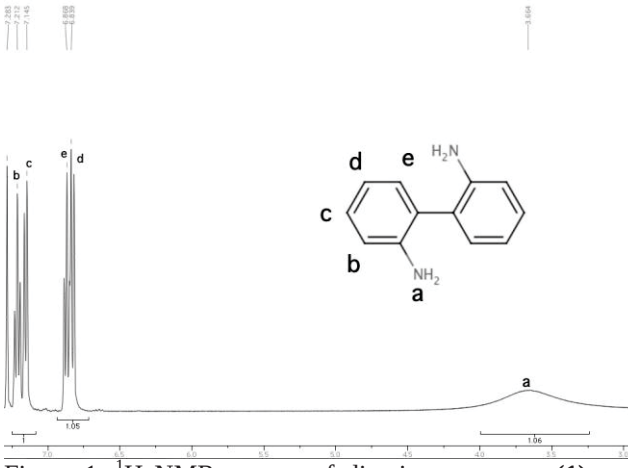

Figure 1. ^{1}H NMR spectra of diamine monomer **(1)**, (400 MHz, $CDCL_3$)

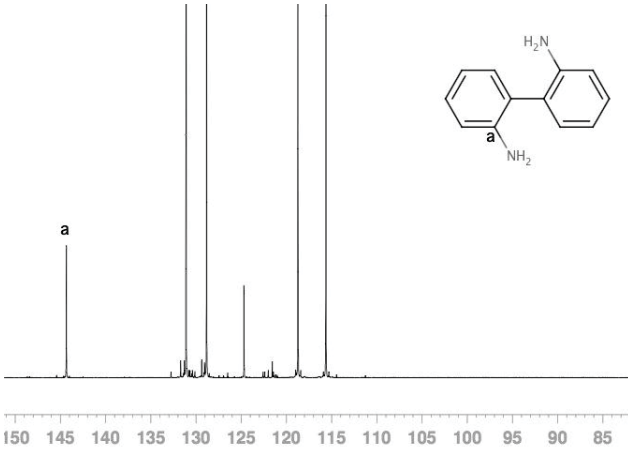

Figure 2. ^{13}C NMR spectra of diamine monomer **(1)**, (400 MHz, $CDCL_3$)

3.2 Polyimide synthesis and film properties

The sample of polyimide film was synthesized by two-steps thermal condensation polymerization as shown in **Scheme 2**. 2,2'diaminobiphenyl**(1)** and 6F-diamine was polymerized with 6FDA to form poly(amic acid)(PAA) and follow by thermal imidiazation.

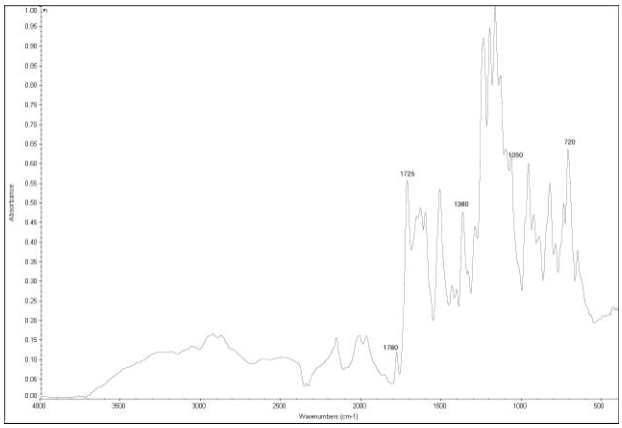

Figure 3 FT-IR spectra of PI film

The film, characterized by FT-IR, showed characteristic imide group absorptions around 1780 and 1725 cm^{-1} (C=O asymmetrical and symmetrical stretch), 1380 (C–N stretch), and 1050 and 720 (imide ring deformation).

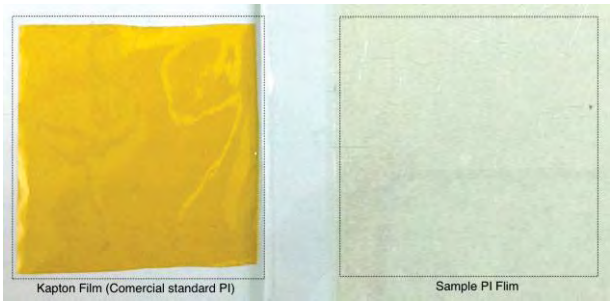

Figure 4 Standard PI Kapton Film (Left) and Sample PI Film (Right)

The Sample PI film was more colourless than standard PI Kapton film, which resulted form monomer such as 6F-Diamine and 6FDA structure containing CF_3 bulky unit and asymmetric structure. The CF_3 bulky unit was effective to reduce the intermolecular and intramolecular charge-transfer complex (CTC) by steric hindrance and decreasing the electron-donating property of diamines. The asymmetric and bulky units in polymer backbone also increased the intermolecular space that affected the reduction of CTC too.

4. Conclusions

The synthesis of 2,2'Diaminobiphenyl could be synthesized successfully by hydrogenation reaction of 2,2 Dinitrobiphenyl with hydrazine monohydrate in H_2 atmosphere using Pd/C as catalyst. The product was purified purely enough to use in polyimide synthesis.

The polyimide film was prepared from 2,2'Diaminobiphenyl with 6Fdiamine and 6FDA by two-step thermal imidization on glass substrate. The obtained PI film was colorless comparing with Kapton PI standard film.

Acknowledgements

We thank Mektec Manufacturing Corporation (Thailand) Ltd. for this work financial support.

References

[1] E.I. Du Pont de Nemours and company, *US Patent Application Publication.* **US2009**/0226642 A1.
[2] S.H. Hsiao, W. Guo, L. C.L. Chung and W.T. Chen, *J. EUR POLYM J.* **46** (2010) 1878–1890.
[3] C.C.Scarborough, B.V.Popp, I.A.Guzei, S.S.Stahl, *J ORGANOMET CHEM,* **690** (2005) 6143-6155.
[4] S. Dehghanpour1 and F. Rominger, *RUSS J COORD CHEM+*, **35** (2009) 259-263

PROPERITES OF POLYPROPYLENE/MODIFIED GROUND TIRE RUBBER POWDER BLENDS

Boonnak Sukhummek[1*], Nipawan Makthepwong[1], Siriporn Suangpo[1]

[1] Department of Chemistry / Faculty of Science, King Mongkut's University of Technology Thonburi, Bangkok, Thailand

[*] Author for correspondence; E-Mail: boonnak.suk@kmutt.ac.th, Tel. +66 24 709557, Fax. +66 24 708843

Abstract: This work aimed to elucidate properties of polypropylene/modified ground tire rubber powder blends with respect to the effect of compatibilizers e.g. maleic anhydride-grafted styrene-ethylene-butylene-styrene (SEBS-g-MA) and styrene-ethylene-butylene-styrene (SEBS). Ground tire rubber powder (GTR) of 80 mesh size was devulcanized by a mixture of diphenyl disulfide:toluene in a ratio of 1:10 for 72 h at 50 °C to obtain the modified GTR. The blend ratio of PP/GTR was varied and investigated. To study the effect of compatibilizers on the properties of thermoplastic natural rubber blend, the blend ratio of 60/40/10 (PP/GTR or modified GTR/compatibilizer) was used. The result showed that increasing in GTR content ratio revealed more rubber-like behavior showing in reduction of mechanical properties; increasing the elongation at break while reducing the tensile strength and modulus properties. Moreover, incorporation of the compatibilizer SEBS exhibited the gradually increase in the elongation at break as SEBS content increased. Incorporation of modified GTR exhibited an increase in the elongation at break and also an improvement in swelling resistance of blends in both oil and toluene as compared to those incorporated with the conventional GTR. The presence of SEBS-g-MA could enhance the rubber-like characteristic of blends.

1. Introduction

The management of the scrap tires worldwide is a great environment challenge. An accumulation of the end-life tires is continuously increased as long as high requirement for the automobiles persists. Although many applications of scrap tires have been available e.g. pavement, playgrounds, footwear, barrier, energy resources [1-3], more extensive research activities and applications of scrap tires are still needed to reduce their volume. The possibilities in recycling ground tire rubber (GTR) powders were published in various research articles and patents. Generally, high compatibility and high entanglement content shows an increasing in blend properties. The interfacial adhesion between the GTR and the thermoplastic matrix is normally very weak [4-6]. Therefore, one of the key points has been focused on the compatibility of GTR, a crossliked rubber thermoset material, and some of thermoplastic materials such as PE, PP, PVC [7-11]. In order to assist this target, the GTR should be devulcanized or partially devulcanized to facilitate the interfacial adhesion or the molecular entanglement between the polymer matrix and the GTR [12-13]. Besides, for further improvement of the interfacial adhesion, the compatibilizer should be added [14-15].

In the present study, attempts have been made to investigate the effect of compatibilizers: maleic anhydride-grafted styrene-ethylene-butylene-styrene (SEBS-g-MA) and styrene-ethylene-butylene-styrene (SEBS) of various concentrations on the properties of PP/modified GTR blends. The physico-mechanical properties, thermal properties and swelling resistance of the blends were analysed.

2. Materials and Methods

2.1 Materials

Polypropylene (PP 1100NK) was kindly provided by IRPC Public Company Limited in Thailand. Maleic anhydride-grafted styrene-ethylene-butylene-styrene (SEBS-g-MA) was obtained from Sigma-Aldrich Co. Ltd. Styrene-ethylene-butylene-styrene (SEBS type GS7033) was supplied by Singapore Polymer Co. Ltd. Diphenyl disulphide was purchased from Merck Schuchardt OHG Co. Ltd., Germany. Ground tire rubber powder (GTR) was kindly supplied by S.L. Rubber Industry (2000) Co. Ltd., Thailand. All chemicals were use as received.

2.2 Modification of GTR

The GTR powder of 80 mesh size, was devulcanized by being immersed in a mixture of diphenyl disulfide:toluene in a ratio of 1:10 for 72 h at 50 °C. After filtering, the received GTR as called modified GTR was put into a vacuum oven at 60 °C for 5 h to completely evaporate the solvent. The modified GTR was characterized by using FTIR-ATR technique.

2.3 Preparation of blends

PP and unmodified GTR powder were melt blended in an internal mixer at 50 rpm. PP was firstly melted at 180 °C for 7 min and then the unmodified GTR powder of 80 mesh size at various weight ratios of PP/GTR e.g. 80/20, 60/40, 40/60 and 20/80 was added. The blending process was continued for 2 min or until the torque curve being constant. Finally, the SEBS compatibilizer at the weight percentage of 0, 10, 20 and 30 wt% was charged into the mixer and mixing was carried on for another 8 min. After melt blending, the blends were removed and left to cool down at ambient temperature. Before moulding by a hydraulic hot press, the blends were granulated by a granulator. The obtained granules were preheated at 80 °C and fully placed into a preheated dumbbell mould. The

filled mould was heated at 190 °C under the pressure of 160 kg/cm^2 for 10 min. After leaving to cool down to room temperature for 10 min, five pieces of dumbbell specimens, according to ASTM D638 (Type IV) were received.

To study the effect of compatibilizers, the blends of PP/GTR 60/40 were compounded. Two types of the compatibilizers: SEBS and SEBS-g-MA were incorporated into the blends with a constant amount of 10 wt% to elucidate their effects on the blend properties both blended with unmodified GTR and modified GTR powders.

2.4 Characterization of blends

Mechanical testing: The tensile properties of the dumbbell specimens were measured using a universal testing machine, Model LR50K, with a cross-head speed of 10 mm/min, the gauge length kept at 25 mm and a full load of 50 kN. The average values and the standard deviation of tensile strength, elongation at break and Young's modulus were calculated by using at least three reading. Hardness test was determined by using a Shore D Durometer according to ASTM D2240. The average values of five readings for each specimen were recorded.

Thermal testing: The thermal analysis was carried out by using a thermal gravimetric analyser (TGA), Model TGA/DSC1, within the temperature range of 40-800 °C at a heating rate of 20 °C/min under nitrogen atmosphere.

Swelling testing: The specimens with dimensions of 25 mm x 50 mm x 2 mm were conducted. The specimens were initially weighed accurately to determine their initial weight before being immersed into toluene solvent and SAE15W40 oil. The specimens were kept in the dark for 7 days at room temperature. After that, the specimens were taken out and the excess liquid on the specimen surface was removed by using tissue. The specimen was reweighed immediately to determine the swollen weight. The percentage of the weight change was recorded.

3. Results and Discussion

3.1 Characterization of modification of GTR

The unmodified GTR and modified GTR powder gave the same density value of 0.61 g/cm^3. The latter showed softer surface as compared to that of the unmodified one. After being devulcanized, the particle size of the modified GTR powder was still constant at 80 mesh. Diphenyl disulfide was found to be one of the most effective devulcanizing reagents [16]. In order to introduce diphenyl disulfide into the vulcanizate rubber, the good organic solvent which gives the high degree of swelling of the crossliked isoprene rubber was needed [16]. Toluene was used as the solvent for diphenyl disulfide in the study. FTIR-ATR spectra of the unmodified GTR and modified GTR powder are shown in Figure 1. Since diphenyl disulfide broke the crosslinking sulphur bonds in the rubber vulcanizate GTR powder, thus, the characteristic peak of C-S stretching at 684 cm^{-1} appeared in the spectrum of the modified GRT powder as seen in Figure 1. Besides, the peak at 1540 cm^{-1} assigned as the stretching frequency of a methyl-assited conjugated double bonds decreased after modification, which showed that the diphenyl disulfide caused a partly breakage of these conjugated double bonds [17].

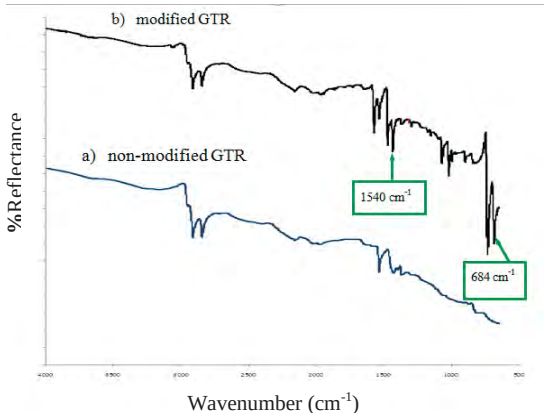

Figure 1. FTIR spectra of a) unmodified GTR powder b) modified GTR powder.

3.2 Effect of SEBS content on mechanical properties of PP/GTR blends

Although both PP and rubber are non-polar materials, but they exhibit an incompatible blend, thus, many researchers try to find a suitable compatibilizer for a particular application. The mechanical properties such as tensile strength, Young's modulus and elongation at break of PP/GTR blends with various contents of SEBS compatibilizer have been studied and shown in Figures 2-4. Without SEBS content, the PP/GTR blends for all composition ratios revealed the highest tensile strength and Young's modulus. Increasing the SEBS content, exhibited a decrement in both mechanical strength properties. The hardness result of the blends also revealed the same trend (did not show here). This might be caused of the plasticizing effect of SEBS in the blends. While, an increase in elongation at break was achieved for all compositions ratios of the PP/GTR blends as increasing the SEBS content. This is due to an efficient stress transfer from the matrix to the dispersed phase, resulting in an increase of the elongation at break [18]. It is worth to note that at 10 wt% of SEBS content, it showed the great changes for all mechanical properties.

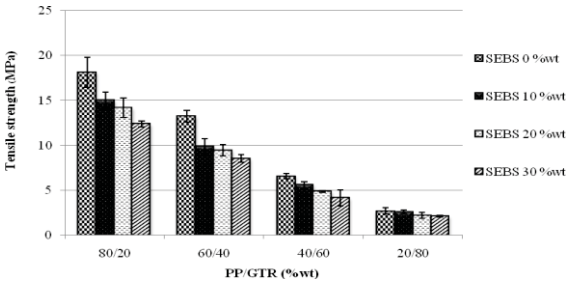

Figure 2. Tensile strength of PP/GTR blends with various SEBS contents.

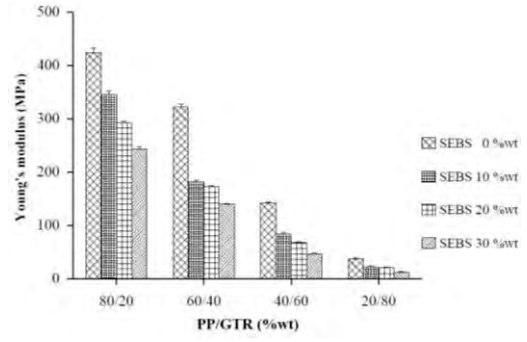

Figure 3. Young's modulus of PP/GTR blends with various SEBS contents.

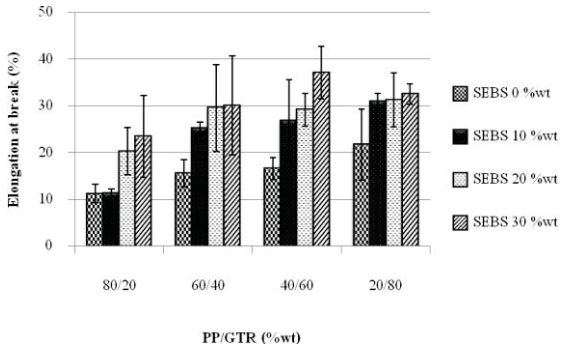

Figure 4. Elongation at break of PP/GTR blends with various SEBS contents.

3.3 Effect of type of compatibilizers on mechanical properties of PP/GTR and PP/modified GTR blends

Generally, the mechanical properties of a thermoplastic are often decreased by adding a rubber phase because of an incompatibility of phases in blends [16]. To improve the compatibility of phases, the compatibilizer is needed. Figures 5-6 show the tensile strength and elongation at break of the PP/GTR blend and PP/modified GTR blends at the composition ratio of 60/40 with 10 wt% of SEBS and SEBS-g-MA. The stress-strain curves of those blends were also revealed in Figure 7.

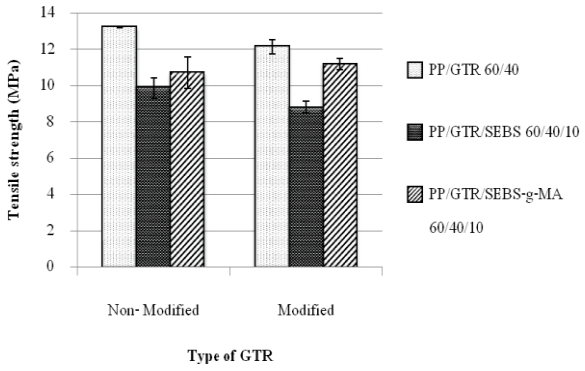

Figure 5. Tensile strength of 60/40 PP/GTR blends with 10 wt% SEBS and SEBS-g-MA.

The addition of both compatibilizers into blends exhibited a decrease in tensile strength, whereas, the elongation at break were increased. This might be caused of the increment of volume fraction of rubber phase in the PP matrix, contributing to improve the dispersion of the rubber phase. Besides, both compatibilizers can be compatible with PP because of the existence of their PEB segment [4]. Incorporation of SEBS-g-MA appeared to improve the tensile strength of blend as compared to that incorporated with SEBS. This is be caused of the MA group in SEBS-g-MA can react with the phenolic OH group in the GTR phase, consequently improving the adhesion between GTR and PP matrix [19-20]. The effect of diphenyl disulfide showed an improvement in the elongation at break as seen in Figure 6 while comparing the properties of PP/GTR blends with PP/modified GTR blends. Because of the devulcanizing effect of diphenyl disulfide, the sulfur crosslinks in GTR powder were broken, subsequently the GTR became less crosslinked and more capable of molecular entanglement, improving the interfacial adhesion between the GTR and PP matrix.

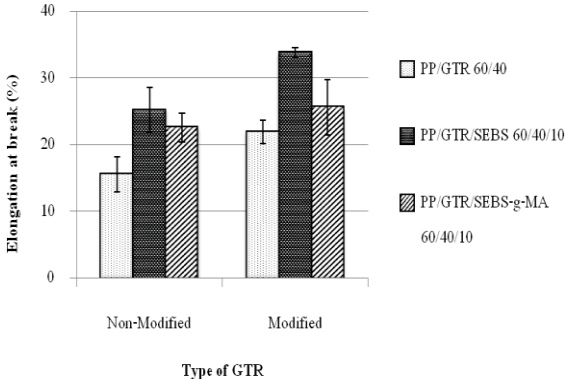

Figure 6. Elongation at break of 60/40 PP/GTR blends with 10 wt% SEBS and SEBS-g-MA.

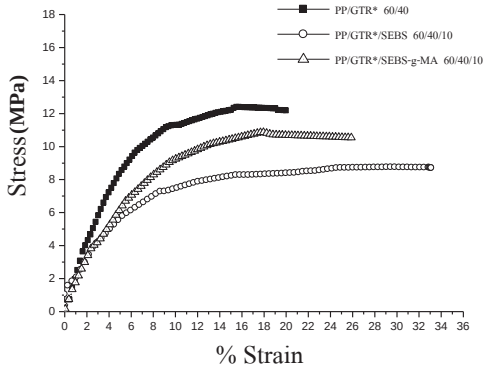

Figure 7. Stress-strain curve of 60/40 PP/modified GTR blends with 10 wt% SEBS and SEBS-g-MA.

3.4 Effect of type of compatibilizers on thermal properties of PP/GTR and PP/modified GTR blends

Thermal properties of PP/GTR and PP/modified GTR blends were shown in Table 1. It can be seen that the thermal stability of PP/GTR blends was decreased as incorporated with the compatibilizers for the ones incorporated with unmodified GTR. This might be because of the high volume fraction of rubber phase in blends. For PP/modified GTR blends, they showed even lower thermal stability than PP/unmodified GTR blends. This might be attributed to the devulcanization

effect of diphenyl disulfide as mentioned before. Surprisingly, incorporation of SEBS showed a marginal improvement of a maximum degradation temperature of the rubber phase, $T_{max, 1}$, of blends.

Table 1: Thermal properties of PP/GTR blends.

Specimen	$T_{max, 1}$	$T_{max, 2}$
PP/GTR (60/40)	389	481
PP/GTR/SEBS (60/40/10)	389	481
PP/GTR/SEBS-g-MA (60/40/10)	364	479
PP/GTR* (60/40)	250	482
PP/GTR*/SEBS (60/40/10)	259	479
PP/GTR*/SEBS-g-MA (60/40/10)	253	478

Remark GTR* represents modified GTR.

3.5 Effect of type of compatibilizers on the swelling resistance of PP/GTR and PP/modified GTR blends

Figures 8 and 9 illustrate the degree of swelling of both PP/GTR and PP/modified GTR blends, in oil and toluene, respectively. It is observed that the degree of swelling of PP/modified GTR in both oil and toluene were lower than those of PP/GTR blends, indicating that the resistance to oil and organic solvent penetration to the rubber phase in PP/modified GTR blends was enhanced. Especially, PP/modified GTR blends exhibited the excellent swelling oil resistance. This might be caused forming copolymer at the interface of the PP matrix and GTR in PP/modified GTR blends inhibited oil and toluene penetration into the blends. Surprisingly, PP/GTR blends incorporated with SEBS showed higher swelling resistance as compared to those incorporated with SEBS-g-MA for both in oil and toluene. To describe this finding, further study was needed.

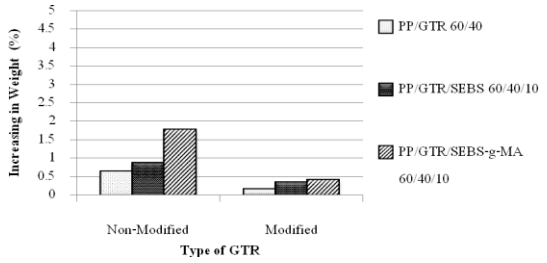

Figure 8. Swelling resistance of PP/GTR and PP/modified GTR blends in oil for 7 days.

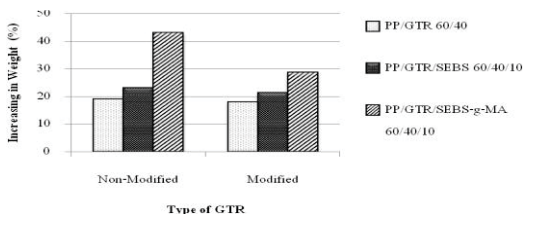

Figure 9. Swelling resistance of PP/GTR and PP/modified GTR blends in toluene for 7 days.

4. Conclusions

In this work, ground tire rubber was modified with diphenyl disulfide in toluene. It is shown that the presence of diphenyl disulfide can improve the elongation at break and swelling resistance, expecially in oil. This is due to the devulcanizing effects of diphenyl disulfide. Moreover, the presence of compatibilizers SEBS and SEBS-g-MA could increase the elongation at break, enhancing the rubber-like characteristic of blends. This originates from the compatibilizing effect and better interfacial cohesion of PP and GTR. Besides, the effect of compatibilizers on thermal stability of PP/modified GTR blends revealed a marginal increase in thermal stability of PP/modified GTR blends.

References

[1] K.D. Jeong, S.J. Lee, S.N. Amirkhanian and K.W. Kim, *Construction and Building Materials* **24** (2010) 824–831.

[2] M. Sienkiewicz, J. Kucinska-Lipka, H. Janik and A. Balas, *Waste Management* **32** (2012) 1742–1751.

[3] R. Gierea and K. Smith, *Fuel* **85** (2006) 2278–2285.

[4] S.L. Zhang, Z.X Xin, Z.X. Zhang and J.K. Kim, *Waste Management* **29** (2009) 1480–1485.

[5] P.K. Pramanik and B. Dickson, *Recycled Plastic Compounds Containing Ground Rubber Tires as Filler*, Conference Proceedings Plastics Engineering: *ANTEC 95*, Conf. Proc., Boston, United State, (1995), pp. 3738–3742.

[6] R. Scaffaro, N.T. Dintcheva, M.A. Nocilla and F.P. La Mantia, *Polym.Degrad. Stab.* **90** (2005) 281–287.

[7] C. Radheshkumar and J.K. Kocsis, *Plast. Rubber Compos.* **31** (2002) 99–105.

[8] P. Rajalingam, J. Sharpe and W.E. Baker, *Rubber Chem. Technol.* **66** (1993) 664–677.

[9] O.P. Grigoryeva, A.M. Fainleib, A.L. Tolstov, O.M. Starostenko, E. Lievana and J.K. Karger, *J. Appl. Polym. Sci.* **95** (2005) 659–671.

[10] M. Awang, H. Ismail and M.A. Hazizan, *Polym. Test.* **26** (2007) 779–787.

[11] A.K. Naskar, D. Khastgir, A.K. Bhowmickkaat and A.K. De, *J. Appl. Polym. Sci.* **84** (2002), 993–1000.

[12] J.K. Kim and J.W. Park, *J. Appl. Polym. Sci.* **16** (2006) 263–268.

[13] A. Radeshkumar and J. Karger-Kocsis, *Plastics Rubber and Composites* **31** (2002) 99–105.

[14] B. Adhikari, D. De and S. Maiti, *Prog. Polym. Sci.* **25** (2000) 909–948.

[15] F. Cavalieri, F. Cadella and F. Cataldo, *J. Appl. Polym. Sci.* **90** (2003) 1631–1638.

[16] M. Kojima, S. Kohjiya and Y. Ikeda, *Polymer* **46** (2005) 2016–2019.

[17] J.L.Koneing, M.M. Coleman and J.R. Shelton, *Rubber Chem. Technol.* **44** (1971) 71–74.

[18] T. Laosee, P. Phinyocheep and F.H. Axtell, *J. Sci. Soc.Thailand* **24** (1998) 251–264.

[19] S.H. Lee, B. Maridass and J.K. Kim, *J. Appl. Polm. Sci.***106** (2007) 3209–3219.

[20] Z.X. Zhang, S.L. Zhang and J.K. Kim, *E-Polymers* **61** (2008) 1–8.

PHOTO-INDUCED SUSPENSION POLYMERIZATION OF METHYL METHACRYLATE USING CAMPHORQUINONE/3°-AMINE INITIATING SYSTEM

Sunisa Kaewsa-ard[1], Panya Sunintaboon [1,2*]

[1] Department of Chemistry, Faculty of Science, Mahidol University, Salaya, Nakhon Pathom 73170, Thailand.
[2] Center of Excellence for Innovation in Chemistry (PERCH-CIC), Department of Chemistry, Faculty of Science, Mahidol University, Bangkok 10400, Thailand.

[*] Author for correspondence; E-Mail: panya.sun@mahidol.ac.th, Tel. +66 840091330, Fax. +66 2 4410511

Abstract: Poly(methyl methacrylate) (PMMA) beads were synthesized *via* a novel photo-induced suspension polymerization. The photoinitiator composed of camphorquinone (CQ)/ethyl 4-dimethylaminobenzoate (4E), and poly(vinyl alcohol) (PVA) was used as a stabilizer. The CQ/4E concentration at (1:1 weight ratio) was varied from 0.1%wt. to 1.0%wt. It was found that the optimum CQ/4E concentration was 0.5%wt with the highest percent conversion up to 60%. From gel permeation chromatography (GPC) results, the molecular weights of PMMA increased with CQ/4E concentration (0.1-1.0%wt.), ranging from 1.02×10^5 - 4.16×10^5 g/mol. The influence of PVA concentration (0.1-1.0%wt.) was also investigated, which was found to affect PMMA average bead size and size distribution, during the course of polymerization. The spherical morphology of PMMA beads was confirmed by scanning electron microscopy (SEM). Their chemical functionality was revealed by fourier transform infrared (FT-IR) spectroscopy.

1. Introduction

Suspension polymerization generally produces polymer particles with a bimodal or broad size distribution, having diameters in a range of 5 – 1000 µm. Also, unintended smaller particles are usually accompanied [1]. Polymer particles were used in many applications in a number of technologies, such as moulding plastics and their largest application is in chromatography separation media (e.g. as ion exchange resins and as support for enzyme immobilization) [2,3]. Suspension polymerization is a process where two immiscible liquids, an aqueous and an organic phases (i.e. initiator is soluble in the monomer), are brought into contact and form a liquid-liquid dispersion (i.e. an emulsion is formed) by the use of continuous stirring and stabilizers. The volume fraction of the monomer phase is usually within a range of 0.1-0.5, since, at higher volume fraction, the concentration of continuous phase may be inadequate to fill the space between droplets [4]. The stabilizers in suspension polymerization are of major importance, as they determine the stability of monomer droplets before and during the polymerization reaction. Poly(vinyl alcohol) (PVA) was used to stabilize droplets by grafted on monomer surface [5]. Since the stabilizer is adsorbed at the oil/water interface it will reduce the interfacial tension, which would itself lead to smaller droplets on break-up. In conventional suspension polymerization, initiating radicals are normally generated by thermal decomposition, especially at elevated temperatures. For some specific purposes (when heat sensitive or thermodegradable components involved), low temperature suspension polymerization is desirable.

In this work, we concentrated on the synthesis of PMMA particles *via* photo-induced suspension polymerization at low temperature, and studied the kinetics of this polymerization system. Camphorquinone (CQ), which absorbs the light in visible region (469 nm) and ethyl 4-dimethylaminobenzoate (4E) were used as photoinitiator and coinitiator, respectively. Poly(vinyl alcohol) (PVA) was used as stabilizer for synthesizing PMMA at 25°C under LED lamp 5 W.

2. Materials and Methods

2.1 Materials

Methyl methacrylate (MMA), camphorquinone (CQ), 4-dimethylaminobenzoate (4E), poly(vinyl alcohol), (PVA) (87-89% hydrolyzed, average M_W 85,000-124,000). MMA were purified by distillation under reduced pressure after removing some inhibitors by NaOH extraction. All other chemicals were commercially available and of analytical grade. Distilled water was used as a continuous phase.

2.2 Polymerization and characterizations

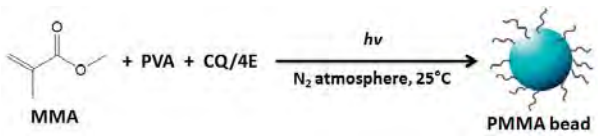

Figure 1. Synthetic scheme of MMA suspension polymerization

The PMMA was synthesized by photo-induced suspension polymerization as shown in Figure 1. The photo-initiator/co-initiator (CQ/4E) (1:1 weight ratio) at certain concentrations pre-dissolved in methyl methacrylate (MMA) monomer was added into a glass

vessel, containing the aqueous solution of PVA. The mixture monomer and initiating couple then emulsified at a stirring speed of 11,000 rpm with the homogenizer apparatus (Ultra turrax) for 1 min. After this, the emulsion was transferred to the reactor in which the temperature was controlled at 25°C. A total reaction volume of 50 ml was generally used. The stirring speed was set at 400 rpm and then nitrogen purging was carried out for 30 min before irradiation. The polymerization occurred when irradiated by 5W LED lamp and proceeded for 3 h. It should be careful that all steps involving CQ before polymerization were done by avoiding light exposure. A gravimetric method was used to measure monomer conversion. Withdrawn small amount of the dispersion by using hypodermic syringe from the reactor at the desired time and transferred into the small weighed aluminium foil dishes to study the kinetic of the system from monomer conversion. The samples, which contained in the dishes were weighed and then quenched by adding 0.01M hydroquinone. The dishes were kept in the oven at 70 C° for at least 24 h. After, the dishes were weighed again to calculate the monomer conversion using a simple mass balance, which was calculated from the following equation:

$$\%\text{conversion} = \frac{\text{wt. of dried latex} - \text{wt. of PVA}}{\text{Initial wt. of MMA}} \times 100$$

Dynamic light scattering (DLS) (Mastersizer 2000), was used for drop/particle size distribution (DSD/PSD) measurements. The unreacted chemicals were removed by centrifugation at 25,000 rpm (25°C) for 30 min, and then washed by distilled water. Then, weight-averaged MW ($\bar{M}w$) of PMMA particles was measured by gel permeation chromatography (GPC). The spherical morphology of PMMA beads was confirmed by scanning electron microscopy (SEM). Their chemical functional groups were revealed by fourier transform infrared (FT-IR) spectroscopy.

3. Results and Discussion

3.1 Synthesis and characterization of PMMA suspension

3.1.1. Effect of initiator concentration

In suspension polymerization, the polymerization kinetics, which is affected by some parameters (e.g. concentration of initiator), can play an important role in the evolution of particle size and size distribution, and Mw of resulting polymers. So, the effect of CQ/4E concentration was studied. In this experiment, the concentration of CQ/4E was varied from 0.1% to 1.0%wt and PVA was fixed with 2.0g/l in all conditions. Figure 2 shows that the slowest rate of polymerization was obtained from 0.1%wt CQ/4E led to the lowest final conversion (48.84%). The rate of polymerization increased with increasing CQ/4E concentration to 0.5%wt CQ/4E, and the highest conversion (58.68%) was obtained. Surprisingly in this system, further increased of CQ/4E concentration up to 1.0%wt CQ/4E, the conversion significantly decreased (48.06%). This means that at high CQ/4E concentration, recombination of free radicals occurred and the conversion decreased. Although 0.5%wt CQ/4E provides the highest rate of polymerization and final conversion, it gives a yellow suspension which does not desire in final product. It can conclude that the optimal concentration of CQ/4E for this system is 0.3%wt.

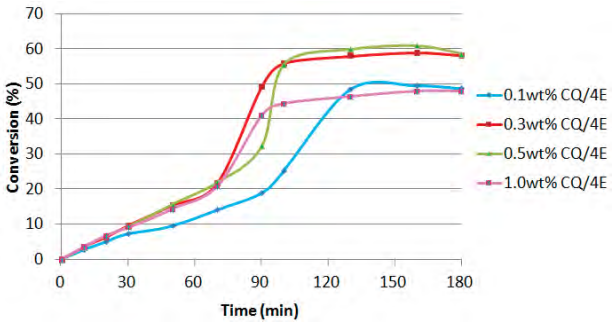

Figure 2. Conversion-time variations for MMA suspension polymerization with different CQ/4E concentrations under stirring speed 400 rpm for 3h.

Table 1: Molecular weights of PMMA particles with different CQ/4E concentrations

MMA (g)	PVA (%wt)	CQ/4E (%wt)	$\bar{M}_w$ (g/mol)	M_w/M_n*
		0.1	416,148	2.9
5	1.0	0.5	161,229	3.0
		1.0	101,899	2.9

*Polydispersity index (PDI)

The molecular weights in particles initiated with different CQ/4E concentrations were shown in Table 2. The $\bar{M}w$ of PMMA particles varied from 1.02×10^5 to 4.16×10^5, depending upon the experimental conditions. The Mw values decreased with increasing initiator concentration. By increasing the CQ/4E concentration, more free radicals were generated in droplets. Thus, shorter chains were produced at the end of reaction with low molecular weight. The PDI values of all conditions were greater than 1, which indicated that the produced chain lengths were not uniform and had varied size.

3.1.2. Effect of stabilizer concentration

In suspension polymerization, the rate of drop break up is a strong function of interfacial tension. Thus, different concentrations of PVA influenced on drops size. In case of particle size and particle distribution, suspension polymerization reactions generally produce particles with a broad size or bimodal size distribution, as already mentioned. From the results, all suspension samples are shown broad

peak with bimodal particle size distribution, as shown in Figure 3.

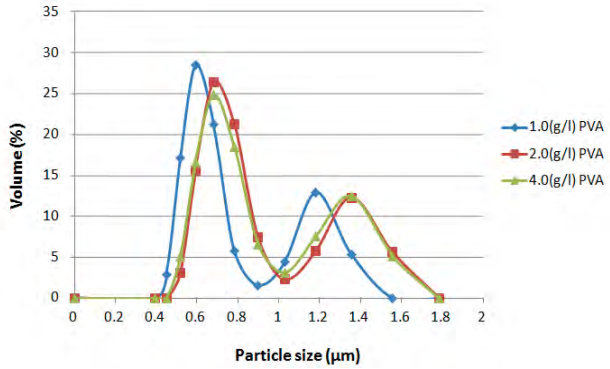

Figure 3. Particle size distribution curve of PMMA latex initiated by 0.3wt% CQ/4E with different PVA concentrations under stirring speed 400 rpm for 3h.

Table 2: Particle sizes and particle size distribution of synthesized PMMA suspension with different PVA concentrations

MMA (g)	CQ/4E (%wt)	PVA (g/l)	D_{32}* (µm)	PDI**
		1.0	0.77	1.24
5	0.3	2.0	0.79	1.25
		4.0	0.78	1.27

* Drop Sauter mean diameter, ** Polydispersity index

Table 2 shows the particle sizes and particle size distribution when using 1.0, 2.0 and 4.0g/l PVA. From the results, all suspension samples would have no significant difference in size because the systems had sufficient PVA molecules covering on the surface of droplets and stabilized particles during the polymerization. Therefore, aggregated particles were not observed during the polymerization.

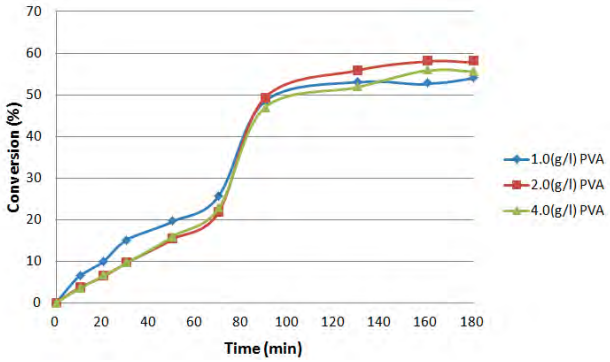

Figure 4. Conversion-time variations for MMA suspension polymerization with different PVA concentrations under stirring speed 400 rpm for 3h.

Figure 4 shows the conversion-time variation for runs with different PVA concentrations. The results showed that PVA concentration does not affect the rate of polymerization. This also indicated that the PVA concentration does not have a significant effect on the kinetic of polymerization [5].

3.2. Particle morphology and composition

SEM images in Figure 5 show that PMMA particles had spherical shape and had different sizes. The larger particle size of larger particles was about 6 µm (Figure 5 (a)), the smaller particles had the size about 200 nm (Figure 5 (b)).

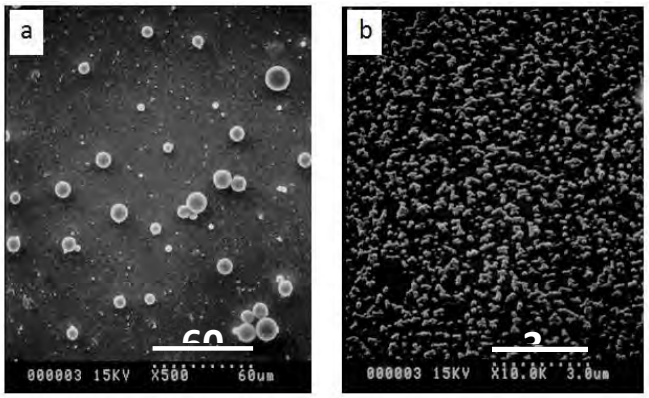

Figure 5. The SEM images of PMMA (centrifuged at 25,000 rpm, 25 °C); a) the larger particle size and b) the smaller particle size.

To confirm the composition of the obtained PMMA particles by photo-induced suspension polymerization, the FTIR was used. The FTIR spectra of the PMMA using difference initiator concentration are shown in Figure 6. In all conditions, the peak around 1440 cm^{-1} the stretching vibration of C-O was observed. The peaks at 1732 and 2955 cm^{-1} were attributed to the stretching vibration of C=O and CH_2, CH_3, respectively.

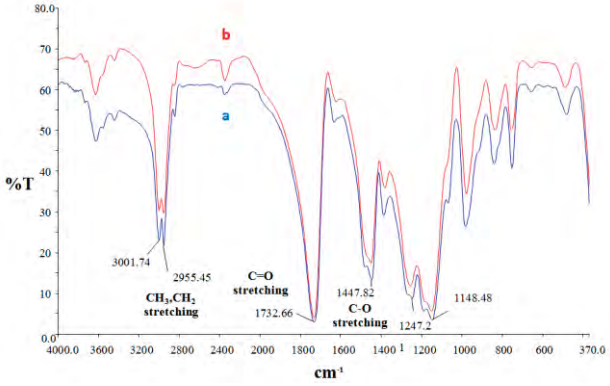

Figure 6. FTIR spectra of PMMA with difference initiator concentration: (a) Initiated by 0.3%wt CQ/4E and (b) initiated by 0.5%wt CQ/4E.

4. Conclusion

The PMMA beads were synthesized *via* the photo-induced suspension polymerization, which was induced by CQ/4E initiating system. The CQ/4E concentrations had an effect on the overall rate polymerization and conversion of the polymerization systems. Moreover, the different PVA concentrations had not significant an effect on the evolution of PMMA particles formation and particle size. The dynamic light scattering (DLS) (Mastersizer 2000), was used for DSD/PSD measurements. The spherical morphology of PMMA beads was confirmed by scanning electron microscopy (SEM). Their chemical functionality was revealed by fourier transform infrared (FT-IR) spectroscopy.

Acknowledgements

This work is funded by Center of Excellence for Innovation in Chemistry (PERCH-CIC), Department of Chemistry, Faculty of Science, Mahidol University, Bangkok 10400, Thailand.

References

[1] Brooks and W. Brian, *Makromolecular Symposium*. **35-36** (1990) 121–140.
[2] N-S. Kwak, Y. Baek and TS. Hwang, *J. Hazard. Mater*. **203-204** (2012) 213-220.
[3] J. Pan, X. Xue, J. Wang, H. Xie and Z. Wu, *Polymer*. **50** (2009) 2365-2372.
[4] M. Munzer and E. Trommsdorff. *C.E. Schildknecht, I Skeist (Eds)*. (1977) 106.
[5] T. Okaya AS, K. Kikuchi, *Colloids Surf., A.* **153** (1999) 123-125.

LLDPE/CLAY NANOCOMPOSITE PRODUCED BY *IN SITU* POLYMERIZATION

Suwimon Poorahong[1*], Bunjerd Jongsomjit

[1] Center of Excellence on Catalysis and Catalytic Reaction Engineering
Department of Chemical Engineering, Faculty of Engineering,
Chulalongkorn University, Bangkok, Thailand 10330

[*] E-Mail: suwimon2531@hotmail.com

Abstract: In the present study, the nanoclay was used as fillers for linear low-density polyethylene (LLDPE) nanocomposites. The LLDPE/clay nanocomposites were synthesized by *in situ* and *ex situ* polymerization of ethylene/1-hexene with zirconocene/MAO catalyst. In this study, two different impregnation methods (*in situ*- and *ex situ* impregnation method) were compared. The properties of LLDPE/clay nanocomposites were characterized using X-ray Diffraction (XRD) and scanning electron microscopy (SEM). It was found that LLDPE/clay nanocomposites synthesized by *in situ* polymerization exhibited higher activities compared with the *ex situ* polymerization. Degree of dispersion of nanoclay in polyethylene matrix was determined by X-ray Diffraction (XRD). These results shown that PE/clay nanocomposite and LLDPE/clay nanocomposite synthesized by *in situ* impregnation and *ex situ* impregnation method show exfoliated degree dispersion of nanoclay in polyethylene matrix.

1. Introduction

Polyolefins are the most important modern commodity polymers. Especially, polyethylene and polypropylene are mainly used as plastic materials worldwide [1]. Because of low cost of production, reduced environmental impact and wide range of application, polyethylene is used as material to produce a lot of product such as clothing, tooth brushes, storage bottles, pipelines, bullet proof jackets, aerospace application and biomedical implants [2].

Polymer nanocomposites (PNC) is the significant development in the nanotechnologies in the recent year, nano-inorganic materials such as SiO_2, Al_2O_3, and clay have brought much attention to this research field. There are probably three methods to prepare polymer nanocomposite: (i) solution method (ii) melt mixing method and (iii) *in situ* polymerization. For *in situ* polymerization, the filler is add directly to system along with monomer during the polymerization. *In situ* polymerization method has three advantages: a one step synthesis of the polymer nanocomposite, improve compatibility between nanoclay and polymer and enhance clay dispersity in the polymer matrix [3].

Zhao et al. [4] studied polyethylene/clay composites that were prepared by melt compounding polyethylene and montmorillonite clay organically modified with different intercalating agents. The mechanical properties of PE and PE/clay composites, with increasing clay loading affects on the strength and modulus of PE/clay composites increase, but the impact strength decreases. The thermal stability of the PE/clay nanocomposites was measured by Thermogravimetric analysis (TGA). PE/clay nanocomposites are more stable than pure PE.

Zapata et al. [3] studied the preparation of clay/PE nanocomposites by the *in situ* polymerization method through two routes: Octadecylamine (ODA) has been widely used as a clay-organomodifier agent in the preparation of polyolefin nanocomposites. Routes 1, homogeneous polymerization in the presence of clay particles show the catalytic activity obtained using clay particles as filler which higher than the pure system. Routes 2, polymerization used clay-supported metallocene catalyst. When Na-Clo was used as support the catalytic activity decreased with respect to the homogeneous system. When ODA-modified clay was used as metallocene support, the polymerization activity tended to increase with the zirconium content. Transmission electron microscopy (TEM) and X-ray diffraction analysis (XRD) show the layer clay exfoliated into polymer matrix.

In this study, metallocene catalyst was used for polyethylene synthesis with nanoclay as support. Moreover, the comparison of the activity of metallocene catalyst in ethylene polymerization by *in situ* and *ex situ* was discussed. The properties of polyethylene/clay nanocomposites were investigated as well.

2. Materials and Methods

2.1 Materials

Ethylene gas (99.9%) was supplied from Linde (Thailand) Co., Ltd. Methylaluminoxane (10% in toluene) was donated from Aldrich Chemical company. The *rac*-ethylenebis(indenyl)zirconium dichloride was supplied from Aldrich Chemical company. Nanoclay (Aluminum Pillared Clay) was supplied from Aldrich Chemical company. Toluene was devoted from SR lab. Ultra high purity argon gas (99.999%) was purchased from Thai Industrial Gas Co., Ltd. Hydrochloric acid (Fuming 36.7%) was supplied from SR lab. Methanol (Commercial grade) was purchased from SR lab. 1- Hexene (99+%) were purchased from Alrich Chemical Company , Inc.

Table 1: Comparison of *in situ* and *ex situ* polymerization

run	Sample	Reaction	impregnation	Polymer yield (g)	Activity (kg PE/mol Zr.h)
1	PE	Homogeneous	-	0.8375	15,931
2	PE/clay	Heterogeneous	in situ	0.7467	10,800
3	PE/clay	Heterogeneous	ex situ	0.7211	6,637
4	LLDPE	Homogeneous	-	0.1072	18,250
5	LLDPE/clay	Heterogeneous	in situ	0.8607	13,414
6	LLDPE/clay	Heterogeneous	ex situ	0.4599	7,828

2.2 Experimental

2.2.1 Preparation of stock catalyst solution

$Et(Ind)_2ZrCl_2$ 0.0083 g ($1.98x10^{-5}$ moles) was added in 20 mL of toluene solution, stirred at room temperature giving yellow transparent solution.

2.2.2 Preparation and characterization of catalyst precursor

The nanoclay was heated in vacuum at 150°C for 2 hr. Then, methylaluminoxane 10 mL and toluene solution 20 mL were added to the nanoclay (1g). The mixture was stirred for 30 min under Ar atmosphere. After toluene was evaporated, the obtained powder was further dried under vacuum, washed with toluene (20 mL × 5) and finally dried under vacuum to give catalyst precursor MAO/nanoclay as powder.

2.2.3 *Ex situ* polymerization

Ex situ polymerization was carried out in a 100 mL semi-batch stainless steel autoclave reactor equipped with a magnetic stirrer. At first, catalyst precursor and stock catalyst solution were put into the reactor along with toluene to make the total volume 30 mL. To start the reaction, ethylene was fed into the reactor which heated up to 70°C. After all ethylene was consumed, the reaction was terminated by addition of acidic methanol and stirred over night. After filtration, the polymer was obtained.

2.2.4 *In situ* polymerization

In situ polymerization was carried out in a 100 mL semi-batch stainless steel autoclave reactor equipped with a magnetic stirrer. Nanoclay 0.0266 g as support, methylaluminoxane 1.1 mL and 1.5 mL of stock catalyst solution were put into the reactor along with toluene to make the total volume 30 mL. Then, the similar procedure as the *ex situ* polymerization was conducted.

2.2.5 Characterization of polyethylene/clay nanocomposite

The Characteristics of polymer are measured by X-ray Diffraction (XRD) and scanning electron microscopy (SEM).

3. Results and Discussion

There were 6 systems for PE and LLDPE in this comparison. The first was the homogeneous system. All materials such as catalyst, MAO and comonomer were in liquid phase, but ethylene introduced in gas phase. Nanoclay was used as support in heterogeneous system.

Catalytic activities with a metallocene catalyst were investigated during copolymerization of ethylene and 1-hexene as shown in Table 1. From this table, for the metallocene catalytic system, the heterogeneous system (*in situ* impregnation and *ex situ* impregnation method) resulted in low activity compared to the homogeneous system because of the lower generation of active sites, affected from interfacial interaction with support, leading to the lower propagation rate. Generally, it is well known that the interactions of catalyst or MAO on the support surface are strong [5].

When focusing on the comparison between both of the heterogeneous systems with different impregnation methods. For two impregnation methods, it was the in *situ* impregnation method should have more active species on the surface because this method was done without washing and drying. Therefore, it reduced in the loss of MAO during preparation. And then, *in situ* impregnation method has higher amount of active site on the support surface. The *ex situ* impregnation method which first the support in the system was contacted with MAO, was investigated by ICP-OES technique. *Ex situ* impregnation methods result from the amount of MAO on the surface of nanoclay supports during copolymerization and interaction between MAO and nanoclay surface.

The results the system with *in situ* impregnation method exhibit slightly higher activity than *ex situ* impregnation method because *in situ* impregnation method has more active species on the surface, but *ex situ* impregnation method loses active sites during processes.

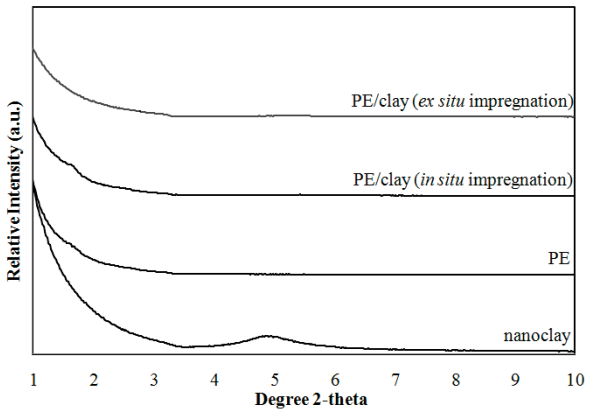

Figure 1. XRD patterns of nanoclay, PE, PE/clay nanocomposite (*in situ* impregnation) and PE/clay nanocomposite (*ex situ* impregnation)

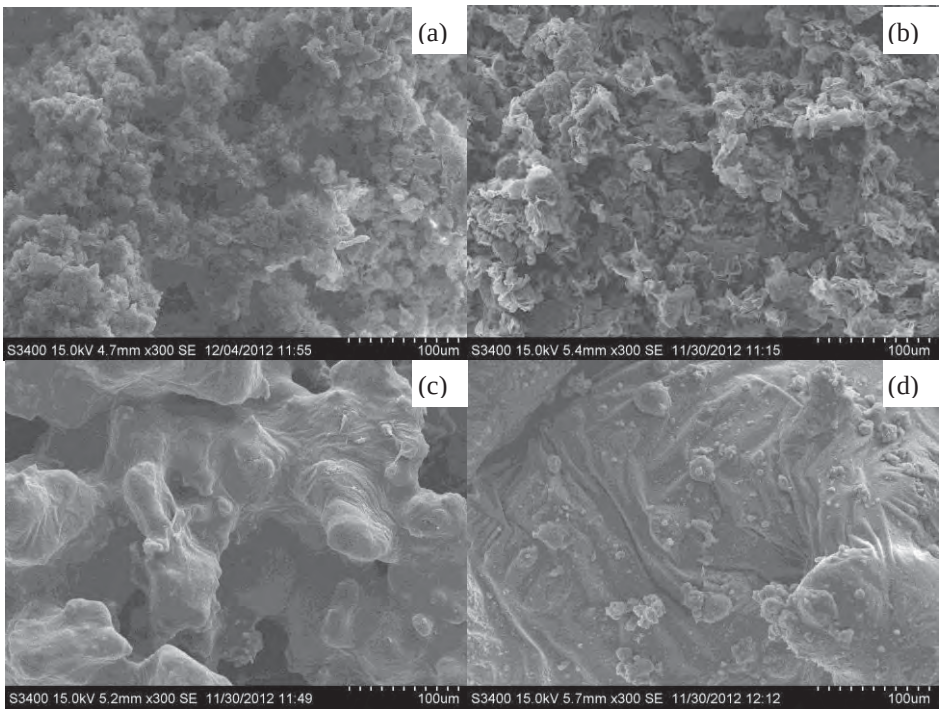

Figure 2. Morphologies of the polymer obtained from the different systems (a) PE/clay (*in situ* impregnation), (b) PE/clay (*ex situ* impregnation), (c) LLDPE/clay (*in situ* impregnation), (d) LLDPE/clay (*ex situ* impregnation).

Degree of dispersion of nanoclay in polyethylene matrix was determined by small angle X-ray diffraction analysis (SAXRD). The SAXRD patterns of clay, pure polyethylene, PE/clay nanocomposite (*in situ* impregnation) and PE/clay nanocomposite (*ex situ* impregnation) are shown in Figure 1. The SAXRD pattern for nanoclay provides diffraction peaks at 2θ = 4.9°, which are the peak of clay. This exfoliated degree dispersion of nanoclay may be due to direct mixing process. The methylaluminoxane (MAO) add during the clay treatment step is expected to react with hydroxyl group on clay surface. After that, the zirconocene catalyst was reacted with MAO-treated clay and modifier, creating covalent bond that helps to avoid catalyst leaching during the polymerization. Thus, it is the cause of well disperse of nanoclay in the polyethylene matrix [6]. Exfoliation became possible through a strong interaction between the polyethylene chains and the clay surface both of *in situ* impregnation and *ex situ* impregnation method.

Morphologies of polymer from scanning electron microscopy (SEM) are shown in Figure 2. The polymers obtained from homogeneous system (run 1 : PE and run 2 : LLDPE) look different from heterogeneous system. However, the polymers obtained from the heterogeneous system exhibited a small difference in morphology because the different interaction of the nanoclay and polymer inside the polymer matrix.

4. Conclusions

The homogeneous reaction provides better activity than heterogeneous reaction caused the generation of active sites with lower propagation rate due to strong interactions of catalyst or MAO on the support surface. The heterogeneous reaction with *in situ* polymerization gives the highest catalyst activity of polyethylene/clay nanocomposite because this method resulted in more the active sites on the support surface. PE/clay nanocomposite and LLDPE/clay nanocomposite synthesized by *in situ* impregnation and *ex situ* impregnation method show exfoliated degree dispersion of nanoclay in polyethylene matrix.

Acknowledgements

We also would like to express our gratitude to Center of Excellence on Catalysis and Catalytic Reaction Engineering, Department of Chemical Engineering, Faculty of Engineering, Chulalongkorn University for supporting the research. Lastly, we would like to extend our gratitude and highest appreciation to the Thailand Research Fund (TRF), the Office of Higher Education Commission (CHE) of Thailand.

References

[1] K.G. Sharma, *Easily processable ultra high molecular weight polyethylene with narrow molecular weight distribution*, Eindhoven University Press, Eindhoven, The Netherlands (2005).

[2] P. Galli, G. Vecellio, *Prog. Polym. Sci.* **26** (2001) 1287-1336.

[3] P. Zapata, R. Quijada, . Covarrubias, E. Moncada and J. Retuert, *Journal of Applied Polymer Science* **4** (2009) 2368-2377.

[4] C. Zhao, H. Qin, F. Gong, M. Feng, S. Zhang and M. Yang, *Polymer Degradation and Stability* **87** (2005) 183-189.

[5] F. Silveira, M.d.C.M. Alves, F.C. Stedile, S.B. Pergher, A. Rigacci and J.H.Z.d. Santos, *Journal of Molecular Catalysis* **298** (2009) 40-50.
[6] Y. Choi and J.B.P. Soares, *Supported Single–Site Catalysts for Slurry and Gas–Phase Olefin Polymerisation*, University of Waterloo, Waterloo, Ontario, Canada (2011).

A NOVEL DERIVATIVE OF CHITOSAN: ANDROGRAPHOLIDE-*GRAFT*-*N*-SUCCINYL CHITOSAN

Siwaporn Srimongkol[1], Pattara Sawasdee[2]*

[1] Petrochemical and Polymer Science Program, Faculty of Science, Chulalongkorn University, Bangkok 10330, Thailand
[2] Natural Products Research Unit, Department of Chemistry, Faculty of Science, Chulalongkorn University, Bangkok 10330, Thailand

* Author for correspondence; pattara.T@chula.ac.th, Tel. +66 22 187624 , Fax. +66 22 187598

Abstract: Andrographolide (AG) is a major compound isolated from *Androgaphispaniculata*. This compound was reported to exhibit a variety of pharmacological effects, such as anti-inflammatory, anti-viral, anti-platelet aggregation, and anti-cancer activities. In this work, andrographolide-*graft*-*N*-succinyl chitosan (AG-*g*-NSCS) was prepared by conjugating chitosan with andrographolide-14*α*-*O*-succinate (AG-Suc). The 2,2-dimethxypropane was used as a protecting group for two hydroxyl groups at the C-9 and C-13 positions of AG before reacting with succinic anhydride. A succinyl moiety was linked at the C-14 position of AG and the AG-Suc chain was further grafted onto chitosan backbone. The degree of AG substitution on chitosan was found to be 18% by ^{1}H NMR analysis. Moreover, in water, AG-*g*-NSCS could self-assemble into particles with the size range of 50-200 nm.

1. Introduction

Andrographis paniculata or Fa-Thalai-Joan is a herbal plant used traditionally in Thailand, China and India to treat various diseases [1]. Its major compound is andrographolide (AG) (Figure 1a), a bicyclic diterpenoid lactone with three hydroxyl groups at C-3, C-19 and C-14 positions [2]. Andrographolide is colorless crystal with bitter taste. It has been reported to exhibit a wide spectrum of pharmacological properties such as anti-inflammatory, anti-viral, anti-platelet aggregation, and anti-cancer activities [3-4].

Chitosan (Figure 1b) is cationic biopolyaminosaccharides which exhibits a lot of superior properties such as low toxicity, biocompatibility, biodegradability, and mucoadhesion resulting in the suitability for using in pharmaceutical and biomedical fields. However, in order to solve its limited solubility problem and to improve physicochemical and biological properties, several chemical modifications of chitosan have been reported [5-6]. In this study, novel chitosan derivatives were designed and synthesized by attaching natural active compound, andrographolide, to amino groups of chitosan. The chemical structures of the chitosan derivatives were characterized by ^{1}H NMR and FT-IR analysis. Self-assembling of the obtained chitosan derivatives into nanoparticulates was also demonstrated and their potential use as drug carrier was discussed.

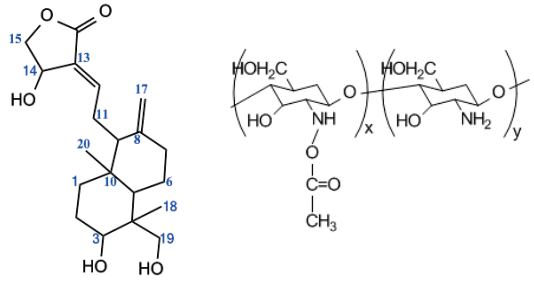

(a) (b)

Figure 1. Chemical structures of (a) andrographolide, and (b) chitosan.

2. Materials and Methods

2.1. Chemicals

Andrographolide was isolated from the whole plant of *A. paniculata* by the method described previously [7]. Chitosan (90% deacetylated chitin, MW 25000 Da) was obtained from Taming Enterprises Co., Ltd (Thailand). Succinic anhydride was purchased from Acros organics (Geel, Belgium). All other chemicals were commercial reagent grade.

2.2. Synthesis of andrographolide-*graft*-*N*-succinyl chitosan

The andrographolide-*graft*-*N*-succinyl chitosan was prepared in three steps as follows.

2.2.1. Synthesis of 3,19-isopropylidene-andrographolide (**2**)

A mixture of AG (**1**, 1.05 g, 3 mmol) and 2,2 dimethoxypropane (1.5 ml, 12 mmol) in 30 mL of a solvent mixture (benzene and DMSO = 7.5:1) with a catalytic amount of pyridinum *p*-toluenesulphonate was refluxed for 5 h. Subsequently, the mixture was cooled to room temperature, then basified by triethylamine, diluted with benzene and washed with distilled water for three times. The organic layer was dried with Na_2SO_4 and concentrated to obtain 3,19-isopropylidene-andrographolide (**2**, 0.92 g, 2.34 mmol, 78%) as a white solid precipitate.

^{1}H NMR ($CDCl_3$, 400 MHz): 400 MHz): δ = 0.95 (3H, s, H-20), 1.19 (3H, s, H-18), 1.36 (3H, s, methyl protons of protecting group), 1.41 (3H, s, methyl protons of protecting group), 2.60-1.24 (12H, methylene and methine protons of AG moiety), 3.19 (1H, d, *J* = 11.6 Hz, H-19b), 3.48 (1H, dd, *J* = 8.8, 3.6 Hz, H-3), 3.97 (1H, d, *J* = 11.6 Hz, H-19a), 4.27 (1H,

dd, *J* = 10.4, 2.0 Hz, H-15b), 4.44 (1H, dd, *J* = 10.6, 6.2 Hz, H-15a), 4.61 (1H, s, H-17b), 4.90 (1H, s, H-17a), 5.03 (1H, t, *J* = 6.2 Hz, H-14) and 6.95 (1H, t, *J* = 6.8 Hz, H-12).

2.2.2. Synthesis of andrographolide-14-α-O-succinate (**3**)

Succinic anhydride (92.4 mg, 0.92 mmol) and dimethylamino-pyridine (6.0 mg, 0.05 mmol) were added to a solution of **2** (0.3 g, 0.77 mmol) in 12 mL of dry dichloromethane. This mixture was stirred under nitrogen atmosphere at room temperature overnight. The solvent was removed under reduced pressure and the residue was purified by a silica gel column chromatography using a gradient system of hexane and ethyl acetate as eluent to afford andrographolide-14-α-O-succinate (**3**, 0.17 g, 0.4 mmol, 49%).

^{1}H NMR (CD_3OD, 400 MHz): δ = 0.69 (3H, s, H-20), 1.18 (3H, s, H-18), 2.55-1.25 (12H, methylene and methine protons of AG moiety), 2.59 (4H, s, methylene protons of succinyl moeity), 3.36-3.31 (2H, m, H-3,19b), 4.09 (1H, d, *J* = 11.2 Hz, H-19a), 4.27 (1H, d, *J* = 11.2 Hz, H-15b), 4.56-4.53 (2H, m, H-15a, 17b), 5.99 (1H, d, *J* = 4.4 Hz, H-14) and 6.93 (1H, t, *J* = 6.2 Hz, H-12).

2.2.3. Synthesis of andrographolide-*graft*-*N*-succinyl chitosan (AG-*g*-NSCS, **4**)

N-hydroxy-succinimide (93 mg, 0.81 mmol) and 1-ethyl-3-(3-dimethyl aminopropyl) carbodiimide (125 mg, 0.81 mmol) were added into a solution of chitosan (130 mg, 0.81 mmol) dissolved in 13 mL of 0.1 % hydrochloric acid. Subsequently, a solution of **3** (365 mg, 0.81 mmol) in 73 mL of dimethylfomamide (DMF) was slowly dropwised into this mixture and was stirred at room temperature for 48 h. The whole solution was dialyzed (dialysis membrane with molecular weight cut-off = 12,000) against distilled water for 3 days to remove excess DMF and other reagents. The product solution was turned to be a milky liquid. This colloidal solution was further subjected to morphological analysis, particles size and zeta potential analyses. The rest of the product solution was further freeze-dried to obtain andrographolide-*graft*-*N*-succinyl chitosan (AG-*g*-NSCS, **4**) powders and stores in desiccator until used for ^{1}H NMR and FTIR analysis.

Degree of andrographolide-14-α-O-succinate substitution: 17.54%. ^{1}H NMR (DMSO-d6, 400 MHz): δ = 0.70 (H-20 of AG moiety), 1.22 (H-18 of AG moiety), 2.40 (methylene protons of succinyl moiety), 2.90 (H-2 of glucosamine, GlcN), 3.50-3.83 (H-2′- of N-acetylglucosamine, GlcNAcm G-3, H-4, H-5 and H-6 of GlcNAc and GlcN) and 4.78 (H-1 of GlcNAc and GlcN); ATR-FTIR (cm^{-1}): 3360 (O-H stretching of hydroxy groups), 2930 (C-H stretching of methyl groups), 1713 (C=O stretching of ester) and 1642 (N-H bending of amide).

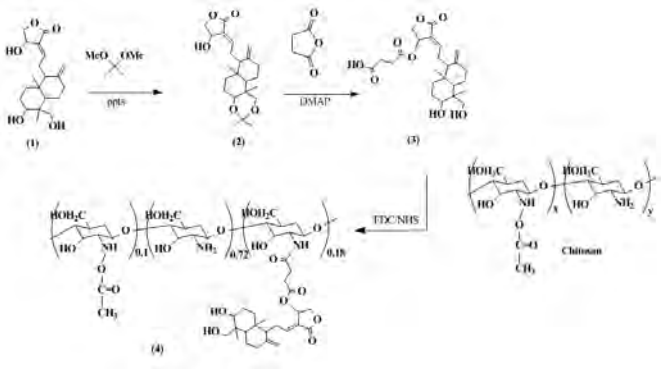

Scheme 1. synthesis of andrographolide-*graft*-*N*-succinyl chitosan.

2.3. Characterization of the andrographolide-*graft*-*N*-succinyl chitosan

2.3.1 ^{1}H Nuclear magnetic resonance (^{1}H NMR)analysis

The ^{1}H NMR spectra were performed on the Varian Mercury 400 MHz NMR spectrometer at ambient temperature using CD_3OD, $CDCl_3$, CD_3OD and DMSO-d6 as solvents for **1**, **2**, **3** and **4**, respectively.

2.3.2.Fourier-Transform infrared (FTIR) measurement

The Fourier-Transform infrared (FTIR) spectra was recorded in the wavelength region 4000–400 cm^{-1} on ATR mode using a Nicolet 6700 and Omnic software was used to control the measurement.

2.4 Morphology, particle size and zeta potential

The shape and surface morphology of the particles were examined by scanning electron micrograph (SEM). The product solution from dialysis was diluted with distilled water and ultrasonic treatment for 10 min. The sample was placed on a double-side sticking tape, air-dried and gold spray-coated before examined under transmission electron microscope (Philips, XL30CP).

The mean hydrodynamic diameter, size distribution and zeta potential of AG-*g*-NSCS micelles were measured in water at 25 °C on a Malvern 3000HSA Zetasizer (UK) based on the dynamic light scattering (DLS) technique.

3. Results and Discussion

3.1 Synthesis and characterization of 3,19-isopropylidene-andrographolide (**2**) and andrographolide-14-α-O-succinate (**3**)

AG is a natural compound which has a wide spectrum of pharmacological activites, especially anti-cancer activity. The synthesis AG analogues had been undertaken to improve bioactivities. Among these, introduction of succinyl group to andrographolide at C-14 significantly enhances cytotoxicity towards human leukemic cell lines and normal cell lines [5]. To synthesize andrographolide-14-α-O-succinate (**2**), two hydroxyl groups at C-3 and C-19 were firstly protected using 2,2-dimethoxypropane in benzene/DMSO.

Succinylation of (**2**) with succinic anhydride yielded andrographolide-14-α-O-succinate (**3**) after purification by column chromatography. The structures of **2** and **3** were confirmed by ^{1}H-NMR analysis (Figure 2). The NMR data of **2** and **3** were in agreement with those of previous report [1, 5]. Two methyl groups at δ 1.36 and 1.41 ppm of the isopropylidene and the separating signals (at δ 3.36-3.31 ppm) of H-3 and H-19 of AG moiety confirmed successful protection of hydroxyl groups (see Figure 2b). The succinate moiety in **3** at C-14 was assured by methylene signals at δ 2.59 ppm together with the downfiled signals of H-14 from δ 5.03 to 5.99 ppm(see Figure 2c). Moreover, the methyl proton signals of isopropylidene were disappeared after reacting with succinic anhydride which indicated the deprotection from AG molecule.

3.2 Synthesis and characterization of AG-*g*-NSCS (**4**)

Andrographolide-14-α-O-succinate (**3**) was grafted on amino groups of chitosan backbone via amide bondind to produce AG-*g*-NSCS **4**. Successful grafting of **3** was confirmed through (i) ^{1}H NMR spectrum of **4** with the apperance of the resonance peak at δ 2.40 ppm from methylene protons of the succinyl moiety together with the signals of AG moiety (Figure 3c.) [8], (ii) the FTIR spectrum of **4** (Figure 4b.) with the absorption band at 1642 cm^{-1} (amide I) increased, indicating that the succinyl moiety took place at the N-position and –NH-CO groups have been formed. Another major change could be observed by the increasing band at 2930 cm^{-1} which assigned to carbon-to-hydrogen stretching band (C-H stretching) of methyl groups. Moreover, the absorption band at 1713 cm^{-1} assigned to carbonyl group was increased [9-10].

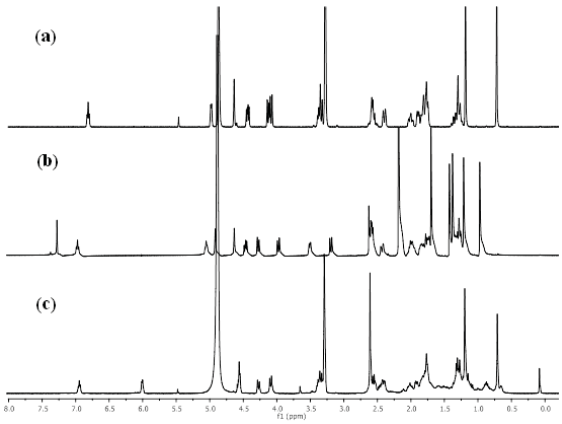

Figure 2. ^{1}H NMR spectra of: (a) AG, (b) 3,19-isopropylidene-andrographolide (**2**) and (c) andrographolide-14-α-O-succinate (**3**).

The degree of grafting was estimated from the ^{1}H-NMR spectrum using the ratio between the integrated area of the resonance peaks from hydrogen atoms at C-2 in glucosamine units (δ 2.90 ppm) and those at C-18 in AG (δ 1.22 ppm). Taking into account, the degree of deacetylation of 0.90 for the starting chitosan, the degree of andrographolide-14-α-O-succinyl grafting was approximated to be 0.18.[8]

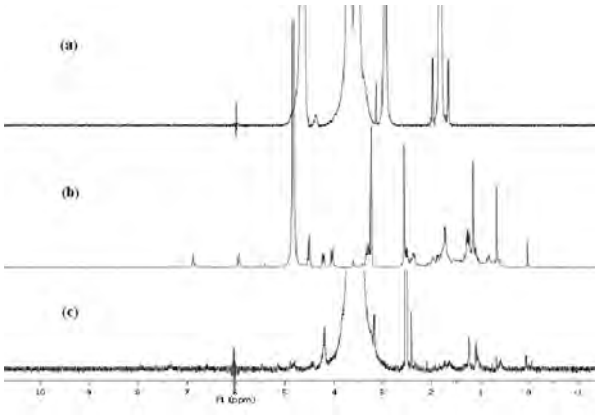

Figure 3. ^{1}H NMR spectra of: (a) Chitosan, (b) andrographolide-14-α-O-succinate (**3**) and (c) AG-*g*-NSCS.

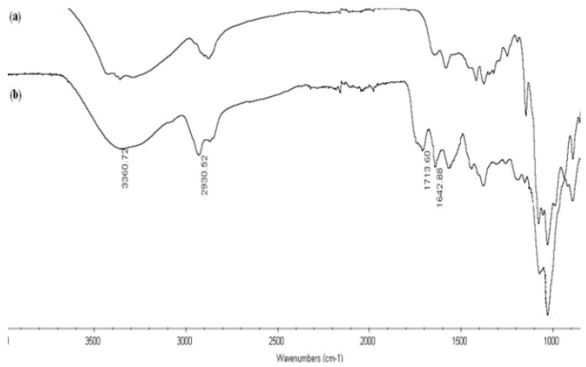

Figure 4. FTIR spectra of: (a) Chitosan and (b) AG-*g*-NSCS (4).

3.3 Morphology study

The SEM image of the dried AG-*g*-NSCS preparation confirmed their spherical morphology with size of 120 ± 2 nm (Figure 5). The hydrodymamic diameter and zeta potential of the hydrated (aqueous suspension) AG-*g*-NSCS were 152 nm (Polydispersity index, PDI of 0.223) and +40 mV, respectively (Figure 6). When comparing the average size from both SEM and DLS, it was found that the product gave different values. This may be attributed to the fact that SEM measurement was carried out on dry particles, while DLS was carried out directly on aqueous dispersed particles [11]. The high positive zeta potential implies stable dispersion of the particles in water with minimal aggregation [12].

Chitosan is only soluble in acidic aqueous medium (pH < 6.5) but insoluble in water due to strong intermolecular hydrogen bonding [13]. Introducing andrographolide-14-α-O-succinate onto chitosan backbone probably disrupts the intermolecular hydrogen bonding. More importantly, the AG-*g*-NSCS is amphiphilic and can automatically self-assemble into stable nanoparticles with the hydrophobic

moieties. They can arrange themselves at the inner cores of the particles, away from hydrophilic water, while the hydroxyl groups of chitosan are at the outer surface of the particles, with maximum contact with water molecules (Figure 7).

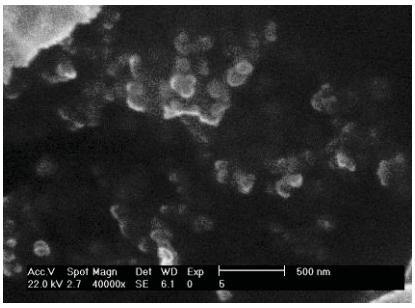

Figure 5. SEM image of AG-*g*-NSCS spheres.

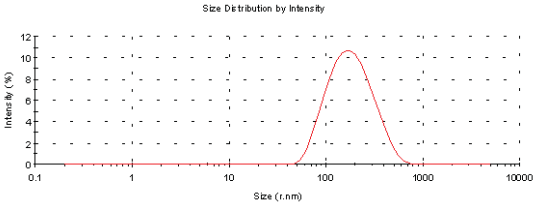

Figure 6. Zeta potential distribution graph of AG-*g*-NSCS nanoparticles.

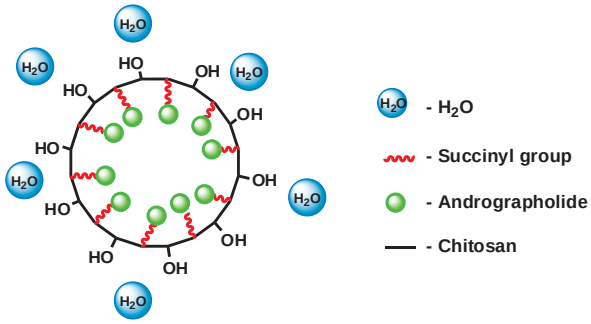

Figure 7. Self-assembled structure model of AG-*g*-NSCS nanoparticles.

4. Conclusions

In this study, novel chitosan derivative, andrographolide-*graft*-*N*-succinyl chitosan (AG-*g*-NSCS), was successfully synthesized. The chemical structures were characterized by ^{1}H NMR and FTIR analysis. AG-*g*-NSCS can self-assemble into spherical morphology in water. NSCS was non-toxic and biocompatible [6]. By attaching the active compound, the created andrographolide was bioactive polymer that could form into spheres. Its biological activity and ability to be used as drug carrier are being investigated.

Acknowledgements

This work was financially supported by the Special Task Force for Activating Research (STAR) from the Centenary Academic Development Project, Chulalongkorn. ST is also grateful to the 90th Anniversary of Chulalongkorn University Fund (Ratchadaphiseksomphot Endowment Fund) for a research fellowship

References

[1] W.-W. Chao and B.-F. Lin, *Chinese medicine.***5:17** (2010) 1-15.
[2] S.R. Jada, G.S. Subur, C.Matthews, A.S. Hamzah, N.H. Lajis, M.S. Saad, M.F.G. Stevens and J. Stanslas, *phytochemistry.* **68** (2007) 904-912.
[3] Y.-T. Wu, W.-C. Lee, L.-C. Lin and T.-H. Tsai, *Chemico-Biological Interactions.* **184** (2010) 458-465.
[4] A.C. Kumoro and M. Hasan, Project No. F0125/2004D
[5] C. Yan, D. Chen, J. Gu, H. Hu, X. Zhao and M. Qiao, *The phamaceutical Society of Japan.* **126(9)** (2006) 789-793.
[6] Z. Aiping, C. Tian, Y. Lanhua, W. Hao and L. Ping, *Carbohydrate Polymers.* **66** (2006) 274-279
[7] C.-F. Chien, Y.-T. Wu, W.-C. Lee, L.-C. Lin and T.-H. Tsai, *Chemico-Biological Interactions.* **184** (2010) 458-465.
[8] T. Tree-udom, S.P. Wanichwecharungruang and J. Seemork, *Carbohydrate Polymers*. **86** (2011) 1602-1609.]
[9] J.Q. Zhou and J.W. Wang, *Enzyme and Microbial Technology*. **45** (2009) 299–304.
[10] X. Xiangyang, L. Ling, Z. Jianping, L. Shiyue, Y. Jie, Y. Xiaojin and R. Jinsheng, *Colloids and Surfaces B: Biointerfaces.* **55** (2007) 222-228.
[11] S.-B. Lao, Z.-X. Zhang, H.-H. Xu and G.-B. Jiang, *Carbohydrate Polymers.* **82** (2010) 1136-1142.
[12] S. Kwon, J.H. Park, H. Chung, I.C. Kwon, S.Y. Jeong and I.-S. Kim, *Langmuir*. **19** (2003) 10188-10193.
[13] M. Rinaudo, *prog. Polym. Sci.* **31** (2006) 603-632.

RESVERATROL-LOADED GELATIN FILMS AND THEIR POTENTIAL FOR USE AS WOUND DRESSINGS

Nattawadee Warakorn[1], Porntipa Pankongadisak[1], Pitt Supaphol[2], Orawan Suwantong[1*]

[1] School of Science, Mae Fah Luang University, Muang, Chiang Rai, 57100 Thailand
[2] The Petroleum and Petrochemical College, Chulalongkorn University, Pathumwan, Bangkok, 10330 Thailand

[*] Author for correspondence; E-Mail: o.suwantong@gmail., Tel. +66 53916771, Fax. +66 53916776

Abstract: Resveratrol-loaded gelatin films were prepared from gelatin powder (5% w/w in 70% v/v of glacial acetic acid) containing 5% w/w of resveratrol (based on the weight of gelatin powder) by solvent casting technique. Various concentrations (0.10%, 0.15%, 0.20%, and 0.25% w/w) of glutaraldehyde (GTA) were added into gelatin solutions to improve the stability of the films. The neat gelatin films showed smooth surface, while, those of the resveratrol-loaded ones showed some aggregates on their smooth surface. The swelling and the weight loss of both the neat and the resveratrol-loaded gelatin films decreased with increasing the GTA concentration. Moreover, increasing submersion time of both the neat and the resveratrol-loaded gelatin films caused the swelling and the weight loss of these films to increase. The release characteristics of resveratrol from the resveratrol-loaded gelatin films were investigated by total immersion method in phosphate buffer solution at 37 ºC. Increasing the GTA concentration caused the total cumulative released amount of the resveratrol to decrease. Lastly, the antioxidant activity of the as-released resveratrol, based on the 2,2-diphenyl-1-picrylhydrazyl (DPPH) assay, was still remained.

1. Introduction

A dressing is essential for the healing of a wound. It should be non-toxic, non-allergenic, non-adherent and easily removed without causing secondary trauma [1]. Many biopolymers, such as cellulose, alginate, chitin, chitosan, collagen, silk and gelatin [2-7], have been fabricated into wound dressings. Among these, gelatin is one of the most utilized biopolymers, owing to its natural abundance. Gelatin is usually obtained from denaturation of collagen from animal tissues [8]. Being derived from collagen, gelatin is biocompatible and biodegradable [9].

Glutaraldehyde (GTA) is one of the most widely utilized crosslinking agent of biocompatible materials, including collagen [10]. Crosslinking of gelatin with GTA is the reaction between free amino acid groups of lysine and/or hydroxylysine amino acid residues of the poly-peptide chains with the aldehyde groups of GTA [11]. Chiou et al. [12] prepared the crosslinked gelatin films using 5% w/w gelatin solution containing GTA of varying concentrations (i.e., 0.25, 0.50 and 0.75% w/w). Bigi et al. [13] studied the effect of GTA concentrations (0.05 - 2.5% w/w) on the swelling behavior of and the release of GTA from crosslinked gelatin films in phosphate buffer solution. At the lowest GTA concentration, gelatin films showed the highest degree of swelling and cumulative amount of GTA released.

In addition, Rattanaruengsrikul et al. [14] studied the swelling and the weight loss behavior of and the release characteristic of silver from the crosslinked nanosilver-loaded gelatin hydrogel pads in three types of medium (i.e., acetate buffer, distilled water, and simulated body fluid buffer). The degrees of the swelling and the weight loss of as well as the cumulative amount of silver released from the hydrogels were found to decrease with an increase the amount of GTA used to crosslink the hydrogels.

Resveratrol (3,4',5-trihydroxy-trans-stilbene) is a polyphenol found in red grapes (including red wine), groundnut, and blackberries [15, 16]. Resveratrol has many biological activities, such as antioxidant, anti-inflammatory, anti-platelet, antiviral and vasorelaxant activities [16-18].

In this study, the resveratrol-loaded gelatin films were prepared with an aim of being used as wound dressings. The films were chemically crosslinked with GTA to stabilize gelatin films. Morphology of these films was characterized by scanning electron microscope (SEM). Furthermore, these films were characterized for the swelling and the weight loss behavior. The release characteristics of resveratrol from the resveratrol-loaded gelatin films were investigated by the total immersion method in phosphate buffer solution at 37 ºC. Lastly, the antioxidant activity of the as-released resveratrol from the resveratrol-loaded gelatin films was also evaluated based on the 2,2-diphenyl-1-picrylhydrazyl (DPPH) assay.

2. Materials and Methods

2.1 Materials

Gelatin powder (M_w = 1,400,000 g·mol^{-1}) and GTA were purchased from Fluka Analytical (Germany). Resveratrol was purchased from Shanghai Angoal Chemical (China). Sodium dihydrogen orthophosphate, anhydrous disodium hydrogen orthophosphate, sodium chloride (Ajax Chemicals, Australia), glacial acetic acid (Carlo Erba, Italy) and all other chemicals were of analytical reagent grades and used without further purification.

2.2 Preparation of resveratrol-loaded gelatin films

Gelatin powder was dissolved in 70% glacial acetic acid to prepare the base gelatin solution at a fix concentration of 5% w/w. The base resveratrol-loaded gelatin solution was prepared by adding 5% w/w of resveratrol in solutions (based on the weight of gelatin powder). GTA was added into the base resveratrol-loaded gelatin solution at various concentrations (0.10%, 0.15%, 0.20% and 0.25% w/w) under mechanical stirring. The obtained solutions were casted onto a polypropylene molding following by evaporation at 55 °C for 28 h. The thicknesses of the obtained films in their dry state measured by micrometer were about 70 ± 10 μm

2.3 Characterization of neat and resveratrol-loaded gelatin films

Morphological appearance of both the neat and the resveratrol-loaded gelatin films was observed by a LEO 1450 VP scanning electron microscope (SEM). Each sample, prior to the observation under SEM, was coated with a thin layer of gold using a Polaron SC-7620 sputtering device.

The swelling and the weight loss behavior of both the neat and the resveratrol-loaded gelatin films were measured in a phosphate buffer solution at the physiological temperature of 37 °C for 6, 12, 24 and 48 h according to the following equations:

$$\text{Swelling (\%)} = \frac{M - M_d}{M_d} \times 100 , \qquad (1)$$

and

$$\text{Weight loss (\%)} = \frac{M_i - M_d}{M_i} \times 100 , \quad (2)$$

where M is the weight of each sample after submersion in a buffer solution for a certain period of time (6, 12, 24 and 48 h), M_d is the weight of the sample after submersion in the buffer solution for a certain period of time (6, 12, 24 and 48 h) in its dry state, and M_i is the initial weight of the sample in its dry state.

2.4 Release of resveratrol from resveratrol-loaded gelatin films

2.4.1 Actual resveratrol content

The actual amount of resveratrol in the resveratrol-loaded gelatin film was determined. Each specimen was dissolved in 20 ml of phosphate buffer. Then 1 ml of solution was quantified the actual amount of the as-loaded resveratrol by using the DPPH assay with a Perkin-Elmer UV-Vis spectrophotometer at the wavelength of 517 nm. The actual amount of resveratrol in the resveratrol-loaded gelatin films was back-calculated from the obtained data against a predetermined calibration curve for resveratrol.

2.4.2 Resveratrol release assay

The release characteristics of resveratrol from the resveratrol-loaded gelatin films in phosphate buffer solution were investigated by total immersion method. Each specimen was immersed in 20 ml of medium at temperature of 37 ºC. At a specified immersion period ranging between 0 and 48 h (2880 min), 1 ml of a sample solution was withdrawn and an equal amount of the fresh medium was refilled. The amount of resveratrol in the sample solutions was determined by using the DPPH assay with a Perkin-Elmer UV-Vis spectrophotometer at the wavelength of 517 nm. The obtained data were calculated to determine the cumulative amount of resveratrol released from the specimens at each immersion time point. The experiments were carried out in triplicate and the results were reported as average values.

2.5 Antioxidant activity

The antioxidant activity of the as-released resveratrol from the resveratrol-loaded gelatin film was evaluated by the DPPH assay. Each specimen was immersed in 10 ml of phosphate buffer solution for 6, 12, 24 and 48 h at 37 ºC. Then, 1 ml of the solution was treated with 1 ml of 100 μM DPPH solution for 30 min at room temperature in darkness. The absorbance of the final solution was recorded spectrophotometrically at the wavelength of 517 nm.

The antioxidant activity (%AA) of the as-released resveratrol was indicated as the percentage of DPPH that was decreased in comparison with that of the control condition (i.e., the testing solution without the presence of the as-released resveratrol), according to the following equation:

$$\%AA = \frac{A_{control} - A_{sample}}{A_{control}} \times 100 , \quad (3)$$

where $A_{control}$ and A_{sample} represent the absorbance values of the testing solution without and with the presence of the as-released resveratrol, respectively. The measurements were carried out in triplicate for without as-released resveratrol and with the presence of the as-released resveratrol.

3. Results and Discussion

3.1 Morphology of both neat and resveratrol-loaded gelatin films

The morphology of both the neat and the resveratrol-loaded gelatin films is characterized as shown in Figure 1. From Figure 1, the neat gelatin films showed smooth surfaces without aggregates of resveratrol on the surface. On the other hand, the resveratrol-loaded gelatin films showed smooth surface with some aggregates of resveratrol on the surface. Since some particles of resveratrol could not be dissolved completely in gelatin solution after adding the GTA as a crosslinking agent.

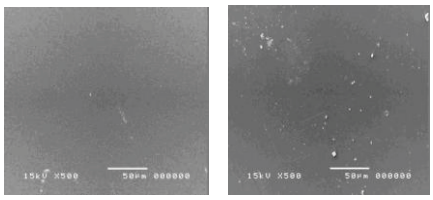

(a) (b)

Figure 1. Selected scanning micrographs of both (a) neat and (b) resveratrol-loaded gelatin films.

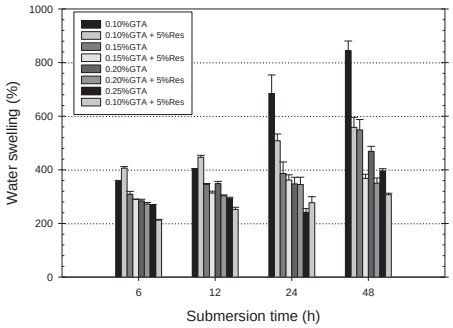

(a)

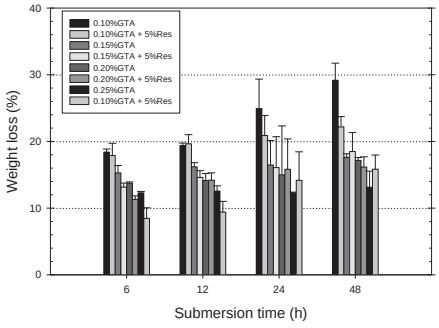

(b)

Figure 2. (a) Swelling and (b) weight loss behavior of both neat and resveratrol-loaded gelatin films.

3.2 Swelling and weight loss behavior of neat and resveratrol-loaded gelatin films

The swelling and the weight loss behavior of both the neat and the resveratrol-loaded gelatin films were examined in a phosphate buffer solution at 37 ºC for 6, 12, 24 and 48 h (see Figure 2a). The swelling of the neat and resveratrol-loaded gelatin films that had been crosslinked with 0.10%, 0.15%, 0.20% and 0.25% w/w of GTA after submersion for 6 to 48 h ranged between ~272% and ~844%. The swelling of the neat and the resveratrol-loaded gelatin films decreased with an increase the GTA concentration. Increasing the submersion time, the swelling was found to increase.

While, the weight loss of the neat and resveratrol-loaded gelatin films that had been crosslinked with 0.10%, 0.15%, 0.20%, and 0.25% w/w of GTA after submersion for 6 to 48 h ranged between ~8% and ~29% (see Figure 2b). The weight loss of both the neat and the resveratrol-loaded gelatin films decreased with an increase the GTA concentration. Increasing the submersion time, the weight loss was found to increase. The results showed that increasing the GTA concentration of both the neat and the resveratrol-loaded gelatin films led to the ability of the water molecules to slowly diffuse in samples resulting in the lower percentage of swelling and weight loss. Since an increase in the GTA content was obviously attributable to the increase in the extent of crosslinking as GTA molecules reacted with the amino groups of gelatin to form a network structure.

3.3 Release of resveratrol from resveratrol-loaded gelatin films

The release characteristics of resveratrol from the resveratrol-loaded gelatin film were investigated. The actual amount of resveratrol in the 5% resveratrol-loaded gelatin film as determined by UV visible spectrophotometer was 95.54 ± 2.64%. Figure 3 shows the cumulative release profiles of resveratrol from the resveratrol-loaded gelatin films that had been crosslinked with varying amounts of GTA in phosphate buffer solution as a function of the submersion time. The release characteristics of resveratrol from the gelatin films could be divided into two stages. The amount of the resveratrol released from the resveratrol-loaded gelatin films increased very rapidly over the first 4 h, after which time it increased gradually with further increase in the diffusion time. The cumulative release of resveratrol released from the resveratrol-loaded gelatin films that had been crosslinked with 0.25% w/w GTA showed the lowest released amount of resveratrol. While the cumulative release of resveratrol released from the resveratrol-loaded gelatin films that had been crosslinked with 0.10% GTA showed the highest of released amount of resveratrol corresponding to results of both the swelling and the weight loss of the crosslinked gelatin films. Since an increase in the GTA content was obviously attributable to the increase in the extent of crosslinking of gelatin to form a network structure.

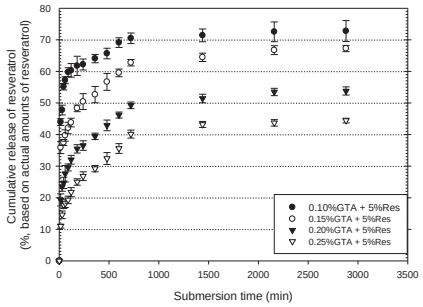

Figure 3. Cumulative release profiles of resveratrol from resveratrol-loaded gelatin films in phosphate buffer solution at 37 ºC.

3.4 Antioxidant activity of as-released resveratrol from resveratrol-loaded gelatin films

The antioxidant activity of the as-released resveratrol from the resveratrol-loaded gelatin films with various GTA concentrations (0.1, 0.15, 0.2 and 0.25% w/w) was investigated by the DPPH assay (Figure 4). The results showed that the antioxidant activity of resveratrol that had been released from the resveratrol-loaded gelatin films that had been crosslinked with 0.10%, 0.15%, 0.2% and 0.25% GTA

after submersion for 6 h ranged between ~24% and ~30%. The antioxidant activity of resveratrol that had been released from the resveratrol-loaded gelatin films that had been crosslinked with 0.10%, 0.15%, 0.2% and 0.25% GTA after submersion for 12 h ranged between ~36% and ~41%. While the antioxidant activity of resveratrol that had been released from the resveratrol-loaded gelatin films that had been crosslinked with 0.10%, 0.15%, 0.2% and 0.25% GTA after submersion for 24 h ranged between ~73% and ~75% and for 48 h ranged between ~75% and ~78%. The obtained results indicated that increasing the submersion time led to increase percentage of antioxidant activity.

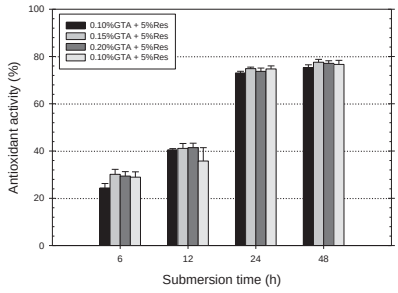

Figure 4. Antioxidant of as-released resveratrol from resveratrol-loaded gelatin films in phosphate buffer solution for 6, 12, 24, and 48 h at 37 °C.

4. Conclusions

In the present contribution, the resveratrol-loaded gelatin films were prepared from 5% w/w gelatin solution containing 5% w/w. resveratrol by solvent casting technique. The morphology of the neat gelatin films showed smooth surfaces without aggregates on the surface. On the other hand, the resveratrol-loaded gelatin films showed smooth surface with some aggregates of resveratrol on the surface. The swelling and the weight loss of the resveratrol-loaded gelatin films were determined by submersion samples in a phosphate buffer solution for 6, 12, 24 and 48 h at 37 ◦C. Both the swelling and the weight loss decreased with an increase the GTA concentration. Increasing the submersion time, the swelling and the weight loss were found to increase. Increasing the GTA concentration, the total cumulative amount of resveratrol released from the resveratrol-loaded gelatin films was found to decrease. Lastly, the antioxidant activity of the as-released resveratrol from the resveratrol-loaded gelatin films increased with an increase the submersion time.

Acknowledgements

The authors would like to acknowledge financial support from 1) the "Integrated Innovation Academic Center : IIAC", Chulalongkorn University Centenary Academic Development Project, Chulalongkorn University and 2) Mae Fah Luang University.

References

[1] H.U. Zaman, J.M.M. Islam, M.A. Khan and R.A. Khan, *J. Mech. Behav. Biomed*. **4** (2011) 1369-1375.
[2] B. Wei, G. Yang and F. Hong, *Carbohyd. Polym*. **84** (2011) 533-538.
[3] K.Y. Lee and D.J. Mooney, *Prog. Polym. Sci*. **37** (2012) 106-126.
[4] R. Jayakumar, M. Prabaharan, P.T.S. Kumar, S. V. Nair and H. Tamura, *Biotechnol. Adv*. **29** (2011) 322-337.
[5] N. Adhirajan, N. Shanmugasundaram, S. Shanmuganathan and M. Babu, *Eur. J. Pharm. Sci*. **36** (2009) 235-245.
[6] A. Schneider, X.Y. Wang, D.L. Kaplan, J.A. Garlick and C. Egles, *Acta Biomater*. **5** (2009) 2570-2578.
[7] B. Balakrishnan, M. Mohanty, P.R. Umashankar and A. Jayakrishnan, *Biomaterials* **26** (2005) 63356342.
[8] D. Olesen, C. Yang, M. Bodo, R. Chang, S. Leigh, J. Baez, D. Carmichael, M. Perälä, E. R. Hämäläinen, M. Jarvinen and J. Polarek, *Adv. Drug Deliver. Rev*. **55** (2003) 1547-1567.
[9] S.E. Kim, D.N. Heo, J.B. Lee, J.R. Kim, S.H. Park, S.H. Jeon and I.K. Kwon, *Biomed. Mater*. **4** (2009) 044106.
[10] I. Rault, V. Frei, D. Herbage, N. Abdul-Malak and A. Huc, *J. Mater. Sci. – Mater. Med*. **7** (1996) 215-221.
[11] L.H.H. Olde Damink, P.J. Dijkstra, M.J.A. Van Luyn, P.B. Van Wachem, P. Nieuwenhuis and J. Feijen, *J. Mater. Sci. – Mater. Med*. **6** (1995) 460-472.
[12] B.S. Chiou, R.J. Avena-Bustillos, P.J. Bechtel, H. Jafri, R. Narayan, S.H. Imam, G.M. Glenn and W.J. Orts, *Eur. Polym. J*. **44** (2008) 3748-3753.
[13] A. Bigi, G. Cojazzi, S. Panzavolta, K. Rubini and N. Roveri. *Biomaterials* **22** (2001) 763-768.
[14] V. Rattanaruengsrikul, N. Pimpha and P. Supaphol, *Macromol. Biosci*. **9** (2009) 1004-1015.
[15] N.J. Miller and C.A. Rice-Evans, *Clin. Chem*. **41** (1998) 1789.
[16] S. Pervaiz and A.L. Holme, *Antioxid. Redox Sign*. **11** (2009) 2581-2897.
[17] D.K. Das and N. Maulik. *Mol. Interv*. **6** (2006) 36-47.
[18] J.J. Docherty, M. Ming Fu, J.M. Hah, T.J. Sweet, S.A. Faith and T. Booth, *Antivir. Res*. **67** (2005) 155-162.

SYNTHESIS AND CHARACTERIZATION OF ULTRA-THICK NEGATIVE PHOTOSENSITIVE POLYIMIDE

Noppamas Wutikunprapan , Supakanok Thongyai*, Piyasan Praserthdam

Center of Excellent on Catalysis and Catalytic Reaction Engineering, Department of Chemical Engineering, Faculty of Engineering, Chulalongkorn University, Bangkok, 10330, Thailand

* Supakanok Thongyai; E-Mail: tsupakan@chula.ac.th, Tel. +66 18695764

Abstract: Photosensitive polyimide (PSPI) is one of the great interesting engineering polymers, especially for microelectronic industry. We investigated and optimized the synthesis conditions for a PSPI that can be used as lithography material. Negative photosensitive polyimide have been synthesized by reaction of 3,3′,4,4′-biphenyltetracarboxylic dianhydride (BPDA) with hexamethylenediamine (HMDA) and 4,4′-oxydianiline (ODA) at stoichiometric dianhydride/diamine ratio of 100:30:70 in N-methyl-2-pyrrolidinone (NMP) solutions by using solution condensation polymerization at room temperature and further imidization at 250°C. The photoinitiator and photo precursor were bis(2,4,6-trimethyl benzoyl) phenylphosphine oxide (Irgacure-819) and 2-hydroxyethyl methacrylate (HEMA), respectively. In this study, we used photosensitive polyimide as insulation layers that created in the form of cover film with their thickness approximately controlled at 12.5 micron. Thus, the thickness of cover film was called as "Ultra-thick". The negative photosensitive polyimides were characterized by Fourier transform infrared spectroscopy (FTIR) while their morphologies were evaluated by Optical and Confocal Microscope. The thermal stability of the polyimide films was analyzed by TGA.

1. Introduction

Polyimides (PIs) are outstanding polymers, which used in many microelectronics and aerospace industries such as high temperature insulators, dielectrics, coatings, adhesives and advanced composite matrices because of their excellent thermal stability, chemical resistance, electrical and mechanical properties. [1-10] In addition, polyimides strongly absorb visible light with wavelength range about 400-700 nm and have relatively high dielectric constants over 3.0. [2,3]

Polyimides or non-photosensitive polyimides can apply as total cover film only (cannot be directly patterned) and require several process steps to be patterning after the active device was totally covered. Thus, photosensitive polyimides can be directly patterned and processed similar to standard photo-resists using photolithography techniques, so the eight-steps conventional polyimide processes can be consolidated into the three-steps processes using photosensitive polyimide. [4] As the consequence, the new process can save time and reduce cost of production. So, photosensitive polyimides (PSPIs) have attracted a great attention nowadays. Typically, photosensitive polyimides usually apply for an insulation layer film in semiconductor microelectronic industry, which the thickness of the film is approximately less than 5 micron. In this research, the photosensitive polyimide was utilized as thick insulation layer, cover film, and the thickness of cover film should be in the range of 12.5 micron, so the thickness of cover film can be considered "Ultra-thick" and the opening size of cover film should be in the range of 4 sq.mm. Photosensitive polyimide can be divided into two categories as negative and positive photosensitive polyimide. Positive photosensitive polyimide cannot be used as the cover film because the films produced usually are very thin and cannot obtained as thick films. Negative photosensitive polyimide can be available in a wide range of viscosities and thickness. [5] Mainly negative photosensitive polyimide is usually used for the cover film applications.

In this study, the synthesis of negative photosensitive polyimides were investigated in order to create ultra-thick cover film, with the thickness approximately controlled at 12.5 micron, and the relation between the size of opening area of cover film and mask size are determined.

2. Materials and Methods

2.1 Materials

3,3′,4,4′-biphenyltetracarboxylic dianhydride (BPDA, Aldrich), Hexamethylenediamine (HMDA, Aldrich), 4,4′-Oxydianiline (ODA, Aldrich), γ – butyrolactone (Aldrich), 2-hydroxyethyl methacrylate (HEMA, Merck) and N-methyl-2-pyrrolidinone (NMP, Merck) were used as received. The photo-initiator, bis (2,4,6-trimethylbenzoyl) phenyl phosphine oxide (Irgacure-819) was grateful provided by Ciba Specialty Chemical Thailand. Copper clad (size= 5x5 cm) was grateful provided by Mektec Manufacturing Corporation (Thailand) Ltd. All of them were used as received.

2.2 Preparation of the negative photosensitive poly (amic acid) (in Scheme 1)

Poly (amic acid) was synthesized by the 3,3′,4,4′-biphenyltetracarboxylic dianhydride (BPDA) with hexamethylenediamine (HMDA) and 4,4′-oxydianiline (ODA) at stoichiometric dianhydride/diamine ratio of 100:30:70 in N-methyl-2-pyrrolidinone (NMP) solutions. The thicknesses of cast films were controlled by number of droplets on plate and concentration of solution of poly (amic acid).

The mixture solutions were stirred by magnetic stirrer for 30 min under Argon atmosphere in order to obtain the poly (amic acid). After that, 2-hydroxyethyl methacrylate (HEMA) photosensitive precursor and Bis (2,4,6-trimethylbenzoyl) phenyl phosphine oxide (Irgacure-819), photosensitive initiator, were added into the mixture solutions to change normal poly (amic acid) into negative photosensitive poly (amic acid).

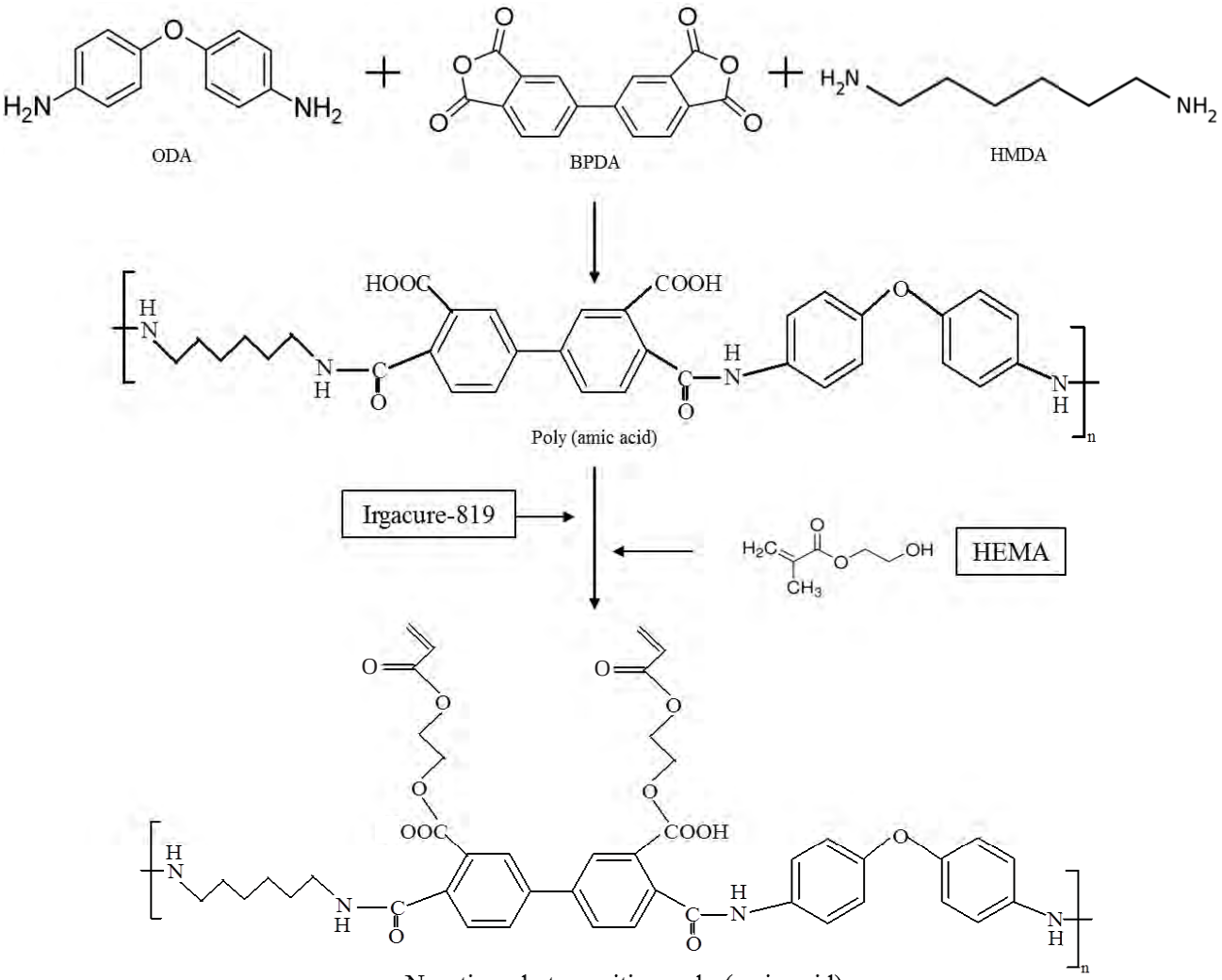

Scheme 1 : Preparing negative photosensitive poly (amic acid)

2.3 Patterning of the negative photosensitive polyimide (NPSPI)

The negative photosensitive poly (amic acid) precursors from methods above were cast onto copper substrate. The film was dried at 55 °C for 2 hours and then exposed to the UV light through a transparent mask for 200 seconds and washed by the γ–butyrolactone (50 ml) to develop patterns. Finally, the developed patterns were cured at 250 °C for 30 min in the oven, so the negative photosensitive polyimide films were obtained.

2.4 Characterization

The FTIR were recorded by Nicolet 6700™ spectrometer in the range of 4000-400 cm^{-1} at a resolution of 1.0 cm^{-1}. The TGA were recorded by SDT Q 600 at a heating rate of 10 °C/min from room temperature to 800 °C under a continuous flow of air at 100 ml/min.

3. Results and Discussion

Table 1 shows the thickness of PI and NPSPI films after curing at 250 °C. When the amounts of droplets of poly(amic acid) solution cast on substrates were increased, the thickness of the PI and NPSPI films were increased accordingly. However, the thicknesses of NPSPI films were thinner than PI film (at the same conditions) due to the loss of Photo-cross-linking agents, 2-hydroxyethyl methacrylate (HEMA) and Igracure, after curing. At approximate, 0.4 ml of poly (amic acid) solution could make 12 micron film's thickness, as required.

Table 1: Thickness of PI and NPSPI films

No.	Poly(amic acid) Solution* (ml)	Film thickness after cured at 250 °C (μm)	
		PI	NPSPI**
1	0.4	24.1	12.3
2	0.5	27.7	22.0
3	1.0	42.4	39.7
4	1.5	67.4	56.6
5	2.0	85.9	72.3

*Conc. of solution = 17.17% wt./vol.
**Negative photosensitive polyimide

Figure 1 shows the FTIR spectrum of polyimide (PI) film after curing. The imide characteristic absorption bands of the prepared materials can be further evidenced by the following absorption bands; 1778 cm^{-1} (C=O sym. str.); 1726 cm^{-1} (C=O asym. str.); and 1380 cm^{-1} (C–N str.). The C–NH (1660 cm^{-1}) as characteristic absorption bands of the polyamic acid disappeared from the spectra, indicating that the imidization reactions were completed.

Figure 2 shows the TGA curves of the NPSPI and PI after cured. The 5% weight loss temperature appeared at 281 and 269 °C for NPSPI and PI, respectively which suggests the enhancement of the thermal stability of NPSPI film.

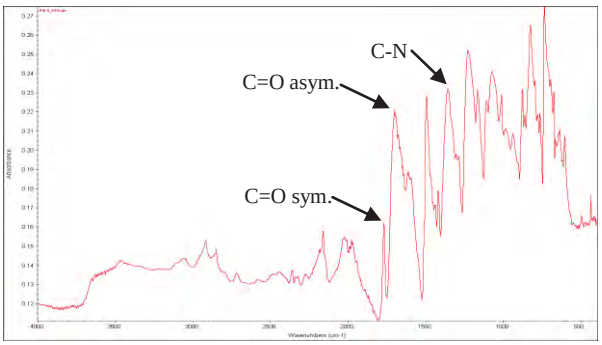

Figure 1. FTIR spectrum of Polyimide (PI) film.

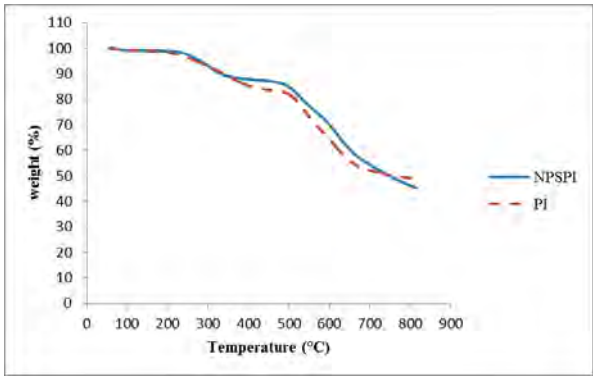

Type	NPSPI	PI
T_d 5 % (°C)	281	269

Figure 2. TGA curves of the NPSPI and PI at the heating rate of 10°C/min.

Figure 3 shows the photograph of the developed pattern of NPSPI. The fade areas were unexposed to UV light. To develop, the films were soaked in the solvent that washed away the unexposed part. The areas that exposed to the UV light were not dissolved out by the solvent during developed processes, so the films' thickness remained, even after cure. The reasons for the incomplete dissolution of the unexposed areas might due to the too short developed time and the too long exposed time (more diffusion of Irgacure radicals).

Figure 4 shows the film thickness and the size of opening areas of NPSPI films by Stylus profiler, which confirmed the successful process of developing.

Figure 5 shows the morphology of the NPSPI film from Confocal Microscope with magnification 5x. The rectangular patterns, appeared as 3x3 sq.mm, were rather clearly observed, but there were few deformations at the end of the opening areas.

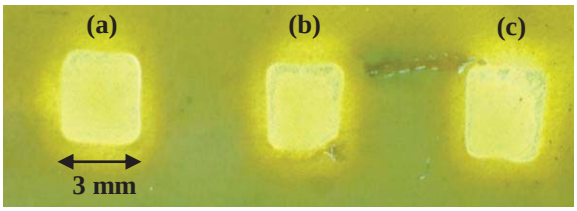

Figure 3. Photograph of NPSPI films

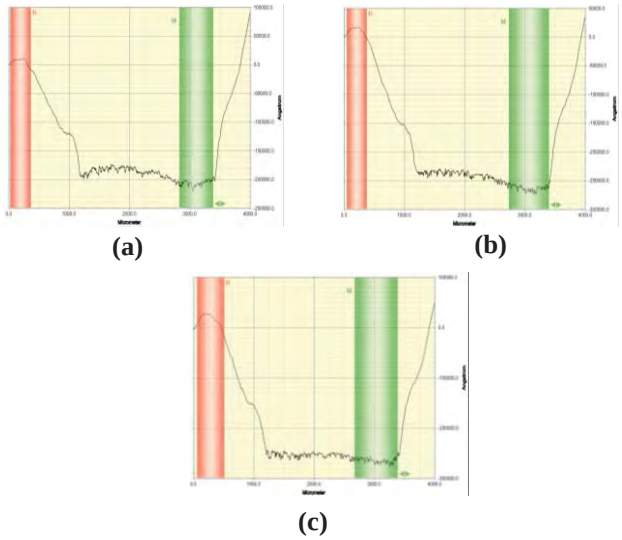

Figure 4. The film thickness and the opening size of NPSPI films by Stylus profiler as the film thicknesses of (a) 19.6, (b) 25.3 and (c) 21.6 µm

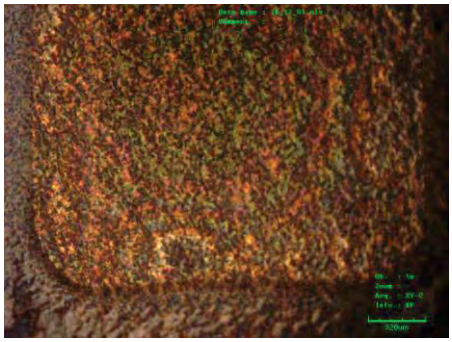

Figure 5. Morphology of NPSPI films on copper foil.

4. Conclusions

The negative photosensitive polyimides with the thickness approximately controlled at 12.5 micron were successfully prepared. The ratio of the size of opening area to mask size were in the range of 0.8 – 0.82 or 80 - 82 % which is acceptable. The prepared negative photosensitive polyimide could have potential applications for patterned electronic and optoelectronic devices.

Acknowledgements

Sincere thanks to Mektec Manufacturing Corporation (Thailand) Ltd. For using analysis & characterize instruments and financial supports of student's scholarship and materials.

Sincere thanks to Ciba Specialty Chemical Thailand Inc. for supplied Irgacure-819.

References

[1] Hong Zhuang. *Synthesis and Characterization of Aryl Phosphine Oxide Containing Thermoplastic Polyimides and Thermosetting Polyimides with Controlled Reactivity.* Blacksburg, Virginia. (1998) 15.

[2] Seunghyuk Choi, Seokkyu Lee, Jihee Jeon, Jaein An, Sher Bahadar Khan, Sangyup Lee, Jongchul Seo and Haksoo Han. *A Photoinitiator-Free Photosensitive Polyimide with Low Dielectric Constant.* InterScience (2010).

[3] http://scienceedu.larc.nasa.gov/EDDOCS/ Wavelengths_for_Colors.html./ (Retrieved March 31, 2012).

[4] Peter Cheang, Lorna Christensen and Corinne Reynaga. *Optimization of Photosensitive Polyimide Process for Cost Effective Packaging.* Surface Mount Technology Seminar (1996) 1-18.

[5] Perfecto, Eric D. et al., *"Factors That Influence Photosensitive Polyimide Lithography Performance."* ICEMM Proceedings. (1993) 40-45.

[6] Kataoka F, Suzuki H. In: Horie K, Yamashita T, editors. *Photosensitive Polyimide.* Lancaster Technomic (1996).

[7] Tessler N, Medveder V, Kazes M, Kan S, Banin U. *Synthesis and properties of new polyimide–silica hybrid films through both intrachain and interchain bonding.* Science 295(2002) 1506.

[8] Sysel P, Pulec R, Maryska M. *Preparation and properties of poly (imide siloxane) segmented copolymer/silica hybrid nanocomposites.* Polym J 29(1997) 607.

[9] Chen Y, Iroh JO. *Synthesis and Characterization of Polyimide/Silica Hybrid Composites.* Chem Mater 11(1999) 1218.

[10] Ahmad Z, Mark JE. *Preparation and characterization of polyimide/silica nanocomposite spheres.* Chem Mater 13(2001) 3320.

[11] Chang CC, Chen WC. *Synthesis and Optical Properties of Polyimide-Silica Hybrid Thin Films.* Chem Mater 14(2002): 4242.

[12] Chang CC, Wei KH, Chen WC. *Spin-Coating of Polyimide-Silica Hybrid Optical Thin Films.* J Electrochem Soc 150(2003) 147.

[13] Suttisak Srisuwan, Supakanok Thongyai, Piyasan Praserthdam. *Synthesis and Characterization of Low-Dielectric Photosensitive Polyimide/Silica Hybrid Materials* 117(2010) 2422–2427.

[14] Sroog C. E., Endrey A. L., Abroma S. V., Berr C. E., Edward W. M., and Oliver K. L. *Aromatic polypyromellitimides from aromatic polyamic acids.* J Polym Sci 3 (1965) 1373.

[15] Takekoshi T., Ghosh M.K. and Mittal K.L. *Polyimides-Fundamentals and Applications.* New York: Marcel-Dekke (1996).

[16] Ghosh MK and Mittal KL. *Polyimides-Fundamentals and Applications.* New York: Mercel-Dekker (1996).

[17] Harris F.W., Wilson D., Stenzenberger H.D, Hergenrother P.M., Chapman and Hall. Polyimides. New York: (1990).

[18] Pravednikov A.N., Kardash I.Y., Glukhoyedov N.P. and Ardashnikov A.Y. Polym Sci USSR 15(2)(1973) 399.

[19] K.Fukukawa and M. Ueda. Recent Progress of Photosensitive Polyimides. 281-296.

[20] Le Thu T. Nguyen, et al. *Synthesis and characterization of a photosensitive polyimide precursor and its photocuring behavior for lithography applications.* Optical Materials 29(2007) 610-618.

[21] Warren W. Flack, Gary E. Flores, Lorna Christensen and Gary Newman. *An Investigation of the Properties of Photosensitive Polyimide Films.* SPIE 27(1996) 26-75.

[22] Steve Lien-Chung Hsu and Ming Hsin Fan. *Synthesis and Characterization of Novel Negative-Working Aqueous Base Developable Photosensitive Polyimide Precursors.* Polymer 45(2004) 1101-1109.

PROPERTIES IMPROVEMENT OF POLY(LACTIC ACID) BY BLENDING WITH LOW Mw POLY(LACTIC ACID)-G-NATURAL RUBBER

Apicha Thepthawat[1], Kawee Srikulkit[1,2*]

[1] Department of Materials Science, Faculty of Science, Chulalongkorn University, Pathumwan, Bangkok, 10330 Thailand
[2] Center of Excellence on Petrochemicals and Materials Technology Center, Chulalongkorn University, Bangkok, 10330 Thailand

[*] E-Mail: kawee@sc.chula.ac.th, Tel. +66 81 675 1003

Abstract: Poly(lactic acid) (PLA) was blended with natural rubber grafted low molecular weight PLA (NR-g-PLA). Firstly, grafting of maleated natural rubber with low molecular weight poly(lactic acid) at weight ratio of 1:1 was carried out in toluene solvent at 80°C. MNRs prepared using maleic anhydride of 10 and 20 wt% was employed. IR spectrum of MNRs showed the absorption band at 1778 and 1853 cm^{-1} which corresponded to the symmetric and asymmetric of C=O vibrations and later the absorption band at 1853 cm^{-1} disappeared from NR-g-PLA spectrum. Next, thus obtained NR-g-PLA was blended with pristine PLA using twin-screw extruder and followed by compression according to ASTM standards to obtain specimens for testings. Pristine PLA to NR-g-PLA weight ratios were as follows: 90:10, 80:20, 70:30, 60:40. Impact strength values according to D256 standard test of PLA/NR-g-PLA blends were measured and compared to those of NR-g-PLAs, and PLA/NR. As found, blending of NR-g-PLA with PLA resulted in the material that exhibited a significant increase in impact strength (ie 196 J/m for recipe 80:20) compare to pure PLA (ie 3.0 J/m). On the other hand, direct mixing NR into PLA produced the material of which the impact strength (ie 182 J/m for recipe 80:20) was inferior to PLA/NR-g-PLA. This indicated that NR-g-PLA exhibited better compatibility than NR. The compatibility, mechanical properties, and thermal properties were be further proven by SEM, universal testing machine, and DSC and TGA, respectively.

1. Introduction

Nowadays, plastics have been consumed extensively for many applications. As a result, the plastic waste disposal causes considerable environmental concern. This has led to an interest in searching for biodegradable plastics.

Poly(lactic acid), PLA is one of promising biodegradable polyesters. It is made from bacterial fermentation of renewable carbohydrate sources such as corn, sugar cane, potato etc. PLA is a trasparent, good strength and easy processability[1]. However, the important application restriction of PLA is brittleness. Attempts to improve flexibility of PLA could be divided into three routes: copolymerization, plasticization and blending [2,6]. Blending of PLA with other biodegradable polymers such as Polycaprolactone, Poly(butylene adipate-co-terephthalate) and Poly(butylene succinate) is a simple route at the expense of reduced strength as well as reduced modulus [2].

Natural rubber (NR) is also an interesting natural polymer for toughening PLA due to its elasticity characteristic, biocompatibility and reactivity [5]. Rubber particles have been used through the incorporation of a second phase for toughened polymer [3]. Rubbers exhibit a compatibilization but they are immiscible with matrix polymer. In the polymer blend, rubber phase acts as energy absorber and crack inhibitor [4-5]. Therefore, NR is a good candidate as an impact modifier to be incorporated into brittle polymer like PLA as reported by Bitinis *et al*. The resultant tensile indicated that elongation at break was increased from 5% (neat PLA) to 200% by the addition 10wt% NR [5]. Nakason *et al*. reported that the shear viscosity of MNR/PMMA blends (MNR containing MA content of 10 wt%, MNR-10) increased with an increase in MNR-10 concentration until reaching maximum at 60 wt% MNR-10. Above this concentration, the shear viscosity decreased due to changing phase. In addition, the Tg values of polymer blends increased with an increase in MA content due to chain mobility restriction as a result of chemical interaction [6].

Moreover, there is still more room to improve properties of poly(lactic acid) especially stiffness-toughness balance and being substantially biodegradability. In this study, maleated natural rubber as compatibilizing agent was synthesized to further prepare NR-g-PLA hybrid. Then, NR-g-PLA copolymer was blended with pristine PLA. The compatibility, mechanical and thermal properties were investigated.

2. Materials and Methods

2.1 Materials

PLA (Mw=138700) was purchased from NatureWorks®. Ribbed smoked sheet rubber (RSS) was kindly supplied by local rubber factory, Thailand. Toluene, acetone and methanol were obtained from Sathaporn group company, Thailand. Maleic anhydride and Benzoyl peroxide initiator were purchased from Sigma-Aldrich, Belgium. Phenolphthalein and NaOH for determining the grafted MA content by titration method was purchased from

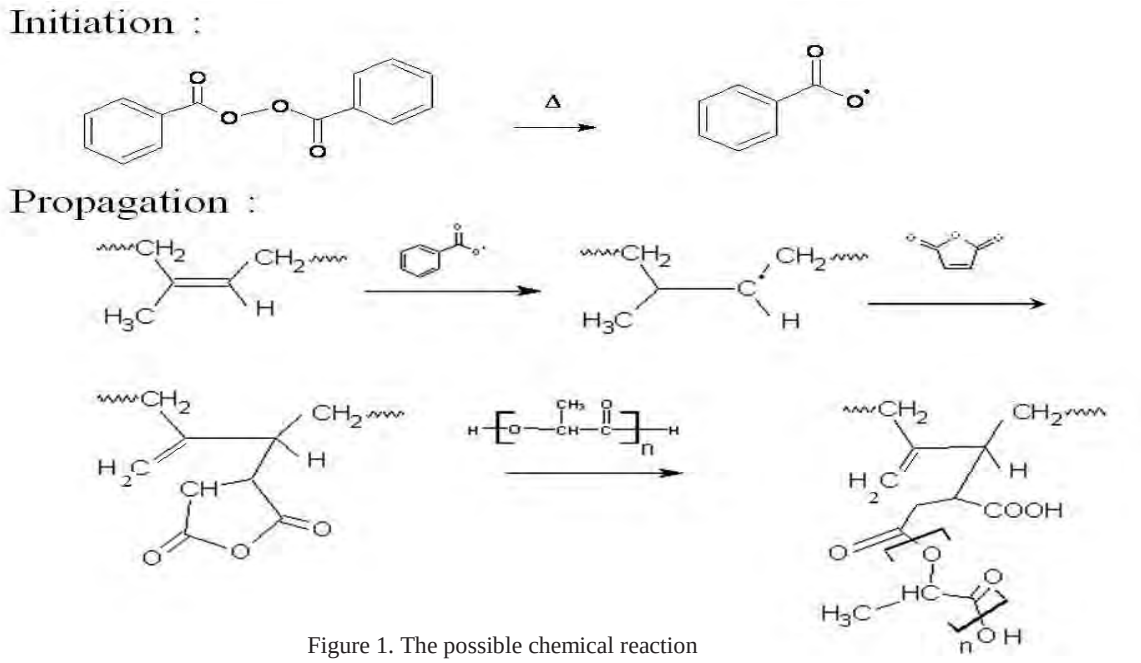

Figure 1. The possible chemical reaction

Ajax Finechem, Pty, Ltd. The tetrahydrofuran (THF) was bought from Burdick&Jackson, SK chemicals, Korea.

2.2 Preparation of NR-g-PLA

2.2.1 Maleated Natural rubber

Maleic anhydride was grafted onto natural rubber in toluene solution at temperature of 80°C for 2 hours. Benzoyl peroxide (3 wt% of NR) was used as a free radical initiator. MA content was varied at 10 and 20 wt% of natural rubber.

2.2.2 Low molecular weight poly(lactic acid) grafted natural rubber

Low molecular weight PLA (Low-PLA) was prepared by twice melt processing of pristine PLA using twin-screw extruder with barrel zone temperature setting of 180, 180, 170, 160, 135 °C.

Thus obtained low-PLA (Mw=42500) was added bit by bit into maleated natural rubber solution at weight ratio of 1:1 for 6 hours. NR-g-PLA was precipitated by pouring the solution mixture into methanol. The precipitate was washed and dried at 50°C for 24 hrs.

2.3 Characterization of MNRs and NR-G-PLAs

Low molecular weightn PLA grafted on natural rubber was analysed by Fourier transformation infrared spectroscopy (FTIR, Nicolet 6700). Maleated natural rubber solution was coating on KBr disk and dried in an oven. The dried NR-g-PLA was mixed with KBr powder and compressed into disk. The record range of IR spectras was 4000 cm^{-1} to 400 cm^{-1}. The glass transition temperature of MNRs and NR-g- PLAs was identified by differential scanning calorimetry (Perkin Elmer DSC, Diamond DSC). The degradation temperature of MNRs and NR-g-PLAs was identified by thermal gravimetric analysis (Mettler Toledo, TGA/SDTA851).

2.4 Preparation of PLA/NR-G-PLA blends

PLA was blended with NR-g-PLA using twin-screw extruder at weight ratio as shown in Table 1. Barrel zone temperatures were set at 135, 160, 170, 180 and 180 °C, for zone 1 to zone 5, respective. Then Polymer extrudate was cut into pellet form and

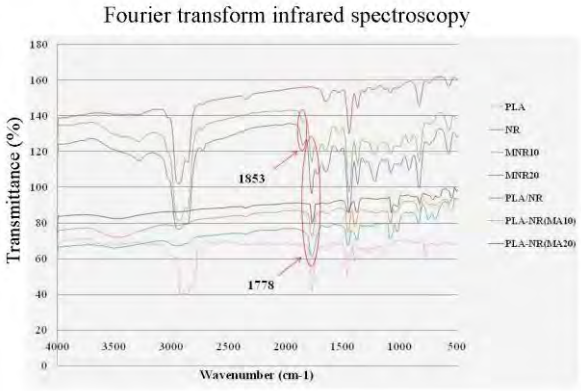

Figure 2. FTIR spectras showed IR absorbance of PLA, MNRs and NR-g-PLAs.

compressed into standard shapes according to ASTM standard.

2.5 The thermal properties

The glass transition temperature and degradation temperatue of PLA and PLA blends was investigated by DSC and TGA technique, respectively.

2.6 Mechanical properties

The impact strength of samples was performed according to ASTM D256 by Impact-charpy impact

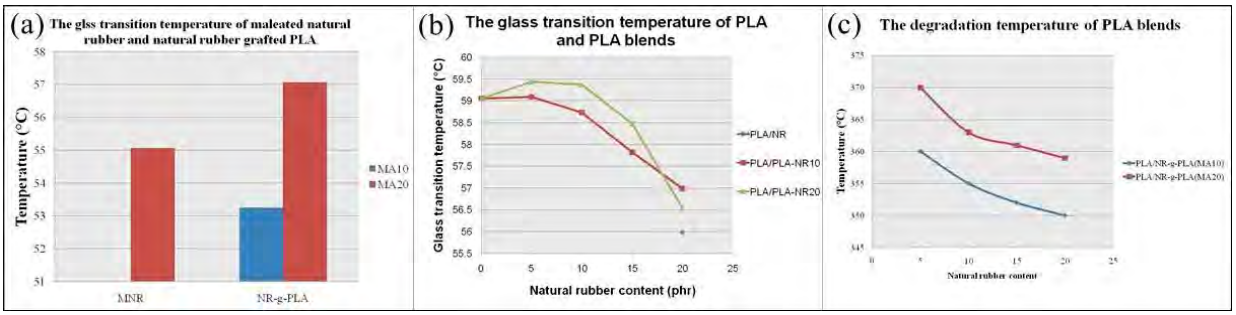

Figure 3. Thermal properties of PLA, NR-g-PLA and PLA blends: (a) Tg of MNR and NR-g-PLA, (b) Tg of PLA blends and (c) Td of PLA blends.

machine (Gotech, GT-7024-MD, Taiwan).

2.8 Morphology

The fracture of dumbbell-shaped specimens was observed by scanning electron microscopy at an acceleration voltage of 22.0 kV. The fracture surface was coated with gold for electrical discharge prevention.

Table 1: The component of PLA blended with NR-g-PLA

Component	MA (wt%)	PLA:MNR wt ratio	PLA/NR-g-PLA (phr)
MNR1	10	1:1	90:10 80:20 70:30 60:40
MNR2	20	1:1	90:10 80:20 70:30 60:40
Blank	-	-	PLA80:NR20
PLA 100%	-	-	100

3. Results and Discussion

3.1 Characterization of MNRs and NR-g-PLAs

Natural rubber was grafted with maleic anhydride using BPO (wt% of NR) as free radical initiator. Maleated natural rubber was identified by Fourier transformation infrared spectroscopy as shown in Fig 2. The IR spectra of MNR showed the absorbance bands at 1778 and 1853 cm^{-1} which correspond to symmetric and asymmetric of maleic anhydride ring C=O vibration [7-8]. Thereafter, low-Mw PLA was grafted onto MNR in toluene solvent at temperature of 80°C. The complete grafting was proved by FTIR. As seen, the IR absorption band at 1853 cm^{-1} corresponding to asymmetric C=O vibration disappeared [7]. The absorbance intensity of at 1778 cm^{-1} also decreased with an increase in MA content [9], confirming that MA grafted on NR. As the result of the reaction, the possible chemical reaction was proposed in Fig. 1 [7].

3.2 Thermal properties

The glass transition temperature (Tg) is indicative of chain mobility as well as miscibility of polymer blend [10]. Fig. 3(a) showed the glass transition temperature of MNR and NR-g-PLA that Tg of MNR did not appear at temperature program. It is found that an increase in Tg of NR-g-PLA is related to an increase in MA content due to the effect of MA side group on the polymer chain mobility restriction [6-8]. Fig. 3(b) showed the effect of MA content on Tg of PLA blends. The similar trend in increasing Tg with MA side group content was observed. The Tg of PLA/NR-g-PLA20 at weight ratio of 80: 20 was higher than Tg of PLA/NR-g-PLA10 at same weight ratio due to PLA chain mobility restriction arising from higher amount of NR bonded PLA [10-11]. It is noted that the Tg of PLA/NR-g-PLA decreased with an increase in flexible NR content [10].

The thermo gravimetric analysis of PLA, NR-g-PLA and PLA blends is shown in Fig. 3(c) The thermal degradation of PLA at temperature range 25 – 950 °C showed 2 degradation steps. Td of PLA and NR were 375°C. The 1st degradation step showed Td of PLA blends decreased with the increasing of NR content and Td of MNR having higher MA content (MA20) was higher than Td of MNR having lower MA content (MA10) due to interaction. The 2nd degradation steps were assumed to be char degradation which is complete at temperature of 600 °C.

3.3 Morphology

Morphology of PLA and PLA blends was observed by scanning electron microscopy. When considering the blends at weight ratio of 80:20 were observed the morphology in case of MNR having higher anhydride content (MNR20), indicating the more compatible than MNR having lower anhydride content and absence anhydride content. As a result, PLA is improved due to enhancing interfacial adhesion [12]. For PLA/NR blend large NR particles with various sizes and shapes are found due to the agglomeration problem.

3.4 Mechanical properties

Improvement of interfacial adhesion between NR and PLA could be achieved through modification of NR with low Mw PLA by grafting technique. The

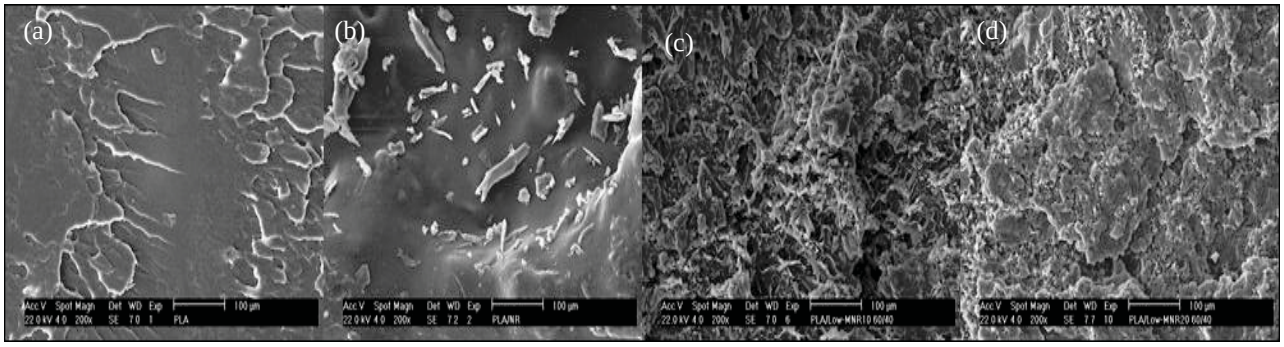

Figure 4. SEM photographs showed morphology of PLA and PLA blends at weight ratio 80:20: (a) PLA, (b) PLA/NR, (c) PLA/NR-g-PLA (MA10), and (d) PLA/NR-g-PLA (MA20).

interfacial adhesion was derived through PLA segment of NR-g-PLA. Interfacial adhesion between dispersed phase and matrix plays an important role in improving mechanical properties of PLA such as impact strength. Prior to testing, PLA blends were compressed into rectangular shape according to ASTM D256. Fig. 5 showed the impact strength. As found, the impact strength of pristine PLA is very low which is derived from the rigidity nature of PLA. The incorporation of NR and NR-g-PLA results in significant improvement of impact strength due to the role of NR in absorbing energy. However, NR-g-PLA with higher anhydride content (MNR20) tends to reduce the impact strength of the blend due to the decrease in a number of double bonds through MA grafting reaction. As a result, MNR20 partially loosed its elasticity when compared to MNR10, consequently loosing ability of energy absorption performance. Despite the loss of elasticity of MNR the impact strength of PLA/NR-g-PLA blends is slightly higher than PLA/NR blend (MA0) due to better interfacial adhesion and more finely rubber particles distribution [12].

4. Conclusions

Low Mw NR-g-PLA was prepared by grafting low-MW PLA with maleated NR (MNR). PLA/NR-g-PLA blend was achieved by melt blending using twin screw extruder. Thermal properties of PLA blends showed the Tg of PLA in the blend containing high anhydride content (MNR20) tended to be higher than that of lower anhydride content (MNR10) due to PLA chain mobility restriction arising from chemical interaction. The incorporation of NR and NR-g-PLA results in significant improvement of impact strength due to the role of NR in absorbing energy. However, NR-g-PLA with higher anhydride content (MNR20) tends to reduce the impact strength of the blend due to the MA grafting reaction. As a result, MNR20 partially loosed its elasticity when compared to MNR10, consequently loosing ability of energy absorption performance decrease in a number of double bonds through MA grafting reaction. As a result, MNR20 partially loosed its elasticity when compared to MNR10, consequently loosing ability of energy absorption performance.

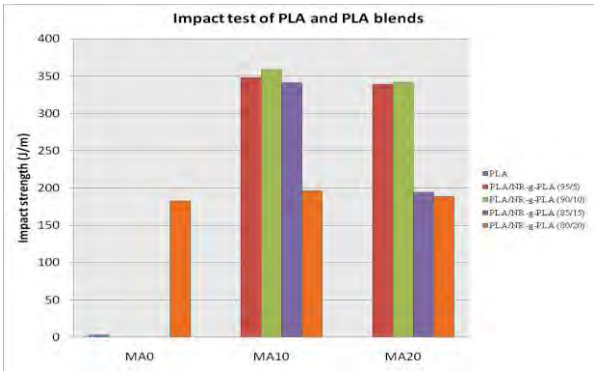

Figure 5 Impact strength of PLA, PLA/NR-g-PLA and PLA/NR

Acknowledgements

The work was supported by the 100th Anniversary of University Fund.

References

[1] A.P. Gupta and V. Kumar, *Eur. Polym. J.* **43** (2007) 4053–4074.
[2] L. Jiang and J Zhang, *Biodegradable and Bbiobased polymer*, Washingtion State University, USA, pp. 145-158.
[3] R.J. Young and P.A. Lovell, *Introduction to polymers*, 2nd edition, Cambridge University Press, UK (1991), pp. 417-424.
[4] *Technology Focus Report: Toughened PLA*, NatureWorks®.
[5] N. Bitinis, R. Verdejo, P. Cassagnau and M.A. Lopez-Manchado, *Mat. Chem. Phy.***129** (2011) 823-831.
[6] C. Nakason, S. Saiwaree, S. Tatun and A. Kaesaman, *Polym. Test.* **25** (2006) 656-667.
[7] C.H. Ho, C.H. Wang, C.I. Lin and Y.D. Lee, *Polymer.* **49** (2008) 3902-3910.
[8] *C. Nakason, A. Kaesaman and P. Supasanthitikul, Polym. Test.* **23** (2004) 35-41.
[9] S.W. Hwang, S.B. Lee, C.K. Lee, J. Y. Lee, J. K. Shim, S. E.M. Selke, H. Soto-Valdez, L. Matuana and M. Rubino, *Polymer Test.* **31** (2012) 333-344.
[10] L. H. Sperling, *Introduction to physical polymer science*, 4th edition, John Wiley & Sons, Inc., USA (2006), pp. 408-409.
[11] V. Thirtha, R. Lehman and T. Nosker, *Polymer.* **47** (2006) 5392-5401
[12] Z. Liu, X. Zhu, L. Wu, Y. Li, Z. Qi, C. Choy and F. Wang, *Polymer.* **42** (2001) 737-7

SYNTHESIS AND CHARACTERIZATION OF A NOVEL TIN(II) POLY(PROPYLENE GLYCOL) ADDUCT FOR USE AS AN INITIATOR IN THE RING-OPENING POLYMERIZATION OF CYCLIC ESTERS

Watcharee Sangsuwan[1], Sujitra Ruengdechawiwat[2], Robert Molloy[2,3], Achara Kleawkla[1*]

[1] Department of Chemistry, Faculty of Science, Maejo University, Chiang Mai 50290, Thailand
[2] Polymer Research Group, Department of Chemistry, Faculty of Science, Chiang Mai University, Chiang Mai 50200, Thailand
[3] Materials Science Research Center, Faculty of Science, Chiang Mai University, Chiang Mai 50200, Thailand

[*] Author for correspondence; E-mail: achara_kleawkla@yahoo.co.uk, Tel. +66 53 873530, Fax. +66 53 873548

Abstract: Tin(II) alkoxides are commonly used as initiators in the ring-opening polymerization (ROP) of cyclic ester monomers to control the reaction kinetics and the molecular weight of the polyesters formed. Examples are poly(ε-caprolactone) and poly(L-lactide) which are used in various biomedical applications. This project has been concerned with the synthesis and characterization of a novel tin(II) poly(propylene glycol) initiator for use in ROP of cyclic ester, namely: ε-caprolactone. The tin(II) poly(propylene glycol) was synthesized via the reaction between anhydrous tin(II) chloride, poly(propylene glycol)400 (PPG400) and triethylamine at 20-16°C under a nitrogen atmosphere. After separation and purification, the product, $Sn(PPG400)_2$, was obtained as fine white powders with approximately 93% yield. The $Sn(PPG400)_2$ was characterized by a combination of analytical techniques such as Fourier-transform infrared spectroscopy (FT-IR), proton nuclear magnetic resonance spectroscopy (^{1}H-NMR) and differential scanning calorimetry (DSC). It was found that polymers with controllable molecular weights could be produced, when $Sn(PPG400)_2$ was used as an initiator (0.1, 0.5 and 1.0 mol%) in the bulk ROP of ε-caprolactone at1 50 °C.

1. Introduction

Aliphatic polyesters are the most widely used biodegradable polymers in biomedical applications. These applications include absorbable sutures, nerve guides, bone fixation devices, drug delivery systems and 3-D scaffolds for tissue engineering [1]. The main method used in the synthesis of biodegradable polyesters is ring-opening polymerization (ROP) of the corresponding cyclic ester monomers. The polyesters formed are versatile polymers having good mechanical properties, hydrolyzability and biocompatibility. The synthesis of novel polymer structures through ROP has been studied for a number of years [2]. The polyesters which have so far found the most commercial importance are those derived from cyclic ester monomers such as glycolide, lactide (L, D and DL) and ε-caprolactone.

Poly(ε-caprolactone), PCL, has attracted particular attention because of its partial compatibility with a number of commercial polymers such as PVC and bisphenol A polycarbonate. It is of interest as a packaging material and in biomedical applications since it is degradable and its degradation products are non-toxic to the human body [3]. PCL is a synthetic biodegradable aliphatic polyester which has been attracting increasing research attention in recent years, notably in the specialist biomedical areas of controlled-release drug delivery systems and 3-D scaffolds for tissue engineering [4-6]. PCL is manufactured commercially via the ROP in bulk of ε-caprolactone, CL, as shown in Figure 1.

Tin(II) 2-ethylhexanoate, commonly known as tin(II) octoate or stannous octoate, $Sn(Oct)_2$, in combination with an alcohol ROH is employed as the initiating system at a temperature of, typically, 140-150 °C [3].

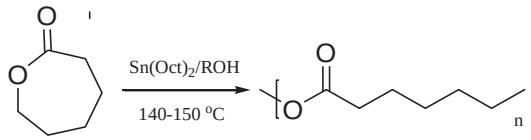

Figure 1. Ring-opening polymerization of ε-caprolactone as employed in its manufacture

Stannous octoate, $Sn(Oct)_2$, is a frequently used initiator in the ROP of lactones and lactides. In combination with an alcohol, ROH, it is a very effective and versatile initiator which is easy to handle and is soluble in common organic solvents and lactones. It also has the advantage, as far as its use in the preparation of biomedical polymers is concerned, that the American Food and Drug Administration (FDA) has approved it as a food additive. However, $Sn(Oct)_2$ is also known to be an efficient transesterification agent which makes it difficult to synthesize controlled microstructures. Furthermore, it has now been established that $Sn(Oct)_2$ is not the true initiating species in the polymerization reaction. Instead, it has been shown that the $Sn(Oct)_2$ initiator and ROH coinitiator react together *in situ* to form the corresponding tin(II) monoalkoxide, Sn(Oct)(OR), and dialkoxide, $Sn(OR)_2$, which are the true initiators. The sequence of reactions is:

$$Sn(Oct)_2 + ROH \rightleftharpoons Sn(Oct)OR + OctH \quad (1a)$$

$$Sn(Oct)OR + ROH \rightleftharpoons Sn(OR)_2 + OctH \quad (1b)$$

where OctH is the octanoic acid by-product.

The generally accepted coordination-insertion mechanism of the ROP of a cyclic ester monomer by a

tin(II) alkoxide, $Sn(OR)_2$, initiator is shown below in equations (2) and (3). This mechanism involves acyl-oxygen (CO-O) bond cleavage in the monomer followed by insertion into the tin-oxygen (Sn-O) bond of the initiator.

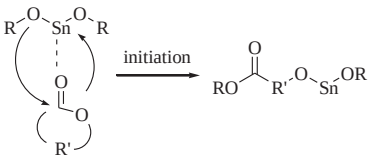

(2)

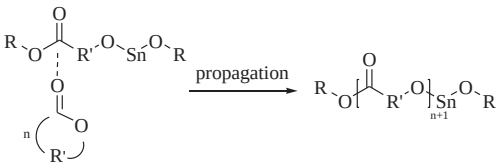

(3)

Since reactions (1a) and (1b) are interdependent equilibrium reactions, the actual [Sn(Oct)(OR)] and $[Sn(OR)_2]$ initiator concentrations are unknown throughout the polymerization. Thus, it is difficult to produce polymers with predictable and reproducible molecular weights and, in the case of copolymers, with consistent chain microstructures. It has therefore been in an attempt to overcome these uncertainties that this work has been focusing its attention on the synthesis of tin(II) alkoxides, $Sn(OR)_2$, so that they can be used directly in accurately known concentrations rather than have to be generated *in situ*.

The synthesis of tin(II) alkoxides, $Sn(OR)_2$, was first reported about 40 years ago by Morrison and Haendler [7]. It involves the reaction between anhydrous $SnCl_2$ and the corresponding alcohol ROH with triethylamine as HCl scavenger, as shown in equation (4) below.

$$SnCl_2 + 2ROH + 2(C_2H_5)_3N \longrightarrow Sn(OR)_2 + 2(C_2H_5)_3N \cdot HCl \quad (4)$$

2. Materials and Methods

2.1 Initiator Synthesis

All chemicals used were purified by distillation. Since tin(II) alkoxides are both moisture and air-sensitive, their synthesis needs to be carried out using pure reagents in an inert atmosphere. Following the method of Morrison and Haendler [7], anhydrous tin(II) chloride was dissolved in poly(propylene glycol)400 (PPG400) and triethylamine added to cause a permanent precipitate. The reaction was stirred at 16-20 ^oC under a dry nitrogen atmosphere. The precipitate was filtered off, washed with methanol and dried under vacuum. This crude product was a mixture of the $Sn(PPG400)_2$ and the $(C_2H_5)_3N \cdot HCl$ by-product, as shown in reaction (5). They were separated by using chloroform to dissolve the hydrochloride after which the $Sn(PPG400)_2$ was purified and characterized.

$$SnCl_2 + 2HOROH + 2(C_2H_5)_3N \rightarrow Sn(OROH)_2 + 2(C_2H_5)_3N \cdot HCl \quad (5)$$

where HOROH = PPG400 = $HO\text{-}[CH_2(CHCH_3)O\text{-}]_n\text{-}H$ (average $n \approx 9\text{-}10$)

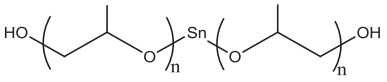

$Sn(PPG400)_2$

The rationale behind the synthesis and use of the novel tin(II) alkoxide, $Sn(PPG400)_2$, as a coordination-insertion initiator in this work has been that, rather than being generated *in situ* in an indeterminate concentration, it could be synthesized separately and added directly into the system in an accurately known initial concentration. The main purpose of the long PPG400 substituents is to help make the initiator more soluble in cyclic ester monomers than conventional $Sn(OR)_2$ compounds synthesized from simple alcohols ROH which tend to be difficult to dissolve due to their tendency for molecular aggregation, $[Sn(OR)_2]_n$, as shown below. This insolubility greatly reduces the activity of the initiator since the Sn-O bonds, which are the active sites for polymerization, are only accessible on the surfaces of the initiator particles.

$$n\ Sn(OR)_2 \quad \rightarrow \quad [Sn(OR)_2]_n$$

non-aggregated
soluble (homogeneous)
active

aggregated
insoluble (heterogeneous)
less active

2.2 Bulk ROP of ε-Caprolactone

The bulk ROP of ε-caprolactone (CL) was carried out at 150 ^oC in a round-bottomed flask with magnetic stirring. $Sn(PPG400)_2$ initiator concentrations of 0.1, 0.5 and 1.0 mol % relative to the CL monomer were weighed accurately into the reaction flask in a glove box under dry nitrogen. After removing the flask from the glove box, it was immersed in a silicone oil bath at a constant temperature of 150 ^oC for 72 hrs. At the end of this period, the polymer was allowed to cool to room temperature. The crude PCL was purified by dissolving in chloroform, precipitating in ice-cooled methanol before finally drying in a vacuum oven at 45 ^oC to constant weight.

The purified polymers were characterized by a combination of analytical techniques, namely: Fourier-transform infrared spectroscopy (FT-IR) and proton nuclear magnetic resonance spectroscopy (^{1}H-NMR) for structural confirmation, differential scanning calorimetry (DSC) for melting point and % crystallinity determinations, and dilute-solution viscometry for weight-average molecular weight, M_w, determination.

3. Results and Discussion

3.1 $Sn(PPG400)_2$ Initiator Characterization

The purified $Sn(PPG400)_2$ initiator product was obtained as a finely divided white powder in 93% yield. Solubility testing in a range of organic solvents showed that it was only partially soluble which indicated that, despite its long PPG400 substituents, it was still aggregated to a certain extent with only the lower aggregates being able to dissolve.

In order to confirm its chemical structure, the $Sn(PPG400)_2$ initiator was characterized initially by Fourier-transform infrared spectroscopy (FT-IR), as shown in Figure 2 below.

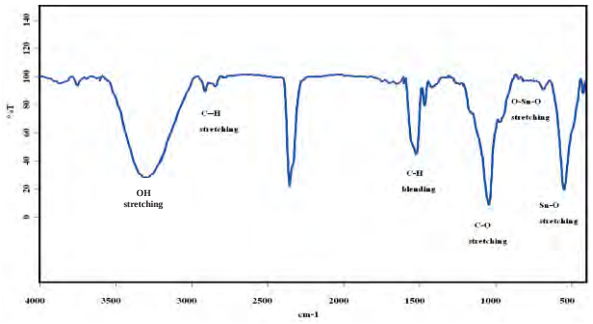

Figure 2. FT-IR spectrum of the $Sn(PPG400)_2$ initiator

The most prominent peaks in the FT-IR spectrum of $Sn(PPG400)_2$ are assigned to their respective bond vibrations as listed in Table 1 below. The appearance of these characteristic peaks is consistent with the chemical structure of $Sn(PPG400)_2$.

Table 1: Vibrational assignments in the FT-IR spectrum of the $Sn(PPG400)_2$ initiator.

Wavenumber (cm^{-1})	Vibrational Assignment
3506	O-H (stretching)
2932	C-H (stretching)
1520	C-H (bending)
1027	C-O (stretching)
676	O-Sn-O (stretching)
539	Sn-O (stretching)

The DSC thermogram of the $Sn(PPG400)_2$ initiator in Figure 3 shows a broad melting peak from 90-150 ^oC with a peak melting temperature (T_m) of 124.5 ^oC. The enthalpy of melting (ΔH_m), which is calculated from the area under the melting peak and is proportional to the % crystallinity, was 60.80 J/g.

The broad melting peak in Figure 3 is a further indication of the $Sn(PPG400)_2$ initiator's molecular aggregation and also the distribution in the degree of aggregation. Larger aggregates would be expected to have a higher T_m than smaller aggregates.

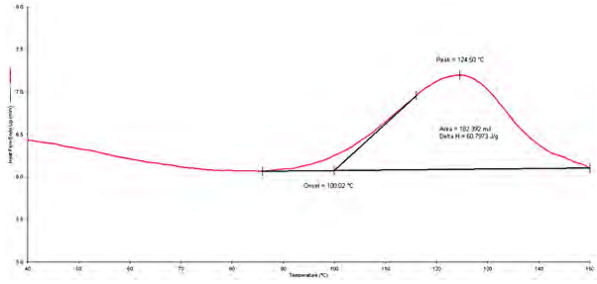

Figure 3. DSC thermogram of the $Sn(PPG400)_2$ initiator (Heating rate = 10 ^oC/min)

3.2 Polymerization of CL Monomer

In this work, bulk polymerization (CL monomer + $Sn(PPG400)_2$ initiator only) was the chosen method of polymerization since (a) it eliminated any complicating solvent effects and (b) biomedical polyesters are invariably synthesized by bulk polymerization in order to avoid potentially toxic trace amounts of solvent impurities remaining in the final product. The results obtained from the three polymerization experiments carried out here are summarized in Table 3 below.

The purified PCL was characterized by nuclear magnetic resonance spectroscopy (^{1}H-NMR) for structural confirmation as shown in Figure 4 and Table 2 below.

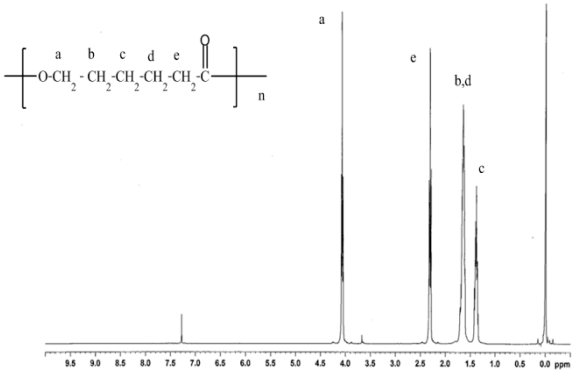

Figure 4. 400 MHz ^{1}H-NMR spectrum of PCL in deuterated chloroform ($CDCl_3$) as solvent.

Table 2: Chemical shifts of the peaks in the ^{1}H-NMR spectrum of PCL in Figure 4.

Proton Assignment		Chemical Shift (δ, ppm)
ε - CH_2	a	4.045
δ – CH_2	b	1.634
γ – CH_2	c	1.383
β – CH_2	d	1.634
α – CH_2	e	2.290

Table 3: Comparison of PCL properties obtained using various initiator concentrations.

[Initiator] % by mol	Yield %	T_m* ^oC	$[\eta]$** dl/g	M_w
0.1	73.8	65.7	0.629	2.82×10^4
0.5	83.8	64.3	0.378	1.53×10^4
1.0	89.5	66.5	0.336	1.32×10^4

* taken as the peak T_m from the DSC melting peak

** intrinsic viscosity measured in chloroform as solvent at 30 ^oC

Under the temperature/time conditions (150 ^oC / 72 hrs) employed, the various initiator concentrations gave high yields (>70%) and reasonably high weight-average molecular weights ($M_w > 10^4$). As expected, the M_w of the PCL decreased with increasing initiator concentration, as shown in Table 3. These M_w values were obtained from dilute-solution viscometry via the

Mark-Houwink Equation below for PCL in chloroform as solvent at 30 ^{o}C [4].

$$[\eta] = 1.298 \times 10^{-4} M_w^{0.828} \text{ dl/g}$$

Table 4 shows the DSC melting parameters and % crystallinities for the PCL samples. The values, which are comparable with those of commercial samples, are similar enough to suggest that, at a molecular weight level of $M_n > 10^4$, the thermal properties and semi-crystalline morphology of PCL are fully developed.

Table 4: DSC melting points, heats of melting and % crystallinities of the purified PCL products.

[Initiator] % by mol	Melting Point T_m (^{o}C)*	Melting Parameters	
		ΔH_m (J/g)**	% Crystallinity***
0.1	65.7	107.8	75.9
0.5	64.3	136.9	96.4
1.0	66.5	87.0	61.3

* taken as the peak T_m from the DSC melting peak

** ΔH_m = heat of melting ($\propto$ area under T_m peak)

*** calculated from the equation:

$$\% \text{ crystallinity} = (\Delta H_m/\Delta H_m^*) \times 100\%$$

where, for PCL, $\Delta H_m^* = 142$ J/g [8]

ΔH_m^* = ΔH_m of a 100% crystalline sample

Regarding initiator solubility, which has been one of the main focal points of this work, it was observed that, during the polymerization of the CL monomer at 150 ^{o}C, the $Sn(PPG400)_2$ initiator gradually but only partially dissolved. Dissolution continued until the system became so viscous that magnetic stirring was no longer possible. Thereafter, the polymerization had to continue in the viscous melt state. However, it can be said that the $Sn(PPG400)_2$ initiator was certainly more soluble than conventional $Sn(OR)_2$ initiators made from simple ROH alcohols.

4. Conclusions

The results presented here have shown that the $Sn(PPG400)_2$ initiator is effective in the bulk ROP of CL monomer and, by varying its concentration, can control the molecular weight of the PCL polymer formed. Moreover, it is easy to prepare and stable on storage in a desiccators. Since PPG alone is already used in biomedical applications, it would be expected to be non-cytotoxic.

However, the observation that the $Sn(PPG400)_2$ initiator did not completely dissolve in CL monomer during polymerization indicates that, despite its long PPG400 substituents, molecular aggregation in the solid state still occurred to a limited extent. Consequently, even though the initiator gave high yields and reasonably high molecular weights, its efficiency would have been slightly impaired by the fact that it was not completely soluble.

In conclusion, the use of a low molecular weight polymeric diol, PPG400, instead of a simple alcohol , ROH, in the synthesis of a tin(II) alkoxide, $Sn(OR)_2$, has succeeded in reducing, but not completely eliminating the tendency for molecular aggregation.

$$n\ Sn(OR)_2 \rightarrow [Sn(OR)_2]_n$$

Based on these results, it is reasonable to conclude that initiators such as $Sn(PPG400)_2$ have considerable potential for the use as initiators in the controlled ROP of cyclic esters, especially where the polymers are designed to be used in biomedical applications.

Acknowledgements

The authors gratefully acknowledge the Department of Chemistry, Faculty of Science, Maejo University and the Polymer Research Group, Department of Chemistry, Faculty of Science, Chiang Mai University, for provision of the research facilities.

References

[1] D.F.Williams (Eds.), *CRC Series in Biocompatibility: Biocompatibility of Clinical Implant Materials*, **Vol. 2**, CRC Press, Inc., Boca Roton (1981).

[2] A.-C. Abertsson (Eds.), *Adv. Polym. Sci.*, **Vol. 157**, Springer Verlag Berlin (2002).

[3] D.E. Perrin, J.P. English, A.J. Domb, J. Kost and D.M. Wiseman, *Polycaprolactone; in Handbook of Biodegradable Polymers*, Harwood Academic Publishers, Amsterdam, Chap. **3** (1997), pp. 63-77.

[4] C.G. Pitt, M. Chasin and R. Langer (Eds.), *Poly(ε-caprolactone) and Its Copolymers; in Biodegradable Polymers as Drug Delivery Systems*, Marcel Dekker, New York, (1991), pp. 71-82.

[5] D.W. Hutmacher, T. Schantz, I. Zein, K.W. Ng, S.H. Tech and K.C. Tan, *J. Biomed. Mater. Res.* **55** (2001) 203-216.

[6] P. Wutticharoenmongkol, N. Sanchavanakit, P. Pavasant and P. Supaphol, *Macromol. Bioscience* **6** (2006) 70-77.

[7] J.S. Morrison and H.M. Haendler, *Inorg. Nucl. Chem.* **29** (1967) 393-400.

[8] H.F. Mark, N.M. Bikales, C.G. Overberger, G. Mengen and J.I. Kroschwitz, *Encyclopedia of Polymer Science and Engineering*, 2nd Edn., **Vol. 11**, Wiley, New York (1988).

REINFORCING THERMOPLASTIC STARCH WITH WATER HYACINTH

Pawee Samngamnoi[1 2], Wanchai Lerdwijitjarud[1 2] *, Amnard Sittattrakul[1 2]

[1] Department of Materials Science and Engineering, Faculty of Engineering and Industrial Technology, Silpakorn University, Nakorn Pathom 73000, Thailand
[2] Center of Excellence on Petrochemical and Materials Technology, Bangkok 10330, Thailand

* Author for correspondence; E-mail: wanchail@su.ac.th, Tel. +66 34 219363, Fax. +66 34 219363

Abstract: Thermoplastic starch (TPS) was reinforced by water hyacinth. Pure cellulose of water hyacinth was obtained from the weed plant by mechanical and chemical treatments (churning, alkaline and sodium chlorite reactions). The treated celluloses were characterized by Fourier Transform Infrared Spectroscopy (FTIR) to confirm the removal of lignin and hemicelluloses from water hyacinth. The morphologies of celluloses and composite materials were investigated by scanning electron microscope (SEM). Starch, glycerol and untreated or treated cellulose (3%wt. and 5%wt.) were mixed in an internal mixer. The TPS without cellulose displayed the modulus more than the composite prepared with celluloses. The elongation at break and tensile strength increased but the impact strength decreased with increasing cellulose content. The composites prepared with treated cellulose displayed impact strength higher than untreated cellulose.

1. Introduction

Nowadays, polymers have been used in many applications due to they have many advantages such as light weight, durability, and ease of fabrication. The typical polymer is produced from petroleum resource. Synthetic polymer is suspected to be a part of environmental pollution since it releases some toxic substances during manufacturing and it takes relatively long time to degrade. Therefore, the natural polymer has been considered to be an interesting candidate as a more environmentally friendly material [1].

Starch is one of the most interesting natural polymers because it is abundant, low cost, and easy to biodegrade. Thermoplastic starch (TPS) can be easily prepared by mixing starch and plasticizer under heating and shearing. However, TPS has a relatively low mechanical properties and high water sensitivity. Adding reinforcing filler is a popular method to enhance the mechanical properties of TPS. Several studies have been dealing with the preparation and characterization of TPS composite with different type of cellulose such as jute fiber [1], cellulose nanofiber [2], bacterial cellulose [1], and vegetable fiber [3]. Cellulose-reinforced TPS is considered to be a bio-based biodegradable composite. The interaction between cellulose reinforcing filler and starch matrix is expected to be high, since both matrix and filler have an identical repeating unit.

Water hyacinth is a weed water plant in a local river in Nakorn Pathom. It is wide spread in the river and grows up very fast. The water hyacinth contains 60% cellulose, 8% hemicelluloses and 17% lignin [4].

The water hyacinth-reinforced thermoplastic starch has been prepared in the present study. The influence of water hyacinth loading on the mechanical properties of composite is investigated. The morphology of biocomposite is also examined.

2. Experimental

2.1 Materials

Octenyl succinic anhydride (OSA) starch (Siam modified starch, Thailand) and glycerol (Ajex Finechem) were used to prepared thermoplastic starch. Water hyacinth was obtained from a local river in Thailand. Sodium hydroxide (RCL Labscan) and Sodium chlorite (Ajex Finechem) were used to treat water hyacinth.

2.2 Preparation of water hyacinth cellulose

This was done according to the method of Sundari and Ramesh [5] with some alterations. A chopped water hyacinth was churned by a kitchen blender and then dried at 80 ^{o}C for 24 h. The dried sample was dewaxed with 2:1 (v/v) mixture of tolulene/ethanol. The dewaxed fiber was bleached with 3 %wt sodium chlorite solutions at pH 4. The suspension was maintained at 80 ^{o}C for 3 h. and settled over night at room temperature. The bleaching process was repeated again, and the resulting fiber was washed with distilled water until free from acid. The product was subsequently treated by 1 %wt of NaOH solution for removing of hemicelluloses at 60 ^{o}C for 24 h. It was washed with distilled water. Lignin was removed by treatment with 1 %wt sodium chlorite solution at pH 4. The reaction was done at temperature of 75^{o}C for 48 h. Sample was washed with distilled water. Then, the remaining hemicellulose was removed by treating with 5%wt of sodium hydroxide solution at 55 ^{o}C for 24 h. Finally, the obtained fiber was washed with distilled water until neutral.

2.3 Composite preparation

Starch, glycerol (30% by weight of dried starch), and untreated/treated cellulose (3 and 5% in dry basis) were pre-mixed and dried at 80^{o}C for 24 h. The mixtures were mixed using an internal mixer (Brabender, 50ETH) at160^{o}C, 100 rpm for 12 min. The testing samples were prepared by using a compression molding machine (Labtech) at pressing temperature of 160 ^{o}C. The samples were called

according to the constituents in the composite as quoted in Table 1.

Table 1. Fomula of TPS composites

	Untreated cellulose (%wt)	Treated cellulose (%wt)
TPS	-	-
3%U-TPS	3	
5%U-TPS	5	
3%T-TPS		3
5%T-TPS		5

2.4 Characterization and Testing

A Fourier transform infrared (FT-IR) spectrometer (Bruker Optik GmbH, Vertex70) was used to examine the functional group of untreated and treated water hyacinth. The dried sample of untreated or treated water hyacinth was grounded and mixed with potassium bromide powder. Subsequently, the mixed powder was compressed into a thin pellet. The FT-IR spectrum was recorded in an absorption mode with a resolution of 4 cm^{-1} in the wave number range of 4000-400 cm^{-1}. The morphologies of water hyacinth and the fracture surface of composite were studied by using scanning electron microscope (Camscan, MX-2000). Sample surfaces were coated with a thin layer of gold.

Tensile properties of the composites were tested according to ASTM D638 by using a universal testing instrument (Instron, 5969) with a crosshead speed of 1 mm/min. A dimension of specimen was based on type V of ASTM D638. The testing conditions were 23±2 ^{o}C and 50±5%RH. Impact tests were done according to ASTM D256 and carried out using an impact tester (Zwick, B5102.202).

One-way analysis of variance (ANOVA) followed by Scheffe comparison tests with a 0.05 significance level was used to analyze the results from mechanical testing.

3. Results and Discussion

3.1 Water hyacinth cellulose

The FT-IR spectra of untreated and treated cellulose were shown in Figure 1. The peaks at wave number around 3400 and 2900 cm^{-1} are due to –OH stretching and –CH stretching of methyl and methylene groups in cellulose, hemicelluloses and lignin.[6] The peak at 1735 cm^{-1} assigned to acetyl and uronic ester linkage of carboxylic group of the ferulic and p- coumeric acids of lignin and/or hemicelluloses and the peaks at 1521 and 1428 cm^{-1} attributed to C=C stretching of aromatic ring of lignin [7,8] are observed for FT-IR spectrum of untreated sample. However, the decrease of intensities of these peaks in the treated sample spectrum confirms the successfulness of lignin and hemicelluloses removal in the chemical-treated process.

3.2 Morphological investigation

SEM images of untreated and treated water hyacinth are presented in Figure 2.

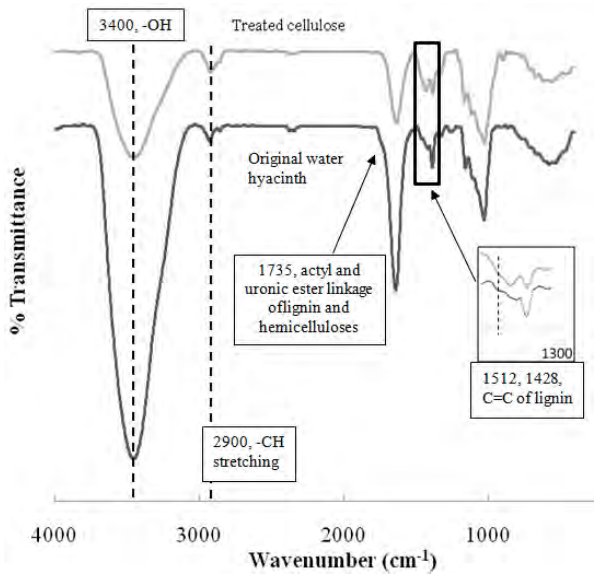

Figure 1. FT-IR spectra of untreated and treated water hyacinth.

Figure 2. SEM images of (a) untreated, and (b) treated water hyacinth.

It can be observed that lignin and hemicellulose are on fiber surface as shown in Figure 2a. After chemical treatment, some cellulose fibrils is found in the SEM image (Figure 2b), which implies the removal of some lignin and hemicellulose.[8,9] The treated fibers also have a relatively rough surface. The rough surface is expected to enhance the adhesion in a cellulose-TPS matrix interface in the production of composites.

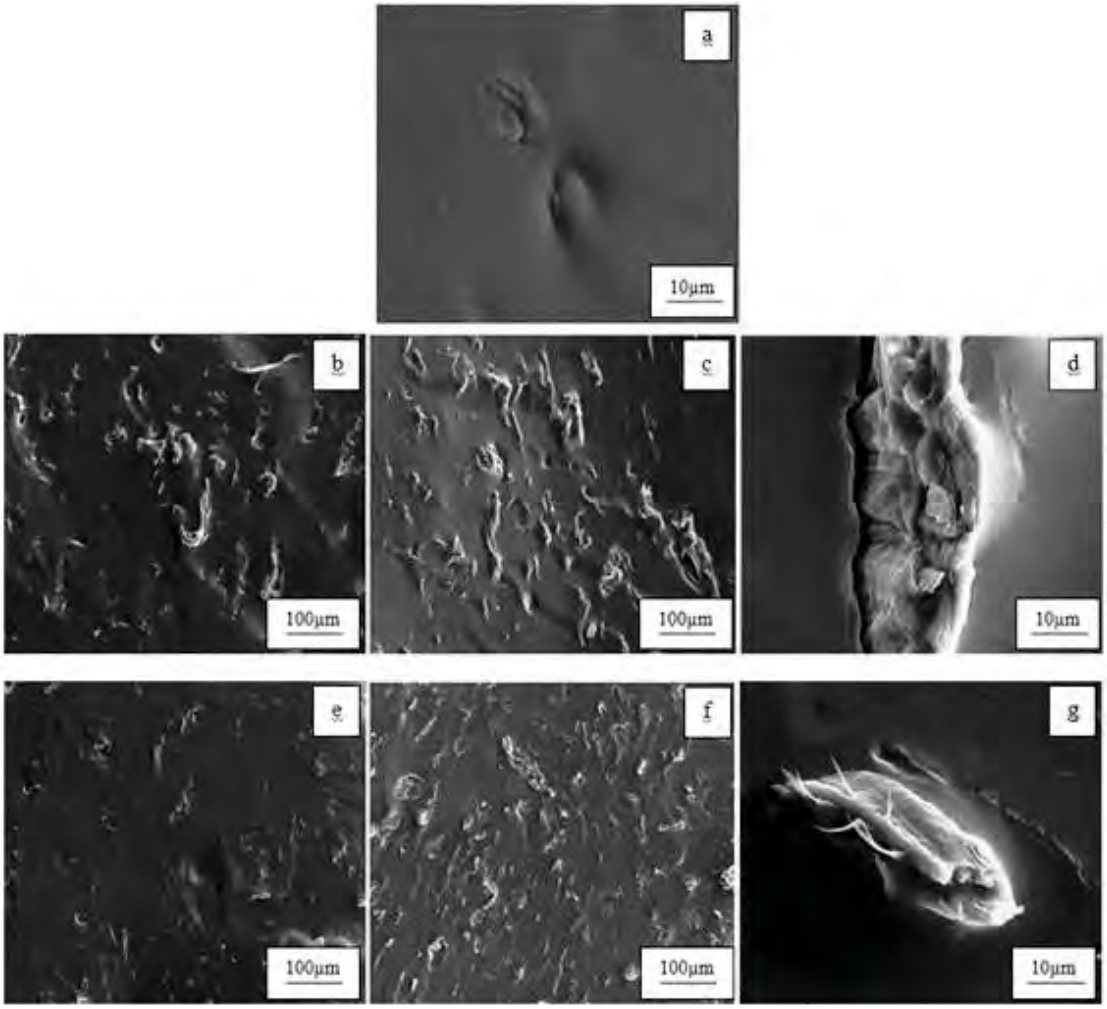

Figure 3. SEM images of (a) TPS, (b) 3%U-TPS, (c) 5%U-TPS, (d) cellulose-TPS interface of 3%U-TPS, (e) 3%T-TPS, (f) 5%T-TPS, and (g) cellulose-TPS interface of 3%T-TPS.

The fracture surfaces of TPS and water hyacinth/TPS composite are shown in Figure 3. A good dispersion of water hyacinth in TPS matrix is observed for all prepared composites. However, the relatively better adhesion between filler and matrix at interface is established for composite prepared by using treated water hyacinth (see Figure 3g and 3d). Cellulose and starch molecule, i.e. amylose and amylopectin, have the identical repeating unit. The lignin and hemicellulose are more hydrophobic than cellulose. Thus, the remaining lignin and hemicelluloses on untreated filler might be the cause of poor adhesion at interfaces.

3.3 Mechanical properties

The results that obtained from the tensile testing were summarized in Figure 4. The results of impact testing are also presented in Figure 5. Although, the mean value of tensile modulus of neat TPS is higher than those of all TPS composites, the effect of water hyacinth content on the tensile modulus is not significant. Moreover, the tensile modulus of all composites is comparable with the unfilled TPS as tested with one-way ANOVA. The mean value of tensile strength increases with increasing filler contents and the composites prepared with treated water hyacinth show the mean values of tensile strength and strain at break better than the composite prepared with untreated water hyacinth. The mean values of impact strengths of all composites are lower than that of unfilled TPS. The average value of impact strength decreases with increasing cellulose content. Cellulose fiber may reduce the molecular mobility of starch molecules, which deteriorates the energy dissipation of the sample. The composites prepared with treated cellulose displayed the average values of impact strength higher than those of the composites prepared with untreated cellulose.

However, the difference among the impact properties and tensile properties of all samples is not significant based on one-way ANOVA analysis. Therefore, the effect of water hyacinth content on the mechanical properties of TPS/water hyacinth biocomposite is not clearly established. This might be a result of a quite low content of filler loading, i.e. 3%wt. and 5%wt., in the present study. Thus, a study on the TPS/water hyacinth composite with higher percent of filler content, i.e. 10 – 40%wt., may be interesting.

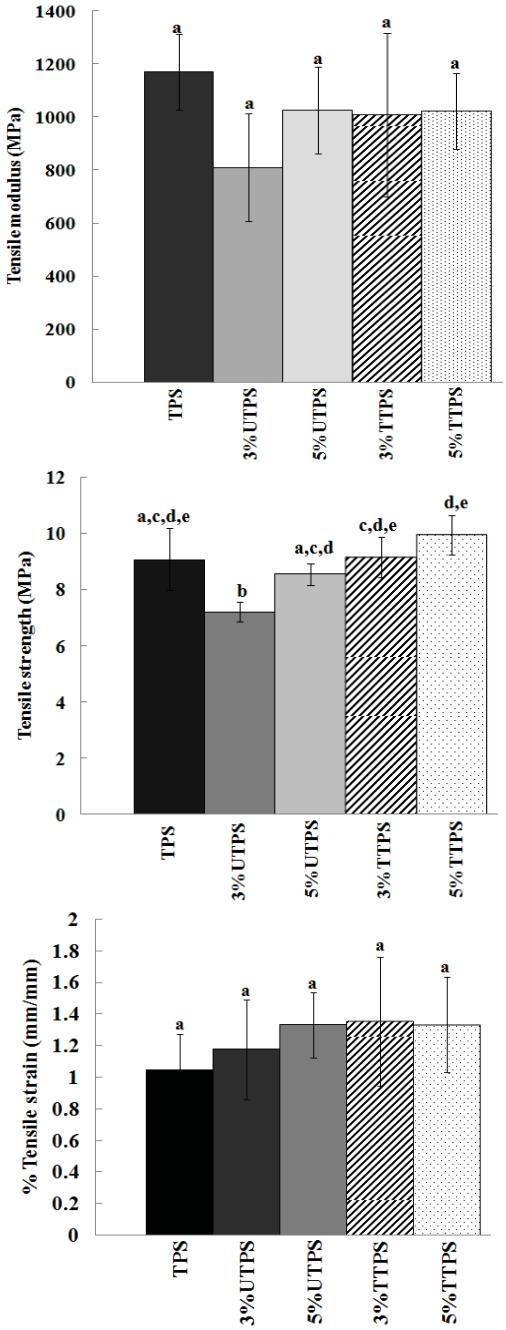

Figure 4. The effect of the water hyacinth contents on the mechanical properties of TPS/water hyacinth composites.

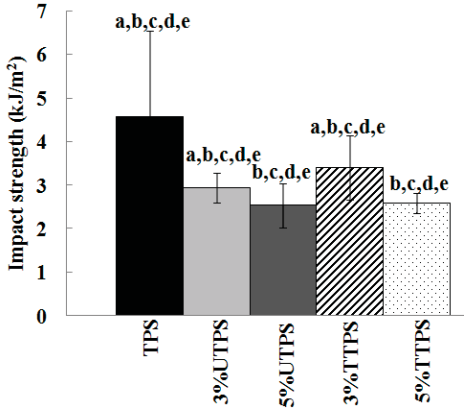

Figure 5. The effect of the fiber contents on the impact strength of studied samples.

4. Conclusions

The water hyacinth-reinforced thermoplastic starch has been prepared in the present study. The water hyacinth was treated with sodium hydroxide and sodium chlorite solutions. From FT-IR and SEM results, the removal of some hemicellulose and lignin on the fiber surface of the treated filler is observed. A good dispersion of water hyacinth into TPS matrix and the good adhesion between treated filler and matrix at interface is found because cellulose and starch molecule have the identical repeating unit. The effect of water hyacinth content on the mechanical properties of TPS/water hyacinth biocomposite is not clearly established based on one-way ANOVA analysis with a 0.05 significance level.

Acknowledgements

The authors would like to thank Department of Materials Science and Engineering, Faculty of Engineering and Industrial Technology, Silpakorn University, Thailand and Center of Excellence on Petrochemical and Materials Technology, Bangkok, Thailand. A support from Siam Modified Starch Co., Ltd. is also acknowledged.

References

[1] N. Soykeabkaew, N. Laosat, A. Ngaokla, N. Yodsuwan and T. Tunkasiri, *Compos. Sci. Technol.* **72** (2012) 845-852.
[2] M. Hietala, A.P. Mathew and K. Oksman, *Eur. Polym. J. In press* (2012).
[3] H.N. Dhakal , Z.Y. Zhang and M.O.W. Richardson, *Compos. Sci. Technol.* **67** (2007) 1674-1683.
[4] A.F. Abdel-Fattah and M.A. Abdel-Naby, *Carbohydr. Polym.* **87**(2012) 2109-2113.
[5] M.T. Sundari and A. Ramesh, *Carbohydr. Polym.* **87** (2012) 1701-1705.
[6] C.U. Maheswari, K.O. Reddy, E. Muzenda, B.R. Guduri and A.V. Rajulu, *Biomass and Bioenergy*. **46** (2012) 555-563.
[7] W. Zhou, D. Zhu, A. Langdon, L. Li, S. Liao and L. Tan, *Bioresource Technol.* **100** (2009) 5366-5369.
[8] W. Chen, H. Yu, Y. Liu, P. Chen, M. Zhang and Y. Hai, *Carbohydr. Polym.* **83** (2011) 1804-1811.
[9] P. Saha, S. Manna, R. Sen, D. Roy and B. Adhikar, *Carbohydr. Polym*. **87** (2012) 1628-1636.

MECHANICAL PROPERTIES OF EPOXIDIZED NATURAL RUBBER/THERMOPLASTIC STARCH BLEND PLASTICIZED WITH N,N-BIS(2-HYDROXYETHYL)ACETAMIDE

Sorraya Preechanon[1 2], Wanchai Lerdwijitjarud[1 2 *], Amnard Sittattrakul[1 2]

[1] Department of Materials Science and Engineering, Faculty of Engineering and Industrial Technology, Silpakorn University, Nakorn Pathom, Thailand
[2] Center of Excellence on Petrochemical and Materials Technology, Bangkok, Thailand

*Author for correspondence; E-mail: wanchail@su.ac.th, Tel. +66 34 219363, Fax. +66 34 219363

Abstract: N,N-bis(2-hydroxyethyl)acetamide (BHA) is a new plasticizer for thermoplastic starch (TPS) that can reduce moisture sensitivity of TPS. However the tensile strain and impact strength of BHA-plasticized TPS are typically lower than those of conventional glycerol-plasticized TPS. In this study, the epoxidized natural rubber (ENR) was used as a toughening filler for TPS. ENR was prepared by in situ epoxidation reaction by using hydrogen peroxide and formic acid as reagents. The percent epoxidation of 14.53% was obtained as determined from ^{1}H-NMR spectrum. Tapioca starch, BHA, and ENR were mixed in an internal mixer. The modulus of BHA-plasticized TPS added with 5%w/w ENR was lower than that of unfilled BHA-plasticized TPS, while the elongation at break and impact strength of TPS added with 5%w/w ENR were significantly higher than those of unfilled TPS. The impact strength of 5%w/w-ENR added TPS was improved about 55%.

1. Introduction

Currently, thermoplastic starch (TPS) is one of the most important bio-based polymers [1]. Plasticizer is an important substance used to produce thermoplastic starch, since it can destroy the strong intermolecular interactions between amylose and/or amylopectin molecules. Type of the plasticizer is one of the key factors, which control the properties of thermoplastic starch. Glycerol is the most common plasticizer for thermoplastic starch nowadays. However, glycerol-plasticized thermoplastic starch shows some disadvantage, such as high moisture sensitivity [2], and retrogradation tendency [3]. To overcome these limitations, many efforts have been done by using other plasticizers, such as sorbitol [4], urea [5], formamide [6], ethanolamine [5], and ethylenebisformamide [7].

N,N-bis(2-hydroxyethyl)acetamide (BHA) is a new plasticizer for TPS that can be synthesized by the reaction between diethanolamine and ethyl acetate. Our previous work [8] reports that the moisture sensitivity of BHA-plasticized TPS is lower than that of glycerol-plasticized TPS. However the tensile strain and impact strength of BHA-plasticized TPS are typically lower than those of conventional glycerol-plasticized TPS.

Natural rubber is one of the bio-based materials that can be used as an impact modifier for polymer. Epoxidized natural rubber (ENR) can be synthesized by in situ epoxidation reaction of natural rubber by using hydrogen peroxide and organic acid as reagents [9]. ENR has the higher polarity comparing with natural rubber, which is theoretically more compatible with starch molecules.

To enhance the flexibility of BHA-plasticized TPS, epoxidized natural rubber (ENR) has been used as a filler in the present study. The mechanical properties and the water adsorption behaviour of the ENR-filled TPS plasticized with BHA are investigated.

2. Materials and Methods

2.1 Materials

Tapioca starch was obtained from Siam modified starch (Thailand). The natural rubber latex (60% DRC), formic acid (90%, Merk), and hydrogen peroxide (Ajex Finechem) were used to prepare ENR. The reagent grade of Diethanolamine (Sigma-Aldrich) and ethyl acetate (Merk) were used to prepare N,N-bis(2-hydroxyethyl)acetamide.

2.2 Preparation of BHA

Diethanolamine (1 mol) was introduced into a flask and then ethyl acetate (1 mol) was added. The reaction mixture was stirred at 70^{o}C for 12 hr. and then the by product, ethanol, was evaporated under reduced pressure. For increasing the product yield, the residue was cooled, followed by addition of 0.05 mol ethyl acetate and stirred at 70^{o}C for 4 hr. Subsequently, the by product was removed. The yield of BHA was about 91%. The synthesized product was characterized by ^{1}H-NMR and FT-IR.

2.3 Preparation of ENR

ENR was prepared by in situ epoxidation reaction. The 60%DRC NR latex was diluted with distilled water to obtain 30 %DRC. In order to stabilize the NR latex, Igepal CO-890 as a non-ionic surfactant was added. Formic acid (0.09 mole/mole of isoprene unit) and hydrogen peroxide (0.9 mole/mole of isoprene unit) were slow droped while the mixture was heated to 60^{o}C for 12 hr. To

terminate the epoxidation reaction, the mixture was cool down to room temperature. Subsequently, the reaction mixture was added into an excess of methanol to precipitate the ENR product. The ENR was washed with water several times and dried in vacuum oven at 60°C for 12 hr. The dried ENR was characterized by ^{1}H-NMR and FT-IR.

2.4 Preparation of TPS specimen

Dried starch was premixed with BHA and ENR. The mixture was leaved at room temperature for at least 24 hr. The weight percent of plasticizer to dried starch was 30%. Then, the premixed powder was melt blended in an internal mixer (Barbender, W50EHT) at 160 °C and 100 rpm. for 15 min. The product was compressed at 170 °C to form the testing specimens.

2.5 Characterization and Testing

The chemical structures of the synthesizing BHA, and ENR were verified by a Fourier-transform infrared spectrometer, FT-IR (Bruker Optik GmbH, Vertex70) and a proton nuclear magnetic resonance spectrometer, ^{1}H-NMR (Bruker, 300 Ultrasheild). To obtain the NMR spectra, D_2O and $CDCl_3$ were used as solvents for BHA and ENR, respectively.

Tensile tests were measured according to ASTM D 638-03 and carried out using a universal testing instrument (Instron, 5969) with a strain rate of 1 mm/min. Impact tests were measured according to ASTM D256 and carried out using an impact testing machine (Zwick, B5102.202) in izod mode.

In order to determine the water vapor adsorption, the specimens were placed in a container at room temperature with a 53%RH atmosphere in equilibrium with a saturated solution of $Mg(NO_3)_2.6H_2O$ for 15 days. The moisture content (W) of the specimen was calculated as follows:

$$\text{Moisture content (W)} = [(Wt-Wo)/Wo]\times 100 \qquad (1)$$

where, Wt is the weight of specimen at specified time and Wo is the weight of the dried specimen.

3. Results and Discussion

3.1 Characterization of BHA

BHA was synthesized by using diethanolamine and ethylacetate as reagents. Chemical reaction was shown in Figure 1.

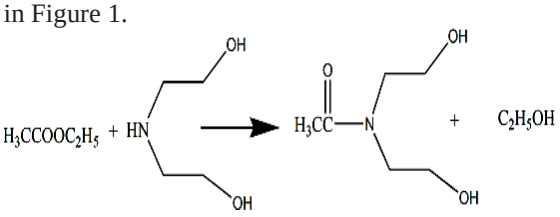

Figure 1. Chemical reaction of synthesizing BHA. [8]

The IR spectra of ethyl acetate, diethanolamine, and BHA are shown in Figure 2. FTIR results imply that BHA was successfully prepared as confirmed by a peak at 1620 cm^{-1} ascribed to the 0=C of the amide group. The characteristic peak of reagents at 3307 cm^{-1} and 1749 cm^{-1} that are attributed to N-H stretching and C=O stretching of ester group, respectively also disappear in the synthesizing BHA spectrum.

The successful reaction is also supported by ^{1}H-NMR technique. The NMR spectrum of BHA is shown in Figure 3. The characteristic peak of the CH_3 group is 2.6 ppm. The proton signal of the OH group is 2.1 ppm and the methylene proton signals are in the range of 3.4-3.7 ppm.

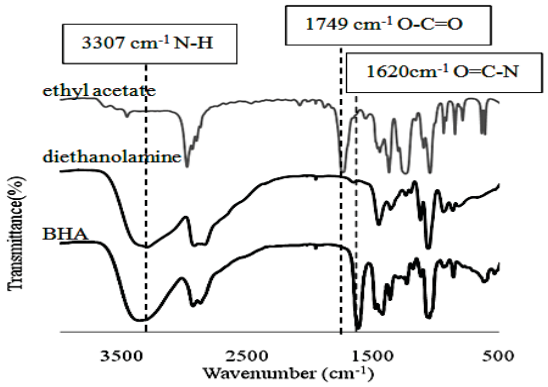

Figure 2. The FT-IR spectrum of ethyl acetate, diethanolamine, and BHA.

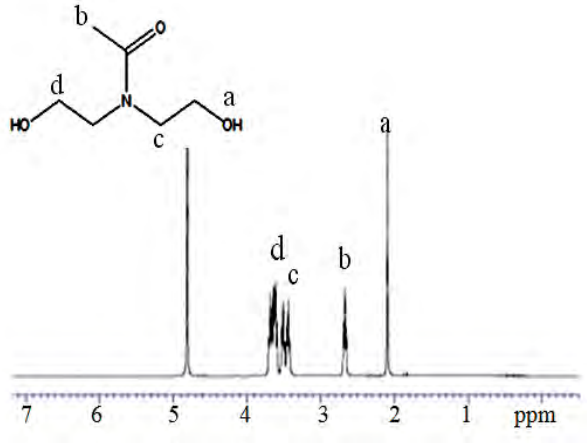

Figure 3. The ^{1}H-NMR spectrum of BHA.

3.2 Characterization of ENR

The IR spectra of NR and ENR are shown in Figure 4. The characteristic peak of the asymmetric epoxide ring stretching that confirms the successful epoxidation reaction is 869 cm^{-1}[9]. In addition, the decrease in peak intensity at 3036 cm^{-1} and 836 cm^{-1} that were attributed to C=CH stretching and C=CH- bending, respectively is also observed.

The ^{1}H-NMR spectrum of ENR is presented in Figure 5. The ENR structure is confirmed by the new proton signals of the CH_3 group and CH group at 1.2 ppm. and 2.7 ppm, respectively[10]. The percent epoxidation of ENR is 14.53% was obtained as

determined from ^{1}H-NMR spectrum using equation (2) [9]:

$$\%\text{Epoxidation content} = \frac{A_{2.7}}{A_{5.1}+A_{2.7}} \times 100 \quad (2)$$

where, $A_{2.7}$ is peak integral at 2.7 ppm representing CH group of epoxide ring and $A_{5.1}$ is peak integral at 5.1 ppm representing CH group of unreacted isoprene unit.

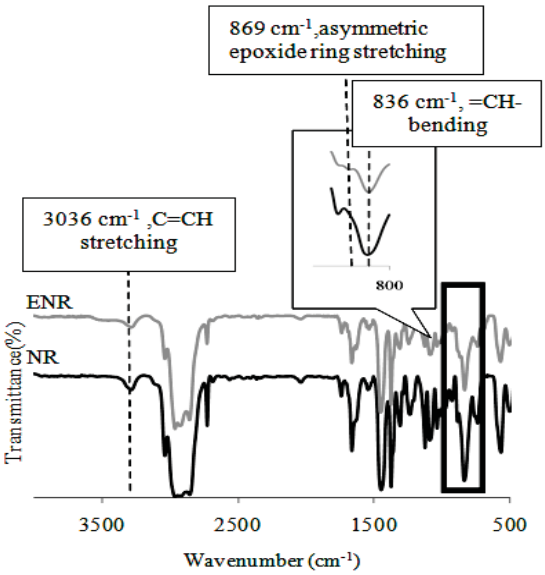

Figure 4. The FT-IR spectrum of NR and ENR.

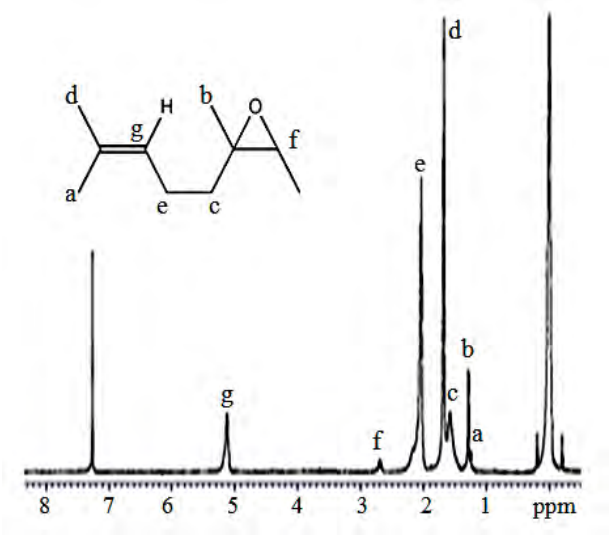

Figure 5. The ^{1}H-NMR spectrum of ENR.

3.3 Mechanical properties

The tensile modulus, tensile strength, % tensile strain at break and impact strength of the TPS and the ENR-filled TPS are shown in Figures 6 and 7. The addition of small amounts of ENR to TPS induces their softening as shown by the corresponding decrease in modulus. The tensile strength and % tensile strain at break of the blends tend to increase with increasing ENR content. The impact strength of ENR added TPS is also higher than that of unfilled TPS. This phenomenon may due to the possibility of energy dissipation within the ENR elastomeric domain. The impact strength of 5%ENR-filled TPS is greater than that of unfilled TPS about 55%.

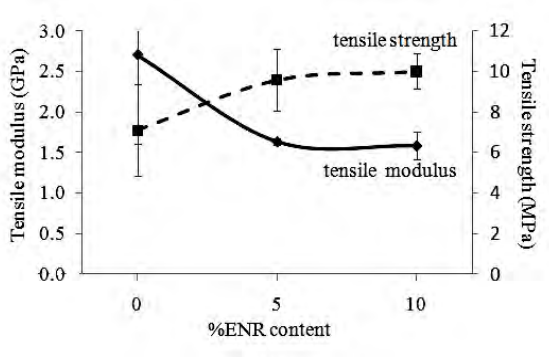

Figure 6. The tensile modulus and tensile strength of the TPS and the blends of TPS with ENR

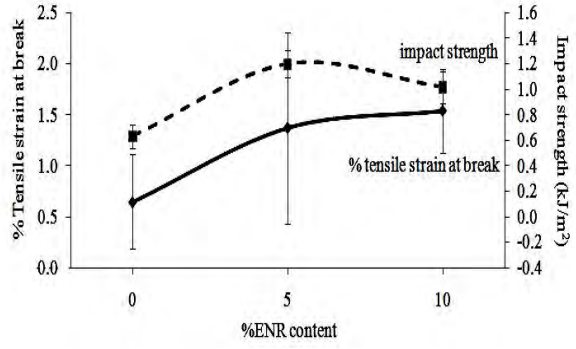

Figure 7. The % tensile strain at break and impact strength of the TPS and the blends of TPS with ENR.

3.5 Moisture adsorption

The percent moisture adsorptions at 53%RH of the TPS and blends of TPS with ENR are tabulated in Table 1. After 15 days of storage, the moisture adsorptions of the blend were similar to those of unfilled TPS. These results indicate that the addition of small amounts of ENR to the TPS does not significantly affect the moisture adsorption.

Table 1: Percent moisture adsorption at 53%RH of the TPS and blends of TPS with ENR after 15 days of storage.

Sample	% Moisture adsorption
TPS	6.20 ± 0.08
5%ENR-TPS	7.06 ± 0.10
10%ENR-TPS	6.44 ± 0.02

4. Conclusions

Blends of BHA-plasticized TPS and ENR were successful prepared in an internal mixer. The modulus of the ENR-filled TPS is lower than that of unfilled TPS, while the % tensile strain at break and impact strength of TPS added with ENR are significantly higher than those of unfilled. The impact strength of 5%ENR-filled TPS is improved about 55%. Therefore, the toughness of BHA-plasticized TPS can be improved by blending with ENR. The addition of small amounts of ENR to the starch blends does not significantly affect the moisture adsorption.

Acknowledgements

The authors would like to acknowledge the support from Department of Materials Science and Engineering, Faculty of Engineering and Industrial Technology, Silpakorn University. The authors would like to thank Center of Excellence on Petrochemical and Materials Technology, Chulalongkorn University.The supports from Siam Modified Starch Co., Ltd. is also acknowledged.

References

[1] X. Tang and S. Alavi, *Carbohydr. Polym*. **85** (2011) 7-16.
[2] R.L. Shogren, G.F. Fanta and W.M. Doane, *Starch/ Starke*. **45** (1993) 276-280.
[3] X.F. MA, J.G. YU and J. FENG, *Chin. Chem. Lett*. **15** (2004) 741-744.
[4] S. Mali, *Carbohydr. Polym*. **60** (2005) 283-289.
[5] X.F. Ma, J.G. Yu and J.J. Wan, *Carbohydr. Polym*. **64** (2006) 267-273.
[6] H. Dai, P. Chang, J. Yu and X. Ma, *Starch - Stärke*. **60** (2008) 676-684.
[7] J.-H. Yang, J.-G. Yu and X.-F. Ma, *Carbohydr. Polym*. **63** (2006) 218-223.
[8] P. Baitahe, W. Lerdwijitjarud and A. Sittattrakul, *N,N-bis(2-hydroxyethyl)acetamide as a plasticiizer for thermoplastic tapioca starch.* Pure and Applied Chemistry International Conf. Proc., Chiang mai, Thailand, (2012), pp. 154-157.
[9] R. Yoksan, *Kasetsart Journal.* **42** (2008) 325-332.
[10] C.S.L. Baker, I.R. Gelling and R. Newell, *Rubber Chem. Technol.* **58** (1985) 67-85.

CYCLODEXTRIN APPLICATION IN ROSELLE EXTRACT STABILIZATION

Charinda Deenumchut[1]*, Pattara Sawasdee[2] and Supason Wanichwecharungruang[2]

[1] Program of Petrochemistry and Polymer Science, Faculty of Science, Chulalongkorn University, Bangkok 10330, Thailand
[2] Department of Chemistry, Faculty of Science, Chulalongkorn University

* Author for correspondence; E-Mail: charinda.deenumchut@clariant.com, Tel. +66 8 11613292, Fax. +66 2 3128901

Abstract: The color stability of roselle extract was improved through the one step semi-purification process coupled with cyclodextrin (CD) complexation. Complexation of β-CD with the two major anthocyanins in the semi-purified roselle extract, delphinidin-3-sambubioside and cyanidin-3-sambubioside, were verified through NMR spectroscopy. Semi-purification process significantly reduced the amount of β-CD required for the optimal color stabilization, comparing to the optimal amount required in the crude extract. In addition, uncomplexed semi-purified extract also showed improved stability on its own when compared with the crude extract.

1. Introduction

Cyclodextrins (CDs) are cyclic oligomers of glucose and are synthesized from starch. It contains D-glucopyranoside building blocks linked together with α-1,4- and α-1,6-glycosidic bonds [1]. The most common natural CDs consist of six, seven and eight glucopyranose units which are α-CD, β-CD and γ-CD respectively [2]. The molecules of CDs shape like conical cylinder or cones with secondary hydroxyl groups extending from the wider edge and the primary groups from the narrow edge [3]. This makes CDs molecule hydrophilic at outer surface and hydrophobic inside, thus allowing other non-polar molecules to insert into its central cavity [4]. CDs can absorb various molecules (guests) and formed into inclusion complexes. This makes change to the chemical and physical properties such as dissolution, evaporation and chemically stability of the guest molecules. The binding of CD with the guest molecules usually takes place through space without a covalent bond [5]. CD complexation can be applied to many industries such as food, cosmetics, pharmaceutical, chemical analysis and medicine [6].

Roselle (*Hibiscus sabdariffa* L.) is a tropical annual shrub with red edible calyces. Because of its unique brilliant red color and good flavor, its calyces are commonly used to make jam and fruit juices in Thailand [7]. Roselle is a good source of anthocyanins and its two main anthocyanins are delphinidin-3-sambubioside and cyanidin-3-sambubioside [8]. Anthocyanins are a group of plant pigments that are widely distributed in nature [9], responsible for the attractive colors of many fruits, grains and flowers [10,11]. Anthocyanins are water-soluble glycosides and acylglycosides of anthocyanidins [12], and they are found in the form of polyhydroxylated and or methoxylated heterosides which derive from the flavylium ion or 2-phenylbenzopyrilium in nature [13-16]. Anthocyanins are valuable as important quality indicators in foods and chemotaxonomic indicators in plants. They show good antioxidant ability [11, 17]. Nevertheless, anthocyanins possess problems on low stability, thus they are easily decomposed during production process and storage. This can be witnessed through the color change from red to brown or colorless [18]. The color stability of anthocyanins depends on a combination of various factors including: structure of anthocyanin, pH, temperature, oxygen, light and water activity [19]. Several papers have been published on the complexation of roselle with different materials such as moltodextrin, trehalose, gum arabic, starch and cyclodextrins [20-22] for improved the color stability of roselle anthocyanins.

The aim of the present study was to improve the stability of roselle extract using either semi-purification process or complexation with β-CD of both.

2. Materials and Methods

2.1 Materials and chemicals

Crude roselle extract (CRE) with the moisture content of 4-5 %, was obtained from Tipco foods (Thailand) Public Co., Ltd. (Prachuap Khiri Khan, Thailand). Its color was brilliant red.

β-CD was purchased from Thai Isekyi Co., Ltd. (Bangkok, Thailand). Delphinidin-3-sambubioside and cyanidin-3-sambubioside were purchased from Tokiwa Phytochemical Co., Ltd. (Chiba, Japan).

2.2 Semi-Purification of CRE by column chromatography

Stationary phase (600 g, SP), Diaion HP-20 resin (Mitsubishi Chemical), was dispersed in ethanol by gently stirring for a few minutes, and let standing for 15 min. Then methanol was removed and water was added. After stirring and let stand for 5-10 min, this suspension was poured into the column (10 cm diameter and 50 cm length). The CRE (20.0 g) was dissolved in water, the undissolved residual was filtered out (Whatman No.1 filter paper), successively. The CRE solution was loaded on the column and eluted with water (4,500 ml), ethanol (3,000 mL) and acetone (1,000 ml), successively. The three fractions, water fraction, ethanol fraction or semi-purified roselle extract fraction (2.05 g, SPRE) and acetone fraction,

were collected and presence of anthocyanins were identified using visual observation, ^{1}H-NMR spectroscopy (400 MHz Varian mercury spectrometer, Variance Inc., USA) and UV/Vis absorption spectrometry (Shimadzu, Japan).

2.3 Total anthocyanin

The total anthocyanin content of CRE and SPRE were determined using the pH-differential method described by Qinxue Ni, et al. [23], using two buffer systems: potassium chloride buffer, pH 1.0 (0.025 M), and sodium acetate buffer, pH 4.5 (0.4 M), and the UV/VIS spectrophotometer at 510 and 700 nm. The percent weight by weight (%w/w) of total anthocyanin in the sample was calculated using the following equation:

$$\%w/w = \frac{A}{\varepsilon L} \times MW \times DF \times \frac{V}{Wt} \times 100\%$$

Where: *A* is the absorbance; ε is the extinction coefficient (26,900 for cyaniding-3-glucoside, cy-3-glc); MW is the molecular weight (449.2 g/mol for cy-3-glc); DF is the dilution factor (1 ml sample was diluted to 20 ml, DF = 20); V is the final volume (40 ml); Wt is the sample weight (0.002 g); L is the cell path length (1 cm). For comparison, the same extinction coefficient was used for other standards to calculate the concentration of each anthocyanin and thus reported results was expressed as Cy-3-glc equivalents.

2.4 Ratio of inclusion complex

Inclusion complex prepared at the ratios of extract to β-CD of 1:0 to 1:10 (by mol) were divided into two parts, one was kept indoor at 50^{o}C, the other was put outdoor under sunlight. Aliquots were taken every 20 min and subjected to UV/Vis spectrophotometry analysis at 520 nm. The experiments were carried out in triplicate.

2.5 The color stability of roselle extract

CRE, SPRE and SPRE-β-CD complex were dissolved in deionize water and adjusted the pH to 3.5 with sodium acetate buffer, pH 3.5. Color stability was determined using UV/Vis spectrophotometry. Degradation of roselle anthocyanins in CRE, SPRE and SPRE-β-CD complex were quantitatively monitored through the decrease of absorbance at 520 nm after being exposed to sunlight for 5 h. The experiments were carried out in triplicate.

3. Results and Discussion

3.1 Semi-purification of CRE by column chromatography

CRE was partitioned on Diaion HP-20 using water, ethanol and acetone as mobile phase. The ethanol fraction was accounted for 10.05 ± 0.8 % of the CRE. This fraction contained the highest amount of anthocyanins comparing to other fractions as analyzed by ^{1}H-NMR and UV/VIS spectrophotometry. Significant reduction of sugar could be achieved as confirmed by smaller resonance signals at the chemical shifts of 3-4 ppm in the ^{1}H-NMR (Figure 1B), comparing to that of the CRE (Figure 1A). Sugar was retained in water eluted fraction (Figure 1C). The UV/VIS absorption profile of SPRE comparing to that of CRE (Figure 2) indicated that through this sugar removal by chromatography, the major anthocyanins and phenolics compounds with absorbance at 490-550 nm and 260-320 nm, were retained in the ethanol fraction.

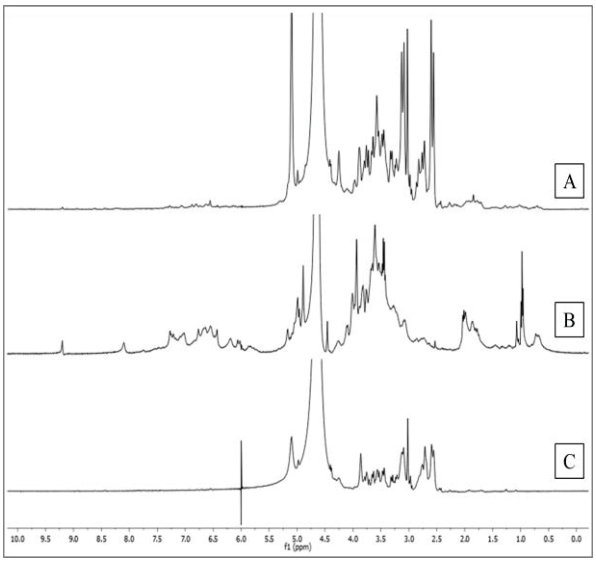

Figure 1. ^{1}H-NMR spectra of CRE (A), SPRE (B) and roselle water fraction (C).

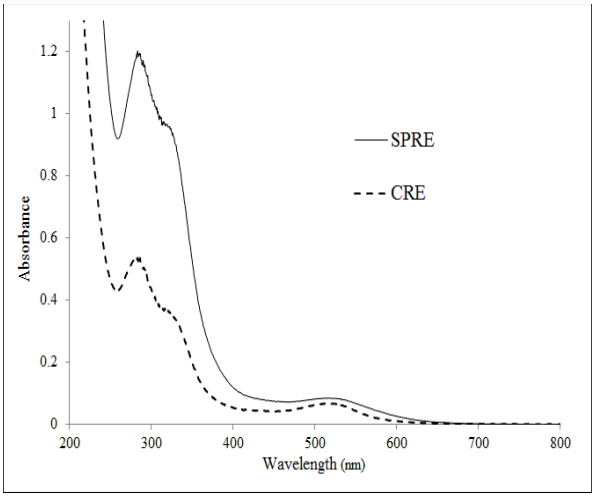

Figure 2. UV/VIS absorption profile of CRE and SPRE.

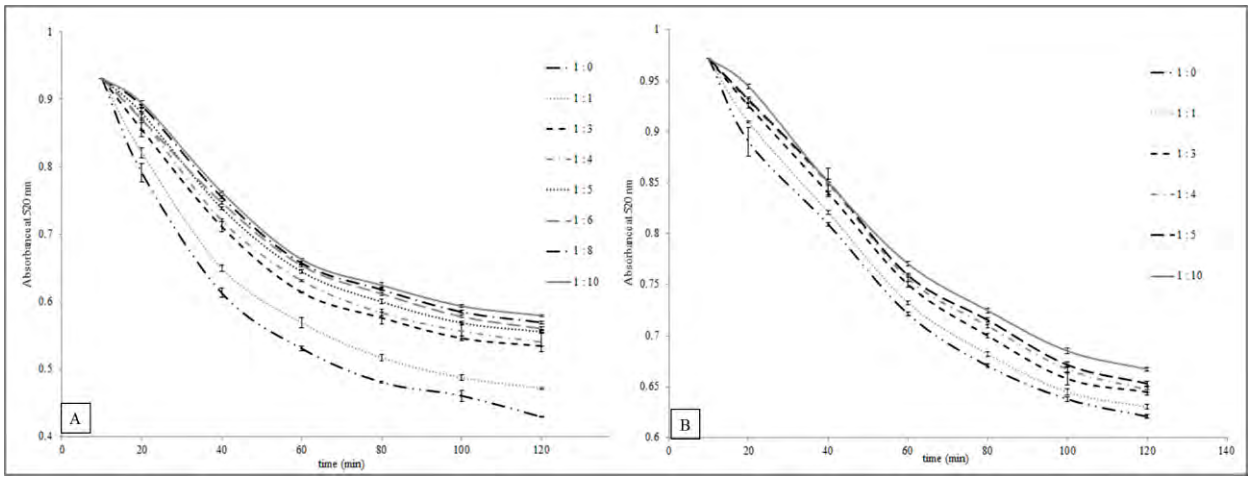

Figure 3. Stability (depicted as absorption at 520 nm) of CRE-β-CD (A) and SPRE-β-CD (B) in aqueous environment when kept indoor at 50°C, for varrious ratios of extract to β-CD.

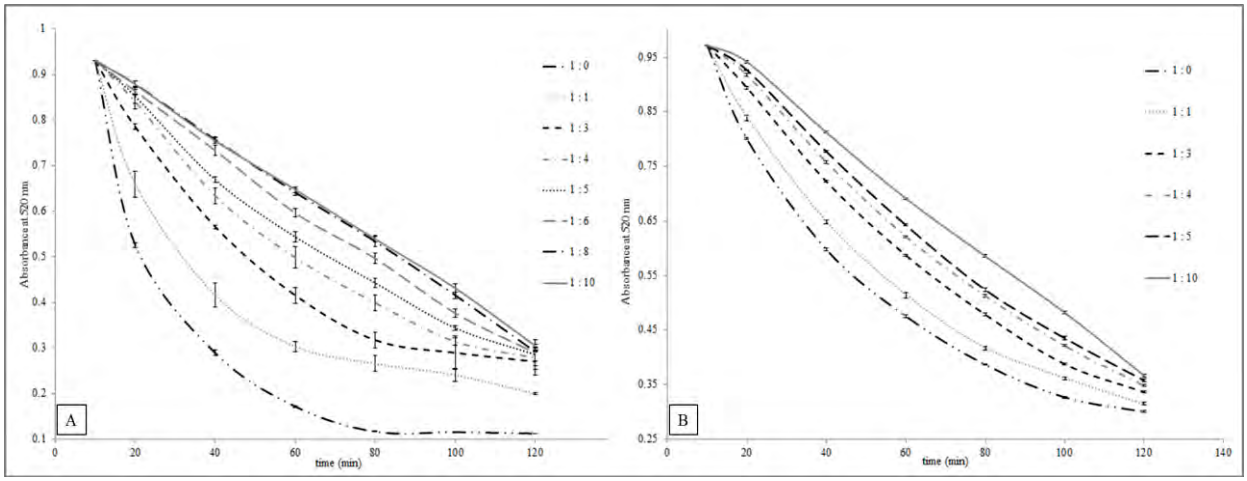

Figure 4. Stability (depicted as absorption at 520 nm) of CRE-β-CD (A) and SPRE-β-CD (B) in aqueous environment when put outdoor under sunlight, for varrious ratios of extract to β-CD.

3.2 Total anthocyanin

Amounts of anthocyanins in CRE and SPRE were 0.88 ± 0.5 and 9.50 ± 0.3 %w/w, respectively, as determined using the pH-differential method. This indicated that more than ten-fold increase in anthocyanin enrichment.

3.3 Ratio of inclusion complex

Optimal ratio between β-CD and roselle extract was determined from color stability of the mixture. Ratios of CRE and SPRE to β-CD (1:0 to 1:10 (by mol)) were investigated and the result indicated that the best ratio of CRE to β-CD was 1:6 (by mol) (Figure 3A and Figure 4A) while the best ratio of SPRE was 1:4 (by mol) (Figure 3B and Figure 4B). This implied less impurity from compounds that could form inclusion complexation with β-CD in SPRE, comparing to the CRE.

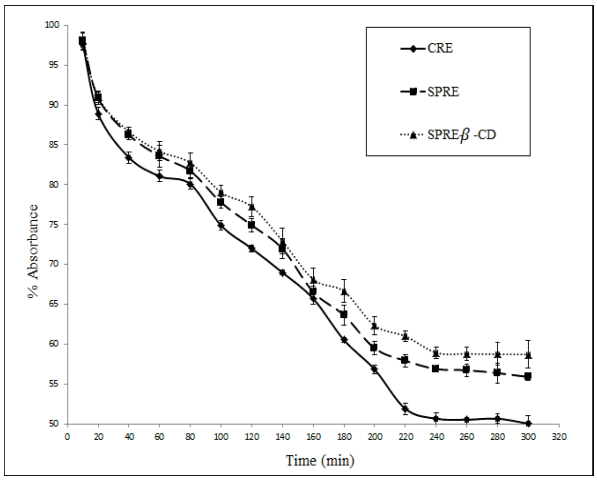

Figure 5. Stability profile of CRE, SPRE and SPRE-β-CD complex after put outdoor under sunlight for 5 h.

3.4 The color stability of roselle extract

Color stability of CRE, SPRE and SPRE-β-CD complex, were monitored under 5 h sunlight exposure (Figure 5). The decrease in absorption at 520 nm (absorption band of anthocyanins) in the UV/VIS absorption spectra of the extract directly corresponded to the degradation of the anthocyanins and therefore was used to monitor the degradation. The results indicated that the SPRE was significantly more stable than CRE. This indicated that removing of sugar could improve the stability of anthocyanins in roselle extract. Upon inclusion complexation with β-CD, the SPRE stability was further improved.

4. Conclusions

In this work, color stabilization of CRE was carried out by combining two strategies, semi-purification impurities and β-CD inclusion complexation. Ridding off some impurities from the CRE using simple column chromatography could sinificantly improve the color stability. Although β-CD can also help improve color stability of CRE, the amount of β-CD required was higher than that required for SPRE. Here we also proved inclusion complexation between the two main anthocyanins, delphinidin-3-sambubioside and cyanidin-3-sambubioside in the extract, and the β-CD.

Acknowledgements

Program in Petrochemistry and Polymer Science, Department of Chemistry, Faculty of Science, Chulalongkorn University.

References

[1] Mark E.Davis, and Marcus E. Brewster, *Nat Rev Drug Discov*. **3 (**2004) 1023-1035.

[2] A. Magnúsdóttir, M. Másson and T. Loftsson, *J. Incl. Phenom. Macroc. Chem.* **44 (**2002) 213-218.

[3] Frömming KH and Szejtli J, *Cyclodextrins in pharmacy*, Kluwer Academic Publishers, Dordrecht (1994).

[4] Arun Rasheed, Ashok Kumar C.K and Sravanthi V. V. N. S. S, *Sci Pharm*. **76** (2008) 567–598.

[5] József Szejtli, *Pure Appl. Chem.* **76** (2004) 1825–1845.

[6] E.M. Martin Del Valle. *Pro. Bio.* **39** (2004) 1033–1046.

[7] Duangmal K., Saicheua B. and Sueeprasan, S., *LWT - Food Sci.Tec.* **41** (2008) 1437–1445.

[8] Du, C.T. and francis F.S., *J. food. Sci.* **38** (1973) 810-812.

[9] Wu, X. L. and Prior, R. L., *J. Agric. Food Chem.* **53** (2005) 3101–3113.

[10] Escribano-Bailón, M. T., Santos-Buelga, C., and Rivas-Gonzalo, J.C., *J. Chrom. A*. **1054** (2004) 129–141.

[11] Kong, J. M., Chia, L. S., Goh, N. K., Chia, T. F. and Brouillard, R., *Phytochemistry.* **64**

[12] Wu, X. L., Gu, L. W., Prior, P. L. and McKay, S., *J. Agric. Food Chem.* **52** (2004) 7846–7856.

[13] De Pascual-Teresa, S., Santos-Buelga, C. and Rivas-Gonzalo, J. C., *J. Sci. Food Agric.* **82** (2002) 1003–1006.

[14] Di Paola-Naranjo, R. D., Sanchez-Sanchez, J., Gonzalez-Paramas, A. M. and Rivas-Gonzalo, J. C., *J. Chrom. A.* **1054** (2004) 205–210.

[15] Lohachoompol, V., Mulholland, M., Srzednicki, G. and Craske, J., *Food Chem.* **111** (2008) 249–254.

[16] Escribano-Bailón, M. T., Santos-Buelga, C. and Rivas-Gonzalo, J. C., *J. Chrom. A.* **1054** (2004) 129–141.

[17] Marco, P. H. and Scarminio, I. S., *Anal. Chim. Acta.* **583** (2007) 138–146.

[18] Jackman R.L., Yada R.Y., Tung M. A. and Speers R.A., *J. Food Biochem.* **11** (1987) 201-247.

[19] Markakis P., *Anthocyanins as food colours.* Academic Press, Newyork, (1982), pp.163-179.

[20] Duangmal K., Saicheua B. and Sueeprasan, S., *Proceedings of the AIC Color and Paints, Interim Meeting of the International Color Association.* **IEEE Xplore** (2004) 55-158.

[21] Zuhaili Idham, Ida Idayu Muhamad, Siti Hamidah Mohd Setapar and Mohd Roji Sarmidi, *J. Food Proc. Pre.* **36** (2012) 176–184.

[22] Ioannis Mourtzinos, Dimitris P. Makris, Konstantina Yannakopoulou,Nick Kalogeropoulos, Iliana Michali, and Vaios T. Karathanos, *J. Agric. Food Chem.* **56 (**2008) 10303–10310.

[23] Qinxue Ni, Guangzhi Xu, Guoquan Lu, Qianxin Gao, Cunshan Zhou and Youzuo Zhang, *Afri. J. of Bio. Technol*. **11**(2012) 3379-3387.

IMPROVED THE ETHYLENE TRANSMISSION RATE OF LLDPE/SEBS BLEND FILM

Rujirek Wiwattananukul[1]*, Tawan Sooknoi, Suparat Rukchonlatee and Chonlada Ritvirulh

[1] Department of Chemistry, Faculty of Science, King Mongkut's Institute of Technology Ladkrabang, Bangkok 10520, Thailand

* Author for correspondence; E-Mail: ji_rujirek@hotmail.com, Tel. +66 72832094

ABTRACT: In this study linear low density polyethylene (LLDPE)/styrene ethylene-butylene styrene copolymer (SEBS) blend films were prepared for the packaging films with improved ethylene transmission rate. An internal mixer was employed to prepare the LLDPE/SEBS blends at 100/0, 90/10, 80/20, 70/30, 65/35 ratios. In some samples, dioctyl phthalate (DOP) plasticizer (5-10%wt) was added into the blend. Thereafter, the film samples were prepared using compression molding. The ethylene transmission rate of the films was investigated together with morphological, thermal and mechanical properties. From the morphological study, SEBS was well-dispersed in LLDPE phase. It can also be seen that increasing SEBS content generally increased size of the dispersed sphere and so ethylene transmission rate of the films. This is because ethylene-butylene segment in SEBS is relatively non-polar and possesses high free volume. Therefore, the ethylene gas can readily permeate through the dispersed SEBS in the film. However, Young's modulus, elongation at break and stress at yield of the films were decreased with increasing SEBS content. Nevertheless, ultimate tensile strength of the film was increased. Addition of plasticizer (5-10%wt) makes the materials become more flexible as free volume of the blends is increased. Therefore, the dispersed phase size was increased with incorporation of the plasticizer, resulting in an enhancement of the ethylene transmission rate. Although the presence of the plasticizer decreased tensile properties of films, the values are still in acceptable ranges for the addition of 5%wt DOP.

1. Introduction

Preserving freshness and quality of fresh produces can be efficiently carried out via proper postharvest management [1]. This is because the ethylene gas from the plant metabolism can cause the produces ripeness and deterioration after harvest [2-3]. Several methods such as perforation of packaging film and addition of ethylene absorbent (zeolite) can be used to promptly eliminate ethylene gas from the fresh produces package [4]. In the previous work [5], it was found that the zeolite-styrene ethylene-butylene styrene (SEBS) composite/perforated polyolefins (LDPE and OPP) double-layered films showed high ethylene transmission rate. However, the films exhibit low ultimate tensile strength and can be easily torn. Moreover, the double-layered films cannot be readily fabricated. Alternatively, polymer blend is an efficient choice of materials with tailored properties, that helps to extend the shelf-life of fresh produces. In this work, linear low density polyethylene (LLDPE) was chosen due to its good mechanical properties, high flexibility and generally cost effective. However, LLDPE exhibits low ethylene transmission rate (ETR) [6]. Hence, styrene ethylene-butylene styrene (SEBS) was selected to be blended with LLDPE. This is because SEBS is non-polar polymer, high flexible and possesses relatively higher free volume as compared with LLDPE.

2. Materials and Methods

2.1 Materials

Two polymers used in this study were linear low density polyethylene (PE 1220G1, MFI of 2.0 g/10 min from Dow Chemical Thailand Co. Ltd,) and styrene ethylene-butylene styrene block copolymer (Kraton G1652 containing 30wt% styrene, MFI of 5.0 g/10 min from Kraton polymer Co. Ltd,). Dioctyl phthalate (DOP) from South City Petrochem Co., Ltd. was used as a plasticizer.

2.2 Film preparation

The LLDPE/SEBS blend ratios and the loading of plasticizer in the film are shown in Table 1. All compounds were mixed using an internal mixer at 190°C and a rotor speed of 60 rpm for 10 min. The films were then prepared by compression molding technique.

Sample	%wt LLDPE	%wt SEBS	%wt DOP in SEBS
LL100	100	-	-
LL90S10	90	10	-
LL80S20	80	20	-
LL70S30	70	30	-
LL65S35	65	35	-
LL70S30+5%wt DOP	70	30	5
LL70S30+10%wt DOP	70	30	10

Table 1: The composition of LLDPE/SEBS films

2.3 Film characterization and testing

The film was cryogenic cracked in liquid nitrogen and then was etched in hot xylene (50°C) for 6 hours in order to extract SEBS phase. The etched cross-section was gold coated prior to characterization by Scanning Electron Microscope (SEM).

The crystalline melting temperature (T_m) and degree of crystallinity of the LLDPE in the films were determined by Differential Scanning Calorimeter (DSC). Film samples were scanned from 25 to 160°C with a heating/cooling rate of 10°C/min.

Tensile properties of all films were performed on a Universal Testing Machine with a gauge length of 25 mm and a crosshead speed of 100 mm/min at room temperature, according to ASTM D882.

Ethylene transmission rate (ETR) of the films were measured by a home-made permeation cell equipped with gas chromatograph-flame ionization detector (GC-FID) at 1 atm and room temperature. The feed gas (ethylene) and carrier gas (nitrogen) were controlled by mass flow controllers at a flow rate of 30 ml/min.

3. Results and Discussion

3.1 Morphology

Figure 1 shows the SEM micrographs of the cross-section of films after SEBS extraction. The holes in the micrographs represent the extracted SEBS domains in the film. All the blend films illustrate good dispersion of SEBS phase in the LLDPE matrix. It exhibits that an increment in SEBS content gives increased size of the dispersed phase.

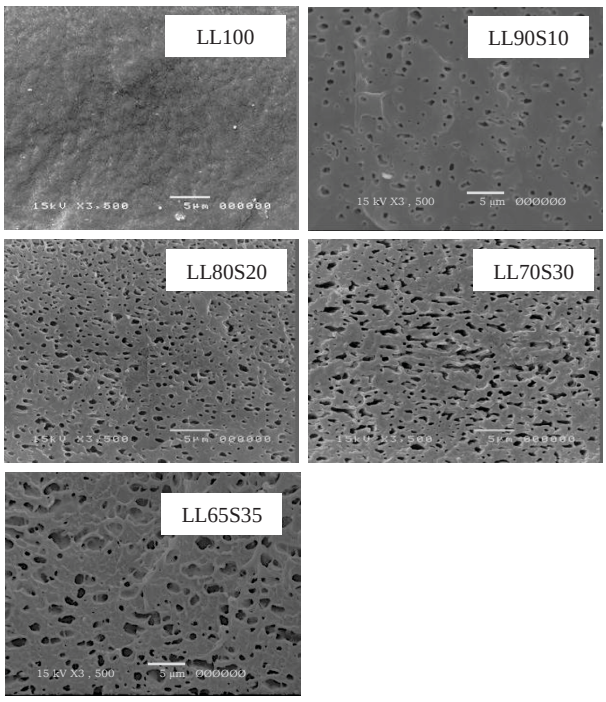

Figure 1. SEM micrographs (3500X) of cross-section of the films containing various SEBS contents.

Morphology of LLDPE/SEBS blend at the ratio of 70/30 with DOP loading (5-10%wt of SEBS) as shown in Figure 2 indicates that addition of DOP increases size of dispersed phase. This is because DOP plasticizer diffuses into the SEBS and enlarges the free volume of the dispersed SEBS.

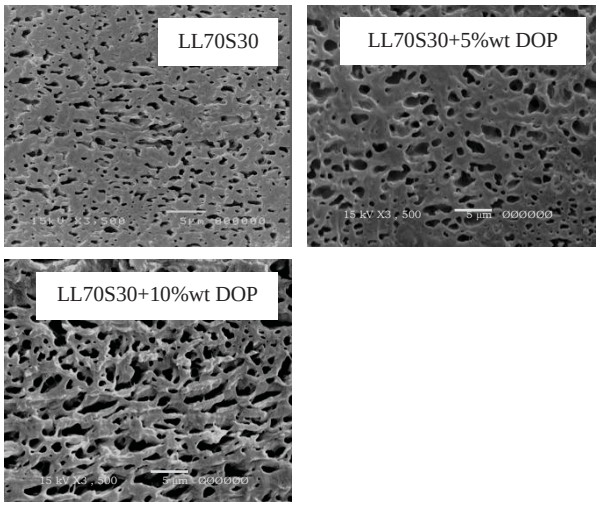

Figure 2. SEM micrographs (3500X) of cross-section of the 70LLDPE/30SEBS films with and without DOP plasticizer.

3.2 Thermal properties

The melting temperature (T_m) and crystallinity of LLDPE in all samples are listed in Table 2. T_m of all the blended films are mostly similar to that of LLDPE film. It is suggested that adding of SEBS has no effect to the crystallization growth of LLDPE phase. However, the crystallinity of LLDPE is decreased when the blends possess the amount of SEBS more than 20%wt. Besides, DOP plasticizer also has no significant effect on both T_m and crystallinity of LLDPE. This is because DOP diffuses into the SEBS phase only as reviewed in Figure 2.

Table 2: Crystalline melting temperature (T_m) and crystallinity of LLDPE in film samples

Sample	T_m (°C)	Crystallinity (%)
LL100	117	29.3
LL90S10	119	26.6
LL80S20	118	22.2
LL70S30	118	23.4
LL65S35	116	24.2
LL70S30+5%wt DOP	117	22.8
LL70S30+10%wt DOP	116	23.2

3.3 Ethylene transmission rate of films

In consistency with the morphological and thermal properties, the ethylene transmission rate of the LLDPE/SEBS films increases with increasing SEBS content as shown in Figure 3. This is because SEBS contains ethylene-butylene segments with relatively non-polar, high free volume and flexible. Therefore, the ethylene gas can soluble in the film and easily permeate through the film. While, the crystalline region in LLDPE acts as barrier for ethylene permeation.

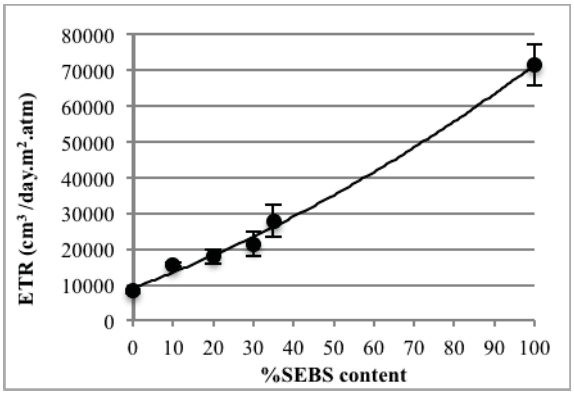

Figure 3. Ethylene transmission rate of LLDPE/SEBS films.

In the presence of 5-10%wt DOP plasticizer (Figure 4), it can be noticed that the ethylene transmission rate of the film is enhanced with increasing amount of DOP plasticizer. This is because DOP exists in SEBS phase leading to increase free volume of SEBS and thus the bigger SEBS sizes can be obtained as discussed earlier. As the result, amorphous region of SEBS is increased and therefore the ethylene transmission rate of the films is improved.

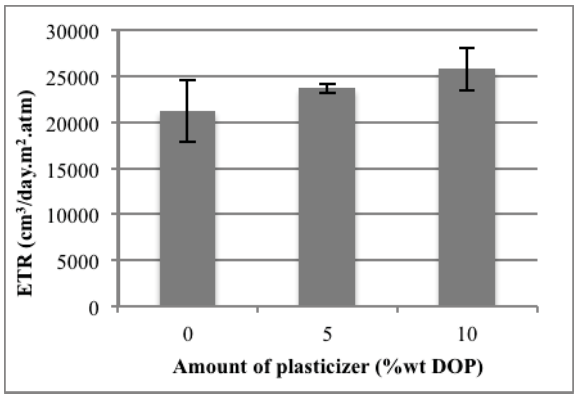

Figure 4. Ethylene transmission rate of 70/30 LLDPE/SEBS films with and without DOP plasticizer.

3.4 Tensile properties

Although high ethylene transmission rate (ETR) is observed from LLDPE/SEBS films, it is clearly seen in Figure 5 that SEBS can easily be deformed as shown by a lower stress at yield when compared with parent LLDPE film. This is because amorphous SEBS has only physical chain entanglement whereas LLDPE is required a higher stress for deformation of the chain in the crystalline region. In addition, Young's modulus and elongation at break of SEBS are lower than those of LLDPE owing to ethylene-butylene segment in SEBS providing soft and flexible nature. Therefore, Young's modulus, elongation at break and stress at yield are decreased with increasing SEBS content. Nevertheless, ultimate tensile strength of film is increased because of styrene segment in SEBS causing an increase in chain rigidity.

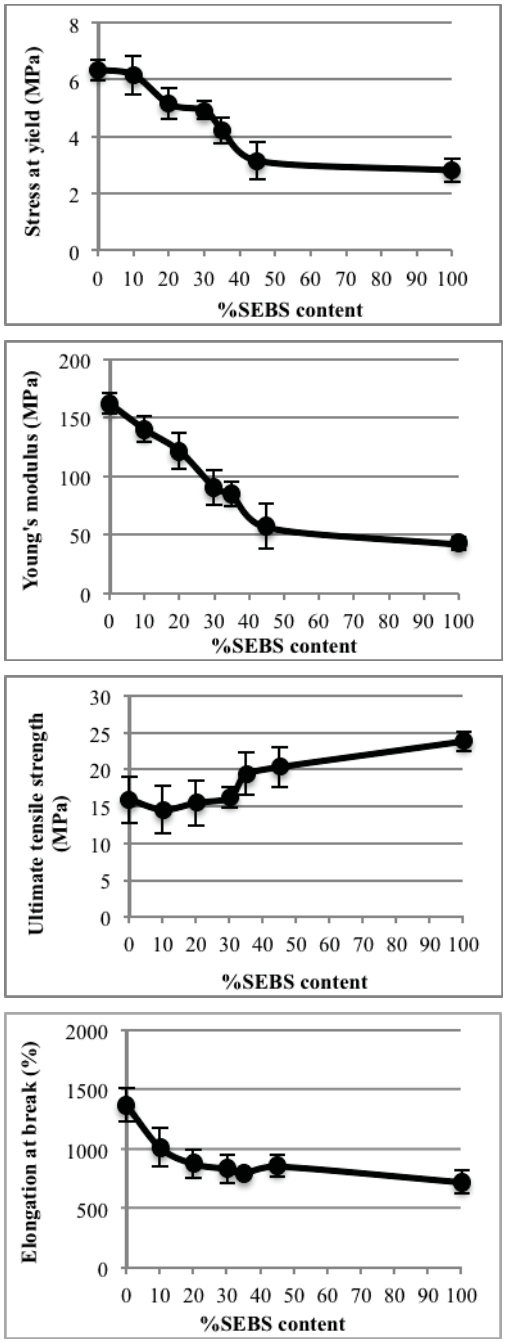

Figure 5. Tensile properties of LLDPE/SEBS films.

It is not surprise to find that, the addition of 5-10%wt DOP plasticizer into the LL70S30 blend led to a decrease in tensile properties. However, the values are still in acceptable ranges for the 5%wt DOP loading as shown in Figure 6.

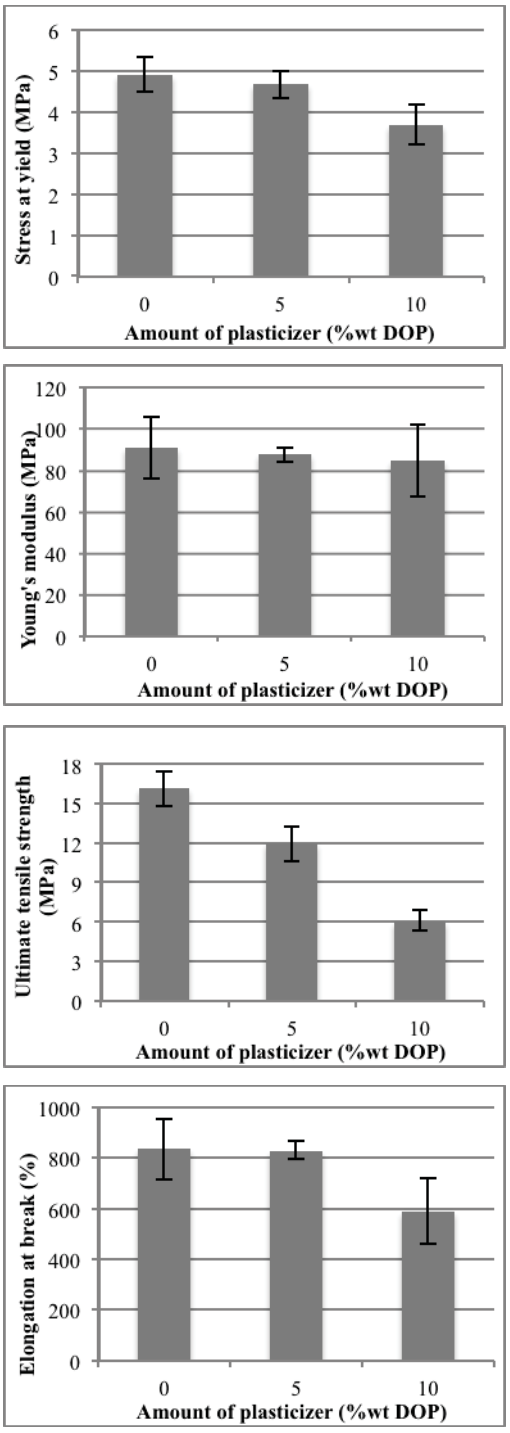

Figure 6. Tensile properties of 70/30 LLDPE/SEBS films with and without DOP plasticizer.

4. Conclusions

In this study, it was found that the addition of SEBS in the LLDPE/SEBS blends can improve ethylene transmission rate of the films. This is because SEBS is amorphous and possesses high free volume. Therefore, the ethylene gas can easily permeate through SEBS phase as compared with LLDPE phase. Although, the tensile properties, i.e., Young's modulus, elongation at break and stress at yield are decreased with increasing SEBS content. Nevertheless, ultimate tensile strength of the films are increased. Furthermore, the ethylene transmission rate of the films are enhanced with an incorporation of 5-10%wt DOP plasticizer. This is clearly because dispersed phase size of SEBS is larger owing to an increase in free volume in SEBS moeties. Although addition of the plasticizer decreased tensile properties of films, the values are still in acceptable ranges for the loading of 5%wt DOP.

Acknowledgements

Faculty of Science, King Mongkut's Institute of Technology Ladkrabang (KMITL) for financial support.

References

[1] F.B. Abeles, *Ethylene in plant Biology*, Academic Press, New York (1973).

[2] M.E. Saltveit, *J. Food Sci.* **15** (1999) 279-292.

[3] C.S. Barry and J.J. Giovannoni, *J. Plant Growth Regul.* **26** (2007) 143–159.

[4] K. Abe and A.E. Watada, *J. Food Sci.* **56** (1991) 1589–1592.

[5] S. Laowakul, *Study on Zeolite-SEBS Composite/Perfo-rated Polyolefins (LDPE and BOPP) Double-Layered Films for Improving Ethylene Permeation*, Master's Thesis, King Mongkut's Institute of Technology Ladkrabang, (2011).

[6] Y. Wang and A.J. Easteal, *Packaging Technology and Science.* **Vol. 11**, Wiley. New York (1998) pp.169-178.

SYNTHESIS OF COIR-DUST/PE COMPOSITES VIA *IN SITU* POLYMERIZATION WITH METALLOCENE/MAO CATALYST

Chatuma Suttivutnarubet[1*], Thanyaluk Yokkloy[2], Ekrarchan Chaichan[2], Bunjerd Jongsomjit[1]

[1] Center of Excellence on Catalysis and Catalytic Reaction Engineering, Department of Chemical Engineering, Faculty of Engineering, Chulalongkorn University, Bangkok 10330, Thailand
[2] Chemistry Program, Faculty of Science and Technology, Nakhon Pathom Rajabhat University, Nakhon Pathom 73000, Thailand

*E-mail: chatuma28@gmail.com

Abstract: In this study, the various amounts of coconut coir dust (0.05, 0.1 and 0.2 g) were used as a catalytic methylaluminoxane supported filler in the *in situ* polymerization of ethylene with metallocene catalyst to produce environmental-friendly polymer composites. The polymer composites were obtained from the *in situ* polymerization with the metallocene catalyst and MAO/supported filler,prepared from immobilizing MAO onto the coconut coir dust by impregnation method. The properties of composite products were investigated, including morphology by scanning electron microscope (SEM) and thermal properties by thermal gravimetric analysis (TGA) and differential scanning calorimetry (DSC). Moreover, it is because in the *in situ* polymerization the fillers have to be introduced during polymerization (generating of polymer), the catalytic activities of the polymerization systems were influenced by the filler that need to be concerned together. It was found that the lower activity the higher amount of coconut coir dust because of too steric hindrance of coir dust particle preventing catalytic active sites from the reaction with MAO in the activation step.

1. Introduction

Polyethylene is a type of thermoplastics which is the most widely used as package, film, toys and cable cover because it has a great deal of advantages, such as easy processibility, appropriate for many applications and low cost. Therefore, a large amount of polyethylene waste is released into the environment leading to severe environmental problems. Using natural materials especially from plants as reinforcement fillers in the polyethylene can induce the polyethylene to be partial biodegradable, consequently resolving the environmental problems to some extent [1].

Since the natural materials are biodegradable, the composites of natural fibers and synthetic polymers (which are non-biodegradable) may offer a new class of materials that can provide environmental protection partially although not fully. By embedding natural fibers e.g. kenaf, jute, coir, sisal etc. into a polymeric matrix, new fiber reinforced materials called "biocomposites" can be produced. Coir is an abundant, versatile, renewable, cheap, and biodegradable which used for making a wide variety of products. Using coir dust as a filler has also been investigated previously with a variety of polymer materials [2]. However, there are major drawbacks of using this coir dust as reinforcements in such matrices including poor interfacial adhesion between polar-hydrophilic coir dust and nonpolar-hydrophobic matrix, and poor dispersion of coir dust inside polymer matrix [3]. Hence, in present article the promising technique to overcome the mentioned drawbacks that is the *in situ* polymerization will be addressed here.

In this study, metallocene catalyst was used for polyethylene synthesis with coir dust as filler. The activity of metallocene catalyst in polymerization systems and the properties of the obtained coir dust/PE composites were investigated.

2. Materials and Methods

2.1 Materials

Ethylene gas (99.9%) was devoted from National Petrochemical Co., Ltd. Thailand. Methylaluminoxane (10% in toluene) was donated from Tosoh Akso, Japan. The rac-Ethylenebis(indenyl)zirconium dichloride ($Et(Ind)_2ZrCl_2$) was supplied from Aldrich Chemical company. Coir dust was supplied from local area. Toluene was devoted from EXXON Chemical Ltd., Thailand. Ultra high purity argon gas (99.999%) was purchased from Thai Industrial Gas Co., Ltd. Hydrochloric acid (Fuming 36.7%) was supplied from Sigma. Methanol (Commercial grade) was purchased from SR lab.

2.2 Preparation of coir dust

The coir dust was heated at 150 °C for 2 h under argon atmosphere with a heating rate of 10 °C min^{-1}.

2.3 Preparation of stock catalyst solution

$Et(Ind)_2ZrCl_2$ 0.0083 g ($1.98x10^{-5}$ moles) was added into 20 mL of toluene solution, stirred at room temperature giving yellow transparent solution.

2.4 *In situ* polymerization

The ethylene polymerization reactions were performed in a 100 ml semi-batch stainless steel

autoclave reactor equipped with a magnetic stirrer. From the beginning, the desired amount of the coir dust (0.05, 0.1 and 0.2 g) and methylaluminoxane (MAO) 1.1 mL ($[Al]_{MAO}/[Zr]$=1135) were mixed together and stirred for 30 min aging at room temperature. Then, $Et(Ind)_2ZrCl_2$ 1.5 mL ($5x10^{-5}$ M) along with toluene (to make total volume of 30 ml) was put into the reactor that was frozen in liquid nitrogen to stop reaction for 10 min. Next, the reactor was evacuated to remove argon before it was heated up to polymerization temperature (70°C) following by, ethylene was fed into the reactor equipped with pressure gauge to start polymerization. After all ethylene was consumed (6 psi from pressure gauge), the reaction was terminated by addition of acidic methanol (0.1% HCl in methanol) and stirred over night. Finally, filtered this suspension to obtain wet polymer, was washed with methanol and dried at room temperature to obtain dry polymer as white powder.

2.5 Characterization

2.5.1 Scanning electron microscopy (SEM):

SEM was used to examine the morphologies of coir dust and polymer composites. The SEM of JEOL mode JSM-6400 was applied.

2.5.2 Differential scanning calorimetry (DSC):

The melting temperature of polymer composites were measured by mean of DSC at heating rate of 10 °C min^{-1} from 30 – 200 ◦C. The heating/cooling cycle was run twice to ensure that the previous thermal history was erased and provided comparable conditions for all samples. Approximately 10 mg of sample was used for each measurement.

2.5.2 Thermo gravimetric analysis (TGA):

TGA was used to determine thermal stability in term of percentage weight in sample as a function of temperature. Sample preparation consists of weighing a crucible, loading the sample about 2-3 mg into the crucible, weighing the full crucible, and setting it on a tray. The analysis was performed under nitrogen atmosphere gas at gas flow rate of 100 mL min^{-1}. The sample was heated from 25°C to 600°C at a constant rate of 10 °C min^{-1} and then cooled naturally.

3. Results and Discussion

3.1 Characterization of coir dust

The morphology of coir dust was characterized by scanning electron microscopy (SEM) as shown in Figure. 1. The isolated particles about 170 – 520 μm with a porous structure were observed.

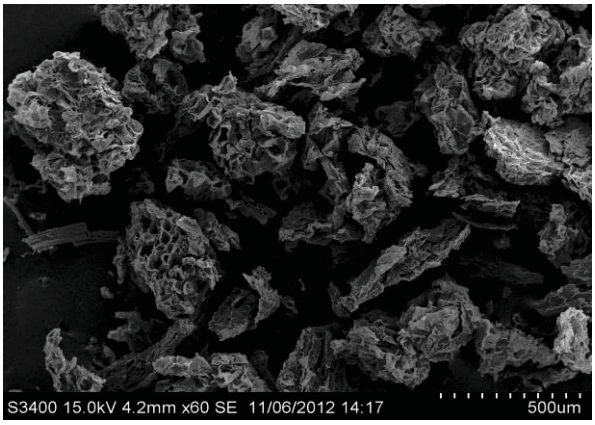

Figure. 1 SEM micrograph of coir dust

3.2 Effect of the amount of coir dust on catalytic activity

After coir dust was covalently bonded with methylaluminixane (MAO), it was introduced into the polymerization system along with the metallocene catalyst. Activities and yields of coir dust/PE composites are shown in Table 1. It is seen that catalytic activity of pure polyethylene (homogenous catalytic system, run 1) is the highest. For the systems with the coir dust filler (heterogeneous system, run 2-4), the catalytic activity was inversely proportional with the coir dust content. In addition, the production yield of the heterogeneous systems was substantially lower than that of the homogenous systems. It may be due to steric hindrance of coir dust particle preventing catalytic active sites from the reaction with MAO in the providing less space for monomer attack in the propagation step[4].

3.3 Characterization of coir dust composites

3.3.1 Differential scanning calorimetry (DSC)

The melting temperature (T_m) of polymer evaluated was by differential scanning calorimeter (DSC) was also shown in Table 1. It can be observed that there was no a significant change in the melting temperature for all systems. This suggests that the coir dust filler does not affect on the crystallization process of the polymers. The results were consistent with those obtained from Zapata et al. [5]. These high melting temperatures of the polyethylene/coir dust composites (131 – 134°C) indicates the branchless structure of the composites [6].

3.3.2 Scanning electron microscopy (SEM)

The morphologies of polymers obtained with various coir dust loadings were observed by scanning electron microscopy technique as shown in Figure. 2. As observed, all coir dust/PE composites upon various coir dust loadings exhibited the similar morphologies. These results indicated that the amount of coir dust did not affect on the morphology of polymer. Furthermore, there was no obviously leaching of coir dust filler from the polymer matrices, indicating good interaction between two materials. In addition, the visual inspection of these coir dust/PE composites looks like powdery particles.

Run	Sample	Filler (g)	Yield (g)	Time (s)	Activity (kg polymer/mol Zr.h)	T_m (°C)
1	polyethylene	-	0.9140	144	15233	132
2	coir dust/PE composites	0.05	0.5848	126	11139	131
3	coir dust/PE composites	0.1	0.6014	186	7760	134
4	coir dust/PE composites	0.2	0.5388	207	6246	132

Table 1: Activity and characteristics of coir dust/PE composites via in situ polymerization with metallocene catalyst.

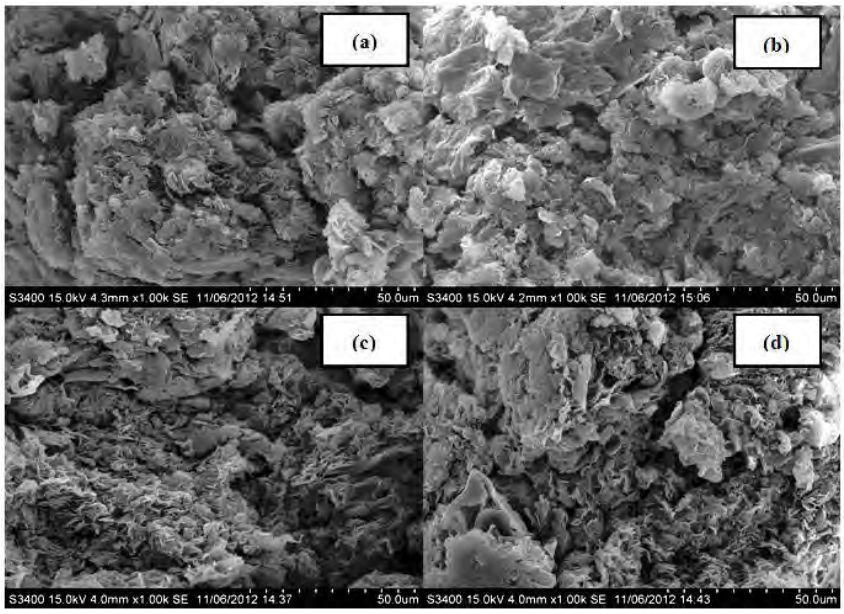

Figure. 2. Morphologies of (a) polyethylene, (b) coir dust/PE composites (0.05 g of filler), (c) coir dust/PE composites (0.1 g of filler) and (d) coir dust/PE composites (0.2 g of filler)

3.3.3 Thermo gravimetric analysis (TGA)

Table 2: The degradation onset temperature off different materials

Sample	Temperature at weight loss(°C)	
	5 %	10%
pure PE	457	441
coir dust	55	171
PE/coir-dust (0.1 g)	271	439

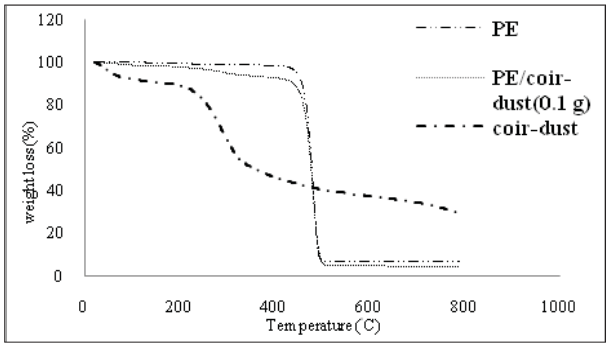

Figure.3. TGA thermograms of pure PE, PE/coir dust (0.1 g) and coir dust

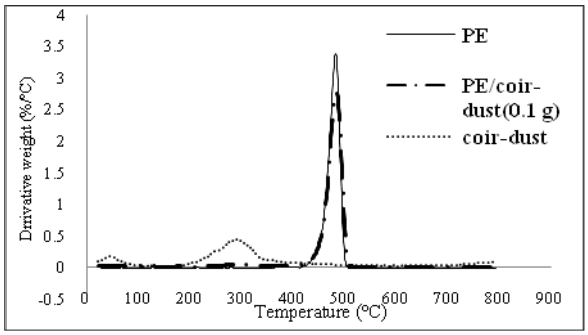

Figure.4. DTA thermograms of pure PE, PE/coir dust (0.1 g) and coir dust

Figures 3 and 4 show the TGA-thermograms and the DTA-thermograms of pure coir dust, pure PE and coir dust/PE composites. Temperatures for all thermal events are summarized in Table 2. It can be seen that the decomposition profiles of the coir dust are characterized by two peaks. The initial weight loss obtained in the region of 50-100 °C was mainly due to moisture evaporation and water adsorbed to the coir dust [7]. Thermal degradation of lignocellulosics starts by hemicelluloses decomposition between 190 and 260 °C followed by cellulose decomposition between 210 and 260 °C followed by cellulose decomposition between 240 and 360 °C. This result was similar to

that reported in literature for in *natura* coconut shell endocarp as expected, since coir dust is a residue from coconut shell process [8].

From the result of TGA, it was observed that in the case of composites of polyethylene with coir dust. The 5% weight-loss temperature and 10% weight-loss temperature of the coir dust/PE composites was lower compared with pure PE. This behavior points out that although the addition of coir dust content led to a decrease in the thermal stability. Reduction of degradation temperature for the coir dust composites may imply that can be easier degraded under the environmental condition than the pure polymer, thus having lower environmental impact. Therefore, the use of coir dust as filler material for polymer-based composites can contribute to; both reduce the solid waste and aggregate commercial value to the final product, increasing the income of the community of coconut producers.

4. Conclusions

In summary, the synthesis of coir dust/PE composites can be achieved via the *in situ* polymerization of ethylene using a metallocene catalyst. The homogenous catalytic system gives the highest activity. The maximum activity was found at the specified condition with the certain amount of coir dust (0.05 g). When the coconut coir dust was increased (0.2 g), the activity decreased because of increasing steric hindrance. No significant change in the melting temperature of coir dust/PE composites was observed by DSC. Based on SEM, it can be seen that all coir dust/PE composites upon various coir dust loadings exhibited the similar morphologies. Considering the 5% weight-loss temperature and 10% weight-loss temperature of the coir dust/PE composites, these were lower compared with pure PE.

Acknowledgements

The authors would like to thank the financial support from the Thailand Research Fund (TRF).

References

[1] J. Tong, B.Z. Moayad, L. Ren and B. Chen, *Int. Agric. Eng. J.* **13** (2004) 71-86.
[2] J. Rout, M. Misra, S.S. Tripathy, S.K. Narak and A.K. Mohanty, *Polym. Compos.* **22** (2001) 770-778.
[3] J.J. Maya and A.D. Rajesh, *Polym. Compos.* **29** (2008) 187-207.
[4] B. Jingsomjit, E. Chaichana, P. Praserthdam, *J. Mater. Sci.* **40** (2005) 2043-2045.
[5] P. Zapata, R. Quijada, C. Covarrubias, E. Moncada and J. Retuert, *J. Appl. Polym. Sci.* **4** (2009) 2368-2377.
[6] T. Nampitch, R. Thipmanee, R. Magaraphan, Agro-Industry, Bangkok: Kasetsart University, Thailand, (2010), pp. 34-41.
[7] R.F. Morsyleide, C. Bor-sen, M.S. Eliton, W.F. Delilah, W.T. Tina, M.H.C. Williams, O.J. William, I.H. Syed, *Bioresource. Technol.* **100** (2009) 5196–5202.
[8] J.S. Macedo, M.F. Costa, M. Tavares, R. Thire, *Polym. Eng. Sci.* **50** (2010) 1466-1475.

PROPERTIES OF THERMOPLASTIC ELASTOMER PREPARED FROM POLYPROPYLENE AND NATURAL RUBBER LATEX BLENDS

Pichaya Tayong, Watcharaporn Ritjarern, Wunpen Chonkaew *

[1] King Mongkut's University of Technology Thonburi, Department of Chemistry, Faculty of Science, Bangmod, Thongkru, Bangkok, 10140, Thailand

* Author for correspondence; E-Mail: wunpen.cho@kmutt.ac.th, Tel. +66 2 4708843, Fax. +66 2 4708843

Abstract: The thermoplastic elastomers based on polypropylene (PP) and natural rubber latex blends were prepared. Two different kinds of natural rubber, i.e. the experimental epoxidized natural rubber (ENR) with mole percentage of epoxide of 24.7 and the unmodified natural rubber (NR), ranged from 0 to 50 part per hundred (pph) were used to blend with PP containing 10 %wt PP-g-MAH compatibilizer at temperature of 190 °C in an internal mixer. The influence of rubber content on thermal and mechanical properties was investigated. The TGA results revealed that PP/PP-g-MAH/ENR blends showed a higher thermal resistance than PP/PP-g-MAH/NR blends. The thermal stability of both blend systems decreased with increasing rubber contents. The melting temperature of the blends did not change significantly, when the rubber was added, as compared to the neat PP. By contrasts, the crystallinity was found to reduce as the ratio of rubber phase increased. Impact resistance and elongation at break of the both blend systems were enhanced by adding more rubber whereas Young's modulus and tensile strength decreased with the rubber addition. However, the Young's modulus and the strength of PP/PP-g-MAH/ENR blends were higher than those of the PP/PP-g-MAH/NR blends.

1. Introduction

Thermoplastic elastomers (TPEs) belong to a class of polymers that combine the processibility of thermoplastic and the functional performance of elastomer [1]. Generally, TPEs can be divided into 2 classes—TPEs based on blocked copolymer and the TPEs based on thermoplastic-rubber blend. Attentions play to the TPEs based on thermoplastic-rubber blend over the year. The continuous plastic matrix allows the melt processing of the blend whereas the dispersed rubber particles help elastic recovery after mechanical deformation [2]. In this work, TPEs based on thermoplastic-rubber blend were prepared by blending natural rubber and polypropylene in varying proportions [3]. Polypropylene is selected for the blends because it has an excellence in molding processability and good mechanical properties. The addition of rubber into PP was reported to enhance toughness while maintaining stiffness, strength and processability [4]. However, unvulcanized natural rubber has a low thermal resistance due to the presence of >C=C< in backbones. The modifying natural rubber with more polar functional groups including epoxidized natural rubber, natural rubber grafted poly(methyl methacrylate), and maleated natural rubber was reported to improve the thermal stability [3]. Moreover, chemical modification of natural rubber molecules enhanced blend compatibilization and improved some useful properties of the blends [3]. Therefore in the work, epoxidized natural rubber was synthesized and blended with polypropylene. The polypropylene grafted with maleic anhydride (PP-g-MAH) was also used as compatibilizer to increase the compatibility between rubber and plastic phases [2]. The purpose of this study was to compare the mechanical and thermal properties of the TPEs prepared from PP/NR and PP/ENR in the presence of the PP-g-MAH compatibilizer without dynamic vulcanization. The effects of blend ratio on the melting behaviour and crystallization of the TPEs were also investigated.

2. Materials and Methods

2.1 Materials

Isotactic polypropylene grade P701J was supplied by SCG Performance Chemicals, Thailand. PP-g-MAH grade PO1020 was supplied by Exxon Mobil Chemical, Thailand. The natural rubber latex (NRL) used was medium ammonia NR latex, and was supplied by Thai Rubber Latex, Thailand. The percentage of dry rubber content (DRC) in the NR latex was 62.13. Hydrogen peroxide, formic acid and methanol used were analytical pure reagent.

To prepare the epoxidized natural rubber latex (ENRL), the NR latex was diluted with deionized water to obtain the 20 % DRC latex. 10 phr triton-X was added to stabilize the NR latex. The mixtures were then epoxidized by slowly adding 0.75 mole formic acid and 0.75 mol hydrogen peroxide to a mole of isoprene unit, magnetically stirred and refluxed at 55 °C for 4 hours. The modified latex was obtained and used to prepare polymer blends.

To investigate the structure, molecular weight and percentage of epoxidation, the latex was precipitated in methanol and dried in air. The dried rubber was then dissolved in toluene, casted on the ZnSe glass. ATR-FTIR spectrum of the modified NR was characterized compared to that of the neat NR. The characteristic peaks for epoxidized ENR were observed for symmetric and asymmetric epoxide stretching at 1248 and 870 cm^{-1}. The epoxidation level of ENRL was examined by T_g determination using DSC, and was found to be 24.75% as compared to the ENR standard. The average molecular weights determined by GPC

were found to be 1.23×10^5 for M_n and 3.93×10^5 for M_w.

2.3 Preparation of thermoplastic elastomers (TPEs)

PP pellets (90 %) were premixed with a PP-g-MAH compatibilizer (10 %) in a beaker. To obtain the TPEs with PP/NR blend ratios of 95/5, 85/15, 70/30 and 50/50, the latex containing 5, 15, 30 and 50 pph rubbers each was directly mixed with the mixed PP (PP + 10 %wt PP-g-MAH) 95, 85, 70 and 50 pph, respectively. The mixtures were dried in an oven at a temperature of 80 ^oC, and then mixed thoroughly using an internal mixer (Chareon Tut, Thailand) at temperature of 180 ^oC with a rotor speed of 45 rpm, and mixing time of 13 minutes. The TPEs obtained were then cut into small pieces and dried in an oven at temperature of 80 ^oC before molding at 135 ^oC into sheets of 3 mm thickness in a laboratory press.

2.4 Mechanical testing

Tensile tests were performed using an Instron tensile tester equipped with 50 kN load cell. Samples were cut in dog-bone tensile specimens with the approximate dimension of 25 mm (gauge length), 7 mm (gauge width) and 3 mm (thickness). The tests were carried out at room temperature using a cross-head speed of 10 mm/min, and at least five samples were tested. The tensile modulus, tensile strength and fracture strain were computed from the measured stress-strain curves.

Izod impact tests were performed at room temperature using pendulum impact tester (Yasuda Seiki Seisakusho 9347, Intro Enterprise) according to ASTM D256-10. At least five specimens were tested and the average results were reported with standard deviation.

2.5 Thermal properties

The melting behavior and crystallinity of the blends were examined by differential scanning calorimetry (DSC) using DSC7, PerkinElmer (USA). Approximately 10 mg samples were placed in aluminum pan, heated from 30 ^oC to 250 ^oC at a heating rate of 10 ^oC/min in nitrogen atmoshere, then held at 250 ^oC for 5 minutes, subsequently scanned from 250 ^oC to 30 ^oC at cooling rate of 10 ^oC/min, held at 30 ^oC for 2 minutes and then heated from 30 ^oC to 250 ^oC at heating rate of 10 ^oC/min. The melting temperature (T_m) was determined as the peak temperature of the second heating scan, the crystallization temperature (T_c) was determined as peak temperature of the cooling curve and % crystallinity (%X_c) was calculated according to Equation (1) [5]:

$$\% X_c = \Delta H_m/(1\text{-}x)\Delta H_{total} \quad (1)$$

where ΔH_m is the enthalpy of fusion determined from the area of the DSC endotherm, ΔH_{total} is the enthalpy of fusion for 100% crystalline PP, which for 100% crystalline PP was taken as 207.1 J/g [5] and x is the weight fraction of NR latex in the sample.

Thermal stability of samples was determined using TGA/DSC1, Mettler Toledo (Switzerland). The tests were carried out in N_2 atmosphere at a heating rate of 20 ^oC/min from 40 to 800 ^oC, and then in air from 800 to 1000 ^oC at the same heating rate. The initial degradation temperatures (T_{id}) and the peak degradation temperatures (T_p) were determined from the thermograms (TGA curves) and the derivative thermograms (DTG curve), respectively.

Table 1: Melting temperature (T_m) and % crystallinity of the neat component and TPEs

Sample	Blend ratio	T_m (^oC)	T_c (^oC)	ΔH_m	% X_c
PP		159.7	106.5	73.7	35.6
PP/NR	95/5	160.0	109.3	54.7	27.8
	85/15	159.5	109.6	35.5	20.2
	70/30	159.9	110.1	32.3	22.3
	50/50	159.2	109.3	23	22.2
PP/ENR	95/5	158.9	108.3	60.6	30.9
	85/15	159.5	109.0	39.1	22.2
	70/30	159.5	110.3	36.1	24.9
	50/50	159.7	111.1	25.5	24.6

3. Results and Discussion

3.1 Melting behaviour and crystallization

The melting temperature (T_m), peak crystallization temperature (T_c), heat of fusion (ΔH_m) and percent crystallinity of the TPEs are given in Table 1. The T_m did not change up on the addition of the NR and ENR. This result implied that the lamellar size, the crystal form and the perfection of a crystal unit [6] of PP did not change with the rubber addition. However, the increase of T_c was observed. The T_c of TPEs increased from 106 ^oC for PP to about 110 for TPEs. The crystallization of TPEs started faster than that of the neat PP. The addition of NR and ENR to PP resulted in the molecular interfering of NR molecules with the PP crystallization [7]. The rubber molecules possibly somewhat facilitated the mobility of PP molecules, leading to an increase in cooling crystallization rate. The heat of fusion (ΔH_m) of all blend compositions was lower than that of the neat PP. Moreover, ΔH_m decreased with decreasing PP compositions. The decrease in heat needed to melt the polymer crystal reflected the decrease in % crystallinity. This confirmed that the crystallization of PP was interfered by the presence of the NR phase. To study the influence of a melt rubber phase on crystallization of PP, % crystallinity of TPEs recalculated for the PP mass (% X_c) was determined (see Equation (1)). % X_c decreased with an increasing NR content in the blends, reached a minimum at about a composition of 15 pph in PP, then increased slightly after 30 pph, and finally levelled off after further

addition. The slight increase in % X_c after the addition of 30 % NR indicated the increase in PP chain mobility by the melt rubber phase. The similar tendency as TPE containing PP/NR was found in TPE containing PP/ENR. However, % X_c of the blends containing ENR was higher than those of the blends containing NR.

3.2 Mechanical properties

The tensile properties of TPEs as a function of rubber content are shown in Figures 1 to 3. It was found from Figure 1 that the Young's moduli of TPEs, prepared both from the blends of PP/NR and PP/ENR decreased as compared to the neat PP. The dependence of modulus on rubber loadings was observed. The higher NR loading, the lower the modulus was observed. The TPEs prepared from the blends of PP/ENR exhibited a higher modulus than those prepared from PP/NR at all blend ratios. The dependences of tensile strength on rubber loadings and types of rubbers were similar to those found in modulus. Tensile strength was observed to be less by about 17 % and 24% in blends of PP/ENR and PP/NR, respectively as compared to the neat PP. The decreases in the Young's modulus and the tensile strength were attributed to the decreases in % crystallinity of the blends (See Table 1).

Figure 3 shows the changes in % elongation at break as a function of blend ratios. It was found that % elongation at break of the TPEs increased slightly by about 5 % to 28 % up on the rubber addition. No difference in % elongation at break was found between the TPEs prepared from PP/NR and those from PP/ENR, except at the highest loading. The PP/ENR blend at composition of 50/50 has a lower value than PP/NR.

Figure 4 shows the impact strength of TPEs as a function of the blend ratios. The addition of the rubber phases, both NR and ENR, promoted the impact resistance of the materials. The impact resistance increased with an increase in rubber loadings. The TPEs prepared from the blend of PP/ENR has a lower impact resistance than those prepared from PP/NR, especially at the blend ratio of 50/50. This result was attributed to the higher % crystallinity of PP/ENR samples.

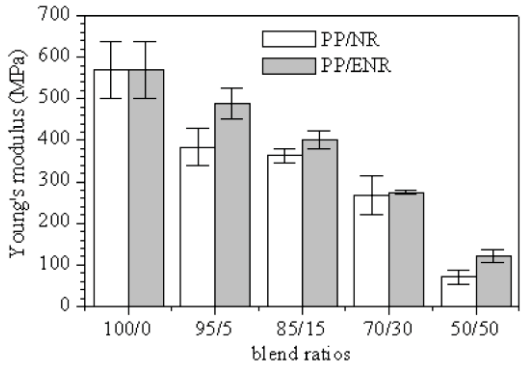

Figure 1. Young's modulus of the TPEs at various blend ratios.

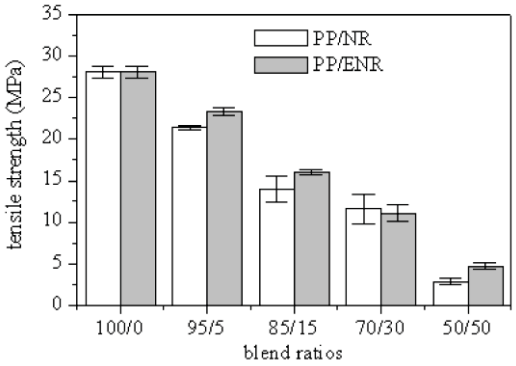

Figure 2. Tensile strength of the TPEs at various blend ratios.

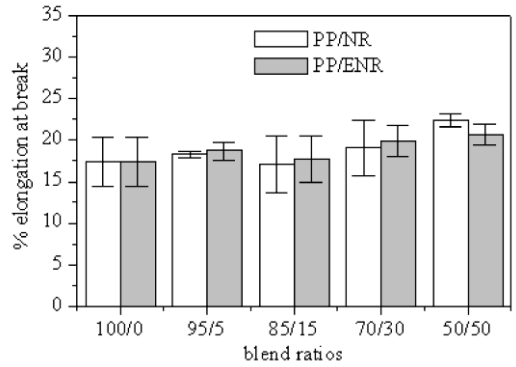

Figure 3. % Elongation at break of the TPEs at various blend ratios.

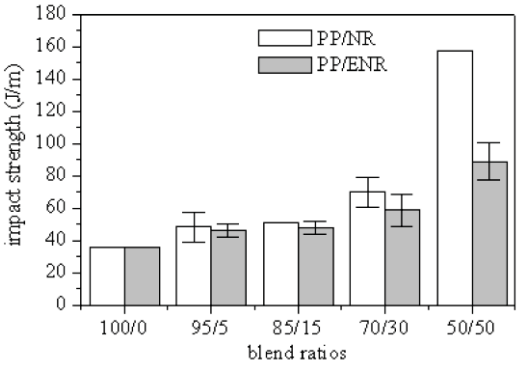

Figure 4. Impact strength of the TPEs at various blend ratios.

3.4 Thermal degradation

The initial degradation temperatures determined from TGA thermograms and the peak temperature determined from DTG thermograms of the TPEs are summarized in Table 2. Degradations of the neat PP and NR were in one stage of weight loss, whereas those of TPEs were in two stages. TPEs prepared from the blends of PP/NR and PP/ENR only at blend ratios of 95/5 and 50/50 were selected for this study. PP started to degrade thermally at 452 ^{o}C whereas NR started at 330 ^{o}C. The one stage of degradation of PP arose from the random chain scission and intermolecular transfer involving tertiary hydrogen abstractions from polymer by the primary radicals [8],

whereas the one step of NR was due to the random chain scission of isoprene units in NR. When a small amount of NR (5 pph) was added in PP, the one stage of degradation retained. The initial degradation temperature (T_{id}) of PP/NR at blend ratio of 95/5 was at an intermediate value (440 ^{o}C). The peak degradation temperature shifted to a higher value as compared to the neat PP. This result indicated the compatibility between NR and PP phases, and was possibly due to the presence of a PP-g-MAH compatibilizer. By further adding the NR phase, i.e. 50 pph NR, the thermal degradation of TPE became two stages, corresponding to the degradation of NR and PP parts, respectively. In case of TPEs prepared from PP/ENR, similar situations were observed. However, the incorporation of ENR, instead of NR, improved the thermal stability of TPEs. The addition of 5 pph ENR increased the T_{id} of TPEs from 440 to 443 ^{o}C and T_p from 474 to 478 ^{o}C. With further addition of 50% pph ENR, T_{id} and T_p of the first and the second stages shifted to much higher degradation temperatures as compared to the neat PP. The thermal degradation of polymer blend depended on morphology and extent of interaction between phases [8]. The improved thermal stability of the blends at 50/50 blend ratio was possibly due to the co-continuous phase of rubber (NR or ENR) formed along with PP.

Table 2: Thermal properties of TPEs at various blend ratios.

composition	1^{o} stage (^{o}C)		2^{o} stage(^{o}C)	
	T_{id}	T_p	T_{id}	T_p
PP	452	472		-
NR	330	356	-	-
PP/NR: 95/5	440	474		-
PP/ENR: 95/5	443	478		-
PP/NR: 50/50	367	392	459	477
PP/ENR: 50/50	403	435	468	481

4. Conclusions

In this study, TPEs were successfully prepared from the blends of PP/NR and from PP/ENR in the presence of a PP-g-MAH compatibilizer without dynamic vulcanization. The incorporation of rubber phase in PP improved the toughness, but scarified with the reduction in Young's modulus and tensile strength. The modulus and tensile strength of TPEs prepared from the PP/ENR blends were found to be higher than those of TPEs prepared from the PP/NR, but an opposite situation was found in case of the impact resistance. The changes in mechanical properties could be explained by the reduction in % crystallinity as compared to the neat PP. The dependence of rubber loadings on the decrease in % crystallinity was found up to 15 pph of rubber contents, but then slightly increased and remained with further additions. The compatibility between PP and rubber was found the in the blends of PP/NR and PP/ENR at small rubber content (5 pph). Thermal stability of TPEs prepared from PP/ENR blends was higher than that of TPEs prepared from PP/NR.

Acknowledgements

Author would like to gratefully thank the Department of Chemistry, KMUTT for financial support throughout this work, and Mettler Teledo, Ltd, Thailand for TGA measurements. Acknowledgements are also given to the Nation University project held at KMUTT.

References

[1] P. Sae-Oui, C. Sirisinha, P.Sa-nguanthammarong and P. Thaptong, *Polym Test.* **29** (2010) 346-351.
[2] Y.-W. Chang, J. K. Mishra, S.-K. Kim and D.-K. Kim, *Mater. Lett.* **60** (2006) 3118-3121.
[3] C. Nakason, S. Saiwari and A. Kaesaman, *Polym. Test*, **25** (2006) 413-423.
[4] H. Ismail and Suryadiansyah, *Polym. Test.* **21** (2002) 389-395.
[5] G.M. Shashidhara and S.H. Kameshwari Devi, *Indian J. Eng. Mater. Sci.* **18** (2011) 69-78.
[6] E.G. Bajsić, A. Pustak, I. Šmit and M. Leskovac, *J. Appl. Polym. Sci.* **177** (2010) 1378-1384.
[7] S.Mahapram and S. Poompradub, *Polym. Test.* **30** (2011) 716-725.
[8] S. George, K.T. Varuhese and S.Thomas, *Polymer* **41** (2000) 5485-5503.